ANGLIA RUSKIN UNIVERSITY

INVESTIGATION OF THREE-PHASE NOZZLE FLOW (WATER- SAND -AIR) IN AN INNOVATIVE SAND-BLASTING SYSTEM

MAJID ABBASALIZADEH RAJBARI

A Thesis in partial fulfilment of the requirements of Anglia Ruskin University for the degree of Doctor of Philosophy

Submitted: JANUARY 2011

Acknowledgement

Firstly, I would like to express my deep and sincere gratitude to my supervisor, Professor Hassan Shirvani who provided a good basis for the present thesis by his personal advice and constant encouragement. His wide knowledge and his logical way of thinking have been of great value for me.

I am deeply grateful to my supervisors, Dr. Ayoub. Shirvani and Dr. Iraj Mirzaee (Urmia University) for their detailed and constructive comments, and for their important support throughout this work

My thanks all also extends to my scholarship sponsor Farrow System Ltd for financing of my study through the university and acknowledge the financial, academic and technical support of the Anglia Ruskin University, particularly in the award of a postgraduate research studentship that contributed to financial support for this research. My warm thanks are due to Dr. A. Ramesanpour for his kind encouragement and comments in this study.

Last but not least, I take this opportunity to express my profound gratitude to my beloved parent and family for their kind support and being patient during my study in the UK which certainly has started me in the exceptional path of my career.

ANGLIA RUSKIN UNIVERSITY

ABSTRACT

FACULTY OF SCIENCE AND TECHNOLOGY

DOCTOR OF PHILOSOPHY

INVESTIGATION OF THREE-PHASE NOZZLE FLOW (WATER- SAND -AIR) IN AN INNOVATIVE SAND-BLASTING SYSTEM

By: MAJID ABBASALIZADEH RAJBARI

JANUARY 2011

The study presented herewith was mainly focused on the numerical analysis of air-sand-water three-phase turbulent flow through converging-diverging nozzle. For this purpose dispersed flow of air-sand-water by various air inlet pressures, ambient air inlet temperature, sand particles and water droplets by different mass flow rates and temperature were considered. This study puts emphasis on sand blasting nozzle which is employed in Farrow abrasive system. Two-way turbulence coupling between particles/droplets and air flow as well as interference between the incident stream of particles and rebounded from the wall were applied in the numerical model. In addition, the shock wave which is produced in supersonic flow at diverging part of nozzle was considered. In order to capture the turbulent flow features accurately, *Standard*, *RNG* and *Realizable k-ε* models as well as *Spalart-Allmaras* and *Reynolds Stress* turbulence models were tested. Meanwhile, *Eulerian Model* and *Discrete Phase Model* were employed for simulating of multi-phase flow through the nozzle. Eventually, *Realizable k-ε Discrete Phase model* was utilized in the present study. Since there is not any experimental or analytical result on three-phase flow through the nozzle, for validation of model, the same turbulent and multi-phase models were utilized on air-water two-phase flow. The obtained results were in good agreement with the experimental data. According to the results of three-phase flow simulation, the averaged exhaust momentum of sand particles had inverse proportion with water mass flow rate. The increasing of air inlet pressure had significant effect on mean exhaust velocity of sand particles. Moreover, the air exhaust velocity had direct proportion with inlet temperature of water droplets and sand particles. This investigation may be used in further studies related to the optimisation of sand blasting nozzle in different working conditions.

Table of Contents

List of Figures

List of Tables

Nomenclature

A	area of the cross section of duct or pipe
A^*	throat area
$\vec{A}$	surface area vector
a_{ij}	linearized coefficient for ϕ_{ij}
a_p	linearized coefficient for ϕ_p
C_D	drag coefficient
C_V	added-mass coefficient
C_μ	an empirical constant (= 0.09)
c_p	specific heat at constant pressure
$c_{vm,q}$	virtual mass coefficient
D	diffusivities, pipe diameter in internal flow
D_a	nozzle internal diameter for any other abrasive
D_H	hydraulic diameter
D_{ij}	turbulent and molecular diffusion
D_s	nozzle internal diameter of sand
d	distance from the wall
dU	exact differential and incremental changes in internal energy
$d_{e,q}$	equivalent spherical diameter of dispersed phase
d_q	disperse phase diameter
e^*	total internal energy per unit mass
$\vec{F}_c$	force due to particle-particle and particle-wall collision
$\vec{F}_f$	frictional force
F_{ij}	production by system rotation
$\vec{F}_{lift,q}$	lift force
F_{Nk}	force imposed on component *N* from other components in *k* direction
$\vec{F}_q$	net external body force
$\vec{F}_{vm,q}$	virtual mass force

f body forces, drag factor

G_p turbulence generation in continuous phase

G_{pe} extra generation of turbulence in continuous phase

G_ν creation of turbulent kinematic viscosity

$\vec{g}$ gravitational acceleration

g_i component of the gravitational vector in the direction of *i*

I turbulence intensity

$\bar{\bar{I}}$ unit tensor

K_{pq} inter-phase momentum exchange coefficient

k turbulence kinetic energy, ratio of specific heats (c_p/c_v), thermal conductivity

L latent heat

L_p length scale of the turbulent eddies

ℓ turbulence length scale, Mixing length

M Mach number

M_t turbulent Mach number

$\dot{M}_j$ mass flow of trajectory

$\dot{m}_a$ mass flow rate of abrasive

$\dot{m}_{pq}$ mass transferring from phase p to phase q

$\dot{m}_s$ mass flow rate of sand

N number of faces enclosing cell, mixture component

N_f number of nodes on the face *f*

n number of phases

P perimeter of the cross section of duct or pipe, static pressure

$\mathrm{Pr_t}$ turbulent Prandtl number

p^* minimum pressure in throat

p_0 total pressure

p_b back pressure

P_{ij} stress production

p_{in} inlet pressure

p_{out} outlet pressure

p_s	static pressure
p_t	total pressure
$Q_{out,N}$	rate of external heat transfer to the phase N per unit length of the duct
$\dot{q}$	internal heat generation
R	ideal gas constant
$\mathrm{Re_r}$	relative Reynolds number
$\vec{r}$	displacement vector from the upstream cell centroid to the face centroid
r_n	nozzle radius
r_p	particle radius
S	scalar measure of the deformation tensor
S_ϕ	source term
S_ϕ	source term of ϕ
$S_{\varepsilon p}$	source term for ε in continuous phase
S_{kp}	source term for k in continuous phase
T	deviatoric stress tensor, static temperature
T_0	stagnation temperature
T_{in}	inlet temperature
T_t	total temperature
t	time
U	internal energy of control volume
U^+	dimensionless velocity
$\vec{U}$	phase-weighted velocities
u'	velocity fluctuation in x direction
u_e	free-stream velocity
$\overline{u}_w$	velocity of wall
V	volume of chamber
$\vec{V}$	fluid velocity, mixture velocity
$V_{0,q}$	initial volume of dispersed phase
$\vec{V}_{dr}$	drift velocity
$\vec{V}_N$	mixture velocity
$\vec{V}_{pq}$	inter-phase velocity

V_* friction velocity

$\vec{v}$ velocity vector

v' velocity fluctuation in y direction

w' velocity fluctuation in w direction

$\vec{x}_q$ disperse phase position

x_{tr} end of laminar flow

Y_M additional dissipation term

Y_ν demolition of turbulent kinematic viscosity

y^* dimensionless wall parameter

y^+ dimensionless wall parameter

Greek Symbols

α weighting geometric factor, under-relaxation factor, phase volume fraction

β volumetric coefficient of thermal expansion

δ boundary layer thickness

δ_{ij} *Kronecker delta*

η_{pq} time scale ratio

ε turbulence dissipation rate

ε_{ij} dissipation

ε_m eddy-viscosity

ϕ general variable of transport equation, viscous dissipation function

ϕ_{ij} pressure strain

$\phi_{ij,1}$ slow pressure strain term

$\phi_{ij,2}$ rapid pressure strain term

$\phi_{ij,\omega}$ wall-reflection term

κ von Karman constant ($\kappa = 0.4187$)

Γ_ϕ diffusion coefficient for ϕ

λ second coefficient of viscosity

λ_q bulk viscosity of phase q

μ viscosity

μ_q shear viscosity of phase q

$\mu_{t,m}$ mixture dynamic viscosity of turbulent

ν kinematic viscosity

$\tilde{\nu}_t$ turbulent kinematic viscosity

$\overline{\Omega_{ij}}$ mean rate-of-rotation tensor

ω specific dissipation rate

ρ fluid density

ρ_a bulk density of any abrasive

ρ_q material density of dispersed phase

ρ_s bulk density of sand

σ standard deviation

σ_{ij} stress tensor

σ_k effective Prandtl Number of k

σ_ε effective Prandtl Number of ε

θ angle between the mean particle velocity and the mean relative velocity

τ shear stress

τ_L Lagrangian integral time scale

τ_q response time of disperse phase (particulate relaxation time)

τ_V particle relaxation time

τ_w wall shear stress

τ_{xy}^R turbulent shear stress

$\bar{\bar{\tau}}$ diffusion term

ω_k angular velocity

Subscripts

N component of mixture

D disperse phase

C continuous phase

k direction within the control volume

p primary phase

q secondary phase

s	solid phase
l	continuous phase
j	trajectory
m	mixture
f	face of cell
n	number of time interval
Pn	cell centre

Superscripts

T	transpose
-	averaged form
′	fluctuation form

Abbreviations

2D	two dimensional
3D	three dimensional
AWJs	abrasive water-jets
BEM	Boundary Element method
CAD	Computer-Aided Drafting
CAE	Computer-Aided Engineering
CD	**c**onverging-diverging
CFD	computational Fluid Dynamics
CFM	cubic foot per minute
CV	control volume
DBCS	Density-Based Coupled Solver
DEM	discrete element model
DPM	discrete Phase model
ESD	equivalent spherical diameter
FDM	Finite Difference method
FVM	Finite Volume method
PBSS	Pressure-Based Segregated Solver
RANS	Reynolds averaged Navier-Stokes
RMS	root mean square

RNG re-Normalisation Group

RSM Reynolds stress model

VOF volume of Fluid

CHAPTER 1

INTRODUCTION

A converging-diverging nozzle is the most important and basic piece of engineering hardware associated to the high speed flow of gases that is used to increase the speed of media in abrasive blasting systems. Interaction of blasting media with air flow inside the nozzle involves complex phenomena which are not yet fully understood, especially when there is an initial temperature difference between blasting media and air flow.

Blasting media which are propelled by high velocity air flow through the converging-diverging nozzle toward work-pieces are widely used in industry. Steel shots, sand particles, seed beads, glass beads and dry-ice pellets are some of the blasting media which are used for cleaning, peening, deburring or finishing of work-pieces. An abrasive blasting system, such as shot blasting or sand blasting, concentrates abrasive particles at high speed (65-110 m/s) and in a controlled manner at the material thereby removing surface contaminates due to the abrasive impact. Meanwhile, water droplets are usually added to the abrasive media and the air flow to suppress the dust, which is generated by hitting the abrasive media to the work surface.

Therefore, flow through the nozzle in an abrasive blasting machine has three phases: the solid phase (such as sand particles or steel shots), the liquid phase (normally water droplets) and the gas phase (usually compressed air). For computing and optimisation of the abrasive blasting nozzle, it needs to simulate this three-phase flow through the nozzle, which is supersonic turbulent multi-phase flow.

This study puts emphasis on the sand blasting nozzle which is employed in the Farrow abrasive system. The Farrow abrasive system is a sand blasting machine with

low inlet air pressure (compared to the other sand blasting machines) and uses heated water which absorbs thermal energy from high temperature compressed air. According to a lot of experimental tests in various conditions there is no doubt that the Farrow Machine, which has been patented in the UK and worldwide, has a much higher performance than existing sand blasting machines, even though this innovative design was based on trial and error like many other achievements in the history of science and engineering.

The Farrow Machine as a wet abrasive blasting system has a specially designed pressure tank. Heated water enters into this tank and mixes with sand particles. High pressure air flow propels the mixture of wetted sand particles and water droplets through the hose and shoots from the nozzle. Rising water temperature can affect the three-phase flow characteristics inside the hose and nozzle. However, since the length of the hose is about 20 times bigger than the length of the nozzle and almost enough to transfer thermal energy from the heated water to the air flow, the mixture enters the nozzle in a nearly equilibrium state.

A literature survey shows a lack of systematic study on the three-phase flow inside the nozzle. This includes all experimental, analytical and numerical research fields. However there is a lot of research on multi-phase fluidized bed and jet flows, which a few of these related to the three-phase flow, and others are just study of the two-phase flow in fluidized bed and jet flows, but the survey shows that there are a few research studies just about two-phase flow through the nozzle.

Air-sand-water as a three-phase flow passes through the converging, throat and diverging part of the nozzle. Although the process starts by subsonic flow in the converging section, the flow may exit from the nozzle in the form of a supersonic, sonic or even subsonic flow. The diverging part of the nozzle with supersonic flow usually includes a shock wave that produces an instantaneous deceleration of the flow to subsonic speeds. The air-sand-water three-phase flow through the nozzle also has other intricacy behaviours which should be considered in simulation. These include two or three-way turbulence coupling, droplet or particle collision, droplet break up and existence of an interference between the incident stream of particles and those rebounding from the wall of the converging part of the nozzle. Therefore, a successful simulation of the air-sand-water three-phase flow through a nozzle needs to utilize an appropriate turbulence model as well as incorporating a proper multi-phase model.

Since the three-phase flow inside the nozzle has a high Reynolds number, using Reynolds averaged turbulence models is the case throughout this research. A primary concern in Reynolds averaged method is to close the *Navier-Stokes* equations, because of extra terms of Reynolds stresses appear in averaged form, which contributes to distinct turbulence models in this category. In Reynolds stress model (*RSM*) the *Navier-Stokes* equations are coupled by an equation for dissipation rate and also three equations for modelling the extra three Reynolds stresses (in two dimension domain). Other models, based on some assumptions, simplifications or empirical observations, add one or more equations to solve closure problem of the averaged *Navier-Stokes* equations. Common "industrial standard" Reynolds averaged model is k-ε model, which employs two equations for turbulence kinetic energy and its dissipation rate. Apart from *RSM*, other Reynolds averaged models simulate turbulence through effective viscosity and diffusion parameters. In this case, the effective diffusion is often considered as a scale of the effective viscosity. Selection of the turbulence model depends on good accuracy, accessible computing tools, domain dimensions and flow features.

The other important part of numerical investigation of multi-phase flows through the nozzle is the employing of an appropriate model to compute and predict different behaviour of phases when the initial and boundary conditions vary. For this purpose the first step is determination of the dominant flow regime inside the nozzle. This will help in selecting the appropriate model for the simulations. Multiphase flow regimes can be grouped into four categories: gas-liquid or liquid-liquid flows (e.g. bubbly flow and droplet flow), gas-solid flows (e.g. pneumatic transport and fluidized bed), liquid-solid flows (such as slurry flow, sedimentation and hydro-transport), and finally three-phase flows (such as air-water-sand flow considered in this study). In fact, the three-phase flows can be considered as a combination of the above mentioned flow mechanisms. For instance, in this study, the air-sand-water flow through the nozzle is determined as pneumatic transport and droplet flow.

Generally, there are two approaches for modelling of multi-phase flows, the *Eulerian-Eulerian* approach and the *Eulerian-Lagrangian* approach. In the *Eulerian-Eulerian* approach, different phases are considered mathematically as interpenetrating continua. Volume fractions for each phase are considered, and in this approach, conservation equations for each phase are applied. In the *Eulerian-Lagrangian* approach, however, just the fluid phase is treated as a continuum. Time-averaged

Navier-Stokes equations are solved for the continuous phase, while the dispersed phase is solved by tracking a large number of particles and droplets through the nozzle.

Three of the most popular and widely used models in the *Eulerian-Eulerian* approach are the *Volume of Fluid* (VOF) model, the *Mixture* model and the *Eulerian* model. For numerical computation of three-phase flow through the nozzle, *Mixture* and *Eulerian* models are applicable. In the *Mixture* model, coupling between the phases should be strong so that it can model the *n*-phases by solving the momentum equation for the mixture and prescribing relative velocities to described phases by using the concept of slip velocities. However, the *Eulerian* model solves a set of *n*-momentum and continuity equations for each phase. Therefore, it could be more complex than the *Mixture* model. The number of secondary phases in the *Eulerian* model is limited only by the memory requirements of the computers and convergence behaviour. The *Eulerian* model is a better choice than the *Mixture* model whenever the accuracy is more important than computational effort; otherwise, the *Mixture* model can be preferred as it uses a smaller number of equations than the *Eulerian* model and therefore is a good option to solve simpler problems. As a result, the *Eulerian* model is suitable for simulation of pneumatic transport of sand particles and water droplets through the nozzle. On the other hand, the *Eulerian* models are appropriate for flows in which the secondary phase(s) volume fraction(s) exceed 10 percent. Flows in which the dispersed-phase volume fractions are less than or equal to 10 percent can be modelled using the *Discrete Phase* model.

The *Discrete Phase* model (*DPM*) is designed for simulation of the flow with a sufficient dilute secondary phase. In this case, it is assumed that a particle-particle interaction is negligible. In *DPM* the transport equations are solved for continuous phase and discrete second phase is simulated in a *Lagrangian* frame of reference. In this case the trajectories of these discrete phase entities are computed as well as heat and mass transfer to/from those.

This research employs the commercial *CFD* (Computational Fluid Dynamics) code, FLUENT, for supersonic turbulent multi-phase flow through the converging-diverging nozzle. Using FLUENT allows employment of the Reynolds averaged models such as *RSM*, two-equation *k*-ε models as well as the *Eulerian* and *Discrete Phase* models.

This thesis is divided into seven chapters. After the current chapter, chapter two describes the relevant background and literature survey for the multi-phase flow through the nozzles used for cleaning, finishing, peening and deburring of surface by employing

sand particles and other abrasive media. This includes the experimental, analytical and numerical research. In addition, the shock wave phenomena inside the nozzle with the multi-phase flow will be reviewed in this chapter.

The third chapter describes the nature of the problem, including blasting methods, abrasive media and physical and geometrical feature of the converging-diverging nozzle. The numerical modelling of multi-phase flows, continuous and dispersed phase equations and multi-phase turbulence modelling are also described in this chapter. The numerical modelling includes the continuity equation of mass, momentum and energy. In the last part of this chapter, the finite volume method which is used to solve the coupled nonlinear partial differential equations for each cell (control volume) in computational domain is described. The numerical method includes discretisation, pressure-velocity coupling in *Navier-Stokes* equations and the setting of the boundary conditions.

Validation of the numerical method is the main intention of Chapter four. In this chapter uncertainty and error sources in CFD simulations are briefly described. Then validation assessments including grid independency tests as well as FLUENT solver error checks are presented. As it will be discussed later in the literature review, since there are not any experimental or analytical results on three-phase flow through the nozzle, therefore the FLUENT solver is checked against the results for the un-premixed air-water two-phase flow through the nozzle. The achieved results from the FLUENT simulation for this flow were then compared with the available experimental results on the subject. As in the sand-blasting system, the air-sand-water three-phase flow through the nozzle is a premixed flow, so the last part of this chapter concentrates on numerical simulation of premixed air-water two-phase flow through the nozzle against an un-premixed flow.

Chapter five presents the numerical results of air single-phase flow and air-sand two-phase flow through the converging-diverging nozzle. For single-phase flow, various turbulent models with different inlet pressure and temperatures are computed. Air-sand two-phase flow through the nozzle is simulated by the *Eulerian* model and the *Discrete Phase* model.

Chapter six presents numerical results of air-sand-water three-phase flow through the nozzle. In this chapter the effect of water droplets on multi-phase flow is computed. In addition, the effect of various mass flow rates of water and sand, inlet pressure and inlet temperature on nozzle flow characteristics are investigated.

Finally, chapter seven assorts conclusions of this research into three main parts including the validation, single and two-phase flows and air-sand-water three-phase flow. This chapter ends with some recommendations for the future works.

CHAPTER 2

LITERATURE REVIEW AND BACKGROUND

Abrasive blasting is the process of propelling a stream of abrasive media, such as sand particles, steel shots, and glass beads against a hard surface under high pressure to smooth a rough surface, roughen a smooth surface, or remove surface rust, colour, or any other surface coating. Blast cleaning is one of the most frequently utilized treatment methods in modern industry.

The first sandblasting process was patented by Tilghman (1870). He not only exhibited the general idea of what is today called blast cleaning, but also presented a number of methods of how to propel the solid particles against the material surfaces. In his patent the sand particles are propelled just by a rapid jet or current of steam, air, water, or other suitable gasses or liquid medium. In the 1930's compressed air was added to the abrasive blasting machines, and a pressurised medium, such as high pressure air or steam, propelled abrasive media toward the material surface. In addition, by utilizing the de Laval Nozzle, supersonic velocity of the medium is obtainable in the exhaust of sandblasting machines.

Nowadays, in sandblasting machines, water droplets which are used for suppression of dust produced by the crushing of sand particles, are mixed with sand particles in the blasting tank. Sand particles along with water droplets are exhausted from the pressurised blasting tank, and propelled toward the nozzle by a blasting hose.

The present chapter is devoted to review the available literature related to the numerical, experimental and analytical studies of the multi-phase flow in a pressurised blasting tank and nozzle. This chapter is divided into three main categories: review of a

pressurised blasting tank or fluidized bed, review of a nozzle and application of multi-phase flow, and review of numerical modelling on multi-phase flow.

2.1. Review of Pressurised Blasting Tank or Fluidized Bed

A fluidized bed generally is a tank with pressurised fluid and tiny solid particulate substance. Under pressure, the solid particles and fluid are mixed together, and consequently the mixture behaves as a fluid. The first fluidized bed was invented by Winkler (1926) which has been applied for gasification of coal. In the Winkler system, small pieces of coal are fed by a screw feeder and are fluidized by the gasifying medium, such as heated air or oxygen, entering through a grate at the bottom.

Gas-liquid flows and three-phase fluidized beds are widely used in industry. The performance of these systems differs according to which of several flow regimes present. Discrete bubble flow, dispersed bubble flow, coalesced bubble flow, slug flow, churn flow, bridging flow and annular flow have been observed in gas-liquid two-phase flow, but only the lower gas velocity flow regimes have received attention in three-phase fluidized beds.

Three-phase flow regimes inside the fluidized bed were investigated by Chen, et al. (1995). In this study, the pressure fluctuation characteristics were applied for recognizing different regimes such as total homogeneous bubble regime, total transient regime, and total turbulent bubble regime. On the other hand, depending on the operating conditions they could observe two or all three regimes simultaneously at different heights of the fluidized bed. In this research air flow, tap water, and glass beads under different conditions have been used.

Chen, et al. (1995) found that the flow regimes are independent on redial positions across the fluidized bed. In addition, three-phase flow regimes inside the fluidized bed depend on operating conditions could vary in axial direction. Finally, the axial distribution of solid particles hold-up in the three-phase fluidized bed is modelled by the exponential function.

The recognizing of boundary between particles and circulating three-phase fluidization regimes are applicable by analysing of the fluctuations of the voltage signals (Vatanakul, et al., 2005). In this method, the particle size, liquid viscosity, gas flow rate, superficial liquid velocity and solid circulating rate have a significantly effect on the characteristic of the voltage signals.

The effects of particle size and density on the flow regime transitions have been presented in the work of Zhang, et al. (1997). The conductivity probe measurement of bubble characteristics was developed to determine flow regime transitions in upward two-phase and three-phase fluidized beds. By applying various velocity of air and/or water in a three-phase fluidized bed, transition of discrete flow to coalesced flow, coalesced flow to slug flow, slug flow to churn flow, churn flow to bridging flow and bridging flow to annular flow have been experimentally recorded. Zhang, et al. (1997) found that the flow regimes in a three phase fluidized bed are qualitatively the same as an air-water two-phase fluidized bed in the same column.

Hydrodynamic modelling of fluidized bed reactors, based on first principles, started about 50 years ago. The first models were able to simulate gas bubble formation, propagation and bursting in a fluidized bed using an inviscid two fluid model. However, the recent models are able to simulate two and three phase fluidized beds by recognizing various flow regimes.

In fluidized beds many transport properties, like heat and mass transfer, can directly depend on the presence and behaviour of bubbles. Therefore, the precise prediction of bubble characteristics, such as the bubble size and size distribution, bubble growth, and bubble frequency are very important. Patil et al (2005) proposed two closure models for modelling of gas-solid fluidized beds simulated by the Eulerian approach. One was the semi-empirical model assuming a constant viscosity of the solid phase, and the second model was based on the kinetic theory of granular flow. Patil et al (2005) compared the performance of these models to describe bubble formation at a single orifice and the time-averaged porosity profiles in the bed. According to this research, the kinetic theory of the granular flow model accounting for the frictional stresses can be more applicable for the wide variety of cases of gas-solid fluidized bed.

Samuelsberg and Hjertager (1996) presented an experimental and numerical study on radial profiles of an axial particle velocity component in a circulating fluidized bed reactor. A two dimensional two phase flow model with a turbulent kinetic energy equation based on kinetic theory of granular flow was verified against the experimental data. They have proposed a comprehensive multi-dimensional CFD model for gas particle flow. The conservation equations for the solid phase have been based on kinetic theory for dense gases. The model was compared against experimental data in a cold flow circulating fluidized bed reactor. The results of the numerical model comparison with experimental data indicated that the turbulence kinetic energy model was capable

to predict reasonable oscillations in the solid phase, but when large scale fluctuations were added, the best results were given when a lower coefficient of restriction was used. Samuelsberg and Hjertager (1996) employed the Laser Doppler anemometry to measurement of mean and root-mean-square particle velocity.

Verification of an appropriate numerical model in a gas-solid two-phase fluidized bed was investigated by Zhao, et al. (2010). A combination of an experimental and numerical study of a fluidized bed with Geldart B magnitude powder shows the *Syamlal–O'Brien* model is most applicable to hydrodynamic simulations of the Geldart B bed. In this research the dependency of fluidization quality and static bed height was investigated. Zhao, et al. (2010) found that in Geldart B magnitude powder, the fluidization quality decreased with raising the static bed height. However, at low static bed height, less than 300 mm, the static bed height only slightly influenced the fluidization characteristics of the bed. In this case, height, pressure drop, and the density of the fluidized bed were stable.

A theoretical solution for a two-dimensional steady flow of a gas-solid mixture exiting in a fluidized bed with a vertical standpipe was presented by Tsinontides (1999). In this solution, the density variation of the mixture inside the fluidized bed and channel was supposed to be very small and that they could be neglected in all terms other than in the fluid-particle interaction force. Tsinontides (1999) reported that the mentioned approximate was more acceptable in the region far from the channel entrance. In practice, the solid fraction could increase rapidly in the entrance of the channel along with rapid decrease of gas pressure. Finally, this analytical study declared that the gas velocity, based on the updated density, had similar magnitude with the particle velocity.

2.2. Review of Nozzle and Application of Multi-Phase Flow

A nozzle with different shapes is a mechanical appliance which is designed to control the direction or characteristics of a fluid flow. Rectangular, square, ellipse, hollow cone, full cone, flat, and air atomizing are some of the different shapes and kinds of nozzle which are used in industry. Meanwhile, the converging-diverging nozzle is the most important and basic piece of engineering hardware associated with the high speed flow of gases. This device was invented by Gustaf de Laval in 1889 (Stevens and Hobart, 1906) to increase the steam jet to supersonic speed, by interchanging of

pressure to kinetic energy of the steam. Therefore the converging-diverging nozzle is often referred to the 'de Laval' nozzle.

The effect of the application of the nozzle in industry such as powder metallurgy and spray forming was investigated by Li, et al. (2008). They calculated the gas flow field in nozzles and out of nozzles for Laval orifice and straight orifice nozzles. According to the results, the flow generated by the Laval nozzle had a higher exit velocity in the vicinity of the nozzle, in comparison with that of the straight nozzle. In addition, the generated flow by the Laval nozzle had less convergence and the velocity gradient along the radial direction was more moderate than with the straight nozzle, which could contribute to a broad distribution of melt particles.

In a sand-blasting machine the nozzle wears off very rapidly, and while the replacement of this part is an expensive proposition, several designs have been used in the past to resolve this problem. Fairchild (1929) proposed to reduce the amount of wearing in the sand-blasting nozzles by having a removable lining of a material which will not wear any faster than the usual nozzle and which may be a better grade of material since there is so much less of it to buy. The nozzle in the invention of Fairchild (1929) has a lining composed of a plurality of sections by the same cross area which are forming together a reversed fluted bore. Stoltz (1991) modified the patent of Fairchild (1929) by producing undesirable turbulences that eat away the lining. One of the main objects of the patent of Stoltz (1991) as he mentioned is “to provide a Nozzle for sand-blasting that includes a unitary frusto-conical inner sleeve component that provides a turbulence-free surface for the existing sand under pressure”. This provides such a nozzle that resists erosion by avoiding the creation of turbulences within the nozzle itself.

Computational fluid dynamics in multiphase flow has become a well accepted and useful tool in the modelling of gas-solid two phase flow during recent years, and much progress has been made toward developing computer codes for describing fluidized beds. However by a review of technical literature, some research can be found in the field of gas-fluid, gas-solid, and fluid-solid two-phase flow through a nozzle, but gas-fluid-solid three-phase flow through a nozzle is the gap in the knowledge. This section is going to present some research which has been done in multiphase flow through a nozzle via experimental, numerical, and analytical investigation.

The Eulerian-Eulerian and Eulerian-Lagrangian approaches are two different tools for the simulating of multiphase flow. In some cases and due to the multi-phase problem

restriction, one of the Eulerian-Eulerian or Eulerian-Lagrangian approaches is applicable. Three of the most popular and widely used models in the *Eulerian-Eulerian approach* are the *Volume of Fluid* (VOF) model, the *Mixture* model and the *Eulerian* model. On the other hand, the *Discrete Phase Model* (DPM) is a popular model in the *Eulerian-Lagrangian approach.*

A pressure based Eulerian-Eulerian gas-fluid two-phase model for non-equilibrium condensation in transonic steam flow was presented by Gerber and Kermani (2004). The model, implemented within a full *Navier-Stokes* viscous flow solution procedure, has employed a pressure based finite-volume discretization of the governing equations of fluid motion. Gerber and Kermani (2004) employed the developed model within the commercial CFD code CFX-TASCflow. The second order discretization utilized for conservation equations of vapour phase. In this phase the solution of the hydrodynamic equations (u, v, w and p) was obtained by a coupled (non-segregated) approach. On the other hand, due to the sharp discontinuity near the nucleation front, the bounded upwind (first order) scheme was employed for liquid phase equations.

Gerber and Kermani (2004) obtained excellent convergence behaviour for all equations on the cases tested, with global conservation 10^{-4} or better (for all conservation equations), and normalized *RMS* residual of the order of 10^{-5} or lower.

A viscous and wet-steam flow through the nozzle, with unstructured and adaptive mesh which was able to focus on regions of rapid flow changes, was presented by Simpson and White (2005). In this research the Reynolds-averaged Navier-Stokes equations have been solved for the two-phase mixture. Simulation of a viscous steady flow through the nozzle indicated that growth of the boundary layer had a significant impact on the predicted pressure distributions and droplet sizes, at least for cases where two-dimensional effects were prominent. Simpson and White (2005) also employed the numerical scheme to compute unsteady flows in a variety of nozzle geometries, covering a range of inlet conditions in each case.

Lemonnier and Selmer-Olsen (1992) investigated a two-phase two-component flow in a converging-diverging nozzle. In this study, parts of an experimental and theoretical study of high quality critical two-phase flows have been presented. Two different designs of an axisymmetric converging-diverging nozzle were investigated by injecting the liquid centrally or at the vicinity of the wall. Lemonnier and Selmer-Olsen (1992) observed that when the liquid was injected centrally, a liquid jet was formed which immediately breaks up and generates small droplets entrained in the gas stream. On the

contrary, when the liquid was injected as a film close to the wall, the entrainment process was totally different. In the second inlet condition, Lemonnier and Selmer-Olsen (1992) found that the film entered the throat of the nozzle and the mixing of the two phases took place farther downstream. The acceleration of the liquid was delayed and this gave a higher level of mechanical non-equilibrium. According to the experimental data, critical flow phenomena related to the liquid fraction entrained at the inlet. Moreover, Lemonnier and Selmer-Olsen (1992) found that by progressively decreasing the outlet pressure that low gas quality flow might remain sub-critical in nature even if the upstream/downstream pressure ratio was as high as 6:1.

2.2.1. Condensation and Atomization

In the de-Laval nozzles, the cross-sectional flow area first decreases to the throat and then increases in the supersonic region. As the steam flows through the nozzle it contracts before the throat and then expands in the diverging section of the nozzle, and the temperature falls rapidly. Because the equilibrium vapour pressure decreases exponentially with temperature, very high super saturation can be achieved. A conservative two-dimensional compressible numerical model for supersonic non-equilibrium spontaneous condensing steam flow through the de-Laval nozzle was studied by Yang and Shen (2009). In this study, the non-equilibrium condensation model was implemented within the commercial CFD code FLUENT. The conservation equations for both liquid and gas phases were discretized using conservative finite-volume integration over a control volume, and second-order upwind schemes were employed.

Also Yang and Shen (2009) reported that the steam flow through the nozzle acquired sufficient super-cooling for spontaneous nucleation of droplets in the diverging section or the supersonic area of the nozzle. Consequently, due to the release of latent heat the flow after the throat decelerated and its pressure increased.

Another application of the nozzle in industry which is widely used is atomization of fluid in the exhaust of the nozzle. This might be used in internal combustion engines, painting apparatus and air refreshing systems amongst other things. Air-assisted atomization is the most popular choice for this purpose. In the nozzle, the gaseous phase is used to facilitate atomization of the liquid phase. An investigation of the nucleation mechanisms which take place during the flow through convergent-divergent nozzles was presented by Cinar, et al. (1997). In this study, the flow equations developed to

compute the pressure, expansion rate and the droplet formation along the nozzle. In addition, a numerical technique was employed to solve the governing equations. For validation Cinar, et al. (1997) carried out an experiment to measure the droplet size and thermodynamic properties of steam expanding through a convergent-divergent nozzle. According to the results, the amount of super-saturation was limited with pressure increase, and the resulting droplet sizes related to the Wilson Pressure[1] and the expansion rate.

A two-fluid model for compressible flow of gas bubbles dispersed in liquid moving through a convergent-divergent nozzle, which is used for a gas-assisted atomization, was presented by Pougatch, et al. (2008, 2009). The model was developed for flows with high values of the gas volume fraction, up to the phase inversion values. Pougatch, et al. (2008) considered the effect of drag force as well as virtual mass force. The virtual mass force was defined as a force which appears due to the acceleration of the continuous phase that was carried away together with the accelerating discrete particle. The two-phase flow through the nozzle was modelled by the mixture $k-\varepsilon$ turbulence model, and a new model was developed to extend the wall functions treatment of a single-phase turbulent flow to the multiphase flow. Pougatch, et al. (2008) found that the developed multiphase flow wall functions model for calculating the tangential shear stress and turbulent quantities near the wall, produced plausible results in the vicinity of the wall. In addition, reasonably good agreement of the pressure loss along the pipe length has been achieved.

A two-fluid *Eulerian-Eulerian* mixture model with a phase inversion was developed for compressible gas-liquid mixtures by Pougatch, et al. (2009). The mixture model computed a single set of differential equations for the whole computational domain regardless of which phase was locally continuous. The discrete phase was assumed to be multi-dispersed, and the particle number density equation was solved to determine the average diameter of bubbles or droplets. The model was applied to the gas-assisted premixed atomization, and reasonably good agreement was achieved for simulated values with experimentally measured of the pressure along the nozzle wall and the water flux profiles at different distances from the nozzle orifice.

[1] The locus of points where condensation will take place regardless of the initial temperature and pressure at the nozzle entrance is called the Wilson line. The related pressure of this line which has 4-5% moisture less than saturation line is called Wilson Pressure.

Zeoli and Gu (2006) developed a numerical model to simulate the critical droplet break-up during the atomization. By integration of the droplet break-up model with the flow field generated high-pressure gas nozzle, this numerical model was able to provide quantitative assessment for the atomization process. To verify the model performance, the melt stream has been initialized to large droplets varying from 1 to 5 mm diameters and injected into the gas flow field for further fragmentation and the break-up dynamics were described in detail according to the droplet input parameters.

Manufacturing of fine metal and alloy powder is the other application of gas-assisted atomization, which uses a convergence-divergence nozzle. For this purpose and breaking up a molten stream the air, nitrogen, helium, or argon are usable. By employing a convergent-divergent nozzle, kinetic energy from a high velocity gas expanded through the nozzle transfer to a stream of liquid metal. Consequently, this stream of liquid metal disintegrates and breaks up into metal droplets that freeze into particles.

High-pressure gas atomization is a close-coupled discrete jet atomization method and is one of the most effective methods of producing such powders. Anderson and Terpstra (2002) employed the developed high-pressure gas atomization nozzles with discrete jets resembling a convergent–divergent nozzle, instead of the cylindrical jet, for producing of fine spherical powders or spherical powders of a narrow particle size class. In this method, a set of 22 jets were used instead of a single cylindrical jet. It conducted to increase atomization efficiency and uniformity, and to reduce the required gas supply pressures. Terpstra (2002) found that the mass flow from high-pressure gas atomization nozzles is significantly greater than that calculated for isentropic choked flow conditions. This has been attributed to an insufficient volume in the atomization nozzle gas manifold that experienced enhanced expansion cooling at increasing pressures. In experiments on 316L stainless steel, the atomization efficiency of the high-pressure gas atomization nozzle with convergent-divergent jets was higher than that of the high-pressure gas atomization nozzle with cylindrical jets, reflecting a lower gas/metal mass flow ratio. In other words, while the powder size distributions were nearly the same for all of the high-pressure gas atomization experiments, the high-pressure gas atomization nozzle with convergent-divergent jets utilized atomization gas with a significantly reduced operating pressure and mass flow rate.

The effects of atomizing gas pressure on the melt delivery tube base pressure and flow separation was investigated by Ydin and Rahmi (2011). The gas-only flow CFD

simulation was modelled in a close-coupled gas atomizer, and the gas field generated with a commercial CFD code, FLUENT 6.3. According to the experimental data, the flow separation, which is a function of atomization pressure and liquid delivery tube extension, had more effect on melt atomization. In addition, Ydin and Rahmi (2011) found that the geometry had significant effects on the nozzle performance than gas pressure, in order to get the highest velocity at the nozzle exit.

Lear and Sherif (1997) presented an optimization analysis of a two-phase flow mixture of a gaseous phase and an incompressible condensed phase through a converging-diverging nozzle used for industrial cleaning applications. The analysis was based on maximizing the condensed phase momentum flux for a set of mixture parameters that included the liquid mass injection ratio, liquid and gas properties, nozzle size, and nozzle stagnation-to-back pressure ratios. Lear and Sherif (1997) concluded that an optimum Mach number of about 1.4 would maximize the normalized momentum flux based on the exit area. The corresponding exit-to-stagnation pressure ratio that gave maximum normalized momentum flux was between 0.3 and 0.35, depending on the flow parameters. The effect of the liquid-to-mixture injection ratio was found to be more significant than either that of the liquid-to-gas specific heat ratio or the gas ratio of specific heats. Model results should be particularly useful for the design optimization of two-phase high speed impact cleansers.

2.2.2. Alternative abrasive media

Besides solvents and chemical aqueous cleaning processes, jet cleaning processes or shot-blasting systems is used to remove soil, paint, and other contaminants over surfaces. In some cases, jet processes with sand, steel and glass balls cause damage to surfaces. On the other hand, solvents and chemicals can often only be applied in relation to material and contamination, and involve high reconditioning and disposal costs. In these cases a dry-ice blasting process might be one of the applicable choices.

Dry-ice blasting has been industrially tested since the 1980s. This process is pneumatic jet-based and operates with dry-ice pellets as the single-way blast medium. Dry-ice pellets consist of solid carbon dioxide (CO_2) at a very low temperature about -80°C (Spur, et al., 1999).

The study of dry-ice blasting process, optimization and application was presented by Spur, et al. (1999). The active mechanism of the dry-ice blasting process and impact force were investigated. In addition, the diameter and velocity of the CO_2 pellets in the

jet were measured. According to this method, the silicone seals in exchange engine production removed without significant changes in structure or surface damage.

Cryogenic blasting is a pneumatic jet based process in which solid carbon dioxide (CO_2) particles impinge upon a surface. It may be employed to remove paint layers from a variety of substrate materials. During this process, the substrate material may be damaged due to the carbon dioxide particles striking the substrate surface. Weston, et al. (2005), and Shipway and Weston (2009) described the damage sustained by an industrial polymer blend when exposed to cryogenic blasting with solid carbon dioxide particles. The main findings of this work concerned the thermo-mechanical effects of the impact of solid CO_2 particles impacting on to a commercial polypropylene blend, Hifax EXP 5479[2]. Several kinds of surface damages, related to solid CO_2 particles' temperature and impact velocities, have been presented in this study.

Shipway and Weston (2009) observed that during particle blasting of polymers, a significant temperature raised in the polymer which was due to heat generation during plastic work. The low thermal conductivity of polymers results in a significant temperature difference between the surface and the bulk being generated to drive the heat flow. In comparison experiments in blasting of aluminium, no such measurable temperature difference was observed.

Plastic media is another alternative media for silica sand. Plastic media blasting is the safe removal of coating from almost any products, such as aircraft, aerospace and panels of honeycomb construction. The hardness of plastic particles varies from 9 to 21 (3.0 to 4.0 Mohs) while other hard abrasives such as sand particles have absolute hardness of about 100 (7.0 Mohs). Plastic media blasting is a process for the rapid, economic and safe stripping of coatings. Because the plastic particles are harder than coatings but softer than underlying substrates, this abrasive can quickly remove coatings without harming sensitive surfaces. Nudelman and Abbott, (2000) presented some advantages of plastic media blasting, and some consideration about use of plastic media blasting. As no one coating removal method is best for all applications, so this article gives some disadvantage of using the plastic media abrasive especially employing the poor media.

[2] Hifax EXP 5479 is an impact resistant polypropylene blended with polyethylene, ethylene propylene diene rubber (EPDM) particles and 20wt% talc

Glass beads were originally used for decorative applications. Their use as a medium in impact blasting came about largely as a result of the aerospace build-up of the 1950s (Mulhall and Nedas, 1999). Impact Media Comparison, bead consumption and some of the advantages of employing glass beads are described by Mulhall and Nedas (1999). The various applications of glass beads, such as cleaning, finishing, peening and deburring are some of the application notes presented in this paper.

The effects of glass beads and stainless steel particle size, speed, impact angle, and stand-off distance on the rate of deposit removal from gas turbine components were investigated by Raykowski, et al. (2001). As deposits on compressor and turbine stage components have brittle characteristics, while substrate deformation is ductile, according to the test results, an impact angle of 90° to the surface was optimal. In addition, Raykowski, et al. (2001) concluded that deposit erosion and substrate deformation were strong functions of particle stream power, particle kinetic energy and impact angle.

Shot peening is a cold working process widely used to improve the fatigue life of aerospace and automobile components. It used to produce a compressive residual stress layer and modify mechanical properties of metals. It is similar to sandblasting, except that it operates by the mechanism of plasticity rather than abrasion. In shot peening each particles function as a ball-peen hammer. The influences of peening velocity and peening time on the resulting residual stress profiles were experimentally investigated by Miao, et al. (2010). The experimental study of intensity and surface coverage on aluminium 2024 performed to relate them with the peening time. One contribution of this work was the developing of quantitative relationships between arc height and coverage with respect to the number of peening passes. Miao, et al. (2010) recognized the peen forming as a suitable manufacturing process for various aircraft components. Stress peen forming was a prevailing technique for the forming of wing skins. Another contribution of this work was to establish a quantitative relationship between the pre-bending moment and resulting arc height based on experimental results.

From an ergonomic point of view, abrasive blasting media by hitting on to the work surface can generate large quantities of dust, which may be toxic. This sort of dust can result in permanent scarring of the lung tissue. Abrasive blasting results in high concentrations of respirable dust. River sand or beach sand that are used in some

abrasive blasting systems make toxic dust. Respiration of silica dust can result in silicosis, stiffening and scarring of the lungs. It results in shortness of breath, coughing, and chest pain. Steel shot and high pressure water flow might be good alternatives to sand particles in abrasive cleaners.

The ergonomics of abrasive blasting, high pressure water flow, and steel shot, were compared and presented by Rosenberga, Yuanb and Fulmer (2006). By utilizing multiple methods including qualitative and quantitative, the advantages and disadvantages of each media were discussed. Yuanb and Fulmer (2006) reported that high-pressure water was environmentally cleaner, less ergonomically stressful, much quieter and less dusty than steel shot; however, it was time-consuming on those tasks where both media could be used.

2.2.3. Micro abrasive blasting

Many modern techniques have been developed to enhance the life of the components in service, such as alloying additions, heat treatment, surface engineering, surface coating, implantation processes, laser treatment and surface shape design. Processes such as thin film technology, plasma spraying and vacuum techniques depositing a range of multi-layered coatings have greatly enhanced the life, use and applications of engineering components and machine tools.

Bombardment with millions of micro shot ranging in size from 4 to 50 μm with a controlled process can lead to remarkable operating life improvements of components. Kennedy, et al. (2005) described the ways in which micro shot blasting of machine tools were employed for improving surface finish and reducing cutting forces in manufacturing. The efficiency of micro blasting depends on many parameters including the shot media and size, the mechanics of impact and the application of the shot via the micro shot blasting unit. Kennedy, et al. (2005) introduced these parameters as well as the control of the process to provide repeatability and reliability in the shot blasting units. According to the results, the micro shot blasting of cutting tips and tools had a very positive effect on component surfaces by increasing toughness, operating life, improving hardness and surface finish.

A line-shaped Laval nozzle has been developed for employing in micro abrasive blasting by Karpuschewski, Hoogstrate and Achtsnick (2004). This nozzle is able to increase the particle velocity by 40% and is more uniform compared to a conventional

round nozzle. A line shaped Laval nozzle, which delivers homogeneous dispersed particles with velocities in the supersonic regime, offers the best prospects.

A one-dimensional isentropic flow model was developed to calculate the particle exit velocity of each individual particle in the airflow through the nozzle by Achtsnick, et al. (2005). This model employed two different types of nozzles, a converging cylindrical and a new developed line shaped Laval-type. The particle size and its position within the air jet were based on probability distribution functions, and the result was the nozzles characteristic energy intensity distribution of the particle beam.

Achtsnick, et al. (2005) found that the Laval-type nozzle was able to increase the particle velocity by more than 30% compared to the converging nozzle. The validity of the presented set of models was proved with respect to particle velocity, blasted surface profile and roughness.

The erosion of brittle materials is another application of micro abrasive jet blasting, which uses the solid micro-particles. The rate of material removal is one of the most important quantities for a machining process. Fan, et al. (2009) developed the predictive mathematical models for the erosion rates in micro-hole drilling and micro-channel cutting on glasses with an abrasive air jet. The predictive capability of the models was assessed and verified by an experimental investigation covering a range of the common process parameters such as air pressure, abrasive mass flow rate, stand-off distance and machining time (for hole machining) or traverse speed (for channel machining). According to the results, the air pressure, stand-off distance and nozzle diameter had a positive exponent, and abrasive mass flow rate carried a negative exponent. For hole machining, the machining time had a negative exponent, while a positive exponent was associated with the traverse speed in channel machining.

2.3. Review of Numerical Modelling on Multi-Phase Flow

Particle processing, conveying and separation are of crucial importance in the process industry. Beside analytical consideration, empirical correlations and experimental investigations, the numerical simulations have gained increasing importance in studying applied particle laden or dense flows. Regardless of the method of investigation it is mandatory to cover the dominant flow regime or the dominant flow regimes of the process. In principle, the numerical modelling approaches could be organized in Lagrangian and Eulerian models.

The interference between an incident stream of spheres and those rebounding from a flat surface was modelled by Ciampini, et al. (2003a, b). The model was capable of examining the effect of the stream angle of incidence, nozzle divergence angle, incident particle velocity and flux, particle size, particle-particle and particle-surface impact parameters and stand-off distance. Ciampini, et al. (2003a) assumed frictionless inter-particle collisions, but friction for particles impacting the surface was considered. The simulation was verified for consistency, and dimensionless parameters identified to aid in the presentation of data. Also this model was employed in nozzle of abrasive blasting by Ciampini, et al. (2003b). According to the results, when the nozzle radius was greater than 15 times the particle radius ($r_n/r_p > 15$), the most important parameters affecting interference between a stream of incident and rebounding spheres were angle of attack, α, stream density, ρ_s and coefficient of restitution for particle surface collisions, e_{ps}. In addition, the stand-off distance, d, was important just for normal incidence. The friction coefficient for particle–surface collisions, f, had a negligible effect. Ciampini, et al. (2003b) concluded that at low stream density, ρ_s, particle interference was negligible and so power availability to the target was approximately equal to the power input of the nozzle[3].

The energy for the creation of a shockwave is taken from the fluid flow. Therefore, the velocity of flow through a shockwave must decrease. This loss of kinetic energy, which happens very rapidly, results in the large pressure and density rise within the shockwave. This is completely in keeping with Bernoulli's equation.

The flow field, that develops when a moving shock wave hits a two-phase medium of gas and particles, has a practical application in industrial accidents such as explosions in coal mines, grain elevators and furthermore to solid propellant combustion in rocket engines. Therefore, a successful prediction of the thermo-fluid mechanical characteristics development of gas and particles is very crucial and imperative for the successful design and operation of rocket nozzles and energy conversion systems. The interaction phenomena when a moving shock wave hits a two-phase medium of gas and particles was presented by Park and Baek (2003). The study focused on the effects of the particle mass density and the particle specific heat on the thermo-fluid mechanical

[3] However this paper had some other results, but abovementioned results are very important and applicable in this thesis.

characteristics. Furthermore, the thermo-fluid mechanical developments were examined for two-dimensional interaction with two-phase flow with reacting particles. Park and Baek (2003) found that in unsteady flow, the velocity as well as temperature relaxation time played an important role. When they were shorter, the interaction between gas and particles were so intense that the dynamic and thermal equilibriums were attained in a shorter time. Park and Baek (2003) exposed that when the particle mass density was decreased, the gas and particles more closely followed the shock front farther upstream and the particle concentration became denser behind the shock wave.

The shock waves in micro convergent–divergent nozzles, which are used in micro-thruster systems for the attitude control of the micro/nanosatellites, were investigated by Xu and Zhao (2007). According to the results, the viscous effect in microscale was important to form the shock wave flow structure in the micro-nozzles.

Separation of supersonic flow in a planar convergent–divergent nozzle with moderate expansion ratio was investigated by Xiao, et al. (2007). The Reynolds-averaged Navier–Stokes equations with a two-equation k-ω turbulence model were employed. The focus of this research was on the structure of the fluid and wave phenomena associated with the flow separation. The study was conducted for an exit-to-throat area ratio of 1.5 and for a range of nozzle pressure ratios. The flow separated by the action of a lambda shock, followed by a succession of expansion and compression waves. The computationally obtained asymmetric flow structures were consistent with experimental flow visualizations studies. In addition, Xiao, et al. (2007) obtained other flow features, such as shock wave location and wall pressure distributions, in good agreement with the experimental data.

2.3.1. Discrete Phase Model

A set of Eulerian, Lagrangian and hybrid particle models were employed in a simulation of coarse particles conveying through the curved and straight rectangular ducts by Pirker, et al. (2010). In addition, the behaviour of mono-disperse coarse glass particles in a pneumatic conveying experiment were considered. Pirker, et al. (2010) applied the different numerical models such as the *Lagrangian Discrete Phase Model (DPM)* and the *Discrete Element Model (DEM)* for granular phase, and the simulation results compared with experimental data. According to the results, for coarse particle conveying, the *DPM* was qualitatively evaluated in gas-particle interaction and

computational efficiency. The inter-particle collisions, particle rotation, volume displacement and qualitative agreement have been evaluated for *DPM*.

A pressure-based algorithm for multi-phase flow for predicting incompressible and compressible phenomena with subsonic, transonic, and supersonic regimes was presented by Moukalled, et al. (2003). The performance of the study was assessed by solving the two-dimensional two-phase flows including the incompressible turbulent bubbly flow in a pipe, incompressible turbulent air-particle flow in a pipe, compressible dilute gas-solid flow over a flat plate, and compressible dusty flow in a converging diverging nozzle. In a converging diverging nozzle the high pressure and temperature gas flow was employed to propel particles through the nozzle. Inlet velocity and temperature of the particles were presumed to be the same as those of the gas phase. Results for two particle sizes of radius 1 and 10 μm with the same mass fraction were presented. According to the results, for the flow with particles of radius 1 μm, a sharp change in particle density was obtained near the upper wall downstream of the throat, and the particle density decreased to a small value. With the large particle flow (10 μm), however, a much larger particle-free zone appeared due to the inability of the heavier particles to turn around the throat corner. These findings were in excellent agreement with other published numerical and/or experimental data which were presented in the article.

In cold spraying, the effect of the nozzle cross-section shape on gas flow and particle acceleration was presented by Yin, et al. (2011). The ideal gas law for N_2 was employed to calculate the density in order to take the compressibility effects into consideration. In order to capture the turbulent flow features accurately, the standard K-ε turbulence model available in FLUENT was utilized for modeling the turbulent flow in the simulation. In addition, the standard wall function was applied for the near-wall flow treatment. On the other hand, copper was used as the spraying particle material. Yin, et al. (2011) computed the particles' acceleration by the utilizing of DPM. Generally this model requires that the discrete phase must be present at sufficiently low volume fractions. In this case, all the spray particles were spherical in shape and hence the spherical drag law has been used to compute the drag coefficient. Particle-particle interactions and the effect of particles on the gas phase could be neglected. Standard no-slip condition was used at the nozzle wall and the substrate surface. The heat transfer process between the gas and the wall has not been considered, thus a fixed heat flux of

zero was enforced at the wall. According to the results, the comprehensive comparison between rectangular nozzles and elliptical nozzles indicated that rectangular nozzles had slightly lower mean particle impact velocity than elliptical nozzles. However, for rectangular nozzles, more particles may achieve relatively high velocity due to the larger sectional area of their potential core.

In addition, Yin, et al. (2011) found that the mean particle impact velocity increases gradually with the decrease in Width/Length ratio (W/L) of the cross-section because of the diminishing bow shock size. Moreover, the systematic study on the powder release position confirmed that releasing particles from the nozzle inlet can ensure that particles achieve a high impact velocity and temperature.

Moshfegh, et al. (2009) presented a simulation of non-reacting dilute gas-solid flow in a truncated ideal contour nozzle with consideration of external stream interactions. The *Eulerian-Lagrangian* approach involving a two-way momentum and thermal coupling between gas and particles exchanges was adopted. The main goal was the determining of the separation point quantitatively and its variations versus the particles diameter and mass flow fraction. Moshfegh, et al. (2009) found that the near-wall Mach number remained approximately unchanged for all cases before the separation point. After experiencing the separation, a prominent reduction in the wall Mach number appeared. Also this study confirmed that the considerable inertia of particles enforced to move close to the centreline of nozzle, and an eminent particles-free zone was created near the nozzle contour. The particles-free zone got smaller as the particles diameter and mass flow fraction was increased.

Ozalp and Kanjirakat (2010) simulated the particle deposition on a solar reactor by using a multi-phase turbulent flow and *DPM*. Solar cracking of methane is a promising technology for emission free hydrogen production, but one of the major problems affecting a methane cracking solar reactors' performance is the carbon particle deposition on the window, walls and at the exit. In this study, a three-dimensional *Computational Fluid Dynamics (CFD)* analysis using the *Discrete Phase Model (DPM)* has been done for qualitative validation of the experimental observations. In order to evaluate the turbulent quantities in the solar reactor; the *RNG k-ε* model was applied. According to the results, the application of the *Discrete Phase Model* with particle tracking successfully predicted particle deposition in a solar thermal reactor.

The *Discrete Phase Model* has also been employed for the simulating of gas-powder two-phase flow jet from a coaxial nozzle by Zekovic, et al. (2007), Kheloufi and Amara (2010), and Zhu, et al. (2011). The k-ε turbulence model was utilized for continuous phase. The continuity and momentum equations were discretized by using a second order upwind interpolation scheme. The performed works confirmed the importance of numerical modeling to manage with a more efficient approach the laser cladding and metal deposition process. The Laser-based direct metal deposition (DMD) was simulated based on three-dimensional (3D) multi-phase gas-powder flow and combined with the experimental results (Zekovic, et al., 2007) to achieve a powerful tool for analyzing the influence of the gas-powder flow characteristics on the process stability and the process output. Different height and width parameters of deposited layers were chosen (Zhu, et al., 2011) to calculate the powder concentration distribution, consequently, and also their effect on additive height of a single-trace cladding layer was studied by experimental investigations.

The dynamic characteristics of ultrahigh velocity water-jets and abrasive water-jets (AWJs), which exit from very fine nozzle, were simulated by Liu, et al. (2004). The water and particle velocities in a jet were obtained under different input and boundary conditions to provide an insight into the jet characteristics and a fundamental understanding of the kerf formation process in AWJ cutting. For the range of downstream distances considered, Liu, et al. (2004) found that a jet was characterised by an initial rapid decay of the axial velocity at the jet centre while the cross-sectional flow evolves towards a top-hat profile downstream. According to the results, by increasing axial location of particles at a given cross-section the velocity profile was more flatted.

Hemidi, et al. (2009) investigated the supersonic ejector in a refrigeration system by employing DPM, and a comparison with experimental achieved data. According to the results, the presence of liquid droplets in the primary stream of the ejector, which could physically come from condensation, was not necessarily harmful to the ejector operation but on the contrary may improve its off-design operation. Hemidi, et al. (2009) concluded that for a real refrigeration situation, a consistent compressible two-phase CFD model needs to be set up. In this sense, a good model for ejectors operating with refrigerants should take into account possible nucleation, growing of condensation droplets, metastable states, and should be consistent in terms of the mixture speed of

sound. Hemidi, et al. (2009) obtained good validation results for a wide range of operating conditions.

2.4. Summary and Conclusions

As can be observed from reviewing the available literature, in the study of the multi-phase flow, a great deal of fundamental research has already been conducted into the fluidized bed. Also investigation of the single-phase and some two-phase (air-water) nozzle flow is extensive in the literature. However investigation into the two-phase air-solid nozzle flow is very scarce and investigation into the three-phase (air-solid-water) nozzle flow is fundamentally non-existent. Finally, reviewing the literature indicates that numerical or experimental investigation into the three-phase heated water nozzle flow is non-existent.

CHAPTER 3

DESCRIBING THE PROBLEM, THEORETICAL BACKGROUND OF MULTI-PHASE TURBULENT FLOW, AND NUMERICAL MODELLING

Introduction

This chapter describes the geometrical characteristic of the air-sand-water three-phase flow through the nozzle as well as glancing at the numerical modelling of the multi-phase turbulent flows. This includes a brief discussion of blasting methods and in particular the main equipment used in Shot-Blasting, and emphasize to the nozzle by enclosing of grid generation and discretization of Nozzle's continues domain. Also in this chapter, different Euler-Euler multi-phase models as well as the Euler-Lagrange model are introduced and appropriate models for different multi-phase systems are presented. The governing equations for the Eulerian Model, as a model of the Euler-Euler approach, and the Discrete Phase model, as a model of the Euler-Lagrange approach, are also discussed. Finally, this chapter presents the numerical methods applied to solve the governing equations of turbulent and multiphase-flow. For this purpose, the Finite Volume method, as a method for representing and evaluating of transport equations, is briefly reviewed. The turbulent multi-phase flow is simulated by utilizing the FLUENT, i.e. computational fluid dynamics (CFD) software package.

3.1 Blasting Methods

Three basic components are essential for all abrasive blasting systems: a blasting pot or abrasive container, a propelling device and a nozzle. Depending on the application, air pressure, water pressure and centrifugal wheels are three different propelling methods that are used in abrasive blasting systems. Abrasive media is blasted by compressed air in air blasting systems, and propelled by high pressure water in water blasting systems. In centrifugal wheel systems, centrifugal and inertial forces are applied as a mechanical propeller to the abrasive media.

As Figure (3.1) shows, the abrasive media in the compressed air pressure system, is contained in the pressure tank or fluidised bed. Compressed air has entered to both the top and bottom of the pressure tank. Consequently, the abrasive media can flow by gravity into the discharge hose without loss of pressure.

There is a slight difference in the design of the compressed air pressure system and the wet abrasive blasting system. As Figure (3.2) shows, the wet abrasive blasting system has a specially designed pressure tank. In this system, the mixture of abrasive media and water is propelled toward the nozzle by compressed air.

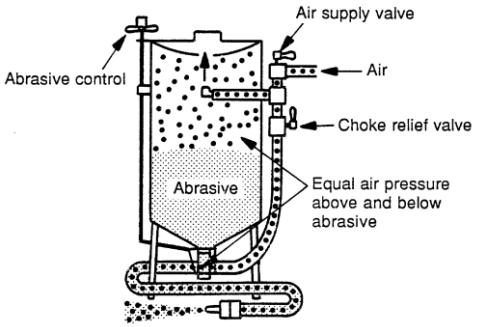

Figure (3. 1). Compressed air pressure

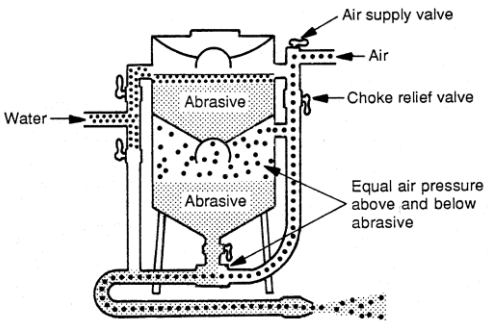

Figure (3. 2). Wet abrasive blasting system

In hydraulic blasting systems, Figure (3.3a), two rubber hoses are connected to a hydraulic blasting nozzle, one hose is connected to the high pressure water supply and the other one is connected to the bottom of the abrasive supply tank. The hydraulic blasting nozzle (Figure 3.3b) consists of a water nozzle that discharges into a larger nozzle. Partial vacuum in the chamber due to the high velocity water jet draws the abrasive into the outer nozzle and forces it out through the discharge opening. Figure (3.3a) shows a typical hydraulic pressure blasting machine.

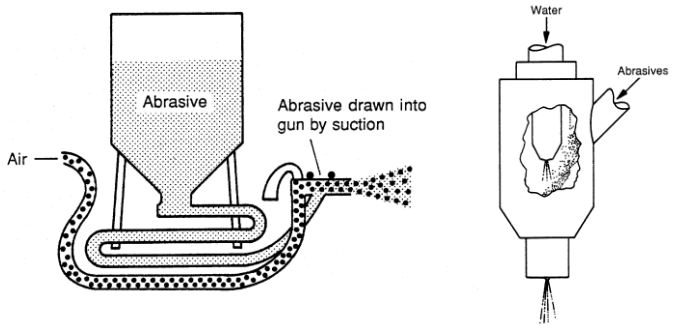

Figure (3. 3). a:Hydraulic blasting system; b: Hydraulic blasting nozzle

Media abrasive consumption mainly depends on nozzle pressure, nozzle minimum diameter and media abrasive bulk density. Table (3.1) shows the amount of sand utilization during blasting operations and for other abrasives and nozzle diameters, Equation (3.1) can be used (Emission Factor Documentation for AP-42, 1997).

$$\dot{m}_a = \dot{m}_s \times \left(\frac{D_a}{D_s}\right)^2 \times \frac{\rho_a}{\rho_s} \qquad (3.1)$$

where $\dot{m}_a$ is the mass flow rate (lb/hr) of abrasive, $\dot{m}_s$ is the mass flow rate (lb/hr) of sand with the nozzle internal diameter D_s from Table (3.1), D_a is the nozzle internal diameter (in.) for any other abrasive, D_s is the nozzle internal diameter (in.) for sand (from Table 3.1), ρ_s is the bulk density of sand (lb/ft^3), and ρ_a is the bulk density of any other abrasive (lb/ft^3).

The bulk density of some common abrasives such as sand, aluminium oxides and steel are 99, 160 and 487 lb/ft^3, respectively.

Table (3. 1): Sand mass flow rate of blasting Nozzle (Ib/hr)

Nozzle Internal Diameter (in) \ Nozzle Pressure (psig)	30	40	50	60	70	80	90	100
1/8	28	35	42	49	55	63	70	77
3/16	65	80	94	107	122	135	149	165
1/4	109	138	168	195	221	255	280	309
5/16	205	247	292	354	377	420	462	507
3/8	285	355	417	477	540	600	657	720
7/16	385	472	560	645	755	820	905	940
1/2	503	615	725	835	945	1050	1160	1265
5/8	820	990	1170	1336	1510	1680	1850	2030
3/4	1140	1420	1670	1915	2160	2400	2630	2880
1	2030	2460	2900	3340	3780	4200	4640	5060

3.1.1 Abrasive Media

Mineral and recyclable media abrasives are generally used in blasting systems. Table (3.2) introduces some of these abrasive media with related properties, applications, advantages and limitations. Depending on application and abrasive cost, one of the following media abrasives could be selected (Occupational Safety & Health Administration).

Table (3. 2): Media abrasive for Shot-Blasting system

Media Abrasive	Properties	Applications	Advantages	Limitations
ALUMINUM OXIDE	Very hard	Fast cutting; matte finishes; descaling and cleaning of coarse and sharp textures Cleaning hard metals (e.g. Titanium)	Recyclable	Must be Reclaimed and Reused for Economy
BAKING SODA(Sodium Bicarbonate)	Natural, water soluble, non-sparking, non flammable	General Paint Removal Stripping Aircraft Skins Cleaning Surfaces in Food Processing Plants Removing Paint from Glass	Less Material Used/Less Cleanup Low Nozzle Pressures (35-90 PSI)	May Damage Soft Brick
COAL SLAG	Hard, uniform density, low friablity	General Paint, Rust & Scale Removal from Steel Paint Removal from Wood	Fast Cutting Creates Anchor Profile	Tendency to Imbed in Mild Steel May Contain Toxic Metals
COPPER SLAG	Hard, sharp edged	General Paint, Rust & Scale Removal from Steel Paint Removal from Wood	Rapid Cutting	Tendency to Imbed in Mild Steel May Contain Toxic Metals
CORN COB GRANULES	Medium hardness, non sparking	Paint & Rust Removal from Wood & Metal	Low Consumption Low Dust Levels Biodegradable	Does Not Create an Anchor Profile
DRY ICE(Carbon Dioxide)	Natural gas in solid state	Cleaning Aircraft Parts Cleaning Exotic Metals	No Residue Remains Minimal Cleanup	
GARNET	Very hard and heavy	General Paint, Rust & Scale Removal from Steel	Lower Nozzle Pressures (60-70 PSI) Low Dust Levels Fast Cleaning Rates Can be Recycled	
GLASS BEADS	Manufactured of soda lime glass	Decorative blending; light deburring; peening; general cleaning; texturing	Recyclable Provide High Luster Polished Surface	Does Not Create an Anchor Profile
NICKEL SLAG	Very hard, sharp edged	General Paint, Rust & Scale Removal from Steel	Rapid Cutting	Used in Wet Blasting May Contain Toxic Metals
NUT SHELLS	Soft, non-sparking	Very light deburring, fragile parts, Cleaning Soft Materials (e.g. Aluminum, Plastic, Wood), Deflashing of plastics, Cleaning Surfaces in the Petroleum Industry	High Removal Speed Non-Sparking Low Consumption	Non-Etching Potential Fire Hazard

Table (3.2) (continue)

Media Abrasive	Properties	Applications	Advantages	Limitations
OLIVINE	Natural mineral, hard, angular	Clean Light Mill Scale & Rust from Steel	Low Chloride Ion Level Low Conductivity	
PLASTIC MEDIA	Soft, non-abrasive, polyester	Cleaning Soft Metals & Composites Cleaning Metal Fabric Screens	Recyclable Does Not Damage Metal Surfaces Low Nozzle Pressures (20-40 PSI)	Anchor Profile Limited to Soft Substrates (e.g. Aluminum and Plastic)
STAUROLITE	Rounded grains, Hard, irregular shape	Cleaning Corroded, Pitted, Weathered Steel Creating Anchor Profile on New Steel	Good Feathering Low Dust Levels Recyclable 3-4 Times	May Contain Up to 5% Free Silica
STEEL GRIT & SHOT	Uniform size and hardness	Paint, Rust & Scale Removal from Steel	Can be Recycled 100-200 Times Low Dust Levels Superior Visibility Portable Blast Rooms Available Creates Anchor Profile	
Silica sand	quickly breaks up	the most commonly used abrasive	Rapid Cutting	High volume of dust created by the sand breaking when hitting the object.

However silica sand, although quickly breaks up, creates large quantities of dust, and has the most negative impact, it is one of the most commonly used abrasives. Silica sand has the ability to remain suspended in water so it could be used in a wet blasting system as well as a dry blasting system. Appendix A presents some chemical and physical properties of sand, which have been used in the numerical analysis of the three-phase flow.

3.2 Nozzle

A nozzle is a mechanical appliance which is designed to control the direction or characteristics of a fluid flow. Perhaps the converging-diverging nozzle is the most important and basic piece of engineering hardware associated with the high speed flow of gases. This device was invented by Gustaf de Laval in 1890 to increase the steam jet to supersonic speed, by the interchanging of pressure to the kinetic energy of the steam, and so the nozzle is often referred to as the 'de Laval' nozzle.

3.2.1 Technical Background of the Nozzle

The usual configuration for a converging-diverging (CD) nozzle, and pressure distribution for various flow conditions, including subsonic and supersonic flows are shown in the Figure (3.4).

Mass flows from a region of high pressure into the converging part of the nozzle, past the throat, through the diverging section and then exhausts into the ambient as a jet. The pressure of the nozzle entrance is denoted by the symbol p_{in} and the pressure of the ambient is referred to as the 'back pressure' and given the symbol p_b .

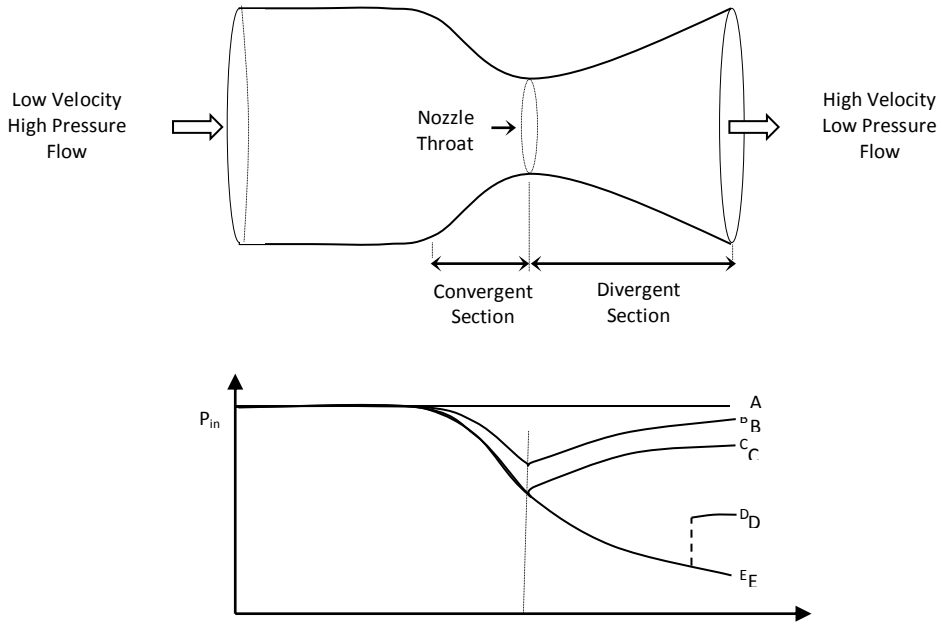

Figure (3. 4). Converging-Diverging Nozzle and pressure distribution

Definitely, the amount of mass flow through the nozzle depends on the pressure difference between the entrance and exhaust of the nozzle. By increasing the pressure difference between p_{in} and p_b (here, just decreasing back pressure p_b), it may be expected that more mass flow will get through the nozzle. This is true, but only up to a point. If the pressure difference raises enough, as Figure (3.5) shows, it comes to a place where the flow rate suddenly stops increasing altogether (curve a-b-c in Figure 3.5).

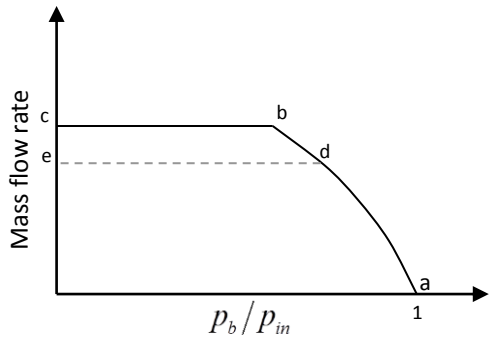

Figure (3. 5). Critical mass flow rate from the Nozzle by constant inlet pressure (Zucker and Biblarz, 2002; Nag, 2008)

This maximum mass flow rate through the nozzle takes place when its throat is at the critical or sonic condition. The nozzle is then said to be choked and can carry no additional mass flow unless the throat is widened. If the throat is constricted further, the mass flow through the nozzle must decrease (curve a-d-e in Figure 3.5). On the other hand, Figure (3.5) shows that the mass flow rate is zero if the pressure ratio, p_b / p_{in}, is equal to 1, and by decreasing the pressure ratio the mass flow rate will increase. There are two common choices for decreasing this ratio. In the first case, the inlet pressure keeps constant and the back pressure decreases. In the second case, the back pressure keeps constant and the inlet pressure is increasing. These two cases have different behaviour on the critical mass flow rate curve, and the Figure (3.5) is valid for the first case. More details about these two cases are expressed in Chapter Five.

For isentropic flow through the nozzle, the maximum possible mass flow is expressed by Equation (3.2) (Zucker and Biblarz, 2002; Balachandran, 2006).

$$\dot{m}_{\max} = \left[\frac{k}{R} \left(\frac{2}{k+1} \right)^{(k+1)/(k-1)} \right]^{1/2} \frac{A^* P_0}{\sqrt{T_0}} \tag{3.2}$$

here $\quad p_0 = p_t = p\left(1 + \frac{k-1}{2} M^2\right)^{k/(k-1)} \quad \& \quad T_0 = T_t = T\left(1 + \frac{k-1}{2} M^2\right)$

here p_0 (or p_t) and T_0 (or T_t) are stagnation (or total) pressure and temperature at a stagnation point, the p and T are static pressure and temperature, respectively, A^* is the throat area (the minimum area of nozzle which is sonic or critical), M is the Mach number, k is the ratio of specific heats (c_p / c_v), and R is the ideal gas constant.

Pressure distribution through the Nozzle: The converging-diverging (CD) nozzle and the pressure distribution through it are shown in Figure (3.4). The fluid enters into

the nozzle with low velocity and high inlet pressure P_{in}, and exits from the nozzle by back pressure, p_b, which is lower than the inlet pressure. For various back pressure, one of the following cases may occur:

Case A. When $p_b = p_{in}$, there is not any pressure difference between the inlet and the exit of the nozzle, and so the flow rate through the nozzle vanishes.

Case B. When $p_{in} > p_b > p_C$, the flow remains subsonic throughout the nozzle and the mass flow is less than the maximum flow which has been expressed in Equation (3.2). By modification of Equation (3.2), actual mass flow at any section of the nozzle is obtained by White (2003, p. 587) as expressed in Equation (3.3):

$$\dot{m} = \frac{A p_0}{\sqrt{R T_0}} \sqrt{\frac{2k}{k-1}\left(\frac{p}{p_0}\right)^{2/k}\left[1-\left(\frac{p}{p_0}\right)^{(k-1)/k}\right]} \qquad (3.3)$$

where A and p are the local area and pressure, respectively. Equation (3.3) is useful for the mass flow rate of the subsonic nozzle if stagnation conditions are known and the flow is not choked.

In this case the fluid velocity increases in the first (converging) section and reaches a maximum at the throat (but $M < 1$). However, most of the gain in velocity is lost in the second (diverging) section of the nozzle, which acts as a diffuser. On the other hand, as Figure (3.4) shows, the pressure decreases in the converging section, reaches a minimum at the throat, then increases at the expense of velocity in the diverging section.

Case C. When $p_b = p_C$, fluid velocity at the throat increases to sonic velocity and the throat pressure becomes p^*. In this case the converging-diverging nozzle achieves maximum mass flow rate. As Figure (3.4) shows p^* is the lowest pressure that can be obtained at the throat. The lowering of p_b further will have no influence on the fluid flow in the converging part of the nozzle or the mass flow rate through the nozzle. However, it will affect the character of the flow in the diverging section.

Case D. When $p_C > p_b > p_E$, the fluid that achieved a sonic velocity at the throat continues accelerating to supersonic velocities in the diverging section as the pressure decreases. This acceleration comes to a sudden stop, wherein a normal shock develops at a section between the throat and the exit. The fluid

then continues to decelerate further in the remaining part of the converging-diverging nozzle. Flow through the shock is highly irreversible, and thus it cannot be assumed as isentropic. By decreasing the back pressure, p_b, the normal shock moves downstream away from the throat and finally it approaches the nozzle exit when $p_b = p_E$ (*Case E*).

3.2.2 Shot Blasting Nozzle

The nozzle is one of the most important devices in shot blasting systems which accelerate the abrasive to achieve high kinetic energy. A common nozzle which is used in shot blasting systems is shown in Figure (3.6a) and (3.6b).

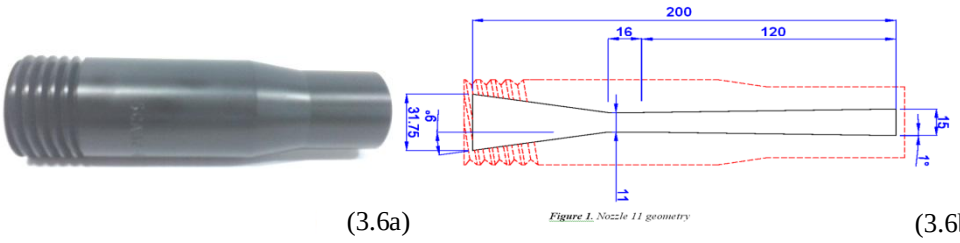

(3.6a) (3.6b)

Figure (3. 6). a: Shot Blasting Nozzle; b: Geometrical dimension of computed Nozzle

Figure (3.6b) shows a schematic sketch and the geometrical dimensions of a shot blasting nozzle, which has been used in the following three-phase simulation in this project.

3.2.2.1 Grid Generation and Discretization

Discretization is the process of transferring a continuous model or geometry into discrete elements to prepare for analysis. This process is essential for numerical simulation and implementation on digital computers. In this study the finite volume method is used to solve turbulence and three-phase flow equations. In the finite volume method, by grid generation, computational domain is transferred into a finite number of contiguous control volumes (CV) and then the integral form of continuity, momentum and/or energy equations are applied to each control volume.

There are some commercial mesh generators such as GridTool (NASA Langley), NEWT MeshTools (Cambridge Flow Solutions) and Gambit (FLUENT Inc.). In the following chapters Gambit as an advance grid generation package is used.

Complex models can be made directly within Gambit's solid geometry modeller, or imported from any major Computer-Aided Drafting (CAD) or Computer-Aided Engineering (CAE) system. Gambit has the capability to generate 2d and 3d grids including structured, unstructured and hybrid, triangles and quadrilaterals, numerous meshing schemes such as map, submap, quad pave, triangulation, triangle primitive and hybrids.

Grid generation has been applied to the shot blasting nozzle shown in Figure (3.6a). For this purpose, structured 2d grids and quadrilaterals have been mapped through the nozzle. Definitely, successful computations of the multi-phase flow require some consideration during the mesh generation which will be expressed in the forthcoming sections. Figures (3.7a) and (3.7b) show the grid distribution of the entire nozzle and the refined grid in the divergent part of the nozzle.

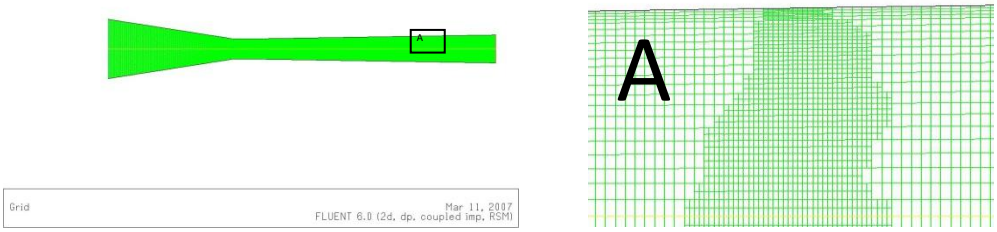

Figure (3. 7). a: Mesh distribution on Nozzle; b: Pressure adapted Mesh

3.3 Multi-phase Models

Following the classification of various multi-phase flow regimes in Chapter One, this section is going to briefly introduce the appropriate models for some general multi-phase flow regimes. Definitely, applying the appropriate models for specified regimes is the first step in the simulating of any multi-phase problem.

Three of the more popular and widely used models in the Euler-Euler approach are the *Volume of Fluid* (VOF) *model*, the *Mixture model* and the *Eulerian model*. In some cases and due to the multi-phase problem limitation, which are discussed in this section, none of above-mentioned models of the Euler-Euler approach is usable and in these

cases the *Discrete Phase Model* (DPM) of the *Euler-Lagrange approach* might be applicable.

Volume of Fluid (VOF) Model: The VOF model is a numerical technique for tracking and locating the free surface or fluid-fluid interface. It is applicable for two or more immiscible fluids, where the position of the free surface or fluid-fluid interface is significant.

In the VOF model, a single momentum equation is solved throughout the domain, and the achieved velocity field is shared among the phases. Obviously, the momentum equation is dependent on the volume fractions of all phases through the properties such as density, ρ, and viscosity, μ. The *Volume of Fluid* (VOF) *model* is mostly applicable for slug flows, for example large bubble motion in pipes or tanks, and stratified or free-surface flows such as boiling and condensation in nuclear reactors.

Since this study is related to air-water-sand three-phase flow, and the VOF model is applicable just for two or more fluid flow problems, it is not suitable for this study; however, more details of this model can be found in the Fluent User Guide (2006).

Mixture model: The mixture model is designed for the simulating of two or more phase flows which include the solid phase as well as gas or liquid phases. Since the mixture model is a model of the Eulerian approach, so the phases are treated as interpenetrating continua. In the *Mixture model*, coupling between the phases should be strong so it can model the n-phases by solving the momentum equation for the mixture and prescribes relative velocities to described phases. The *Mixture model* is widely used in homogeneous flows on pneumatic transport such as transport of cement.

Eulerian model: The *Eulerian model*, as well as the *Mixture model*, is designed for the simulating of the flow of n phases, including fluids and particles. The *Eulerian model* solves a set of n momentum and continuity equations for each phase; so it could be more complex than the *Mixture model*. The number of secondary phases, in the *Eulerian model*, is limited only by memory requirements and convergence behaviour. The *Eulerian model* is a better choice than the *Mixture model* whenever the accuracy is more important than computational effort, otherwise, the *Mixture model*, since it uses a smaller number of equations than the *Eulerian model*, is a good option to solve a simpler problem. For example, in hydro-transport and slurry flows, both the *Mixture* and the *Eulerian models* are applicable.

The *Eulerian model* mainly is suitable for granular flows on pneumatic transport, for example the transport of grains or metal powder, granular flows on fluidized beds such as circulating fluidized beds and sedimentation, for example in mineral processing.

Discrete Phase Model: The *Discrete Phase model* (DPM) is designed for simulating of the flow with a sufficient dilute secondary phase, and it assumed that a particle-particle interaction is negligible. In practice, the volume fraction of disperse phases in the *DPM* must be less than 10-12%; however, the mass flow of the secondary phases may be equal or more than the primary phase (Fluent, 2006). For example, in bubbly and droplet flows such as cavitations and atomizers, if the phases mix and/or dispersed-phase volume fractions be less than 10-12%, *DPM* must be used, otherwise, the *Mixture model* or the *Eulerian model* are applicable.

3.4 Numerical modelling in multi-phase flows

Governing equations for fluids dynamic, mass and heat transfer for turbulent single phase flow can be found in different fluid dynamic textbooks, such as Bejan and Kraus (2003) and White (2003). Here, the proper forms of these equations for multi-phase flow are presented, and transport equations of mass, momentum and energy are assigned for different multi-phase flow models such as the *Mixture*, *Eulerian* and *Discrete Phase Model*.

3.4.1 Governing Equations

The generic transport equation, that describes fluid dynamics and heat transfer of the multi-phase flow, is a general partial differential equation which may be written as:

$$\frac{\partial(\alpha\rho\phi)}{\partial t} + \nabla\cdot\left(\alpha\rho\vec{V}\phi\right) = \nabla\cdot\overline{\overline{\tau}} + S_\phi \qquad (3.4)$$

Where ϕ, α, ρ, $\vec{V}$, $\overline{\overline{\tau}}$ and S_ϕ have various definitions and values for different multi-phase models:

- In the Mixture model, ϕ is a mixture variable, α is unity, ρ is the mixture density, $\vec{V}$ is the mixture velocity, $\overline{\overline{\tau}}$ is the diffusion term and S_ϕ is the source term.
- In the Eulerian model, ϕ is a phase variable, α is the phase volume fraction, ρ is the phase density, $\vec{V}$ is the phase velocity, $\overline{\overline{\tau}}$ is the diffusion term and S_ϕ is the source term.

- In the Discrete Phase model: ϕ is a continuum phase variable, α is unity, ρ is the continuum phase density, $\vec{V}$ is the continuum phase velocity, $\bar{\bar{\tau}}$ is the diffusion term and S_ϕ is the source term.

3.4.2 Continuity equation for conservation of mass:

The continuity equation for a disperse multi-phase flow expresses that, in any steady state process, the mass flow of component N into the control volume is equal to the rate of mass that leaves from that control volume subject to having no phase change or chemical reaction for that component. In an unsteady state process, the net rate of mass of component N which passes through the surfaces of control volume plus the rate of increasing mass into the control volume should be zero if there is not any phase change or chemical reaction.

The general continuity equation for individual component, *N*, including the phase change, might be written as (Crowe, 2005):

$$\frac{\partial(\rho_N \alpha_N)}{\partial t} + \nabla \cdot \left(\rho_N \alpha_N \vec{V}_N\right) = \sum_{P=1}^{n} \left(\dot{m}_{PN} - \dot{m}_{NP}\right) \tag{3.5}$$

where *n* is the number of phases, and the right hand of Equation (3.5) is the net mass transfer between phase *N* and other phases. If the mass transfer between the phases be negligible, the right of the Equation (3.5) vanishes and the continuity equation might be simplified as:

$$\frac{\partial(\rho_N \alpha_N)}{\partial t} + \nabla \cdot \left(\rho_N \alpha_N \vec{V}_N\right) = 0 \tag{3.6}$$

Equation (3.6) is the continuity equation for an individual component, and the sum of this equation for all phases yield the combined phase continuity equation:

$$\frac{\partial \rho}{\partial t} + \nabla \cdot \left(\sum_N \rho_N \alpha_N \vec{V}_N\right) = 0 \tag{3.7}$$

where ρ is the mixture density and given by:

$$\rho = \sum_N \rho_N \alpha_N \tag{3.8}$$

With zero relative velocity of phases, the mixture velocity is equal to the phase velocity, $\vec{V}_N = \vec{V}$, and Equation (3.7) might be written as:

$$\frac{\partial \rho}{\partial t} + \nabla \cdot \left(\rho \vec{V}\right) = 0 \tag{3.9}$$

Finally, Equation (3.9) is called the Mixture Continuity Equation which is identical to the Equation (3.5) that is for single phase flow of density ρ.

3.4.3 Continuity equation for conservation of Momentum:

Prior to using the general partial differential Equation (3.4) for momentum, it is better to modify the control volume in order to avoid any cutting of the disperse phase particles. For this purpose, the bounding surfaces of the control volume could be deformed. In this case, the momentum equation in the *k* direction might be written as (Brennen, 2005):

$$\frac{\partial}{\partial t}\left(\rho_N \alpha_N u_{Nk}\right)+\frac{\partial}{\partial x_i}\left(\rho_N \alpha_N u_{Nk} u_{Ni}\right)=\rho_N \alpha_N g_k-\delta_N \frac{\partial}{\partial x_i}\left(\delta_{ik} p-\sigma_{Cki}^{D}\right)+F_{Nk} \tag{3.10}$$

where the first term in the left of Equation (3.10) is the rate of increase of momentum of component N in the *k* direction within the control volume, and the second term in the left of Equation (3.10) is the net flux of momentum in the *k* direction through a side perpendicular to the i direction. In the right hand of Equation (3.10), the first term is the gravitational forces in the *k* direction, and δ_{ik} is the Kronecker delta such that $\delta_{ik} = 1$ for $k = i$ and $\delta_{ik} = 0$ for $k \neq i$. Second term in the right of Equation (3.10), including two terms inside the parentheses, is the force due to the tractions on the control volume. These terms are defined just for the continuous phase and for the disperse phase, they are equal to zero. The first term inside the parentheses is the pressure gradient in the *k* direction, and the second term is the deviatoric stress of the continuous phase. The last term in the right of Equation (3.10), F_{Nk}, is the force that is imposed on the component *N* by the other components within the control volume in the *k* direction. Equation (3.10) is applicable for both the disperse phase ($N = D$) and the continuous phase ($N = C$). Finally, δ_N in the momentum equation of the disperse phase is $\delta_N = \delta_D = 0$, and for the continuous phase is defined as $\delta_N = \delta_C = 1$.

The equivalent one-dimensional or duct flow form of Equation (3.10) is:

$$\frac{\partial}{\partial t}\left(\rho_N \alpha_N u_N\right)+\frac{1}{A}\frac{\partial}{\partial x}\left(A\rho_N \alpha_N u_N^2\right)=\rho_N \alpha_N g_x-\delta_N\left(\frac{\partial p}{\partial x}+\frac{P\tau_w}{A}\right)+F_N \tag{3.11}$$

where A(x) and P(x) are the area and perimeter of the cross section of the duct or pipe flow, respectively, τ_w is the wall shear stress, and F_N is the force that is imposed from other components to the component N.

With zero relative velocity of phases, the Equation (3.11) is simplified and reduces to:

$$\frac{\partial}{\partial t}(\rho u)+\frac{1}{A}\frac{\partial}{\partial x}\left(A\rho u^2\right)=\rho g_x-\left(\frac{\partial p}{\partial x}+\frac{P\tau_w}{A}\right) \tag{3.12}$$

In the following section, the momentum equations for fluid-fluid and granular multi-phase flows, as solved by FLUENT, are presented.

3.4.3.1 Momentum equations of fluid-fluid:

Since in the fluid-fluid multi-phase flow both phases are fluid, so the continuous phase is called the primary phase, p, and the other phase, with less volume fraction than the primary phase, is called the secondary phase, q. The conservation of momentum for a fluid phase q is:

$$\frac{\partial}{\partial t}\left(\rho_q\alpha_q\vec{V}_q\right)+\nabla\cdot\left(\rho_q\alpha_q\vec{V}_q^2\right)=\rho_q\alpha_q\vec{g}-\alpha_q\nabla p+\nabla\cdot\overline{\overline{\tau}}_q+F_{pq} \tag{3.13}$$

where $\overline{\overline{\tau}}_q$ is the phase stress-strain tensor and is defined as (Brennen, 2005):

$$\overline{\overline{\tau}}_q=\alpha_q\mu_q\left(\nabla\vec{V}_q+\nabla\vec{V}_q^T\right)+\alpha_q\left(\lambda_q-\frac{2}{3}\mu_q\right)\nabla\cdot\vec{V}_q\overline{\overline{I}} \tag{3.14}$$

Here $\nabla\vec{V}_q^T$ is the transpose of $\nabla\vec{V}$, μ_q and λ_q are the shear and bulk viscosity of phase q, and $\overline{\overline{I}}$ is the unit tensor. The last term in the right hand of Equation (3.13), F_{pq}, might be modeled as (Brennen, 2005):

$$F_{pq}=\sum_{p=1}^{n}\left(K_{pq}\left(\vec{V}_p-\vec{V}_q\right)+\dot{m}_{pq}\vec{V}_{pq}-\dot{m}_{qp}\vec{V}_{qp}\right)+\left(\vec{F}_q+\vec{F}_{lift,q}+\vec{F}_{vm,q}\right) \tag{3.15}$$

where K_{pq} is the inter-phase momentum exchange coefficient (described in Section 3.4.3.3), $\vec{F}_q$ is the net external body force, $\vec{F}_{lift,q}$ is the lift force, $\vec{F}_{vm,q}$ is the virtual mass force, $\dot{m}_{pq}=-\dot{m}_{qp}$ is the mass transferring from phase p to phase q, and $\vec{V}_{pq}$ is the inter-phase velocity, defined as follows:

$$\begin{cases}\dot{m}_{pq}>0 & then \quad \vec{V}_{pq}=\vec{V}_p\\ & or\\ \dot{m}_{pq}<0 & then \quad \vec{V}_{pq}=\vec{V}_q\end{cases} \quad and \quad \begin{cases}\dot{m}_{qp}>0 & then \quad \vec{V}_{qp}=\vec{V}_q\\ & or\\ \dot{m}_{qp}<0 & then \quad \vec{V}_{qp}=\vec{V}_p\end{cases}$$

The lift force, $\vec{F}_{lift,q}$, could be applied for larger particles and when the velocity gradients in the primary phase flow field is significant, but the FLUENT model assumes that the particle diameter is much smaller than the inter-particle spacing. So the lift force is not applicable for closely packed particles or for very small particles.

In multi-phase flows, the "virtual mass effect" occurs when a secondary phase accelerates relative to the primary phase. Due to the acceleration difference between the primary and secondary phases, a "virtual mass force" exerts on the particles:

$$\vec{F}_{vm,q} = c_{vm,q}\alpha_p\rho_p\left(\frac{\partial}{\partial t}\Delta\vec{V}_{qp} + \left(\vec{V}_q \cdot \nabla\right)\Delta\vec{V}_{qp}\right) \tag{3.16}$$

where $c_{vm,q}$ is the virtual mass coefficient, $c_{vm,q} = 0.5$, and $\Delta\vec{V}_{qp}$ is the velocity difference of the secondary and primary phase, $\Delta\vec{V}_{qp} = \vec{V}_q - \vec{V}_p$, (Kolev, 2007).

The virtual mass effect is significant when the secondary phase density is much smaller than the primary phase density (FLUENT, 2006).

3.4.3.2 Momentum equations of fluid-solid:

The conservation of momentum for the solid phase *s* is similar to Equation (3.13) and it might be written as:

$$\frac{\partial}{\partial t}\left(\rho_s\alpha_s\vec{V}_s\right) + \nabla\cdot\left(\rho_s\alpha_s\vec{V}_s^2\right) = \rho_s\alpha_s\vec{g} - \alpha_s\nabla p - \nabla p_s + \nabla\cdot\bar{\bar{\tau}}_s + F_{ls} \tag{3.17}$$

where p_s is the solid pressure of phase *s*, and $\vec{F}_{ls}$ is the net forces that exerts to the phase *s* from continuous phase, *l*, and external body force:

$$\vec{F}_{ls} = \sum_{p=1}^{n}\left(K_{ls}\left(\vec{V}_l - \vec{V}_s\right) + \dot{m}_{ls}\vec{V}_{ls} - \dot{m}_{sl}\vec{V}_{sl}\right) + \left(\vec{F}_s + \vec{F}_{lift,s} + \vec{F}_{vm,s}\right) \tag{3.18}$$

where K_{ls} is the momentum exchange coefficient between the fluid and solid phase, and $\vec{F}_s$, $\vec{F}_{lift,s}$ and $\vec{F}_{vm,s}$ are the net external body force, lift force, and virtual mass force, respectively, that are exerted to the phase *s*.

Further details and extensive discussions of the momentum equation of the disperse phase may be found in Brennen (2005), FLUENT (2006) and Kolev (2007).

3.4.3.3 Interphase Exchange Coefficients

The coefficient of the first term in the right hand of equations (3.15) and (3.18) is called the interphase exchange coefficient. This coefficient, K_{pq} in fluid-fluid and K_{ls} in fluid-solid, has a main role in the momentum exchange between the phases.

Fluid-Fluid Exchange Coefficient: In fluid-fluid multi-phase flow the continuous phase that is the predominant fluid, should be modelled as the primary phase, p. Whereas the sparser fluid is more likely to form droplets or bubbles, is called the secondary or disperse phase, q. For fluid-fluid momentum exchange coefficient between the primary and disperse phases, FLUENT uses the following equation:

$$K_{pq} = \frac{\alpha_p \alpha_q \rho_q f}{\tau_q} \tag{3.19}$$

where f is the drag factor, and τ_q is called "response time of disperse phase" or "particulate relaxation time", that is defined in terms of the disperse phase density, disperse phase diameter, d_q, and the viscosity of the primary phase, μ_p.

$$\tau_q = \frac{\rho_q d_q^2}{18\mu_p} \tag{3.20}$$

In Equation (3.19) the factor f is defined as:

$$f = \frac{C_D \operatorname{Re}_r}{24} \tag{3.21}$$

Here, $\mathrm{Re_r}$ is the relative Reynolds number. The relative Reynolds number between primary and secondary phases is defined as:

$$\operatorname{Re}_r = \frac{\rho_p \left|\vec{V}_q - \vec{V}_p\right| d_q}{\mu_p} \tag{3.22}$$

In Equation (3.21) C_D is the drag coefficient. In FLUENT, drag coefficient, C_D, is proposed by several models such as the *Schiller and Naumann* model, the *Morsi and Alexander* model, and the *symmetric* model.

Fluid-Solid Exchange Coefficient: In a fluid-solid multi-phase flow, the continuous phase or fluid should be modelled as the primary phase, *l*, and the particles or disperse phase, denoted by s, is considered as a secondary phase. The fluid-solid momentum exchange coefficient between the primary and disperse phases is introduced by FLUENT as:

$$K_{sl} = \frac{\alpha_s \rho_s f}{\tau_s} \tag{3.23}$$

where τ_s as the "particulate relaxation time", is defined in terms of the particle density and diameter, and the viscosity of the fluid, μ_l.

$$\tau_s = \frac{\rho_s d_s^2}{18\mu_l} \tag{3.24}$$

In order to couple the momentum transfer between fluid and solid phases, Fluent propose some models for the drag force. The *Syamlal-O'Brien* model (Syamlal and O'Brien, 1989), which is applicable for fluidized or settling beds; the *Wen and Yu* model (Wen and Yu, 1966), is appropriate for dilute systems, and finally the *Gidaspow* model (Gidaspow, Bezburuah and Ding, 1992) is recommended for dense fluidized beds. In this study, since the disperse phase volume fraction is less than 10%, the *Wen and Yu* model is applicable. In FLUENT fluid-solid exchange coefficient, with regard to the *Wen and Yu* model (Wen and Yu, 1966), are expressed as the following form:

$$K_{sl} = \frac{3}{4} C_D \frac{\alpha_s \alpha_l \rho_l \left|\vec{V}_s - \vec{V}_l\right|}{d_s} \alpha_l^{-2.65} \tag{3.25}$$

where

$$C_D = \frac{24}{\alpha_l \mathrm{Re}_r}\left[1 + 0.15(\alpha_l \mathrm{Re}_r)^{0.687}\right] \quad , \quad \mathrm{Re}_r = \frac{\rho_l d_s \left|\vec{V}_s - \vec{V}_l\right|}{\mu_l} \tag{3.26}$$

In other words, by attention to the Equations (3.23) to (3.26), the factor *f* in the *Wen and Yu* model is defined as:

$$f = [1 + 0.15(\alpha_l \mathrm{Re}_r)^{0.687}]\alpha_l^{-2.65} \tag{3.27}$$

Here $\mathrm{Re_r}$ is the relative Reynolds number and is defined by Equation (3.26), where the subscript *l* is for the l^{th} fluid phase, *s* is for the s^{th} solid phase, and d_s is the diameter of the s^{th} solid phase particles.

3.4.4 Continuity equation for conservation of Energy:

The principle of energy conservation or the First Law of Thermodynamics for single phase flow might be summarized as:

$$\left\{\begin{array}{c}\text{Net flux of total internal energy to CV}\\ +\\ \text{Rate of increase of total internal energy in CV}\end{array}\right\} = \left\{\begin{array}{c}\text{Rate of heat addition to the CV}\\ +\\ \text{Rate of work done on the CV}\end{array}\right\}$$

Consequently, the energy equation in a single phase flow can be written as (Bejan, 2004):

$$\frac{\partial}{\partial t}\left(\rho e^{*}\right)+\frac{\partial}{\partial x_i}\left(\rho e^{*} u_i\right)=Q+W-\frac{\partial}{\partial x_j}\left(u_i \sigma_{ij}\right) \tag{3.28}$$

where σ_{ij} is the stress tensor, and e^{*} is the total internal energy per unit mass that is equal to the internal energy plus kinetic energy and potential energy:

$$e^{*}=e+\frac{1}{2}u_i^2+g z \tag{3.29}$$

Similarly, the total internal energy for each component N becomes:

$$e_N^{*}=e_N+\frac{1}{2}u_{Ni}^2+g z \tag{3.30}$$

And for each component, the conservation of energy states:

$$\left\{\begin{array}{c}\text{Rate of increase of total internal energy of N in CV}\\ \text{Net flux of total internal energy of N out of CV}\end{array}\right\}=\left\{\begin{array}{c}\text{Rate of heat transfer to N from outside CV}\\ +\\ \text{Rate of heat transfer to N within CV}\\ +\\ \text{Rate of work done to N by surrounding}\\ +\\ \text{Rate of work done to N by other component}\end{array}\right\}$$

By attention to the above statement of energy conservation for component N, the individual phase energy equation may be written as (Brennen, 2005):

$$\frac{\partial}{\partial t}\left(\rho_N \alpha_N e_N^{*}\right)+\frac{\partial}{\partial x_i}\left(\rho_N \alpha_N e_N^{*} u_{Ni}\right)=Q_{out,N}+Q_{in,N}+W_{out,N}+W_{in,N}-\delta_N\frac{\partial}{\partial x_j}\left(u_{C,i}\sigma_{C,ij}\right) \tag{3.31}$$

where δ_N in the energy equation of the disperse phase is $\delta_N=\delta_D=0$, and for the continuous phase is defined as $\delta_N=\delta_C=1$.

The equivalent one-dimensional or duct flow form of Equation (3.31) is:

$$\frac{\partial}{\partial t}\left(\rho_N \alpha_N e_N^{*}\right)+\frac{1}{A}\frac{\partial}{\partial x}\left(A\rho_N \alpha_N e_N^{*} u_N\right)=Q_{out,N}+Q_{in,N}+W_{out,N}+W_{in,N}-\delta_N\frac{\partial}{\partial x}\left(p u_C\right) \tag{3.32}$$

where *A* is the cross sectional area of the duct. Unlike the Equation (3.31), which is written for control volume, and is two or three dimensional, the Equation (3.32) just depends on x. In other words, for example in Equation (3.32) $Q_{out,N}$ is the rate of external heat transfer to the phase N per unit length of the duct.

3.4.5 Dispersed Phase Equations

There are two more popular, accurate and widely used approaches to modelling the dispersed phases. One approach, that follows individual particles or sample particles, is the *Lagrangian* approach. The second approach is the *Eulerian*, which treats the particles as a cloud.

The *Lagrangian* approach is applicable to both dilute and dense flows. In dilute flows, there is just particle-fluid interaction and the motion of the particles is the influence of the particle-fluid interaction, body forces and particle-wall collisions. The Trajectory method, that is a form of the *Lagrangian* approach, is applicable for steady and dilute flows.

The dense and unsteady flows as well as the dilute and steady flows can use the *Lagrangian* approach. In dense flows, not only particle-fluid interaction, body forces, and particle-wall collision are important, but also particle-particle collision effects on the motion of the particles. The Discrete element method, which is briefly described in this section, is applicable for unsteady and dense flows (Crowe, 2006).

3.4.5.1 Trajectory method of the Lagrangian approach

The dilute dispersed flow through the chamber at a steady rate is computed by the trajectory method. The velocity of the disperse flow in the flow field for given mass amount and initial disperse velocity is calculated from:

$$\frac{d\vec{v}}{dt} = \frac{\vec{F}_f}{m} + \vec{g} \tag{3.33}$$

where $\vec{g}$ is the gravitational acceleration, and $\vec{F}_f$ is the frictional force between the continuous phase and the disperse phase of mass m. Integrating of the Equation (3.33) gives the velocity vector of the disperse phase. Hence, the trajectory of the disperse phase is obtained from:

$$\frac{d\vec{x}_q}{dt} = \vec{v} \tag{3.34}$$

where $\vec{x}_q$ is the droplet or particle (disperse phase) position.

The dispersed phase temperature distribution, along the trajectory, can be calculated from:

$$\frac{dT_q}{dt} = \frac{1}{mc_q}\left(\dot{Q}_q + \dot{m}L\right) \tag{3.35}$$

where $\dot{Q}_q$ is the total heat transfer to the disperse phase, and L is the latent heat of the disperse phase if the phase transition occurs in the flow field.

If the mass flow entering into the chamber breaks up into j trajectories, the number of the dispersed phase that flow per second along trajectory j can be obtained from:

$$\dot{n}_j = \frac{\dot{M}_j}{V_{0,q}\rho_q} \tag{3.36}$$

where $V_{0,q}$ and ρ_q are the initial volume and material density of the dispersed phase, and $\dot{M}_j$ is the mass flow of each trajectory. For irregular shapes of the dispersed phase, such as sand particles, the $V_{0,q}$ can be calculated from the equivalent spherical volume:

$$V_{0,q} = V_{eq} = \frac{\pi}{6} d_{e,q}^3 \tag{3.37}$$

where $d_{e,q}$ is the equivalent spherical diameter (ESD) of the dispersed phase in the entrance of the chamber. For droplets and other spherical particles, $d_{e,q}$ is equal to the initial droplets or particles diameter. The total number of the dispersed phase, N, into the chamber and during a time interval (Δt) can be determined from:

$$N = nV = \sum_{traj} \dot{n}_j \Delta t_j \tag{3.38}$$

where n is the dispersed phase number concentration, V is the volume of the chamber, and Δt_j is the time required for the dispersed phase to pass through the chamber on trajectory j. The mean volume fraction of the dispersed phase into the chamber can be described from:

$$\alpha_q = \frac{\sum_{traj} \dot{n}_j \bar{V}_q \Delta t_j}{V} \tag{3.39}$$

where $\bar{V}_q$ is the average volume of the dispersed phase along trajectory j in the chamber. In the same way, the bulk density and temperature of the dispersed phase in the chamber can be obtained from:

$$d_q = \frac{\sum_{traj} \dot{n}_j \bar{d}_q \Delta t_j}{N} \tag{3.40}$$

and

$$T_q = \frac{\sum_{traj} \dot{n}_j \bar{c}_q \bar{T}_q \Delta t_j}{N c_q} \tag{3.41}$$

where, $\bar{d}_q$, $\bar{c}_q$, and $\bar{T}_q$ are the average density, heat capacity and temperature of the dispersed phase along trajectory j in the chamber.

3.4.5.2 Discrete Element method of the Lagrangian approach

Same as trajectory method, if the dense dispersed flow enters into the chamber, by known initial velocity and mass, the velocity of disperse phase might be written as (Crowe, 2006):

$$\frac{d\vec{v}}{dt} = \frac{\vec{F}_f + \vec{F}_c}{m} + \vec{g} \tag{3.42}$$

where $\vec{F}_f$ and $\vec{F}_c$ are the forces due to particle-particle and particle-wall collision.

In the discrete element method, each element includes the N_e dispersed phase which had been emerged along the trajectory j in time interval Δt_e. The velocity, bulk temperature and other properties of the elements during the one time interval are obtained by integrating the particles properties. The particle-particle collisions might be affected on the elements distribution during the time step.

The dispersed phase number concentration and the mean volume fraction of the dispersed phase into the chamber can be determined from:

$$n = \frac{\sum_e N_e}{V} = \frac{\sum_e \dot{n}_e \Delta t_e}{V} \tag{3.43}$$

and

$$\alpha_q = \frac{\sum_e N_e \bar{V}_{q,e}}{V} \tag{3.44}$$

where V is the volume of the chamber, and $\bar{V}_{q,e}$ is the average volume of the dispersed phase in each element.

Other properties of the chamber such as bulk temperature and density could be obtained, similarly:

$$d_q = \frac{\sum_e N_e \bar{d}_q}{N} \tag{3.45}$$

and

$$T_q = \frac{\sum_e N_e \bar{c}_q \bar{T}_q}{N c_q} \tag{3.46}$$

where, $\bar{d}_q$, $\bar{c}_q$, and $\bar{T}_q$ are the average density, heat capacity and temperature of the dispersed phase along trajectory j in the element e.

3.4.6 Turbulence Modelling:

The effects of turbulent fluctuations of velocities and scalar quantities, such as pressure, in the multi-phase flow are considerably more complex than the single phase flow. This is because of the number of terms in the momentum and energy equations in multi-phase flows that are larger than single phase flows.

Here some common turbulence models, which are applicable in the multi-phase flow, are briefly expressed.

3.4.6.1 *k-ε* Mixture turbulence model

The *Mixture* turbulence model has reliable results if phases behave like separate flows or stratified flows. In these cases, the turbulence kinetic energy, *k*, and its rate of dissipation, *ε*, for the mixture phase are obtained from the following transport equations (FLUENT user guide, 2006):

$$\frac{\partial}{\partial t}(\rho_m k) + \frac{\partial}{\partial x_i}(\rho_m k \bar{u}_{i,m}) = \frac{\partial}{\partial x_j}\left[\left(\frac{\mu_{t,m}}{\sigma_k}\right)\frac{\partial k}{\partial x_j}\right] + \mu_{t,m}\left(\frac{\partial \bar{u}_{i,m}}{\partial x_j} + \frac{\partial \bar{u}_{j,m}}{\partial x_i}\right)\frac{\partial \bar{u}_{i,m}}{\partial x_j} - \rho_m \varepsilon \tag{3.47}$$

and

$$\frac{\partial}{\partial t}(\rho_m \varepsilon) + \frac{\partial}{\partial t}(\rho_m \varepsilon \bar{u}_{i,m}) = \frac{\partial}{\partial x_j}\left[\left(\frac{\mu_{t,m}}{\sigma_\varepsilon}\right)\frac{\partial \varepsilon}{\partial x_j}\right] + c_{\varepsilon_1}\frac{\varepsilon}{k}\mu_{t,m}\left(\frac{\partial \bar{u}_{i,m}}{\partial x_j} + \frac{\partial \bar{u}_{j,m}}{\partial x_i}\right)\frac{\partial \bar{u}_{i,m}}{\partial x_j} - c_{\varepsilon_2}\rho_m \frac{\varepsilon^2}{k} \tag{3.48}$$

where ρ_m and $\bar{u}_{i,m}$, the mixture density and velocity, are computed from

$$\rho_m = \sum_{j=1}^{N} \alpha_j \rho_j \tag{3.49}$$

and

$$\bar{u}_{i,m} = \frac{\sum_{j=1}^{N} \alpha_j \rho_j \bar{u}_{i,j}}{\sum_{j=1}^{N} \alpha_j \rho_j} \tag{3.50}$$

In equations (3.47) and (3.48), $\mu_{t,m}$ is the mixture dynamic viscosity of turbulent flow and is defined as:

$$\mu_{t,m} = \rho_m c_\mu \frac{k^2}{\varepsilon} \tag{3.51}$$

The model constants in equations (3.47), (3.48) and (3.51), $\sigma_k, \sigma_\varepsilon, c_{\varepsilon 1}, c_{\varepsilon 2}, c_\mu$ have the following values:

$$\sigma_k = 1, \quad \sigma_\varepsilon = 1.3, \quad c_{\varepsilon 1} = 1.44, \quad c_{\varepsilon 2} = 1.92, \quad c_\mu = 0.09$$

In equations (3.49) and (3.50), N is the number of phases.

3.4.6.2 *k-ε* Dispersed Turbulence Model

The dispersed turbulence model is suitable for the multi-phase flow, which has a clearly primary continuous phase and dispersed dilute secondary phases. In this case, since the volume fraction of secondary phases is very low, so interparticle collisions are negligible and the fluctuating quantities of the secondary phases are the influence of the primary phase turbulence.

3.4.6.2.1 Turbulence in the Continuous Phase

Turbulence in a continuous phase is usually modelled by using the transport equations for turbulent kinetic energy, *k*, and energy dissipation rates, *ε*. The modified *k-ε* model for a primary phase, or a continuous phase, are computed by the following transport equation for k and ε (Ranade, 2002):

$$\frac{\partial}{\partial t}\left(\alpha_p \rho_p k_p\right) + \frac{\partial}{\partial x_i}\left(\alpha_p \rho_p k_p \bar{u}_{i,p}\right) = \frac{\partial}{\partial x_i}\left[\left(\alpha_p \frac{\mu_{t,p}}{\sigma_k}\right)\frac{\partial k_p}{\partial x_i}\right] + S_{kp} \tag{3.52}$$

and transport equation for ε is:

$$\frac{\partial}{\partial t}\left(\alpha_p \rho_p \varepsilon_p\right) + \frac{\partial}{\partial x_i}\left(\alpha_p \rho_p \varepsilon_p \bar{u}_{i,p}\right) = \frac{\partial}{\partial x_i}\left[\alpha_p\left(\frac{\mu_{t,p}}{\sigma_\varepsilon}\right)\frac{\partial \varepsilon_p}{\partial x_i}\right] + S_{\varepsilon p} \tag{3.53}$$

where σ_k and σ_ε are the effective *Prandtl Number* for continuous phase, *p*, which relate the eddy diffusion of k and ε to the momentum eddy-viscosity: $\sigma_k = \varepsilon_m / \varepsilon_k$ and

$\sigma_\varepsilon = \varepsilon_m / \varepsilon_\varepsilon$. The continuous phase dynamic viscosity of turbulent flow, $\mu_{t,p}$, is computed from:

$$\mu_{t,p} = \rho_p c_\mu \frac{k_p^2}{\varepsilon_p} \tag{3.54}$$

In Equations (3.52) and (3.53) S_{kp} and $S_{\varepsilon p}$ are the corresponding source term for k and ε in a continuous phase, p. The source term for turbulent kinetic energy can be written as:

$$S_{kp} = \alpha_p [(G_p + G_{pe}) - \varepsilon_p] \tag{3.55}$$

And the source term for the turbulence dissipation rate, ε, can be defined as:

$$S_{\varepsilon p} = \alpha_p \frac{\varepsilon_p}{k_p} \left[c_{\varepsilon 1} (G_p + G_{pe}) - c_{\varepsilon 2} \varepsilon_p \right] \tag{3.56}$$

where G_p is turbulence generation in continuous phase, p, and G_{pe} is extra generation of turbulence in phase p. Turbulence generation, G_p, can be calculated from:

$$G_p = \frac{1}{2} \mu_{t,p} \left(\frac{\partial u_i}{\partial x_j} + \frac{\partial u_j}{\partial x_i} \right)^2 \tag{3.57}$$

All constants in Equations (3.52), (3.53), (3.54) and (3.56) have the same values as in the *k-ε mixture turbulence model*.

In Equations (3.55) and (3.56), the extra generation or damping of turbulence, G_{pe}, represent the influence of the dispersed phases on the continuous phase, p. Some formulations for G_{pe}, suitable for gas-liquid and gas-solid flows, have been presented in Ranade (2002) and FLUENT (2006). In the absence of adequate information, in many cases, extra generation terms usually vanish (Ranade, 2002).

3.4.6.2.2 Turbulence in the Dispersed Phase

In the multi-phase flow, the motion of the dispersed phase is controlled not only by the continuous phase and dispersed phase interactions but also by the inter-collisions of the dispersed phase. In the dilute dispersed phase the effect of inter-collisions of the dispersed phase can be vanished. In this section, the effects of turbulence on the dilute dispersed phase are discussed, and for more simplification, solid particles are assumed to be the only dispersed phase.

Fluid velocity imposes the lift and drag forces to the particles. On the other hand, in the turbulent flow, the fluid velocity is the instantaneous velocity and is decomposed

into a mean value and a fluctuating part. Here, there are two problems for calculating of the particles motion. First, it needs a proper technique for the simulating of velocity fluctuating. For this purpose, the *Reynolds stress* model and *k-ε* models for single phase are applicable. The second and significant problem is the fact that the particles do not follow the fluid path. So evaluating the fluid velocity in the particle location needs to follow the particle trajectory. The particle motion, without any body force, is influenced by the particle mass, and drag force. When body force, such as gravitational force, is not negligible in comparison to the drag force, a relative mean velocity is generated between the discrete particle and the fluid flow. Therefore, the particle passes different trajectory than carrier fluid, and particle trajectory crosses several eddies in the chamber. In both cases, the particle relaxation time, τ_V, the Lagrangian integral time scale, τ_L and the time scale ratio, η_{pq}, are key parameters. Particle relaxation time, τ_V, is the particle response to any fluid velocity fluctuation:

$$\tau_V = \alpha_q \rho_p K_{pq}^{-1} \left(\frac{\rho_q}{\rho_p} + C_V \right) \tag{3.58}$$

where C_V is the added-mass coefficient and $C_V = 0.5$ (FLUENT, 2006). The Lagrangian integral time scale, τ_L, is the relevant scale for fluctuating velocities,

$$\tau_L = \frac{3}{2} c_\mu \frac{k_p}{\varepsilon_p} \tag{3.59}$$

and the time scale ratio, η_{pq}, is the scale for quantifying the influence of turbulence on the particle motion.

$$\eta_{pq} = \frac{\tau_L}{\tau_V} \tag{3.60}$$

The *Lagrangian* integral time scale in the turbulent multi-phase flow with gravity along the discrete particle trajectory can be derived in the form:

$$\tau_L^p = \frac{\tau_L}{\sqrt{1 + \beta^2 \xi^2}} \tag{3.61}$$

In FLUENT β and ξ are defined as:

$$\beta = 1.8 - 1.35 \cos^2 \theta \tag{3.62}$$

and

$$\xi = \frac{\left|\vec{V}_{pq}\right|\tau_L}{L_p} \tag{3.63}$$

where θ is the angle between the mean particle velocity and the mean relative velocity, and L_p is the length scale of the turbulent eddies

$$L_p = \sqrt{\frac{3}{2}} c_\mu \frac{k_p^{3/2}}{\varepsilon_p} \tag{3.64}$$

where k_p and ε_p are the turbulent kinetic energy and dissipation rate of the primary phase (continuous phase), which are computed from equations (3.52) and (3.53), and $c_\mu = 0.09$. The turbulent kinetic energy of the dispersed phase is written in terms of the turbulent kinetic energy of the primary phase and time scale ration:

$$k_q = k_p \left(\frac{b^2 + \eta_{pq}}{1 + \eta_{pq}} \right) \quad , \quad b = \left(1 + C_V\right) \left(\frac{\rho_q}{\rho_p} + C_V \right)^{-1} \tag{3.65}$$

where C_V is the added-mass coefficient and $C_V = 0.5$ (FLUENT, 2006).

Interphase turbulent momentum transfer

In FLUENT, the drag force of the turbulent multi-phase flows due to the dispersed phase and continuous phase interaction is modelled as:

$$K_{pq}\left(\vec{V}_p - \vec{V}_q\right) = K_{pq}\left(\vec{U}_p - \vec{U}_q\right) - K_{pq}\vec{V}_{dr} \tag{3.66}$$

Here, K_{pq} is the interphase exchange coefficient, mentioned in Equation (3.25), $\vec{U}_p$ and $\vec{U}_q$ are the phase-weighted velocities, and $\vec{V}_{dr}$ is the drift velocity which is defined as

$$\vec{V}_{dr} = -\left(\frac{D_p}{\sigma_{pq}\alpha_p} \nabla \alpha_p - \frac{D_q}{\sigma_{pq}\alpha_q} \nabla \alpha_q \right) \tag{3.67}$$

where σ_{pq} is the dispersion Prandtl number and as the default value FLUENT assumes $\sigma_{pq} = 0.75$. In Equation (3.66), D_p and D_q, the primary and dispersed phases diffusivities, are defined as:

$$D_p = \frac{1}{3} k_{pq} \tau_L + \left(\frac{2}{3} k_p - b \frac{1}{3} k_{pq} \right) \tau_V \tag{3.68}$$

and

$$k_{pq} = 2k_p\left(\frac{b+\eta_{pq}}{1+\eta_{pq}}\right) \tag{3.69}$$

The drift velocity results from the volume fraction's fluctuation due to the turbulence, and the drift velocity multiplied to the interphase exchange coefficient has a correction effect on the momentum exchange for the turbulent flow.

3.5 Numerical Solutions of Governing Equations

Laminar, transient and supersonic flows as well as single-phase and multi-phase flows are numerically solved by choosing one of the two numerical methods, the *Pressure-Based Solver* and the *Density-Based Solver*. Depending on the flow characteristics, required precision and simulating time/cost, *FLUENT* allows for the selection of one of the abovementioned solvers.

However, the pressure-based approach was developed for low-speed incompressible flows, it has been extended and reformulated to solve and operate for a wide range of flow conditions, such as turbulent and some multiphase models, beyond their traditional or original intent. Unlike the pressure-based approach the density-based approach was mainly used for high-speed compressible flows.

3.5.1 Pressure-Based Solver

In the *Pressure-Based* approach, the pressure field is extracted by solving a pressure equation which is derived from the continuity and the momentum equations in such a way that the velocity field, corrected by the pressure, satisfies the continuity (FLUENT user guide, 2006). In this method, in the same way as the *Density-Based* method, the velocity field is obtained from the momentum equations.

Two pressure-based solver algorithms are available in FLUENT, a *Segregated* algorithm and a *Coupled* algorithm. These two approaches are discussed in the sections below.

3.5.1.1 Segregated Algorithm

In the segregated algorithm, the individual governing equations for the solution variables, such as velocity components and pressure, are solved one after another. On the other hand, whereas the governing equations are non-linear and coupled, the solution loop must be iterated in order to obtain a converged numerical solution.

Before starting the loop iteration, the flow properties such as density, viscosity and specific heat must be initialised. The solution loop of the segregated solver consists of the steps illustrated in Figure (5.2) and put in plain words below:

1. The flow properties are updated based on the current solutions.
2. Each momentum equation for velocity components are solved by using current pressure, face mass fluxes and turbulence variables.
3. The pressure correction is solved by using the recently obtained velocity field and mass-flux to apply new corrections on pressure, velocity components, and face mass fluxes. The continuity equation is satisfied by applying new corrected data.
4. Energy and turbulence equations (where appropriate) are solved, and segregated by using updated velocity components, pressure, and other current values of the solution variables.
5. The convergence check is carried out and if the solution is not converged the next iteration begins from step 1 otherwise the solution is completed.

The updated fluid properties in step 1 include viscosity, specific heat capacity, and thermal conduction coefficients, which are updated based on the new temperature field in each Control Volume.

3.5.1.2 Coupled Algorithm

The Pressure-Based Coupled algorithm solves momentum equations and the pressure-based continuity equation in a coupled method. Thus, in this method, Step 2 and 3 in the section 3.5.1.1 are coupled and the system of equations solved simultaneously. In the mentioned mixed step, momentum and continuity equations are rewritten in terms of velocity correction and pressure correction variables.

The rate of solution convergence in a pressure-based coupled solver significantly improves when compared to the segregated algorithm, as in this algorithm the momentum and continuity equations are solved in a closely coupled manner. However, the memory requirement increases by 1.5 - 2 times in comparison with the segregated algorithm (FLUENT user guide, 2006).

The coupled algorithm is compatible with all reacting flow models, multiple species problems, mixture multiphase models including cavitations and the VOF multiphase model.

3.5.2 Density-Based Solver

The density-based solver solves the governing equations of continuity, momentum, and if any energy and species transport simultaneously. Governing equations for additional scalars will be solved as a segregated from one another and from the coupled set. This method, in the same way as the *Pressure-Based* method, extracts the velocity field from the momentum equations. Five coupled equations solve five unknown variables u, v, w, ρ and T. In the Density-Based method, the pressure fields are computing from ideal gas law.

After inserting the initial flow properties such as density, viscosity and specific heat to the model, the solution loop of the *Density-Based* solver will be started by the following steps and illustrated in Figure (5.2).

1. The flow properties are updated based on the current solutions.
2. The continuity, momentum, and if any energy and species transport are solved simultaneously.
3. Where appropriate, governing equations for additional scalars such as turbulence and radiation are solved using updated velocity components, pressure, and other current values of the solution variables.
4. When interphase coupling is to be included, the source terms in the appropriate continuous phase equations are updated with a discrete phase trajectory calculation.
5. The convergence check is carried out and if the solution is not converged the next iteration begins from step 1 otherwise the solution is completed.

The density-based solution method gives the choice of using either an implicit or explicit linearization of the governing equations. This choice applies only to the coupled set of governing equations. Transport equations for additional scalars such as turbulence and radiation are solved as the segregated from the coupled set.

In Chapter Six the Pressure-*Based* method is compared with the *Density-Based* solver by the numerical solution of the air-sand-water three-phase flow through the nozzle.

3.5.3 Convergence rate control or Under-relaxation factors

In nonlinear equations related to the turbulent flow or multi-phase flows, under-relaxation as a technique is used for improving the stability of a computation, particularly in solving steady-state problems. As Figure (3.8) shows, pressure-based segregated and coupled solvers as well as a density-based solver are computed in the base of iteration. Because of the nonlinearity of the equation set being computed by the abovementioned solvers, it is necessary to control the change of ϕ. This is applicable by use of under-relaxation of variables which reduces the change of ϕ produced by each iteration. An under-relaxation factor α specifies the amount of under-relaxation, ranging from none at all for $\alpha = 1$ and increasing in strength as $\alpha \to 0$.

In a simple form, the value of variable ϕ within a cell in iteration of n for subscription in iteration $n+1$ which is denoted as ϕ' is calculated from:

$$\phi'^{n} = \alpha\phi^{n} + (1-\alpha)\phi^{n-1} \tag{3.70}$$

where α is the relaxation factor, and if $0 < \alpha \leq 1$ it is called an under-relaxation factor and improves the stability of computation. Apart from unknown variables, the under-relaxation is also applied for eddy viscosity coefficient. The default values of under-relaxation factors are 0.3, 1.0, 1.0, 0.7, 0.8, 0.8, 1.0, 1.0 and 0.5 for pressure, density, body forces, momentum, *k*, ε, turbulent viscosity, energy and discrete phase sources respectively. In FLUENT, the default under-relaxation parameters for all variables are set to values that are near optimal for the largest possible number of cases. However, in turbulent multi-phase flows it is prudent to reduce the under-relaxation factors initially.

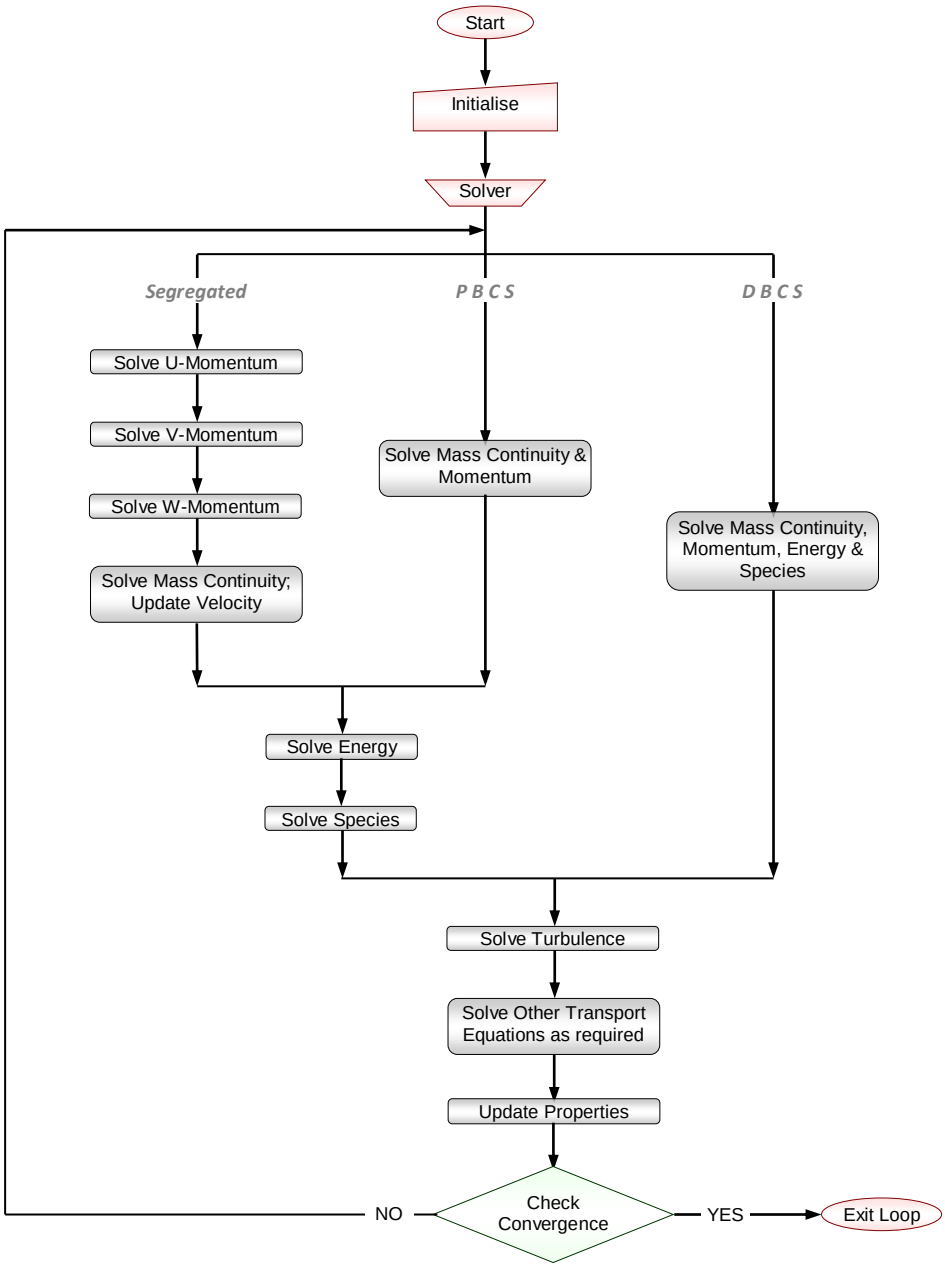

Figure (3. 8). Flow diagram of FLUENT solvers

3.6 Boundary Conditions

Boundary conditions specify the flow and thermal variables on the boundaries of a physical model. They are, therefore, a critical component of simulations and it is important that they are specified appropriately. In the following subsections, the boundary condition options applicable in this study are briefly described.

3.6.1 Inlet boundary

The inlet boundary of duct flows, such as multi-phase flow through the nozzle can be specified by three types of boundary: pressure, velocity and mass flow inlet boundary conditions. In the nozzle of a shot-blasting system the inlet pressure or mass flow rate of the nozzle are quantifiable, hence this section is going to give more details of these boundary conditions.

3.6.1.1 Mass flow inlet boundary conditions

Mass flow boundary conditions can be used in FLUENT to provide a prescribed mass flow rate or mass flux distribution at an inlet. The mass flow inlet boundary conditions can be applied to multi-phase models if at least one phase is compressible.

In Section 4.3 for validation assessments the mass flow inlet boundary conditions are applied. In that simulation, mass flow rate of water, air inlet pressure, total temperature, water static pressure, flow direction, turbulence parameters and discrete-phase boundary conditions are specified.

In FLUENT and in the mass flow inlet panel, the turbulence parameter, depends on the turbulence specification method, must be specified. The following relationship for turbulence intensity, turbulence length scale, turbulence viscosity ratio and hydraulic diameter are used in FLUENT whenever one of the Intensity and Length Scale, or Intensity and Viscosity Ratio, or Intensity and Hydraulic Diameter methods are used instead of specifying explicit values for k and ε.

Turbulent intensity: The turbulence intensity, I, is defined as the ratio of the root-mean-square of the velocity fluctuations, u', to the mean flow velocity, u_{ave}. It is dependent on flow conditions, for example in internal flows it depends on the upstream history of the flow. An empirical correlation which is applicable for the estimating of turbulence intensity in the FLUENT boundary condition's panel is:

$$I \equiv \frac{u'}{u_{ave}} = 0.16\left(\mathrm{Re}_D\right)^{-1/8} \tag{3.71}$$

Equation (3.71) provides turbulent intensity at the core of a fully-developed pipe flow as well as duct flow. For duct flow, the Reynolds number in Equation (3.71) must be computed by applying the hydraulic diameter.

The turbulent intensity for air-sand-water three-phase flow through the nozzle which is simulated in Chapter Six is 3.6%, according to correlation (3.71). For this computation, the inlet pressure is 2 atm, water and mass flow rate are 0.03 kg/s and 0.01 kg/s, respectively. As Figure (5.3) and (5.4) show the Reynolds number at the core of the entrance and exhaust of the nozzle is 1.5×10^5 and 1.7×10^5, and the nozzle inlet and exhaust diameters are 3.175 cm and 1.5 cm, respectively.

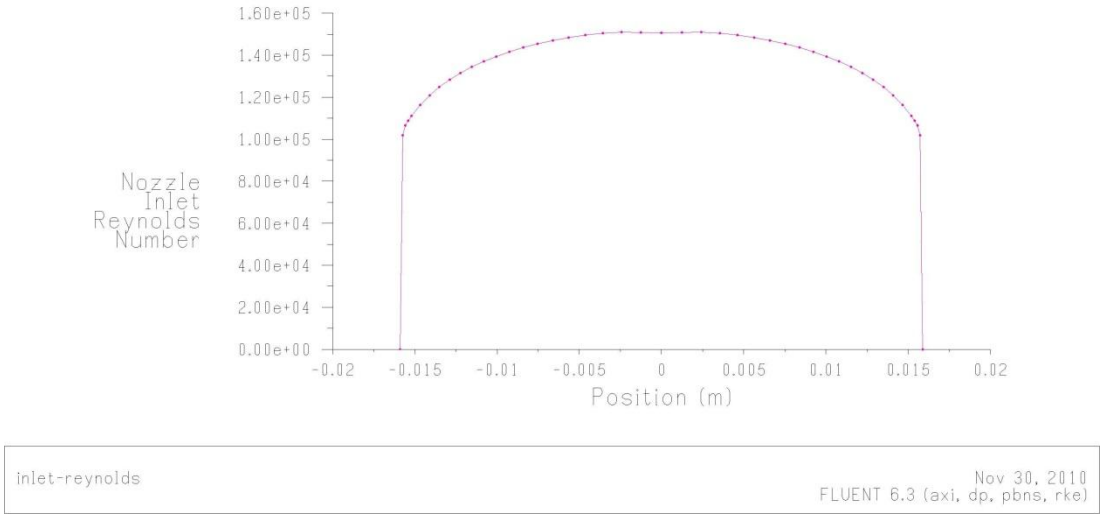

Figure (3. 9). Reynolds number at Nozzle entrance for air-sand-water three-phase flow

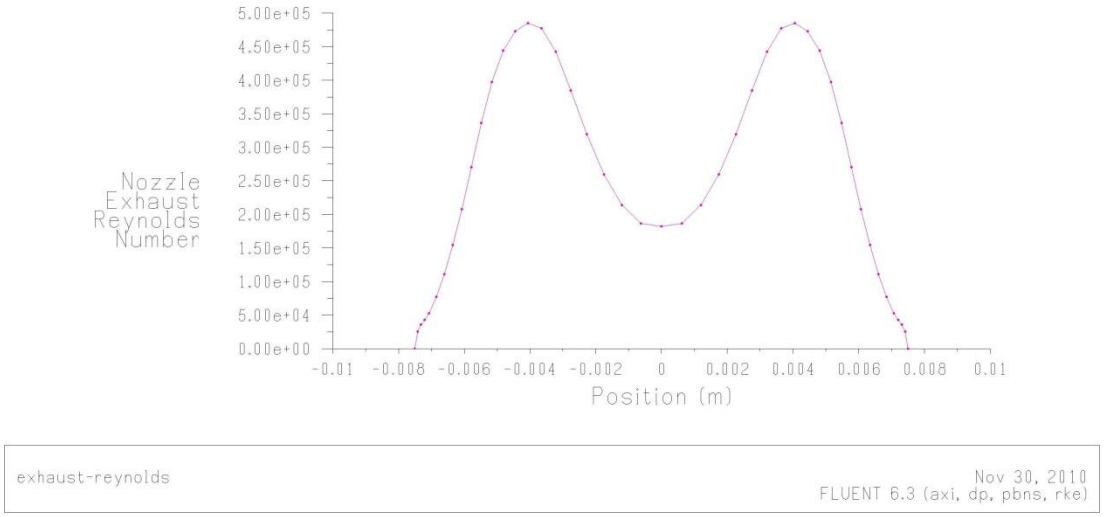

Figure (3. 10). Reynolds number at Nozzle exhaust for air-sand-water three-phase flow

Turbulence length scale: The turbulence length scale, ℓ, is a physical quantity related to the size of the large eddies that contain the energy in turbulent flows. This length is restricted by the pipe diameter in the internal flow and can be estimated by:

$$\ell = 0.07D \tag{3.72}$$

In fully-developed duct flows, Equation (3.72) is applicable by the replacing of hydraulic diameter, D_H, instead of *D*.

Turbulent Viscosity Ratio: The turbulent viscosity ratio, μ_t/μ, is proportional to the k and ε, and typically it sets between 1 and 10, or $1 < \mu_t/\mu < 10$.

Estimating turbulent kinetic energy, *k*, and dissipation rate, ε : In the panel of the mass flow inlet boundary conditions of FLUENT, if turbulence intensity, *I*, and mean flow velocity are known, the turbulent kinetic energy can be determined from:

$$k = \frac{3}{2}(u_{ave}I)^2 \tag{3.73}$$

If the turbulence length scale, ℓ, is known, the turbulent dissipation rate, ε, can be estimated from:

$$\varepsilon = C_\mu^{3/4}\frac{k^{3/2}}{\ell} \tag{3.74}$$

where C_μ is an empirical constant and in most turbulent models is assumed to be 0.09.

The mass flow inlet boundary conditions are used in Chapter Four for the simulating of air-water premixed and un-premixed two-phase flow through the nozzle.

3.6.1.2 Pressure inlet boundary conditions

Pressure inlet boundary conditions are applicable for both compressible and incompressible fluid flow as well as multi-phase flows. In this boundary condition, the fluid pressure is defined at flow inlets, along with all other scalar properties of the flow. The pressure inlet boundary conditions can be used in many practical situations, including boundary-driven flows such as shot-blasting machines.

The panel of pressure inlet boundary conditions in FLUENT is similar to the mass flow inlet boundary conditions except the Mass Flow Specification Method and Mass Flow Rate parameters which were replaced with Gauge Total Pressure. The gauge total pressure for incompressible and compressible flow is computed from Equation (3.75) and (3.76), respectively:

$$p_0 = p_s + \frac{1}{2}\rho|\vec{v}|^2 \tag{3.75}$$

$$p_0 = p_s\left(1+\frac{\gamma-1}{2}M^2\right)^{\gamma/(\gamma-1)} \tag{3.76}$$

where p_0 is the total pressure, p_s is the static pressure, M is the Mach number, and γ is the ratio of specific heats $\left(c_p/c_v\right)$.

The pressure inlet boundary conditions are widely used in Chapters Five and Six for the simulating of multi-phase flow through the nozzle.

3.6.1.3 Pressure outlet boundary conditions

The specification of a static pressure at the outlet boundary panel in FLUENT is only required in subsonic flows. For supersonic flows as it will no longer be used it is set to zero, and as well as all other flow parameters it will be extrapolated from the flow in the interior.

3.6.1.4 Wall boundary conditions

A wall boundary as an unavoidable boundary, which bounds fluid and solid regions, is used in all internal flows. Some different information depends on the flow simulation model must be specified in the wall boundary panel. Stationary wall, no-slip shear condition, and constant heat flux are selected in the simulation of the multi-phase flow through the nozzle in the following chapters. Reflect, trap, escape, wall jet, wall film, and user define are all boundary condition types for secondary phases in the Discrete Phase Model (DPM) Conditions on the panel of Boundary Conditions of FLUENT.

Unfortunately, there is no choice for selecting different boundary condition types or parameters for various secondary phases such as sand particles and water droplets in the three-phase flow. Therefore, in this study the reflect boundary condition type with the same discrete phase reflection coefficients are selected for both dispersed phases.

The wall surface in all cases of this study is considered smooth and effects of roughness are neglected; therefore, the logarithmic law of the wall for smooth walls is always the case.

3.7 Interaction of discrete phase with continuous phase

The discrete phase interacts with continuous phase in DPM when the option of Interaction with Continuous Phase in the DPM panel is selected; otherwise the single phase flow is computed.

3.7.1 Physical models

Various physical models in DPM are available in FLUENT, which depending on the flow characteristic, one or more models can be selected.

Thermophoretic Force: Thermophoretic Force arises from a thermal gradient in gas temperature on suspended small particles in the direction opposite to that of the gradient.

Brownian Motion: Brownian Motion is the seemingly random movement of sub-micron particles suspended in a fluid. It is intended only for non-turbulent models.

Saffman's Lift Force: The Saffman's lift force, or lift due to shear, can also be included in the additional force term as an option. Small particles in a shear field experience a lift force perpendicular to the direction of flow. The shear lift originates from the inertia effects in the viscous flow around the particle and is basically different from aerodynamic lift force.

Erosion and Accretion: Particle erosion and accretion is the other option which can be activated in the tab of Physical Models. These parameters are proportional to the particles diameter, impact angle of the particle with the wall face and relative particle velocity.

Two-Way Turbulence Coupling: While the continuous phase always impacts the discrete phase, the effect of discrete phase trajectories can also be incorporated on the continuous phase. This two-way coupling is accomplished by alternately solving the discrete and continuous phase equations until the solutions in both phases have stopped changing.

Finally, the in air-sand-water three-phase turbulent flow through the nozzle, the Two-Way Turbulence Coupling model in comparison with other models is more considerable. The Two-Way Turbulence Coupling option in the DPM panel is activated for all the multi-phase simulation in Chapters Four to Six.

3.7.2 Parameter tracking for the discrete-phase model

There are two parameters to control the time integration of the particle trajectory equations in the DPM panel under the Tracking tab.

Max. Number of Steps: The maximum number of time steps is used to abort trajectory computations if even the particle does not exit from the flow domain. Whenever the Max. Number of Steps is not an adequate amount to exhaust the particle from the computational domain, the FLUENT reports the trajectory fate as "incomplete". In this case this number can be increased, and after sufficient iteration, the mentioned report should be eliminated.

Length Scale: The length scale, *L*, is proportional to the integration time step, Δt, and is equivalent to the distance that the particle will travel before its motion equations are solved again and its trajectory is updated.

$$L = \Delta t \cdot \left(u_p + u_c \right) \tag{3.77}$$

where u_p and u_c are the velocity of the particle and continuous phase, respectively. Equation (3.77) states that the length scale is a parameter to control the integration time size used to integrate the equations of motion for the particle.

3.7.3 Drag Parameters

There are four drag laws for the particles that can be selected in the Drag Law list under Drag Parameters. The spherical, non-spherical, Stokes-Conningham, and high-Mach-number laws are available in FLUENT for all steady and unsteady particle tracking as well as various physical models.

In this study, due to turbulence multi-phase flow conditions and FLUENT restriction, the spherical and high-Mach-number laws are applicable. However the high-Mach-number drag law which is similar to the spherical law with correlations to account for a particle Mach number greater than 0.4 at a particle Reynolds number greater than 20, is more appropriate than spherical drag law.

Finally, for simulating of the air-sand-water three-phase flow, there are some other parameters especially in Interaction, Particle Treatment, Numerics and Injections tabs in the DPM panel which depend on flow characteristics and domains must be selected.

3.8 Summary and Conclusions

In this chapter, the problem was described and also the theoretical background of the multi-phase turbulent flow and numerical modelling were discussed. The Eulerian and the Discrete Phase model as the applicable models for simulating of the air-sand-water three-phase flow through the nozzle were introduced. It was concluded that the Discrete Phase model which utilizes the Lagrangian scheme is the best model for simulating the sand blasting system. Also in this chapter numerical modelling in multi-phase flows was introduced. Different available solvers of multi-phase flow were discussed and regarding the computing cost/time of the Pressure-Based Segregated model were recommended. Finally, boundary conditions, including the various inlet conditions and also interaction of the discrete phase with the continuous phase were discussed.

CHAPTER 4

VALIDATION OF THE NUMERICAL METHOD

Introduction

In Computational Fluid Dynamics (CFD), validation refers to the process of ensuring that the simulation results satisfy pre-achieved results from experimental or theoretical work for a similar study. On the other hand, validation is the process for verifying the CFD procedure, including discretisation, the initial and boundary values, as well as creditability and uncertainties of the model. Definitely, due to some simplification of the CFD models and some error source in CFD simulation, the final results could be slightly different than the actual values of theoretical results. Depending on the problem circumstances, the maximum admissible error or difference should be verified.

This chapter briefly presents the error source in CFD simulation, as well as different methods of verification and validation assessments. In the second part of this chapter, grid-dependency check or validation of the discretisation process is expressed. The last section presents the validation of the *RNG k-ε* models and the *Discrete Phase* model of the multiphase flow through the nozzle. As the literature review shows, because of the complexity of the air-sand-water, three-phase turbulent flow through the nozzle, there is no related experimental data. Therefore, in this chapter, the two-phase flow is considered for validation purposes, and the three phase flow will be treated in the same technique as the two phase flow.

4.1 Uncertainty and Error sources in CFD Simulations

The accuracy of the CFD solutions is identified and quantified in terms of "*uncertainty*" in the modelling process and in terms of acknowledged and unacknowledged "*errors*". Based on the American Institute of Aeronautics and Astronautics definitions (AIAA G-077, 1998), the uncertainty is "*A potential deficiency in any phase or activity of the modelling process that is due to the lack of knowledge"*, and the error is "*A recognizable deficiency in any phase or activity of modelling and simulation that is not due to lack of knowledge"*.

There is not a lot known about multi-phase turbulence flow, and what is known has not been properly modelled, so the lack of knowledge and accuracy of the CFD solution that could be affected due to the *uncertainty*. One approach for determining the level of uncertainty and its effect on one's analysis is to run a number of simulations with a variety of turbulence models and see how the modelling affects the results. For example, in this chapter for some special cases, the *Eulerian* and *Lagrangian* approaches are used. Consequently, the simulation results achieved on these different models for multi-phase turbulent flow indicate the *uncertainty* of models.

Unlike the *uncertainty*, the *error* is not due to lack of knowledge and the sources of error in the CFD simulation are briefly described in this section.

4.1.1 Acknowledged errors

In the CFD solution there are some error sources which can be identified and it is possible to remove them. These errors, which are called acknowledged errors include: the physical approximation error, the computer round-off error, the iterative convergence error and the discretisation error.

Physical approximation errors come out from any simplification of the complex model. The CFD solution of physical phenomenon needs to formulate them, and in complex cases, such as the multi-phase turbulent flow through the nozzle, it is applicable after simplification. Consequently, it makes some error due to uncertainty in the formulation of the model. Sometimes phenomenon is not thoroughly understood, or sometimes parameters used in the model are known but with some degree of uncertainty. Even when a phenomenon is completely known and physical modelling with a high level of accuracy is applicable, a simplified model may be used within the CFD solution for the convenience of a more efficient computation.

Computer round-off error is the difference between the calculated approximation of a number and its exact mathematical value. In advanced computer resources, which data are typically stored with 32 or 64 bits, the round-off error in comparison with other errors is not considered significant. There is another error, *iterative convergence error*, which is due to the stopping criterion of iteration. The *iterative convergence error* exists because the iterative methods used in the simulation must have a stopping point eventually.

Discretisation errors arise due to the representation of the governing transport equations of flow as algebraic expressions in a discrete domain of time and space, such as finite-difference or finite-volume. The *discretisation error* is the most considerable error in the CFD, because it is dependent on the quality of the grid; however, it is often difficult to exactly indicate the relationship between the grid's quality and solution's accuracy before starting the simulation. By increasing the grid quantity and so refining the mesh, the solution should become less sensitive to the grid spacing and approach the continuum solution. As well as mesh sizing, the time step might be refined, and finally the solution can be independent on the grid and time step size, which is called *grid convergence*. The grid convergence study is a useful procedure for determining the level of discretisation error existing in a CFD solution.

4.1.2 Unacknowledged Errors

In comparison with acknowledged errors, expressed in Section 4.1.1, there are some other errors, which there have no clear procedure for finding them and may be continued within the code or simulation. These errors which are called *unacknowledged errors* include the c*omputer programming error* and *usage error*.

The *computer programming error* is due to the programmer's mistake and is discovered by systematically performing verification studies of the code, reviewing the lines of the code, and performing validation studies of the code. Even if the programming errors have been removed from the code prior to release, some other errors might happen due to the user, called *usage errors*. *Usage errors* are due to the application of the code in a less-than-accurate or improper manner. The potential for *usage errors* increases with an increased level of options available in a CFD code. These errors can exist in the CAD, grid generation and post-processing software, in addition to the CFD code. *Usage errors* might be decreased by accumulation of

experience, comprehensive study of theory and the user guide of the CFD code and proper training.

4.2 Validation Assessments

The validation and verification assessments, for multi-phase flow through the nozzle by attention to the uncertainty and error sources, which have been expressed in Section 4.1, are presented in the following sections. These procedures are going to be carried out in two different approaches. First, acknowledged errors and consequently discretisation error, which is the most important error source in this approach, are discussed. Then, in the second approach and for *computer programming error* check, the experimental data will be compared with numerical simulation results which have been computed for the two-phase flow through the nozzle.

The consistency of the numerical method may be examined by checking out the physical reliability of the results, such as mass conservation analysing through the nozzle by comparison of the mass flow through the inlets and outlets, and the trends of pressure distribution along the shocks. This survey will be expressed in the following sections.

4.2.1 Grid independency test

The grid independency test shows the accuracy of the results in relation to the grid size and assures the proper size of grid is applied in the numerical model. For near wall turbulence modelling, the size of the grid should be considered according to proper dimensionless wall coordinate for the applied near wall turbulence model. The grid independency test near the wall should be implemented both by changing the grid size parallel to the wall and, more sensitively, the grid size normal to the wall, where high gradients of the variables exist.

Successful computations of turbulent flows require some consideration during the mesh generation. It is therefore recommended to resolve the regions with sufficiently fine meshes, where the mean flow changes rapidly and include shear layers with a large mean rate of strain.

The most common dimensionless wall coordinate for considering the mesh size in the near-wall turbulence model is y^+.

In the grid generating process the following key points have been considered:

- As wall functions cease to be valid in the viscous sublayer, so using an excessively fine mesh near the walls was avoided.
- A y^+ value close to the lower bound ($y^+ \approx 30$) was most desirable.
- Using excessive stretching in the direction normal to the wall has been avoided.
- Inside the boundary layer at least a few cells have been considered.

4.2.1.1 Grid generation and grid dependency check in the Shot Blasting Nozzle

A schematic sketch and the geometrical dimensions of the shot blasting nozzle, is shown in Figure (3.6) in Chapter 3. The following section is going to show the grid independency analysis for the mentioned nozzle. For this purpose, a comparison of static and dynamic pressure distribution through the nozzle for various mesh sizes are expressed. Four mesh sizes, 10488, 13860, 17280 and 21286 grid numbers are discussed here representing all of the various grid numbers which had been generated and investigated. On the other hand, a near-wall grid independency test is discussed by plotting the y^+ value distribution for each mesh size in the nozzle. All these studies have been done for single and multi-phase flow, separately.

Single Phase Flow: Figure (4.1) shows static pressure distribution through the nozzle for various grid sizes. In this figure, air flow through the nozzle has been simulated, and all curves have been computed for the same condition except grid size. The static pressure is plotted for the centre line of the nozzle, and the flow has been assumed as axisymmetric. As figure (4.1) shows, the abovementioned grid sizes have not made any significant difference for static pressure distribution through the nozzle. Almost the same trend is observed for dynamic pressure distribution of the single phase flow through the nozzle, which has been sketched in figure (4.2).

The y^+ distribution for various grid numbers is shown in figure (4.3). Unlike the pressure distribution through the nozzle shown in figures (4.1) and (4.2), this figure not only shows a significant difference between the y^+ distributions for the grid number 10488 and other grid numbers, but also it states that the y^+ distribution for the grid number 10488 is far from the proposed range in the literature. However each wall-adjacent cell's centroid should be located within the log-law layer, $30 < y^+ < 300$, but a y^+ value close to the lower boundary ($y^+ \approx 30$) is most desirable.

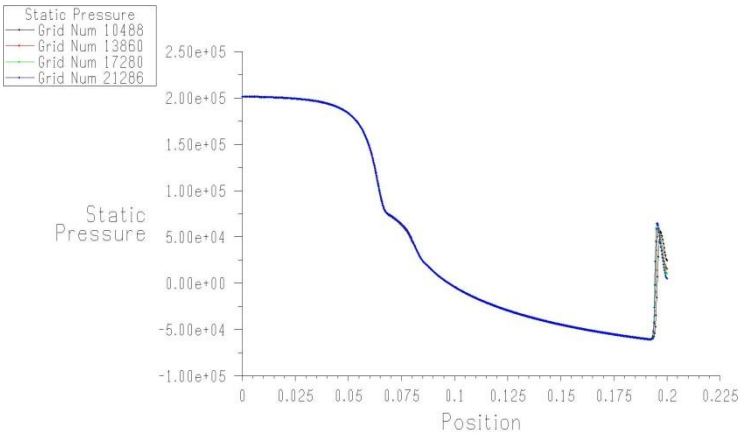

Figure (4. 1). Static pressure distribution through the Nozzle with different grid number

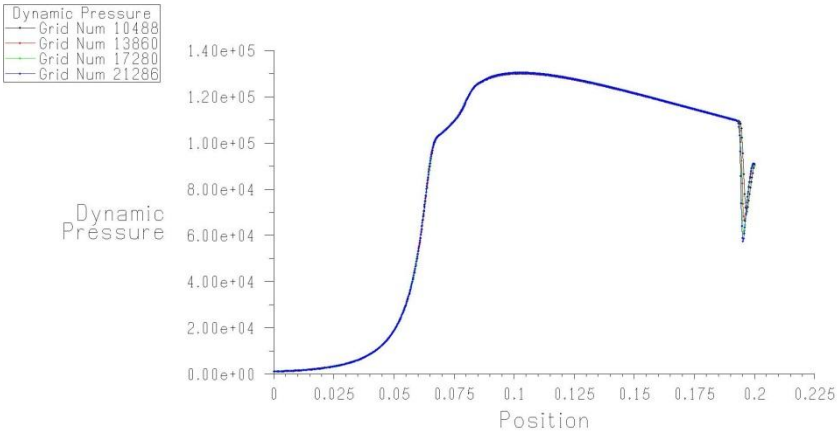

Figure (4. 2). Dynamic pressure distribution through the Nozzle with different grid number

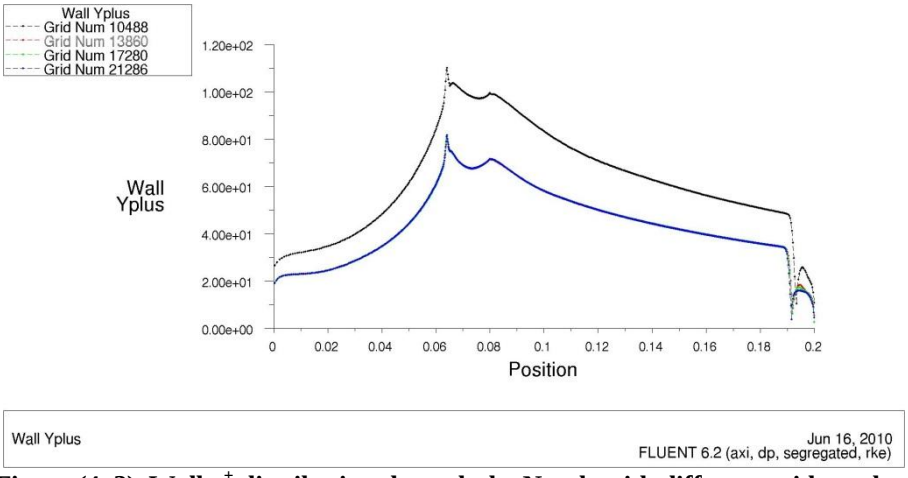

Figure (4. 3). Wall y^+ distribution through the Nozzle with different grid number

Multi-Phase Flow: As the main object of this research is the simulating of the multi-phase flow through the nozzle, so the grid independency test has been investigated for the abovementioned grid sizes by applying the air flow with water

droplets and sand particles. An obvious difference is perceived for the static pressure distribution between grid number 10488 and the other grid numbers 13860, 17280 and 21286 in Figure (4.4). As Figure (4.5) shows, this error is significant for dynamic pressure distribution.

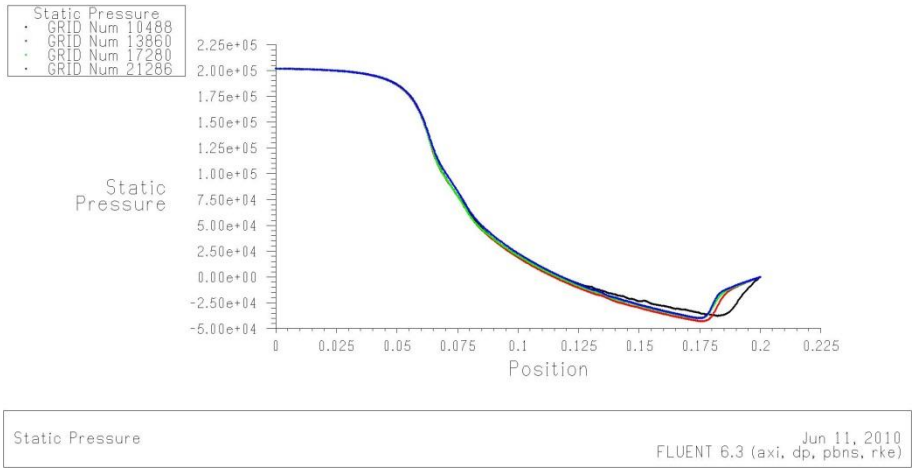

Figure (4. 4). Static pressure distribution of multi-phase flow through the Nozzle with different grid number

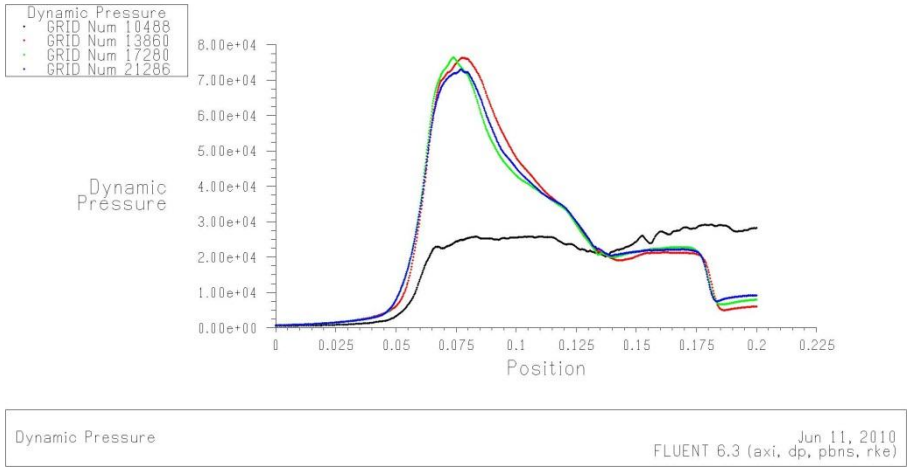

Figure (4. 5). Dynamic pressure distribution of multi-phase flow through the Nozzle with different grid number

The y^+ distribution for the multi-phase flow and various grid numbers is shown in figure (4.6). As in Figure (4.3), the considerable difference between the y^+ distributions for the grid number 10488 and the other grid numbers is shown in Figure (4.6).

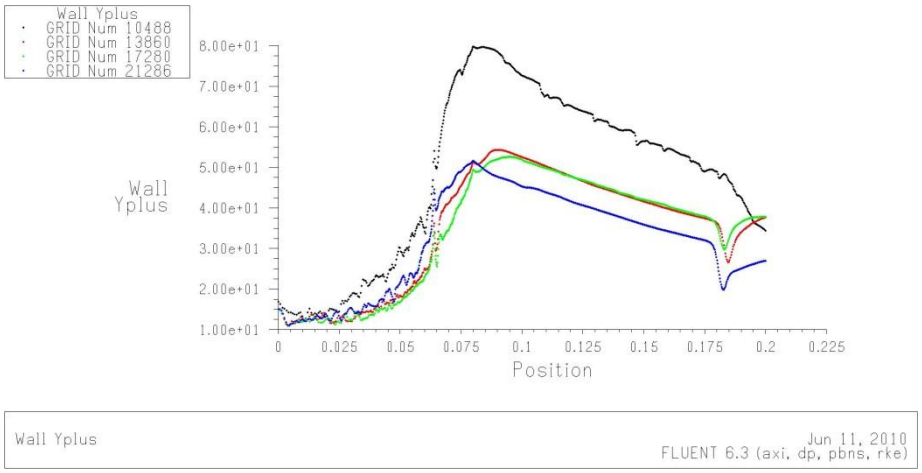

Figure (4. 6). Wall y+ distribution of multi-phase flow through the Nozzle with different grid number

Consequently, Figures (4.3) to (4.6) show that the grid number 10488 is an unacceptable grid size because the simulation parameters are independent to the grid number. However, pressure and y^+ distribution, as representative of simulation parameters, for the grid numbers 13860, 17280 and 21286 almost have the same trend, but due to the simulation cost and time, the grid number 13860 has been preferred to the other grid numbers.

4.2.2 FLUENT Simulating Error Check:

In this study, three-phase flow through the nozzle is simulated by utilizing the *FLUENT* package. Therefore, the *computer programming error* and *usage error* check is focused on utilization of *FLUENT* software for the simulating of the three-phase flow through the nozzle. As a first step, the simulation results of the multi-phase flow through the nozzle must be validated by experimental data. Due to the massive complexity of the air-water-sand three-phase flow through the nozzle, there is no related experimental work in any literature. Hence, in the following sections the simulation results of air-water two-phase flow through the similar nozzle has been compared by existing experimental data.

In the second part of the *computer programming error* check for three-phase flow, in the one hand, the k-ε turbulence modelling, which is widely used in this study, is compared with the Reynolds stress model (RSM), and on the other hand, the *Eulerian* model is going to be compared with the *Discrete-phase* model.

4.2.2.1 Experimental investigation of un-premixed air-water two-phase flow through the nozzle

Two-phase flow through the converging-diverging nozzle by applying the separated flows of air and water experimentally has been investigated by Lamonnier et al. (1991). Figure (4.7) shows the schematic sketch and dimensions of the aforementioned nozzle with a 5 mm throat diameter.

In this experiment the liquid injection flow rate is 93 kg/h, and the upstream pressure is 6 bar. For constant inlet conditions, a gradual decrease in back pressure down to atmospheric has been exerted for the exit of the nozzle. The back pressure amounts are given in Table (4.1) along with the experimentally measured and analytically calculated air mass flow rate. More information of the test equipments, experimental procedure, and physical modelling is given by Lamonnier et al. (1991).

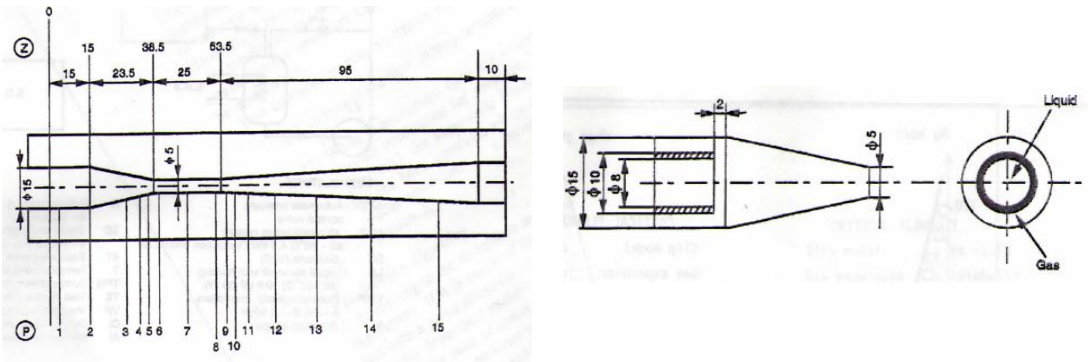

Figure (4. 7). Converging-diverging nozzle with un-premixed air-water two-phase flow

Table (4. 1). The back pressure and air flow rate of nozzle

	Air flow rate (kg/h)	
P_{out} (Bar)	Experimented	Calculated
5.38	37.2	32.9
4.64	54.1	49.6
4.30	58.4	52.0
3.80	61.1	52.7
3.10	62.0	52.7
2.00	62.1	52.7
1.28	62.4	52.7
0.81	62.2	52.7

Figure (4.8) shows pressure profiles measured for the nozzle sketched in figure (4.7). The experimental data points in figure (4.8) resemble the well-known topological behaviour of the single-phase compressible nozzle flow under similar conditions.

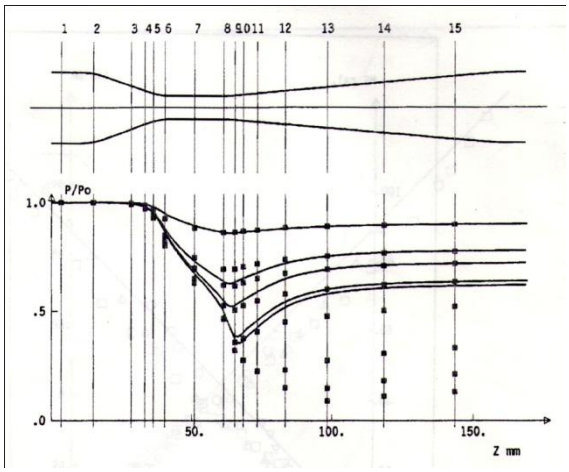

Figure (4. 8). Pressure distribution measured vs. calculated through the Nozzle

In the following section, the numerical modelling and simulation of the abovementioned nozzle and two-phase flow is presented, and for validation of the multi-phase simulation through the nozzle, the simulation results are compared with experimental data.

4.2.2.2 Numerical simulation of un-premixed air-water two-phase flow through the nozzle

The *Eulerian* approach as well as the *Lagrangian* approach might be applicable for simulating of the air-water two-phase flow through the nozzle of figure (4.7). Depending on the secondary phase volume fraction, as explained in Section 4.2, the *Eulerian* and *Lagrangian* models are selected. For the defined problem in Section 4.2.2.1, the calculated secondary phase volume fractions are printed in Table 4.2. In this table secondary phase volume fractions have been calculated by assuming the water flow rate 93 kg/h with constant density of 1000 kg/m^3, and air flow rates from Table 4.1. The density of air has been calculated using the ideal gas law, $\rho = p/(RT)$.

Table (4. 2). The secondary phase volume fractions

P_{out} (Bar)	Experimented Air flow rate (kg/h)	Estimated secondary phase volume fraction (%)
5.38	37.2	1.48
4.64	54.1	1.02
4.30	58.4	0.95
3.80	61.1	0.90
3.10	62.0	0.89
2.00	62.1	0.89
1.28	62.4	0.89
0.81	62.2	0.89

As the secondary phase volume fraction values, shown in table 4.2, are less than 10%, so regarding the multi-phase limitation which presented in Section 4.1, for numerical simulation of this problem the *Lagrangian approach* or the *Discrete-Phase* model is the best choice.

For mesh generation of the un-premixed nozzle, sketched in Figure (4.7), the *GAMBIT* software can be used. For this purpose the similar procedure of Section 4.2.1 has been applied for the grid independency test. Figure (4.9) shows the grid independency test results on pressure distribution through the nozzle, grid numbers of 5634, 13728, 63600 and 86775, and for back pressure of 4.30 Bar.

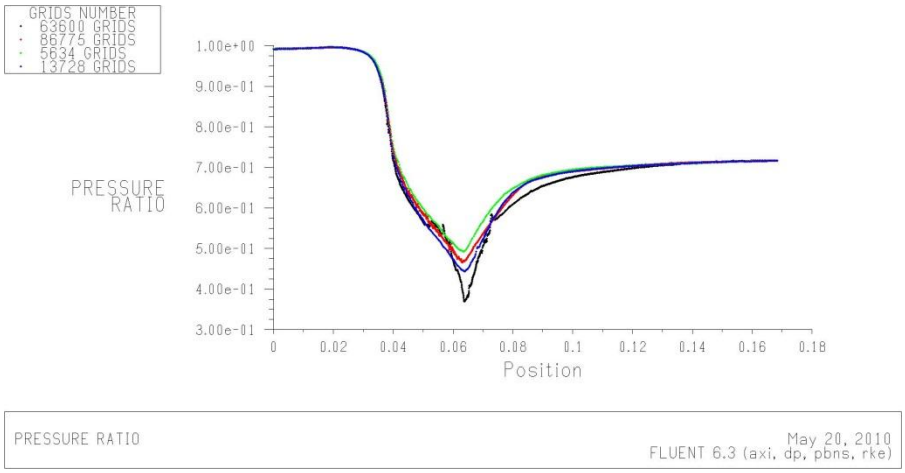

Figure (4. 9). Pressure ratio distribution through the Nozzle with different grid number

As Figure (4.9) shows, the grid number 13728 has a more reliable trend than grid number 5634, and it has almost the same trend with grid numbers 63600 and 86775 with about five times less grid numbers. Therefore, in the following simulation the applied grid number for the nozzle is 13728.

The simulation results for pressure distribution through the nozzle with similar conditions experimented by Lamonnier et. al., (1991) are shown in Figure (4.10). The comparison between Figure (4.8) and Figure (4.10) expresses the higher accuracy of numerical simulation than analytical computation. Also Figure (4.10) shows the numerical results have reliable matches with experimental data especially in the exhaust of the nozzle, which is very important in many nozzle applications.

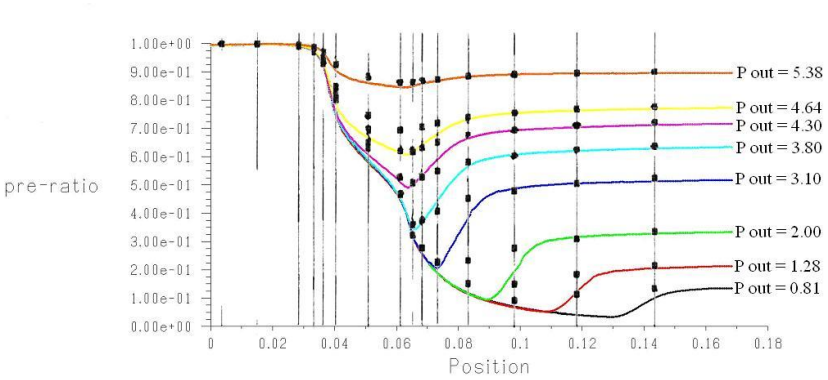

Figure (4. 10). Comparison of simulated pressure distribution with experimental results

For a more accurate check of the numerical simulation, the gas flow rate through the nozzle has been compared with the numerical and experimental values in table 4.3.

Even though the pressure profiles do not give any indication of choking, the mass flow-rate is barely affected by the reduction in back pressure.

Table (4. 3). The back pressure and air flow rate of nozzle

	Air flow rate (kg/h)	
P_{out} (Bar)	Experimented	Numerically Simulated
5.38	37.2	42.3
4.64	54.1	57.65
4.30	58.4	60.66
3.80	61.1	61.41
3.10	62.0	61.81
2.00	62.1	61.48
1.28	62.4	61.38
0.81	62.2	61.35

Finally, although the simulation achieved results of un-premixed air-water two-phase flow through the nozzle indicated high and reliable accuracy, due to the fact that the shot blasting nozzle has a premixed flow, in the following section the premixed and un-premixed flow of the nozzle will be compared.

4.2.2.3 The numerical simulation of premixed air-water two-phase flow through the nozzle vs. un-premixed flow

The premixed air-water two-phase flow with a similar inlet pressure and water flow rate has been simulated in the nozzle of Figure (4.11). All geometry and dimensions of this nozzle are similar to the nozzle of Figure (4.7) except the flow entrance that is

unlike Figure (4.7) is un-separated. Therefore in this study, the homogeneous two-phase flow has been assumed to enter the nozzle.

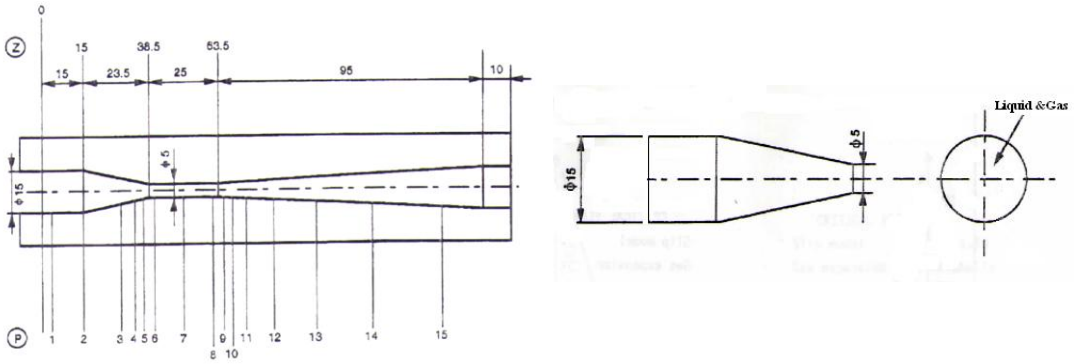

Figure (4. 11). Converging-diverging nozzle with premixed air-water two-phase flow

The validation of the simulating of air-water two-phase un-premixed flow has been discussed in the Section 4.2.2.2. So in the following section the simulating of premixed flow is compared with un-premixed flow results. Figure (4.12) shows the comparison of pressure profiles between premixed and un-premixed air-water two-phase flow through the nozzle. As this figure shows there is a very good agreement between the two different kinds of flow.

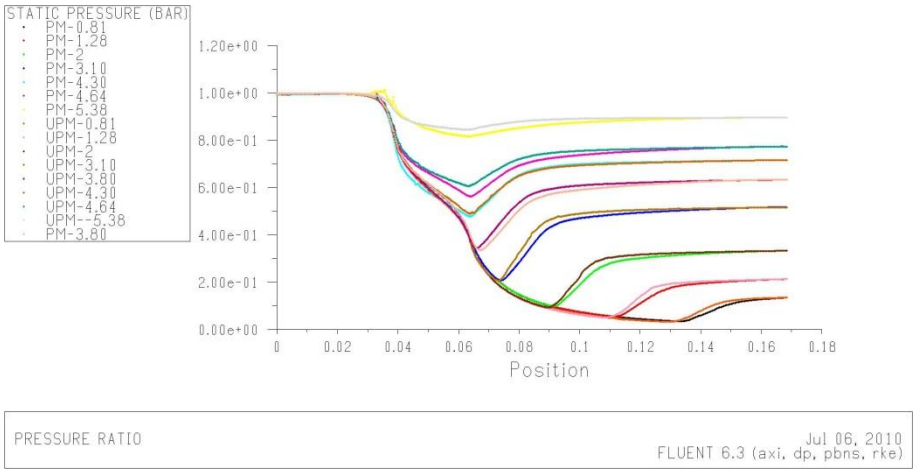

Figure (4. 12). Pressure distribution through the Nozzle for premixed and un-premixed flow

For a more in depth study of premixed and un-premixed effects on two-phase flow through the nozzle, air velocity distribution inside the nozzle has been compared for different back pressure in Figures (4.13a) to (4.13h).

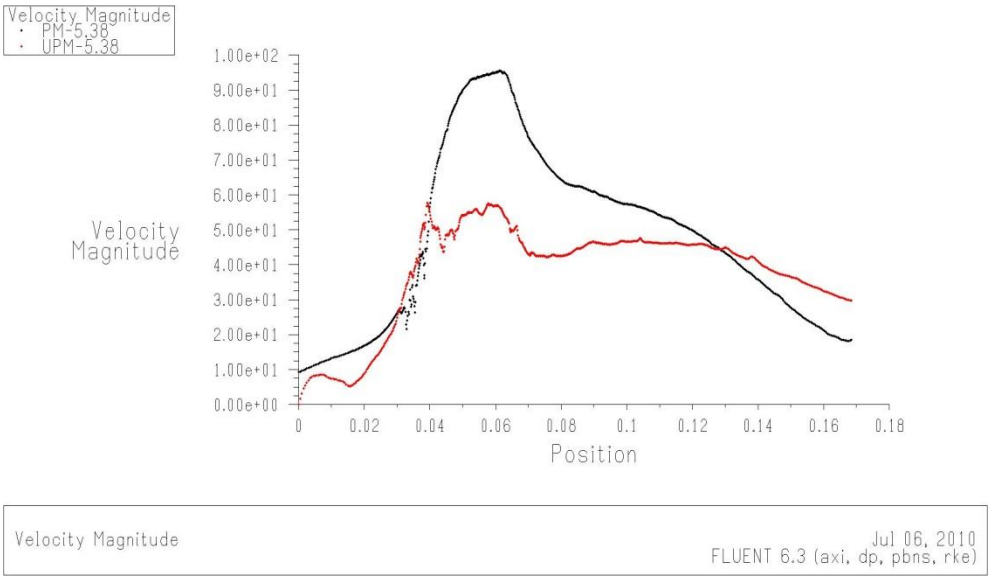

(4.13a)

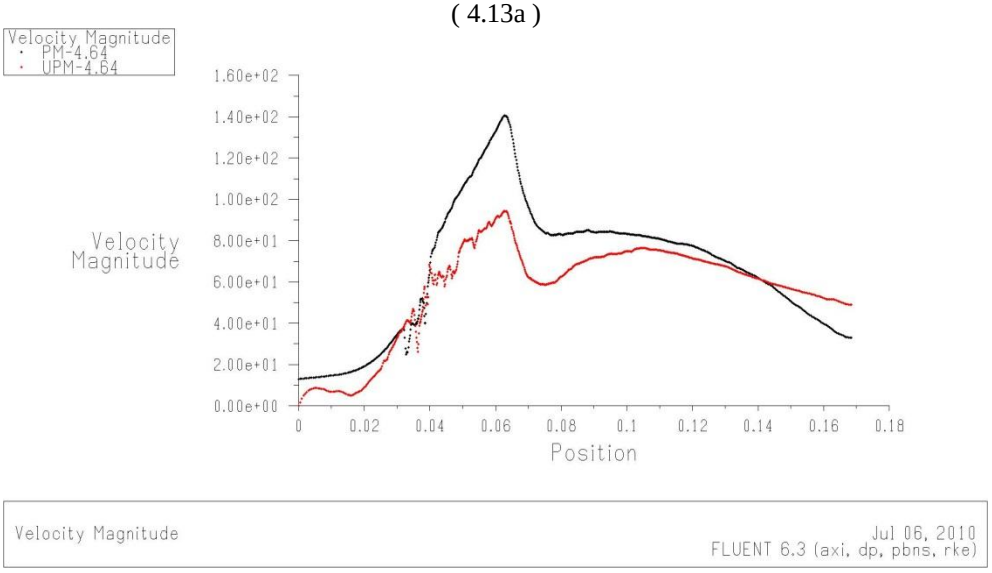

(4.13b)

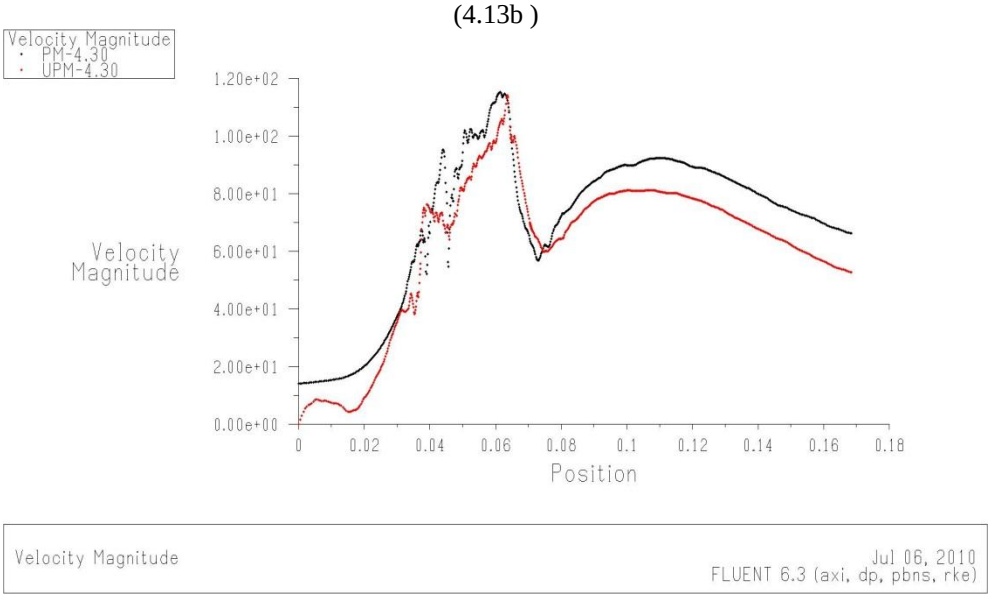

(4.13c)

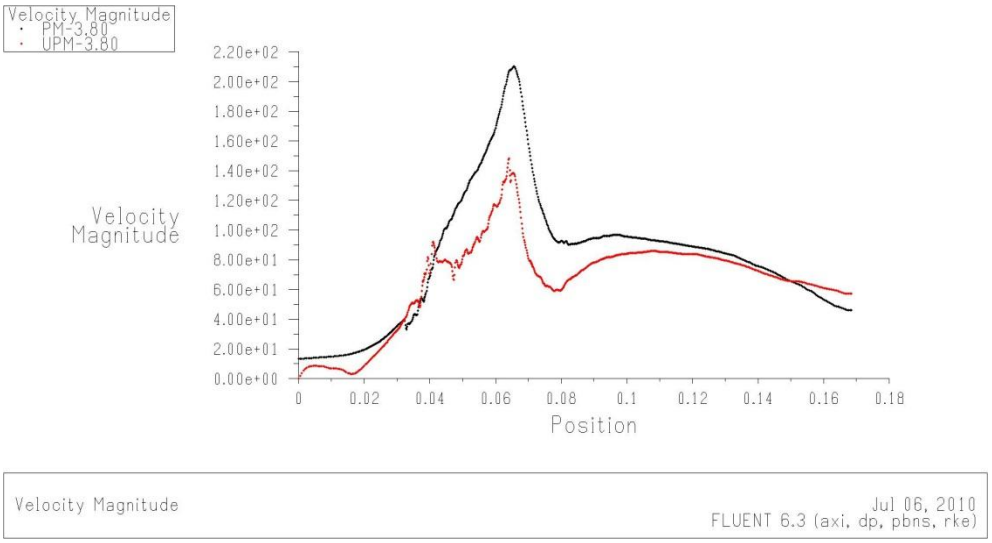

(4.13d)

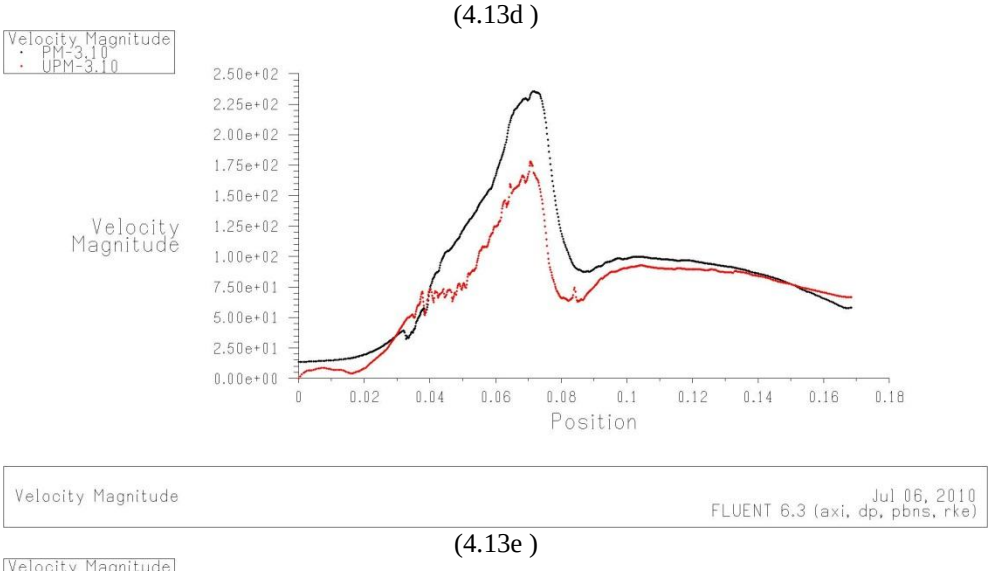

(4.13e)

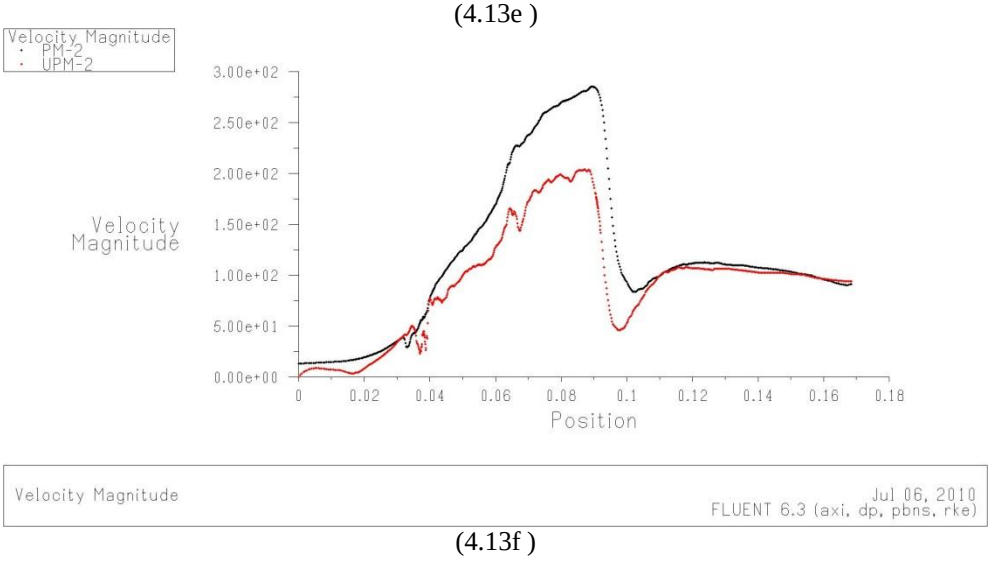

(4.13f)

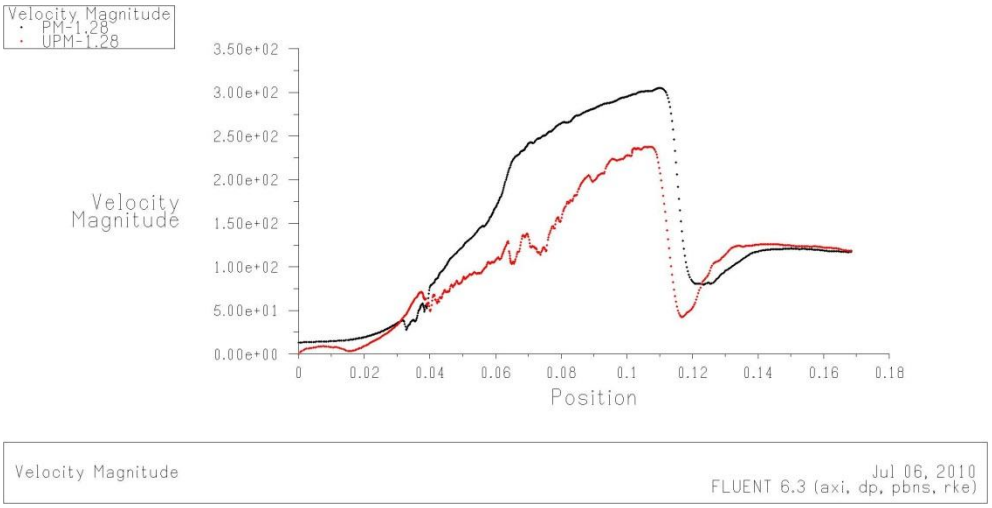

(4.13g)

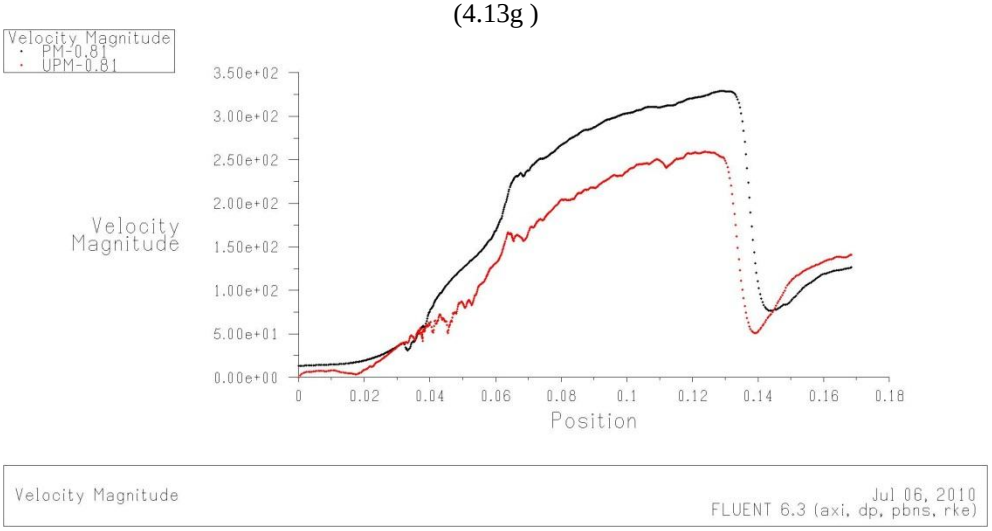

(4.13h)

Figure (4. 13). Air velocity distribution inside the nozzle

Obviously, the flow of air and consequent water droplets are because of the pressure difference, and by increasing the pressure difference between the inlet and back pressure the momentum of flow is increased. On the other hand, the raising of momentum helps to improve the air-water mixture quality. This phenomenon has been clearly shown in Figures (4.14) and (4.15).

By decreasing the back pressure from the 5.38 Bar in Figures (4.13a) to the 3.80 Bar in Figure (4.13d) the nozzle exhaust quality goes up and the air-water two-phase flow is going to have a good mixture by decreasing the back pressure from the 3.80 Bar to the 0.81 Bar on Figure (4.13h).

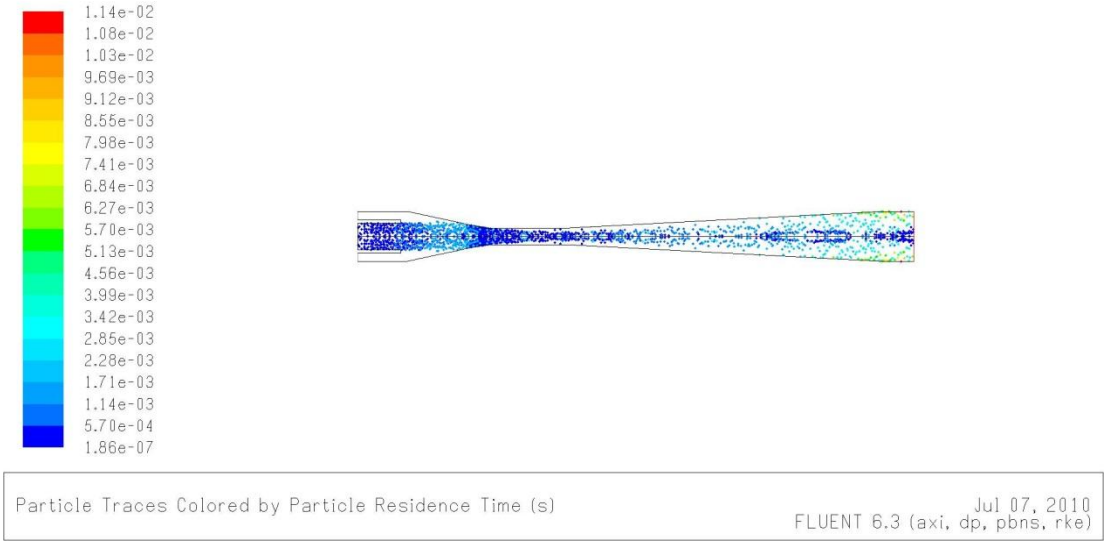

Figure (4. 14). Water droplets distribution through the Nozzle with exhaust back pressure of 5.38 Bar

Figure (4. 15). Water droplets distribution through the Nozzle with exhaust back pressure of 0.81 Bar

Finally, the simulation results, which have been expressed in this chapter, illustrate the accuracy of the Discrete-Phase model on the simulating of multi-phase flow. This model as well as the *Eulerian* model will be widely used in Chapter Five.

4.3 Summary and Conclusions

In this chapter, validation of the numerical method was analysed. The error sources, including acknowledged and unacknowledged errors, and the validation assessment were introduced. To arrive at a conclusion on the resolution of the computational mesh, it was necessary to pave the nozzle geometry with various numbers of meshes. By computing the wall y^+ distance for various generated grids inside the nozzle and

comparison of y^+ distributions through the nozzle, it was possible to conclude that the quadrilateral meshes with a resolution of 44×630 were an ideal choice of shape and size.

In addition, the *computer programming error check* and *usage error check* were employed and they focused fundamentally on utilization of *FLUENT* software for simulating of the three-phase flow through the nozzle. For this purpose, the available experimental and analytical results of the air-water nozzle flow were analysed. The *Realizable k-ε* and *Discrete Phase* models were employed for the modelling of the air-water premixed and un-premixed two-phase nozzle flow. In this study the correlation between the numerical and experimental results was even higher than those between the analytical and experimental results.

Finally, regarding this part of the study, the *Discrete Phase* model was selected as the best multi-phase model for simulating the flow throughout the sand-blasting nozzle.

CHAPTER 5

RESULTS AND DISCUSSION: PART I- AIR SINGLE-PHASE FLOW & AIR-SAND TWO-PHASE FLOW

Introduction

The nature of flow in shot-blasting systems is basically a multi-phase flow; consequently, any process for improving the shot-blasting efficiency requires to deeply challenging with multi-phase flow. On the other hand, in the wet shot blasting system the abrasive media is wafted with low pressure but high velocity air flow, which is accelerated in the nozzle. Therefore, increasing the performance of shot-blasting systems is related to improving the nozzle efficiency, which strongly depends on the multi-phase flow through the converging-diverging nozzle.

For the nozzle efficiency on a shot-blasting system, the main parameter to evaluate is the dynamic pressure of abrasive media in the exhaust of the nozzle. On the one hand, this parameter depends on the flow characteristic such as pressure difference and temperature; on the other hand it strongly depends on the phase interactions with each other and their behaviour on the multi-phase flow. For example, the shock wave, as a type of propagating disturbance and energy wasting source, could be influenced in the multi-phase flow with various flow characteristics.

In the following chapter, the effects of different boundary conditions as well as related multi-phase flow parameters on the nozzle's performance have been presented. For this purpose, the simulation begins with air single-phase flow through the nozzle,

and the simulation results will be briefly presented. These results are used not only for validation of the single-phase flow with available analytical data, but also for assessment of the effects of secondary phases on the nozzle's performance. The study is continued with simulation of air-sand two-phase flow through the nozzle with various boundary conditions. Two different multi-phase models, the *Eulerian approach* and the *Lagrangian approach* (*Discrete-phase* model) are used for the simulating of the two-phase flow through the nozzle.

The nozzle geometries, discretisation and grid dependency test have been expressed in chapter six.

5.1 Single-Phase flow

The compressible air flow through the nozzle with various pressure differences and so with different flow velocities has been simulated in this section. This study has been focused on the comparison of different turbulence modelling effects on the nozzle's performance. On the other hand, the effect of inlet temperature on the nozzle's performance, as one of the most important plan of this thesis, is analyzed.

5.1.1 Standard, RNG and Realizable k-ε models vs. Spalart-Allmaras and Reynolds Stress turbulent models

Pressure based simulation of air flow through the nozzle due to the constant boundary conditions is assumed to be steady flow. As Figure (5.1) shows the local Reynolds number through the nozzle is higher than the critical Reynolds number limit for internal flow. Therefore the air flow through the nozzle is turbulent flow.

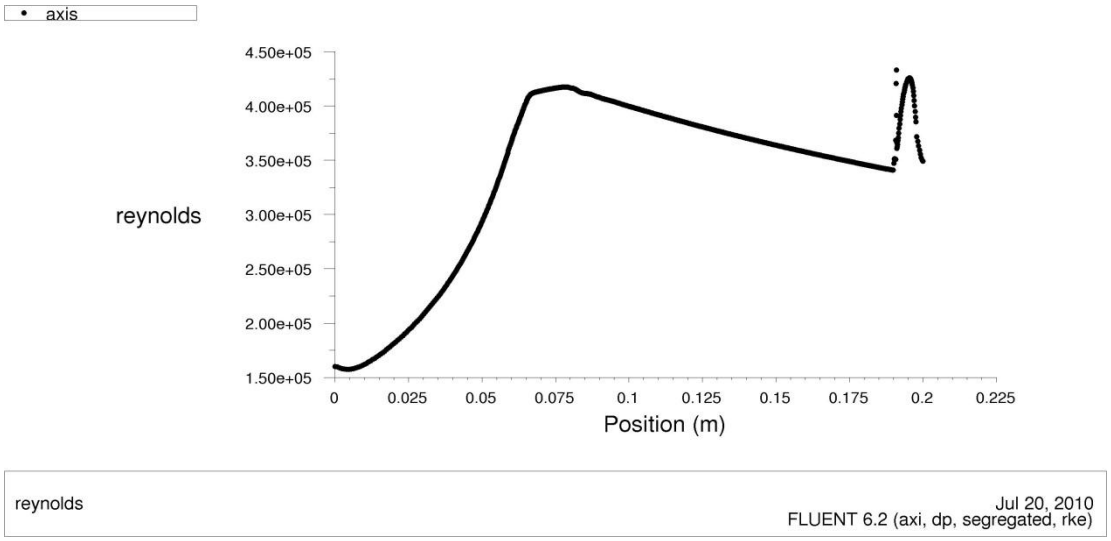

Figure (5. 1). Reynolds number profile on Nozzle centre-line

Turbulent flows are delineated by fluctuating velocity fields. These fluctuations affect transported quantities such as momentum and energy, and make them fluctuate too. Since these fluctuations can be small scale and high frequency, the instantaneous simulation of these transport quantities will be too expensive. Therefore, instead of the instantaneous transport equations, by applying the time-averaging technique, fluctuates can be modelled, and modified equations will computationally less expensive to solve. However, the modified equations contain additional unknown variables, and turbulence models are needed to determine these variables in terms of known quantities.

The Standard, RNG and Realizable k-ε models, Spalart-Allmaras and Reynolds Stress models are some popular turbulence models which applicable in multi-phase flow. The Standard k-ε model is valid only for high Reynolds number and fully turbulent flows. RNG k-ε model have some improvements compared to Standard k-ε model. This is included improvements in the ε equation which have additional term to increase the accuracy of model when it uses in rapidly strained flows. In addition, the effect of swirl turbulence is included in the RNG k-ε model and also it utilizes the variable Prandtl numbers. Finally, the RNG k-ε model is applicable in lower Reynolds number than in Standard model. The realisable k-ε model has new formulation for the turbulent viscosity and also for dissipation rate of kinetic energy (ε). This model predicts more accurately the spreading rate of planar and round jets than Standard model. In Spalart-Allmaras model a single conservation equation is used for the turbulent viscosity. This model is preferred for attached wall-bounded flows and flows with slight separation and recirculation. However, it is not recommended for massively

separated flows and free-shear flows. Reynolds Stress model (RSM) closes the Reynolds-averaged Navier-Stokes equations by solving additional transport equations for the six independent Reynolds stresses. Reynolds Stress model is recommended for accurately predicting complex flows such as Cyclone flows, rotating flow passages and flows involving separation (Wilcox, 1994, and Cebeci, 2003).

Here the Standard, RNG and Realizable k-ε models, Spalart-Allmaras and Reynolds Stress models are used for the simulating of air flow through the nozzle. The simulation results for pressure difference 2 atm and inlet temperature 300 K are shown in Figures (5.2) and (5.3).

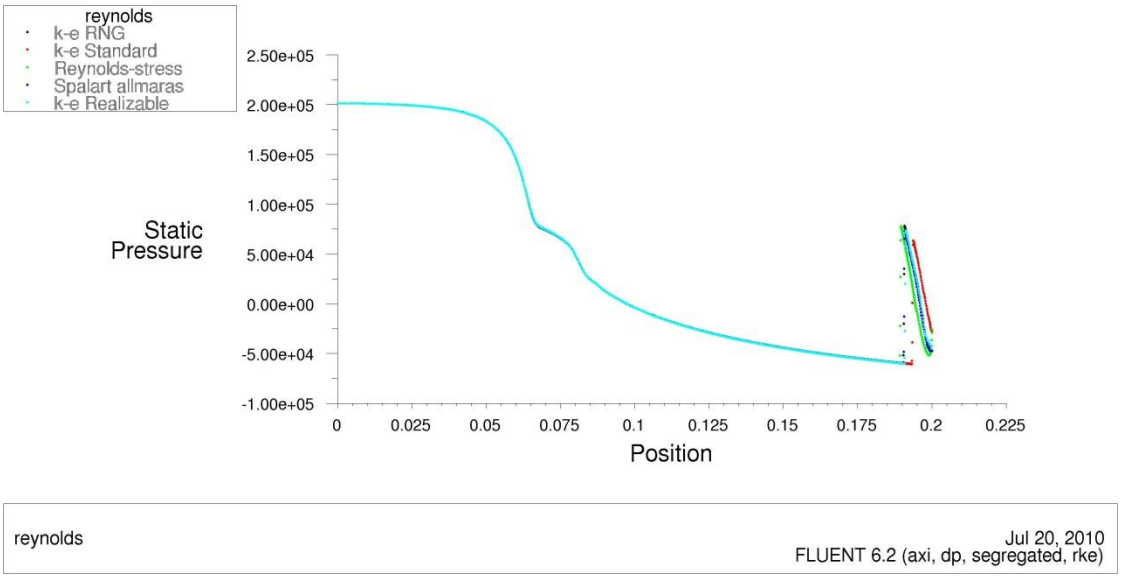

Figure (5. 2). Pressure profiles on Nozzle centre-line

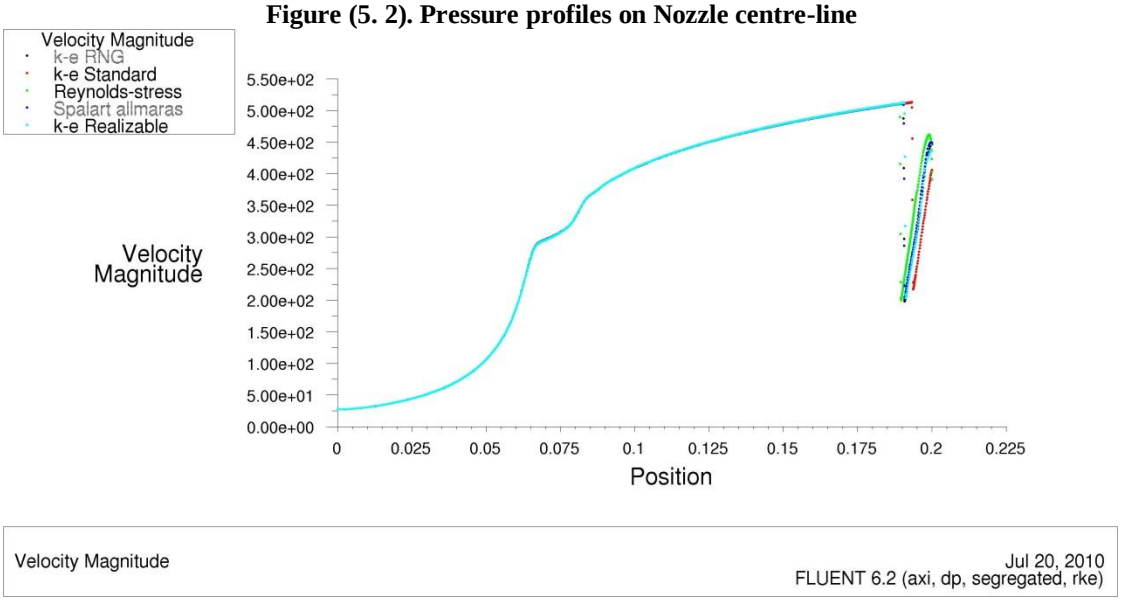

Figure (5. 3). Velocity profiles on Nozzle centre-line

Figure (5.2) shows the pressure distribution inside the nozzle and along the centre-line. Sudden jumping of the pressure profile after decreasing in the converging, flat and

some parts of the diverging sections of the nozzle indicate the event of a shock wave inside the nozzle. The same trend has been illustrated for the velocity profile in Figure (5.3).

Figure (5.2) shows two slight differences in comparison with the pressure profile for the *de Laval* Nozzle shown in curve D on Figure (5.4). One of these differences is the small bending on the pressure profile after the converging section. Since the *de Laval* Nozzle is made from just converging and then diverging sections, and in the simulated nozzle in this project, shown in Figure (3.6), the converging and diverging sections have been separated by the flat section, so the mentioned slight bending in Figure (5.2) is due to the flat part of the nozzle.

The second difference is the pressure distribution after the shock wave. Figure (5.4) shows that the pressure profile is raised suddenly after the shock wave, on the other hand, it means the shock wave happens in the very thin path through the nozzle, which this path, as Figure (5.4) shows, is sufficiently close to zero, and the flow is stable after the shock wave. However, the simulation results show not only that this path is not zero, but also the flow needs some distance to be nearly stable (Figures 5.6 to 5.9), and obviously during this distance the pressure can oscillate. Definitely, the flow distribution decreases by moving from the nozzle axis area toward the nozzle's wall. Therefore, the static pressure profile on the wall is expected to be more similar to curve D on Figure (5.4) than the static pressure distribution at the nozzle's centre line.

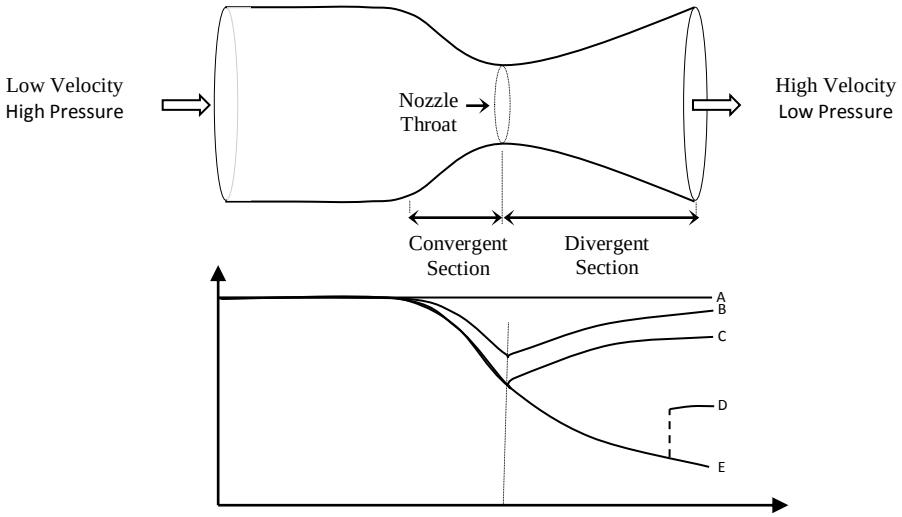

Figure (5. 4). de-Laval Nozzle and pressure distribution

Figure (5.5) shows the static pressure profile along the wall of the nozzle for similar boundary conditions which are applied in Figure (5.2). The comparison between Figures

(5.5) and (5.4), especially the curves after the shock wave, show the same trend for static pressure, i.e. smooth increasing of the pressure after the sharp rising.

Finally, Figures (5.2) and (5.3) show the various turbulent models, including the *Standard*, *RNG* and *Realizable k-ε* models, *Spalart-Allmaras* and *Reynolds Stress* turbulent models, have no significant effects on the single-phase flow distribution through the nozzle. Therefore, in the following sections for the single-phase flow the *Realizable k-ε* model has been chosen as the turbulence model.

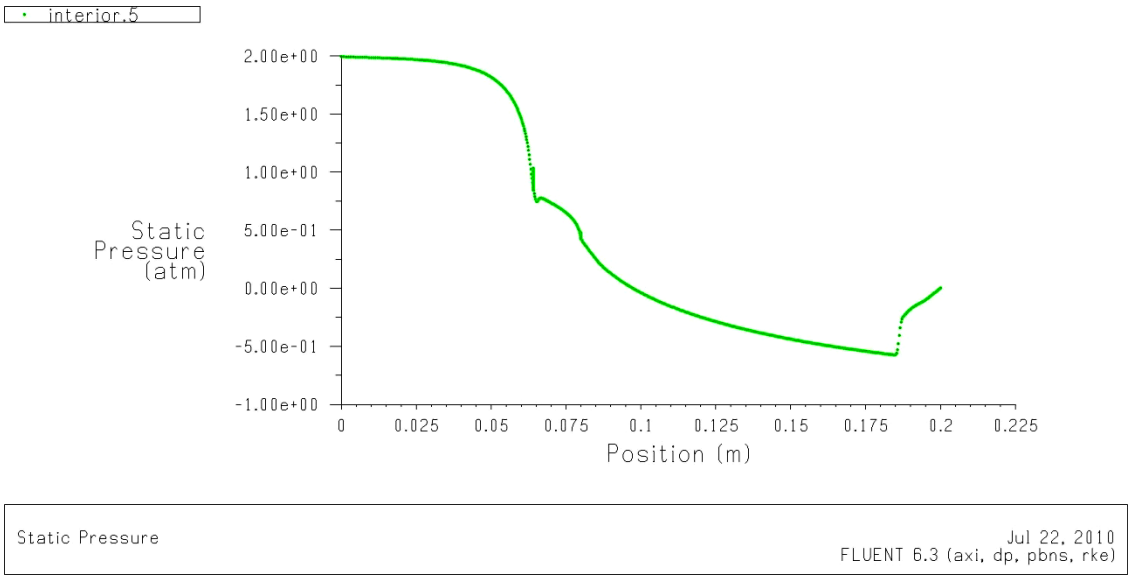

Figure (5. 5). Pressure profiles on Nozzle wall

5.1.2 Various inlet pressure on Nozzle single-phase flow

In a shot blasting system the exhaust static pressure of the nozzle is ambient pressure, and so the nozzle gauge pressure in the exhaust is zero. By increasing/decreasing the inlet pressure the flow velocity is controlled. Depending on the pressure difference, the shock wave can appear inside the nozzle and has got a different position on the diverging part of the nozzle.

Figure (5.6) shows the pressure profiles for various inlet pressure and constant temperature, 300 K. These profiles have been plotted in the axis of the nozzle and show that by increasing inlet pressure the shock wave moves through the exit of the nozzle. For inlet pressures 0.0667 and 0.1429 atm, or the pressure ratio of 0.9375 and 0.875 respectively, the flow inside the nozzle is subsonic, and for inlet pressure 3 atm, or the pressure ratio of 0.25, however the flow is supersonic but the shock wave has moved outside of the nozzle.

The contours of the Mach number and shock wave places in the CD nozzle are shown in Figures (5.7a to 5.7f). The Mach number distributions which have been shown in Figures (5.7a to 5.7f), and the profiles plotted in Figure (5.8), confirm the abovementioned trend. On the other hand, Figure (5.8) confirms the nozzle supersonic flow principle which has been discussed in Chapter 3. Regarding the abovementioned principle, the throat's Mach number should not exceed more than one, and Figure (5.8) shows all the curves of the supersonic flow have the same values and are equal to one in that section.

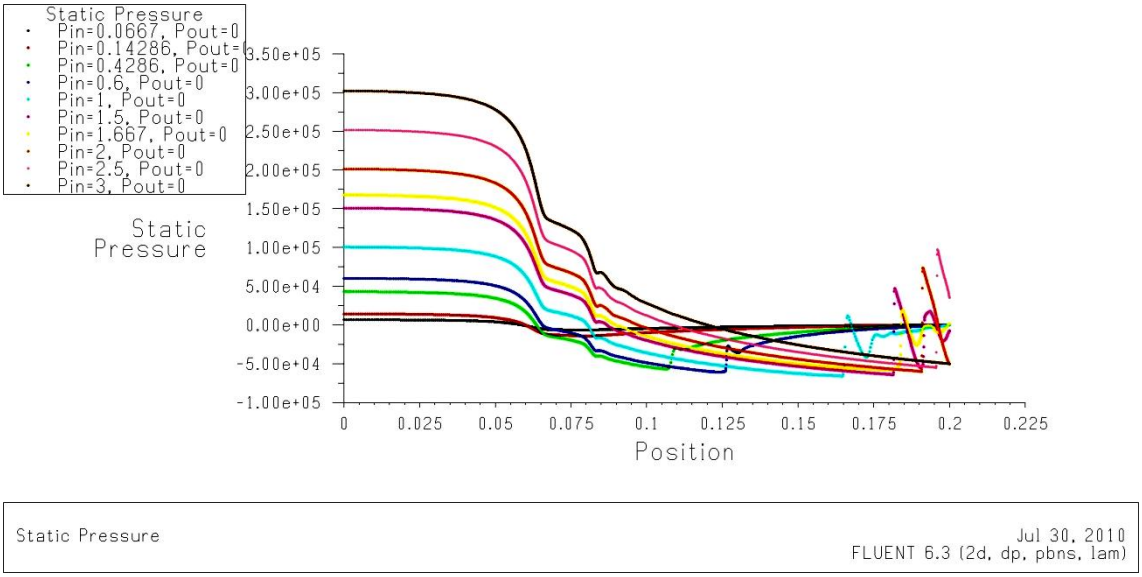

Figure (5. 6). Pressure profiles on Nozzle axis

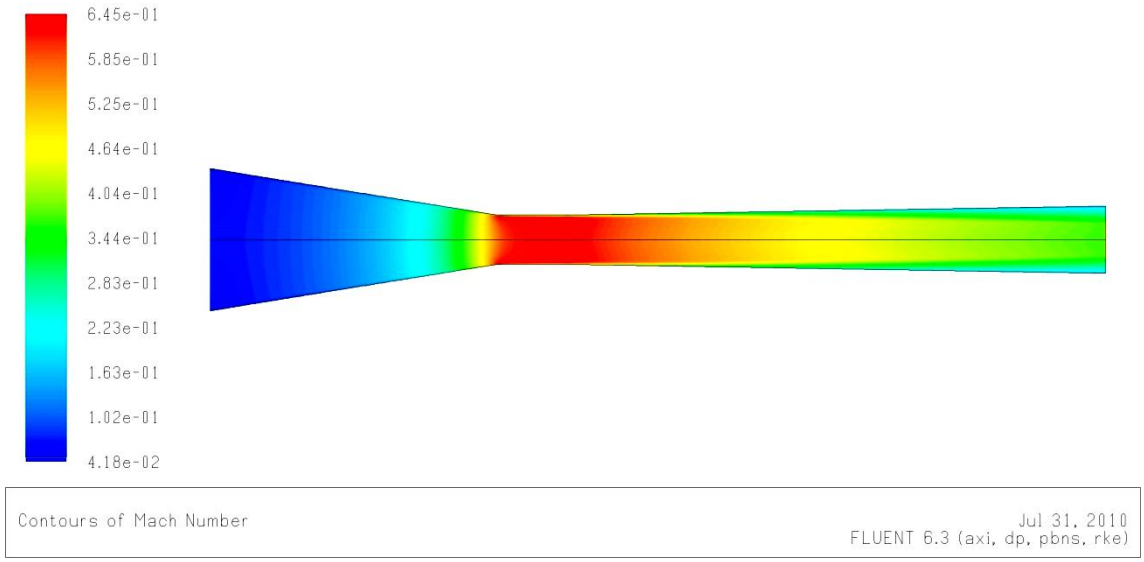

Figure (5. 7). a: Contours of Mach number for inlet pressure = 0.1429 atm

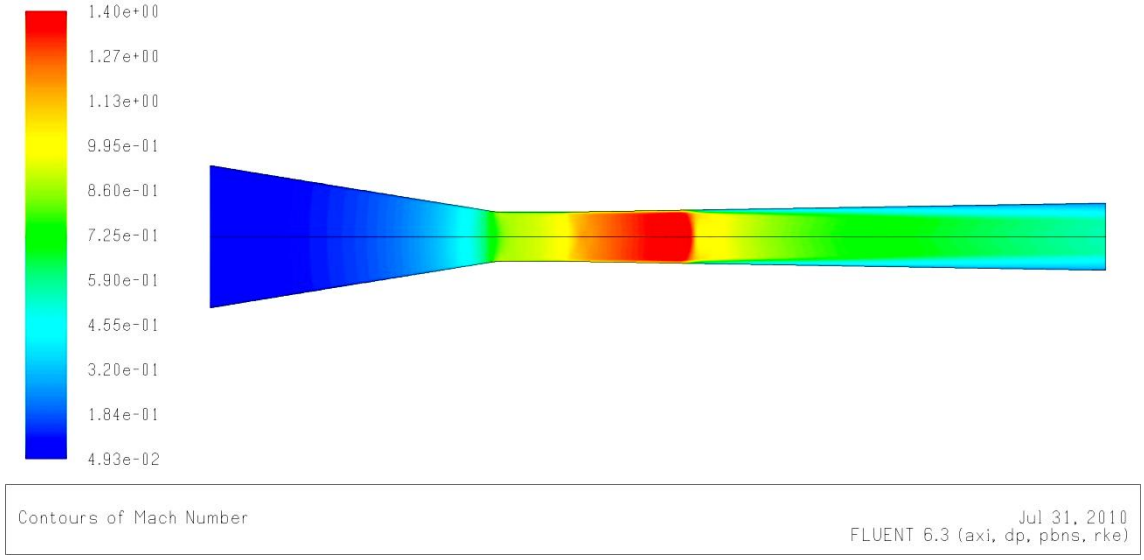

Figure (5.7). b: Contours of Mach number for inlet pressure = 0.4286 atm

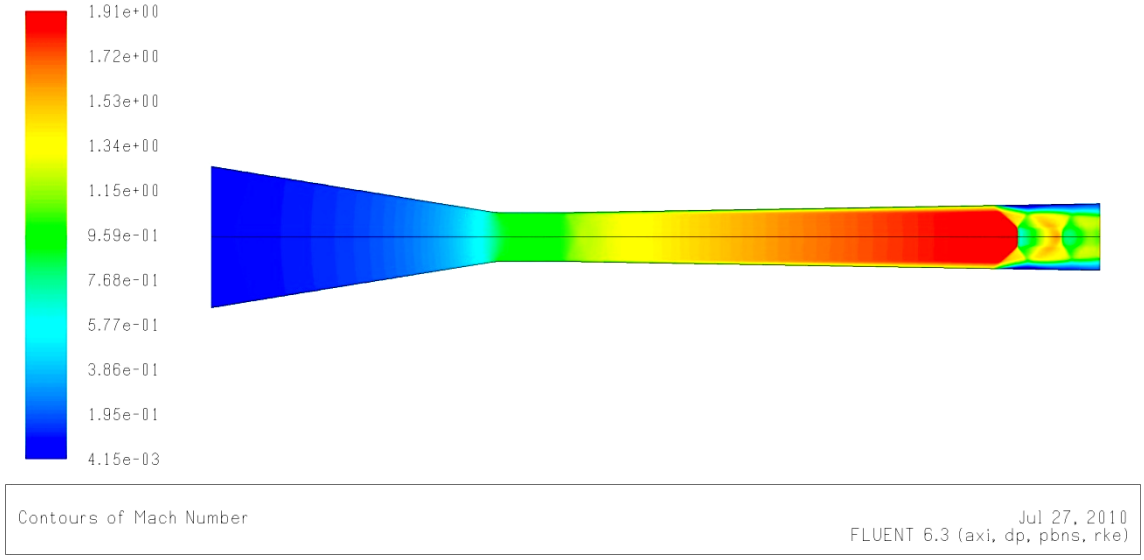

Figure (5.7). c: Contours of Mach number for inlet pressure = 1.5 atm

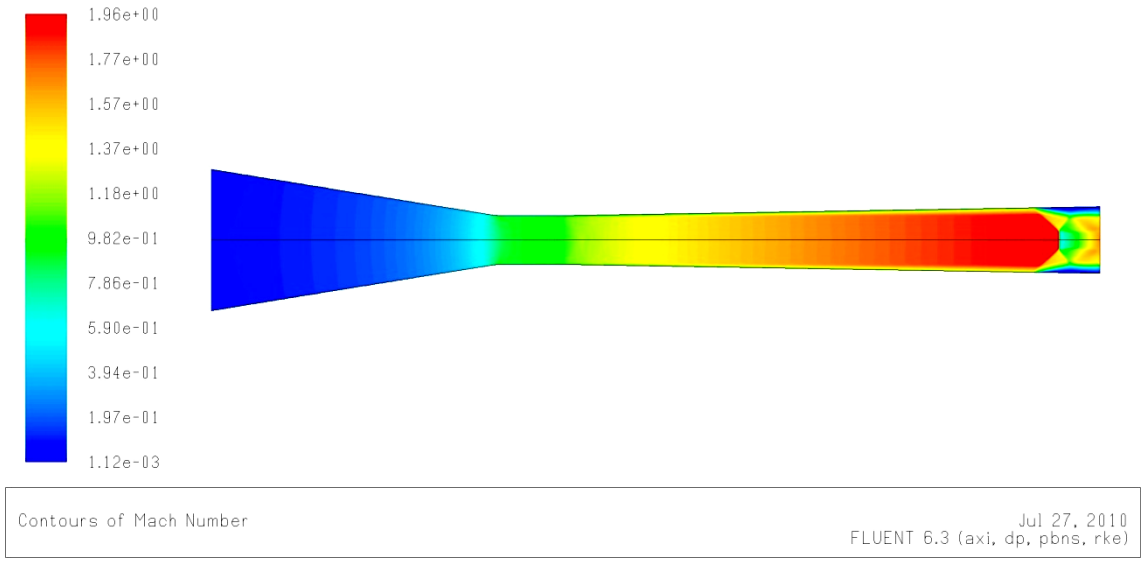

Figure (5.7). d: Contours of Mach number for inlet pressure = 2 atm

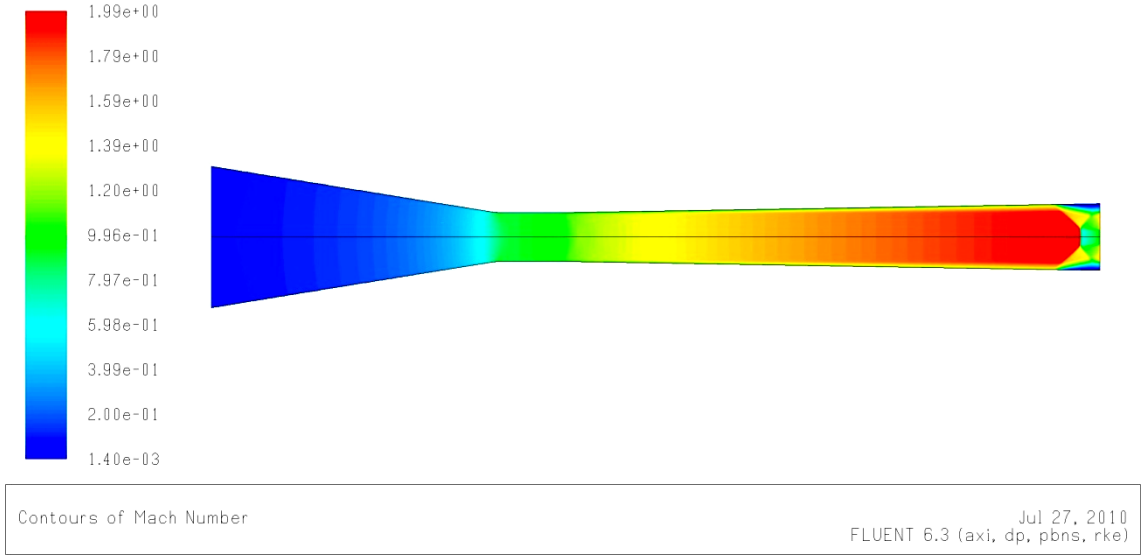

Figure (5.7). e: Contours of Mach number for inlet pressure = 2.5 atm

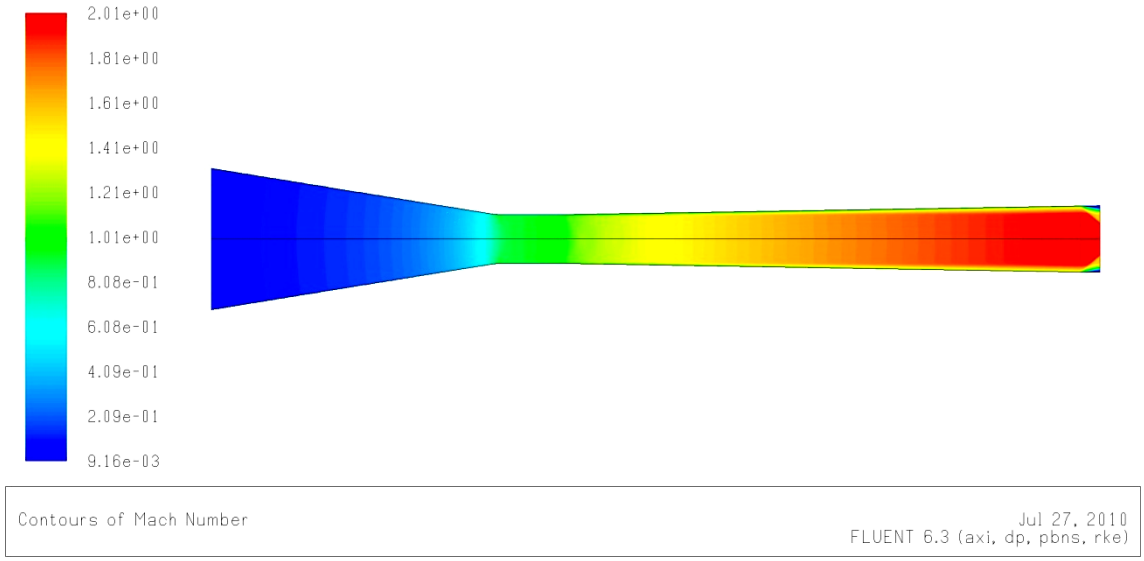

Figure (5.7). f: Contours of Mach number for inlet pressure = 3 atm

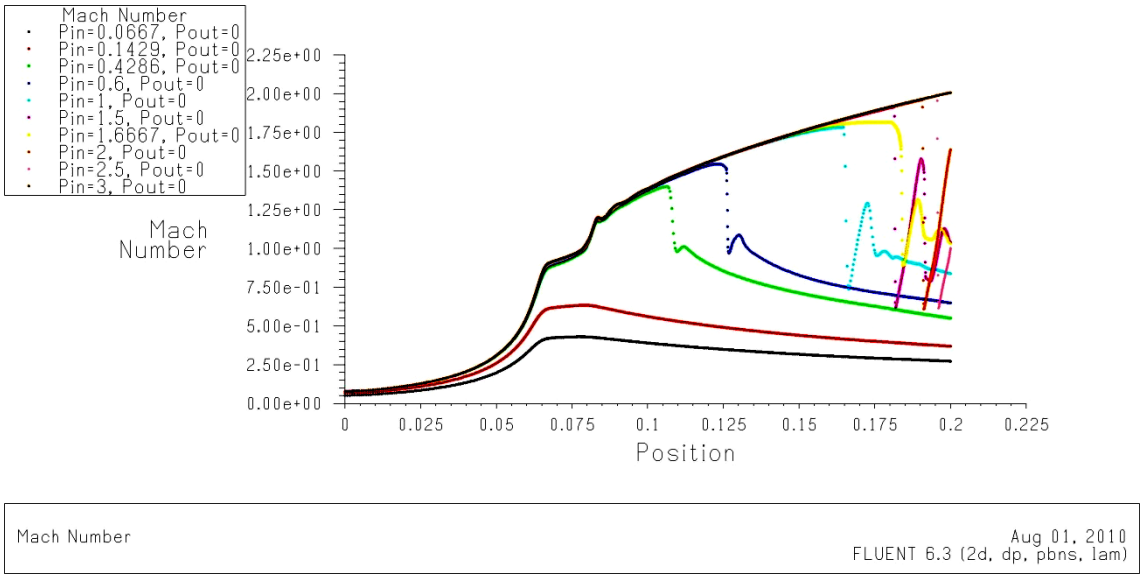

Figure (5. 8). Mach number profiles on Nozzle axis

Finally, the comparison of the simulation results shown in Figure (5.6) and the pressure distribution on the nozzle, which were discussed in Chapter 3 and Figure (3.4), expresses a conflict between these two curves. The main reason for this conflict and more discussion on the boundary conditions effects on the nozzle's performance are discussed in the next section.

5.1.3 Various inlet pressure vs. various outlet pressure on Nozzle single-phase flow

This section is going to shows the effects of inlet pressure, outlet pressure, pressure difference and pressure ratio p_{out}/p_{in} on mass flow rates and nozzle performance. Obviously, for blasting the fluid through the nozzle, the inlet pressure should be more than the outlet pressure, and it means the pressure difference, and pressure ratio should be negative, and less than one, respectively.

In Figure (5.6) pressure profiles have been traced for different inlet pressures while the outlet pressures are constant. However, as Figure (5.9) shows, for various outlet pressure and constant inlet pressure, the set of pressure profiles have different trends from Figure (5.6).

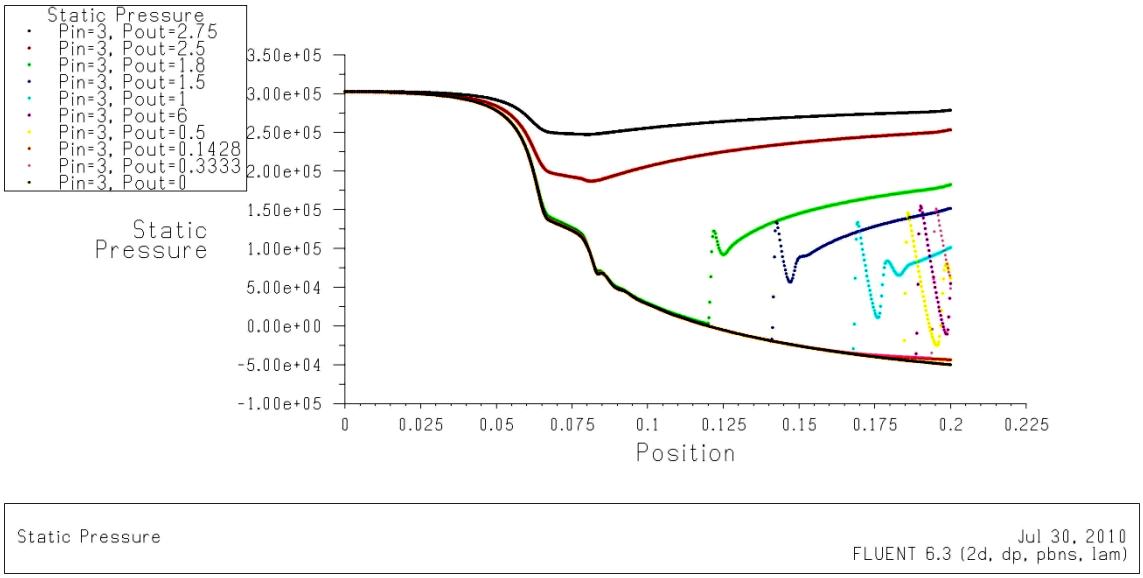

Figure (5. 9). Pressure profiles for constant inlet pressure and different outlet pressure on Nozzle axis

Figure (5.9) shows all supersonic pressure profiles traverse the same curve until the shock wave. These trends are the same as the pressure distribution which has been discussed in Chapter 3 and shown in Figure (5.4) for the de-Laval Nozzle. Definitely, different boundary conditions, shown in Figures (5.6) and (5.9), have other effects on the nozzle's performance and the nozzle's flow characteristics. Here, the effects of different boundary conditions on the nozzle's mass flow rates, velocities, flow temperature and Mach number are expressed.

Various sets of inlet and outlet pressure might have the same pressure difference, for example the inlet and outlet pressure 2 and 1 atm, respectively have the same pressure difference with 3 and 2 atm. But these two sets of pressure have different pressure ratios which are 0.5 and 2/3, respectively.

Table (5.1) shows the computed mass flow rates for various pressure ratios and in two different cases. In case A the inlet pressure is constant and the mass flow rate increases by decreasing the outlet pressure. This case is widely used in technical literature and the most pressure curves in the literature are in the base of the constant inlet pressure. However, case B is a practical case and it is applicable for shot-blasting nozzle flows. In case B the outlet pressure assumes constant, and mass flow rates increase by raising the inlet pressure. This table shows that for the same pressure ratio, case A and case B have different amounts of mass flow rates. On the other hand, the green and blue printed data in Table (5.1) state for the same pressure difference in case A and case B, the mass flow rates have different values. All the pressures in Table (5.1)

are absolute pressure.

Table (5. 1). Computed mass flow rates for various pressure ratio and boundary conditions

Pressure Ratio p_{out}/p_{in}	CASE A Constant Inlet Pressure			CASE B Constant Outlet Pressure		
	$p_{in,A}$	$p_{out,A}$	$\dot{m}_A$	$p_{in,A}$	$p_{out,A}$	$\dot{m}_A$
0.937	4	3.75	0.061	1.067	1	0.0154
0.875	4	3.5	0.0778	1.143	1	0.0214
0.775	4	3.1	0.0848	1.290	1	0.0276
0.7	4	2.8	0.0875	1.429	1	0.031
0.625	4	2.5	0.088	1.6	1	0.035
0.5	**4**	**2**	**0.088**	2	1	0.0439
0.4	4	1.6	0.088	2.5	1	0.055
0.375	**4**	**1.5**	**0.088**	2.667	1	0.0586
0.333	4	1.333	0.088	**3**	**1**	**0.066**
0.286	4	1.143	0.088	**3.5**	**1**	**0.077**
0.25	4	1	0.088	4	1	0.088
0.2	4	0.8	0.088	5	1	0.1

Figure (5.10) shows the mass flow rates of case A and case B. A comparison of this figure and Figure (3.5) in Chapter 3, shows very good consistency between the experimentally measured mass flow rates and the computed results in case A. In case A on Table (5.1) or the curve of $p_{in} = 4atm$ on Figure (5.10) by decreasing outlet pressure the mass flow rates increase up to a maximum 0.088 kg/s, whereas, there is not any limit for mass flow rates in case B. For realizing the abovementioned different trend of the two cases, this section is going to compare the flow Mach number, temperature, velocity, density and mass flux rate for case A and case B.

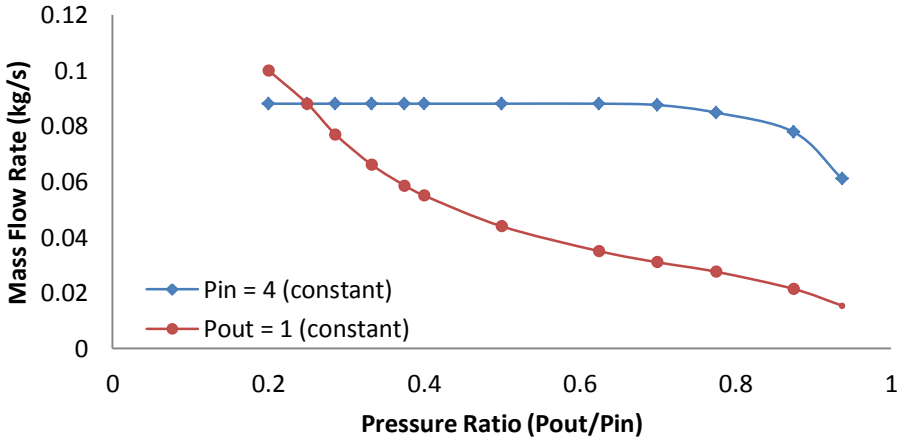

Figure (5. 10). Mass flow rates for different boundary conditions and pressure ratio

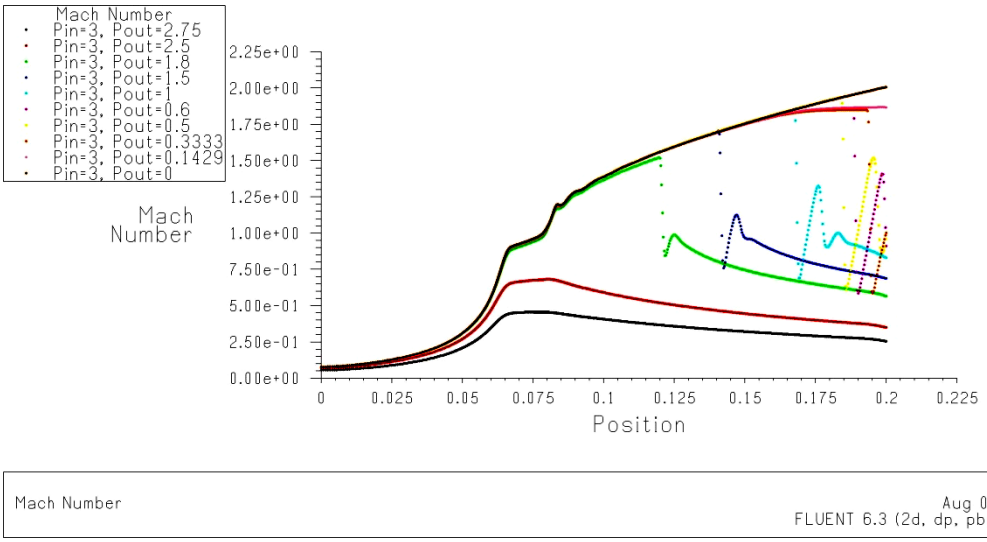

(5.11) Case A

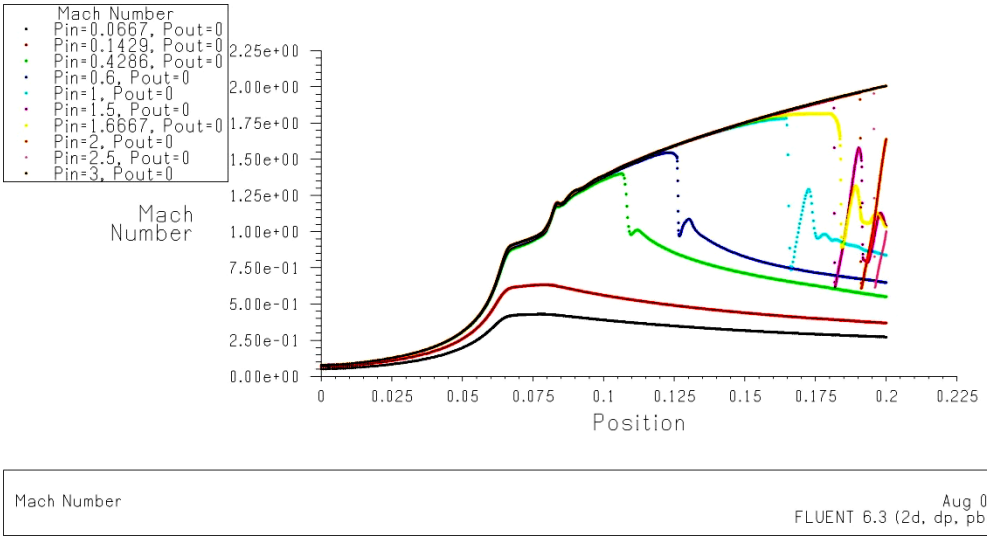

(5.11) Case B

Figure (5. 11). Mach number profiles for different boundary conditions on case A and case B

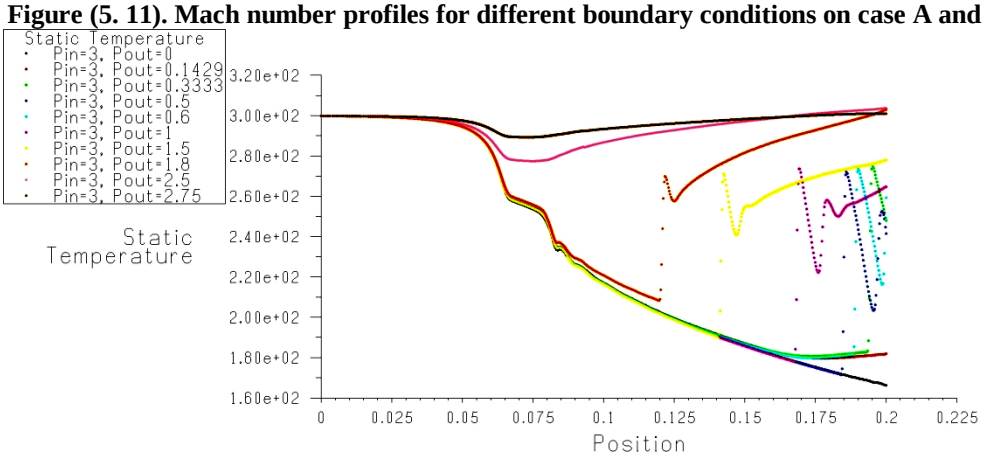

(5.12) Case A

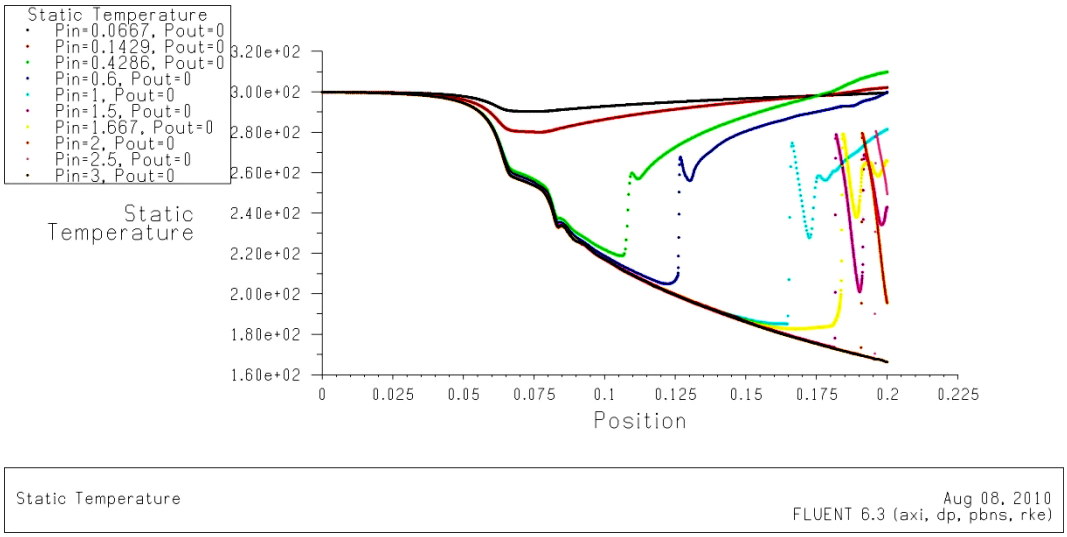

(5.12) Case B

Figure (5. 12). Temperature profiles for different boundary conditions on case A and case B

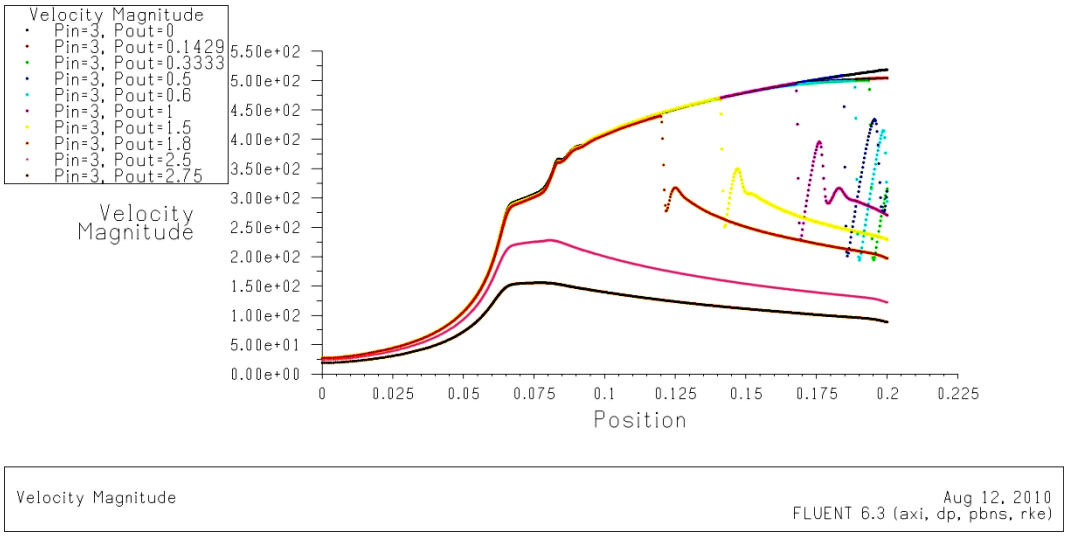

(5.13) Case A

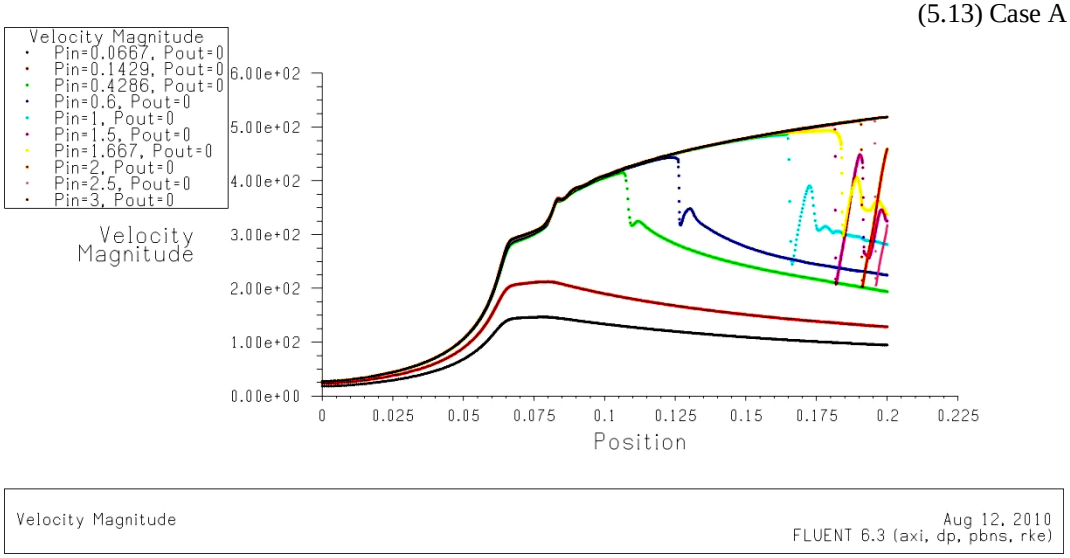

(5.13) Case B

Figure (5. 13). Velocity profiles for different boundary conditions on case A and case B

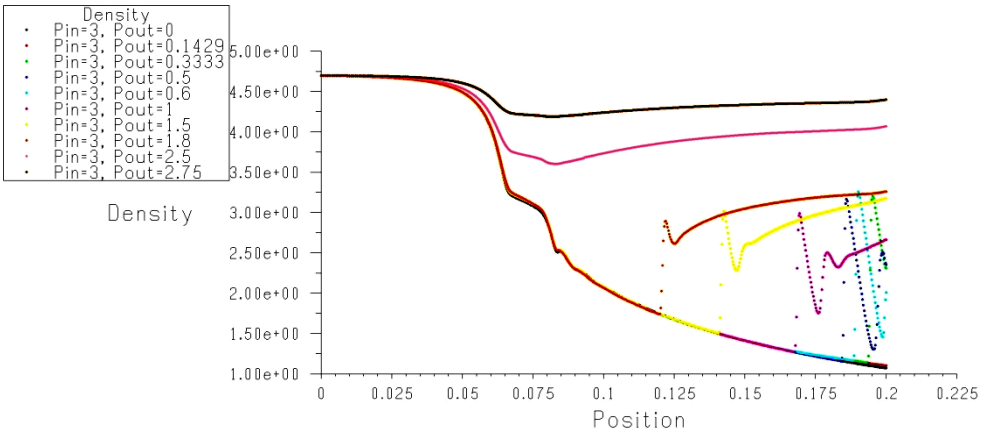

(5.14) Case A

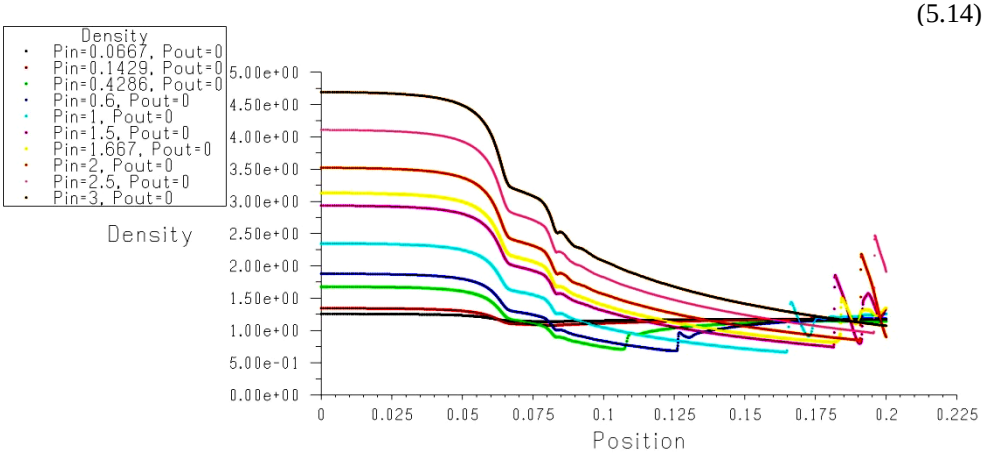

(5.14) Case B

Figure (5. 14). Density profiles for different boundary conditions on case A and case B

The Mach number, temperature and velocity profiles for constant inlet pressure vs. constant outlet pressure have been shown in Figures (5.11) to (5.13). These figures confirm that the constant inlet or outlet pressure cases have no significant effects on the Mach number distribution, temperature or velocity profiles through the nozzle. The density profiles shown in Figure (5.14) have almost the same trend of pressure profiles, sketched in Figures (5.6) and (5.9), for both cases. It means the flow density has been affected directly by pressure. On the other hand, for constant inlet pressure, case A, Figures (5.13) and (5.14) state all supersonic flows have the same velocity and density until the shock wave. Therefore, the mass flow rate for all supersonic flows in case A have to be the same and remain constant by decreasing the outlet pressure. Finally, the density multiplying to the velocity named mass flux rate profiles have been shown in figure (5.15).

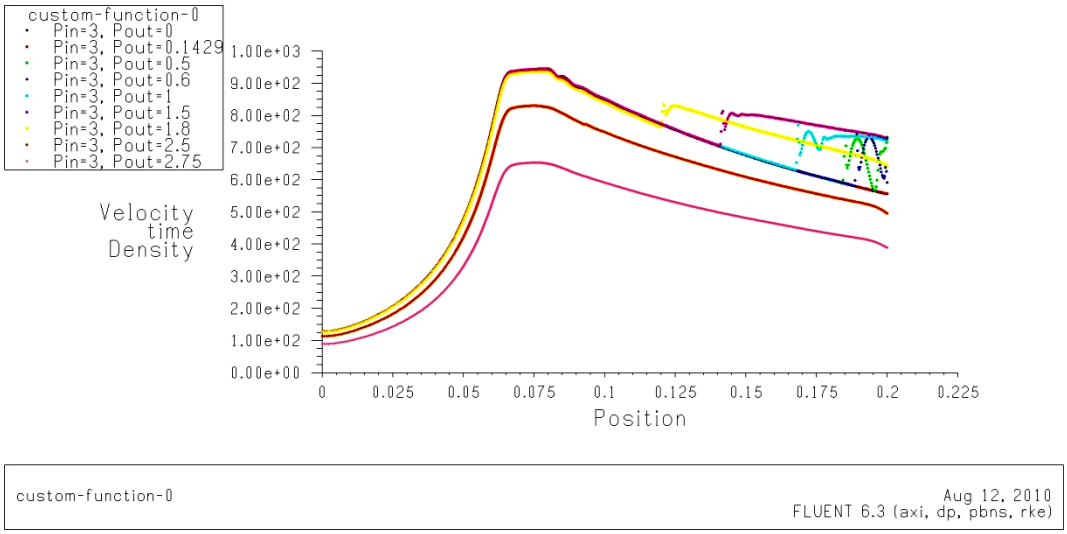

Case A

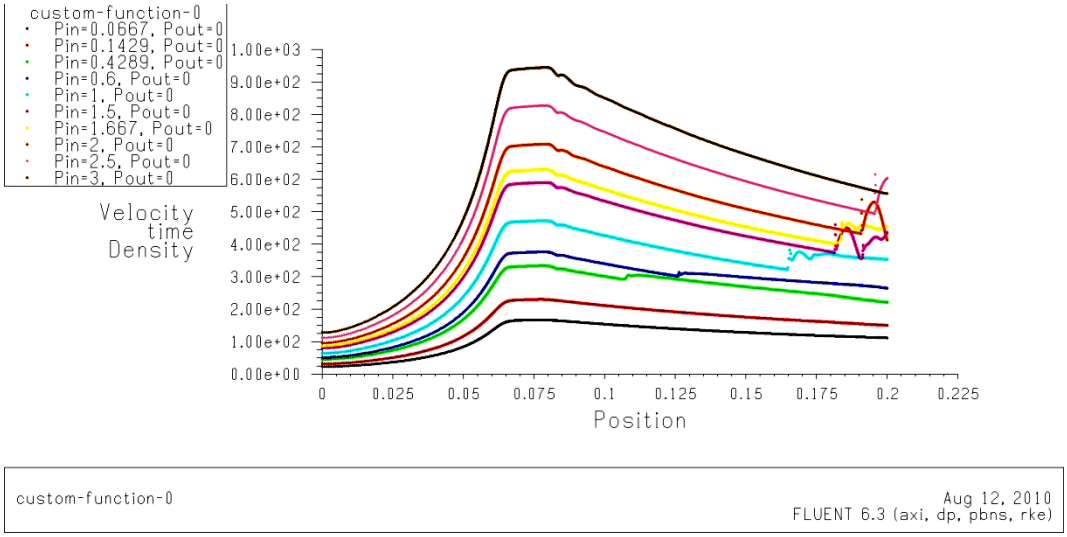

Case B

Figure (5. 15). Mass flux rate (ρu) profiles for different boundary conditions on case A and case B

These profiles confirm the behaviour of the mass flow rates shown in Figure (5.10). Case B in Figure (5.15) shows that there is not any limit to increasing the mass flux by increasing the inlet pressure; however, in case A by decreasing the outlet pressure, the mass flux rates increase just in subsonic flows and for supersonic flow the mass flux is independent of outlet pressure.

As in the shot-blasting system, case B is more applicable than case A, so in the following sections all studies, related to the various pressure differences, have been focused on case B.

5.1.4 Various inlet temperature on Nozzle single-phase flow

Temperature is the measure of the average kinetic energy of the particles in a

substance, which is related to how hot or cold that substance is. In the nozzle single-phase flow the temperature is directly related to the kinetic energy of flow and it might affect outlet velocity, as this is the most important parameter in the nozzle appliance.

In this section the effects of various inlet temperatures on static and dynamic pressure, velocity, density and Mach number have been expressed.

Figures (5.16) to (5.21) show the inlet temperature has no significant effect on the Mach number or the Static and Dynamic pressure; however, the nozzle flow velocity, density and temperature profiles considerably depend on inlet temperature.

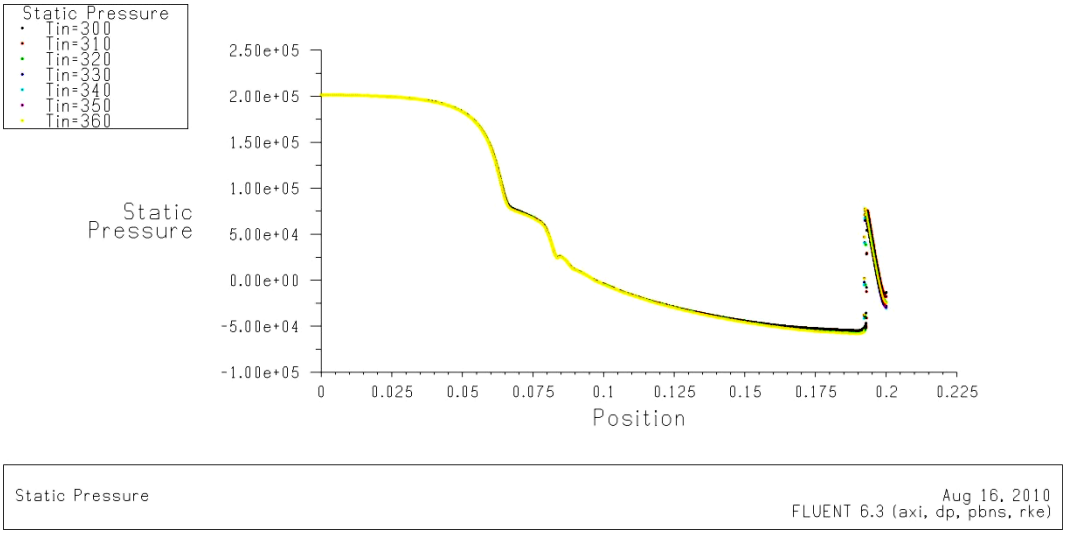

Figure (5. 16). Static Pressure profiles for different inlet temperature

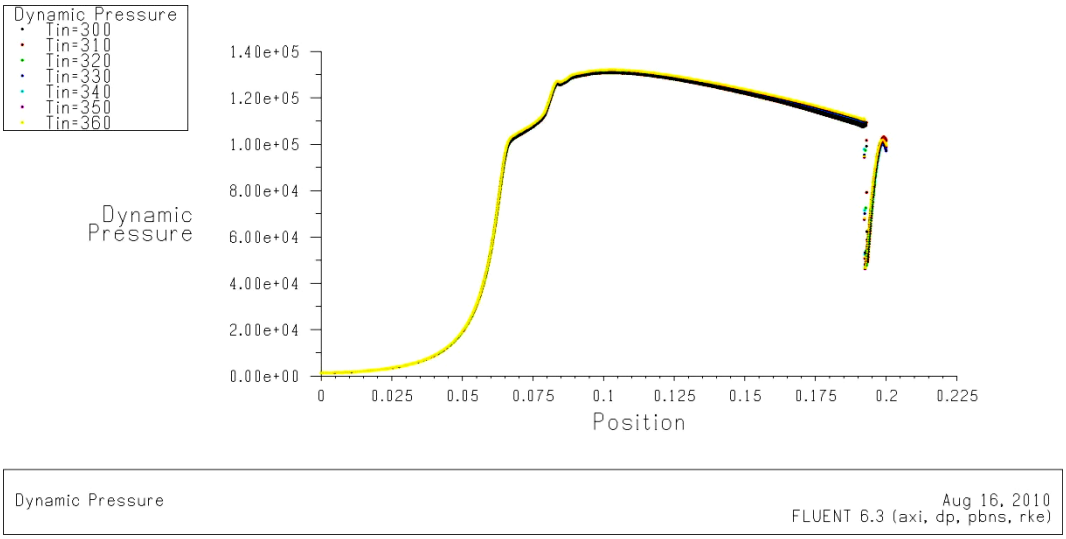

Figure (5. 17). Dynamic Pressure profiles for different inlet temperature

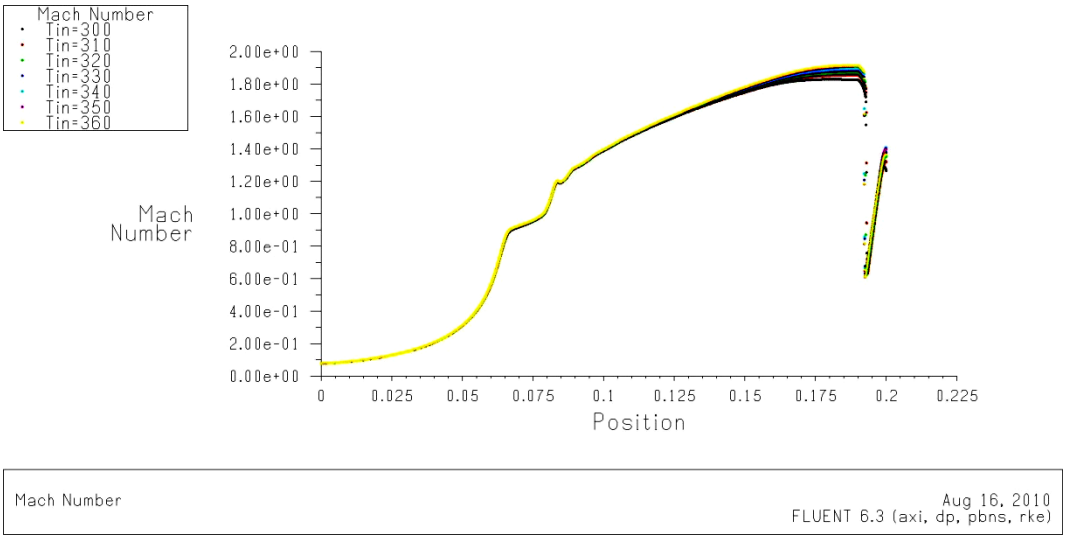

Figure (5. 18). Mach number profiles for different inlet temperature

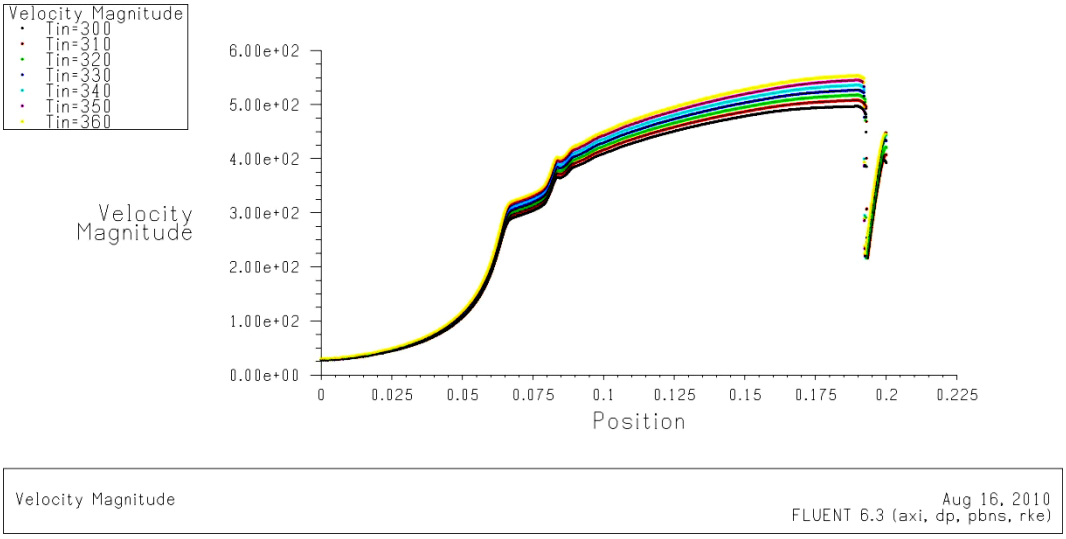

Figure (5. 19). Velocity profiles for different inlet temperature

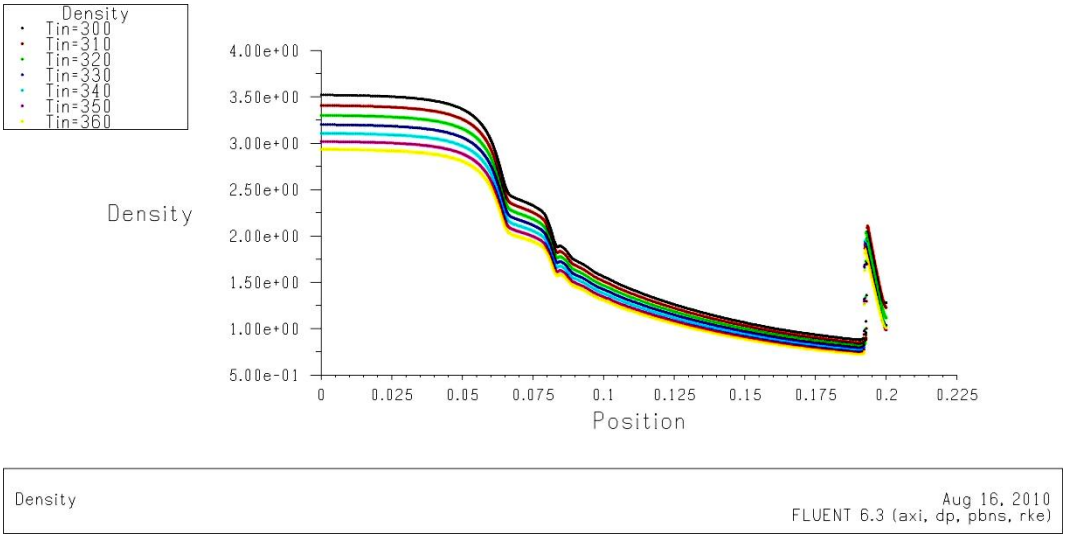

Figure (5. 20). Density profiles for different inlet temperature

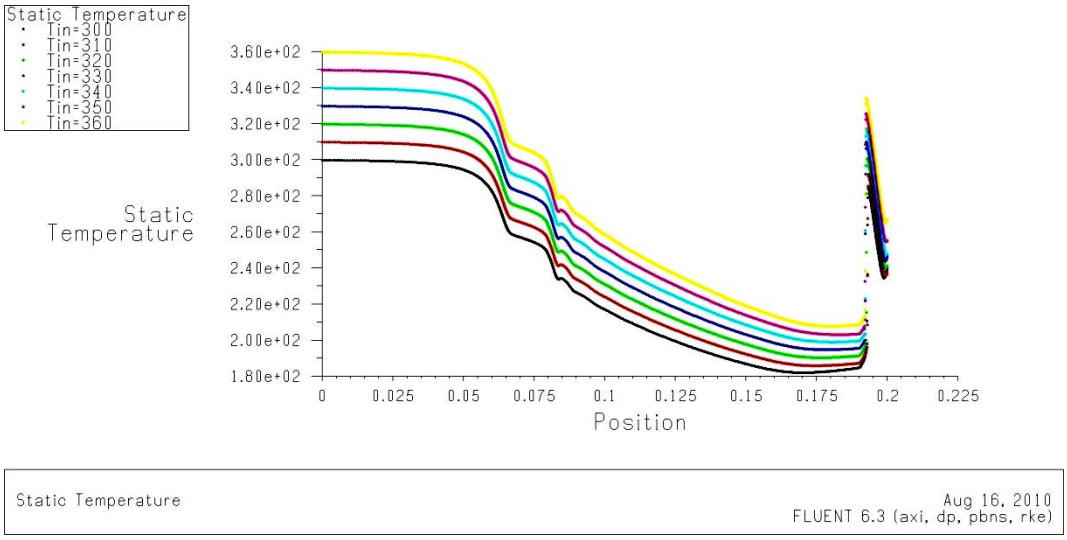

Figure (5. 21). Temperature profiles for different inlet temperature

Figure (5.19) shows that by increasing the inlet temperature the air flow outlet velocity goes up, and this is due to the decreasing of the flow density. This is because based on the principle of mass conservation, the multiplication of flow density and velocity will remain constant, and it is independent on flow temperature. Finally, the nozzle outlet velocity for air single-phase flow and various inlet temperatures is shown in Figure (5.22). By increasing 20 percent of the inlet temperature, Figure (5.22) states the nozzle outlet velocity increases about 13 percent.

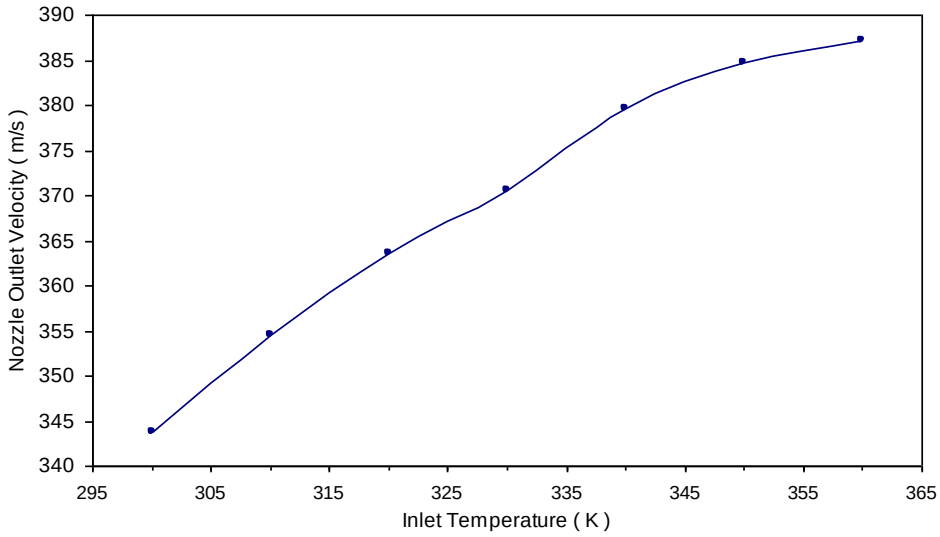

Figure (5. 22). Nozzle outlet velocity as a function of inlet temperature

Actually, in the shot-blasting system, which has been patented by Farrow, heated water mixed with sand particles is blasted with compressed air, and in this system the air flow is never heated directly via any heating sources. However, it can be quite rationally expected that heat transfer is done between water droplets, sand particles and

air flow. So more details of heating to the water droplets, and heat transfer to the air flow and sand particles is expressed in Chapter 6.

5.2 Air-Sand Two-Phase flow

Sand blasting is the operation of forcibly propelling a stream of sand particles against a surface under high pressure to smooth a rough surface, roughen a smooth surface, or remove surface contaminants. The air flow and sand particle interaction quality helps to transfer the momentum from compressed air to dense particles. Inlet pressure and temperature for air flow not only have an effect on flow characteristics, such as air momentum and energy, but also two phase flow interaction coefficient is influenced by inlet conditions.

This section is going to express the effects of various inlet conditions as well as the sand volume fraction on the nozzle air-sand two-phase flow performance. Depending on the secondary phase volume fraction, the *Eulerian* and *Discrete-phase* models have been applied for the simulating of the two-phase flow.

5.2.1 The Eulerian model for simulation of air-sand two-phase flow

The *Eulerian* model is suitable for granular flows on pneumatic transport, so it might be good for the simulating of sand particles blasting through the nozzle. As in the *FLUENT* user-guide mentioned, in this case, the volume fraction of sand particles must be more than 10-12%; otherwise, the *Discrete Phase* model will be applicable.

This section is going to simulate the air-sand two phase flow on various volume fractions, 10% and more, and different inlet pressure. The flow of sand particles throughout the Nozzle is analyzed, and average and maximum particles velocity are compared for different inlet air pressure.

5.2.1.1 The effect of Nozzle inlet pressure on air-sand two-phase flow

The pressure difference between the inlet and the exit of the nozzle blasts the sand particles through the nozzle. In the sand-blasting machines the nozzle exhaust pressure is the ambient pressure and the pressure difference is due to the increase of the inlet pressure. Low velocity and high pressure air flow enters into the nozzle and the air velocity increases in the converging section of the nozzle. However, as the single phase

flow depends on the inlet pressure, the air velocity is expected to increase or decrease in the diverging section of the nozzle. On the other hand, sand particles enter from the hose to the nozzle with low kinetic energy but due to the air flow and sand particles interaction forces, the sand particles have got the higher speed in the exhaust of the nozzle. According to the principle of momentum conservation, by increasing the particles velocity, the air momentum is expected to abate. The abovementioned phenomenon is illustrated by the following simulation results of the air-sand two-phase flow through the nozzle.

In this section, various inlet pressures from 0.5 atm to 3 atm have been exerted to the air flow.

Static pressure profiles for the air-sand mixture flow and various inlet pressures have been shown in Figure (5.23). Very smooth curves start from different inlet pressure and are ended in the same exit pressure that is zero atmosphere.

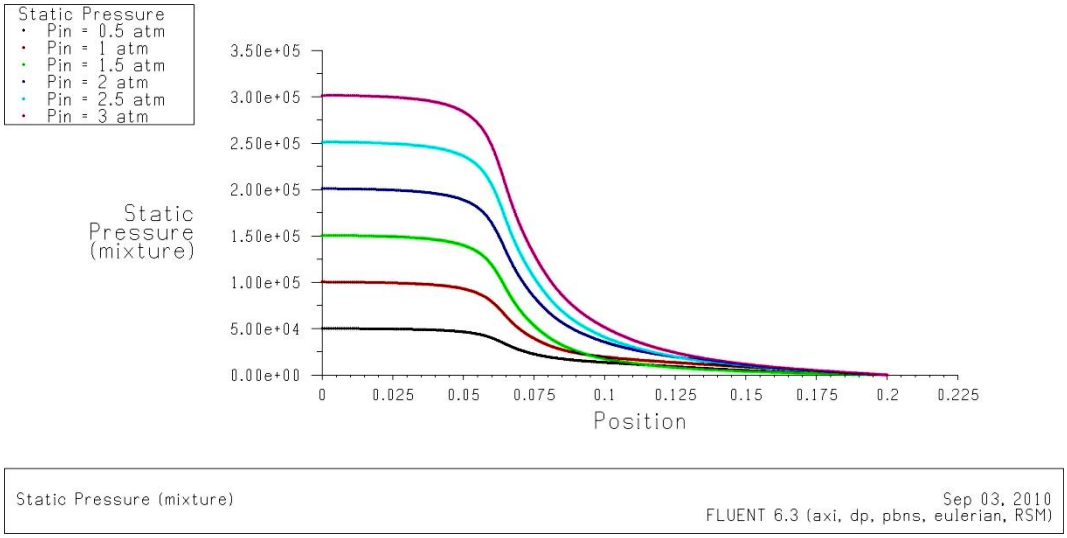

Figure (5. 23). Static pressure profiles for different inlet pressure in air-sand two-phase flow

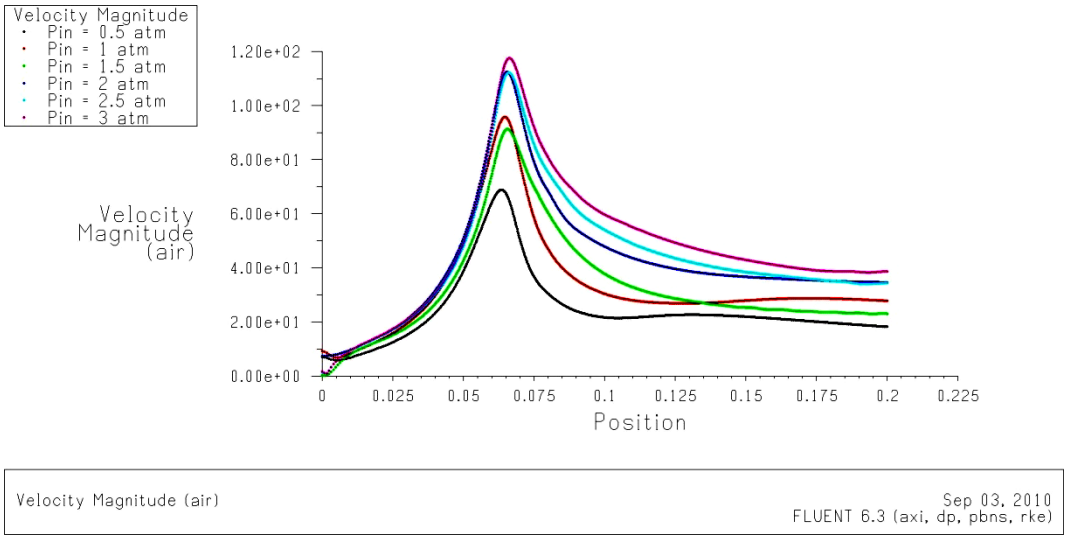

Figure (5. 24). Air velocity profiles for different inlet pressure in air-sand two-phase flow

Figure (5.24) shows the air velocity magnitude profiles for different inlet pressure. All velocity profiles rise until the throat and then decrease in the diverging section of the nozzle. Regarding the pressure profiles, shown in Figure (5.23), it was expected that velocity profiles have to increase in the diverging section of the nozzle as well as the converging section. However, Figure (5.24) shows the converse behaviour, and this is due to the sand particles with air flow through the nozzle. Definitely, sand particles absorb some kinetic energy of the air flow, and momentum transferring from the air flow to the sand particles, increases the sand particles speed. The sand particles profiles shown in Figure (5.25) confirm the above statement. On the other hand, Figure (5.24) shows the air maximum velocity, which is obtained for the inlet pressure of 3 atm, is about 120 m/s and it means about three times less than the sound velocity. Therefore, as Figures (5.23) and (5.24) show, all the profiles are very smooth and there is not any shock wave through the nozzle.

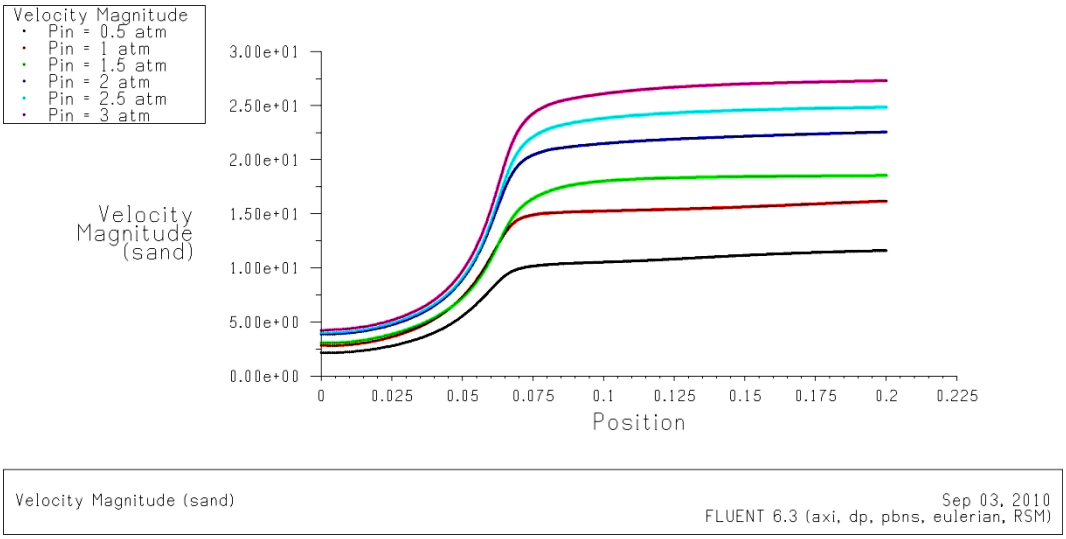

Figure (5. 25). Sand particles velocity profiles for different inlet pressure in air-sand two-phase flow

The simulation results of the sand particles velocity for various air inlet pressures are shown in Figure (5.25). Sand particles with low velocity enter into the nozzle and with increasing air flow velocity in the converging section of the nozzle, as Figure (5.25) shows their speed sharply goes up. Then the velocity gradients of the sand particles through the nozzle are declined where the air flow velocity, as shown in Figure (5.24), decreases.

The Mach number profiles for the air flow in various inlet pressures are shown in Figure (5.26). Similar to the velocity distribution through the Nozzle, the Mach number is increased in the converging part of the nozzle and then descended in the diverging section.

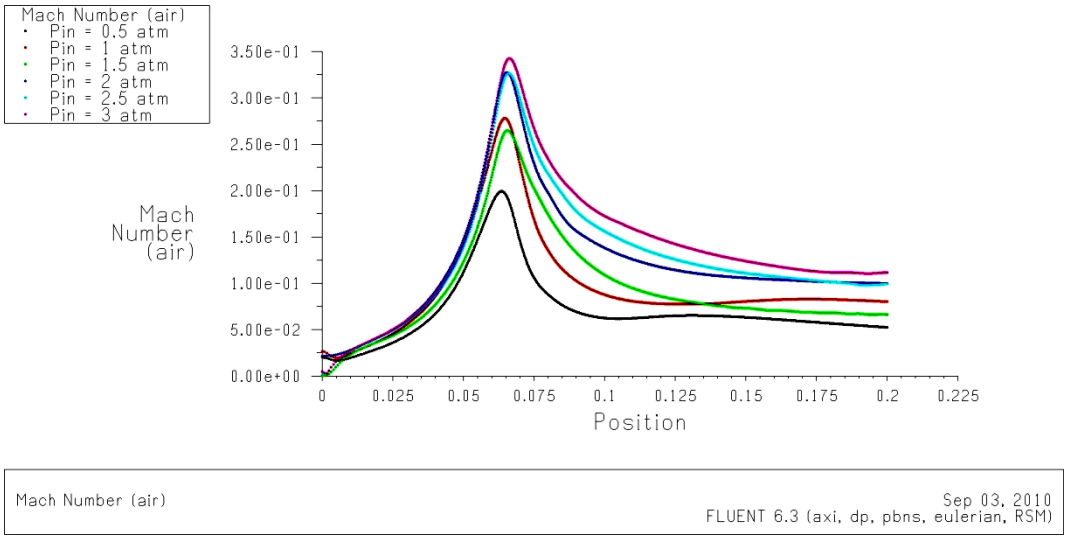

Figure (5. 26). Air flow Mach number profiles for different inlet pressure in air-sand two-phase flow

As Figure (5.26) shows, the maximum Mach number in the air-sand two-phase flow is obtained in the nozzle's throat and for the inlet pressure of 3 atm. This maximum Mach number is significantly less than 1, it means the flow inside the nozzle should be subsonic; however, as Figure (5.8) shows, in the same inlet conditions the Mach number for the air single phase flow through the nozzle is more than 1 and the air flow is supersonic. A comparison between the air single-phase flow and the air-sand two-phase flow has been illustrated in Figures (5.27) and (5.28).

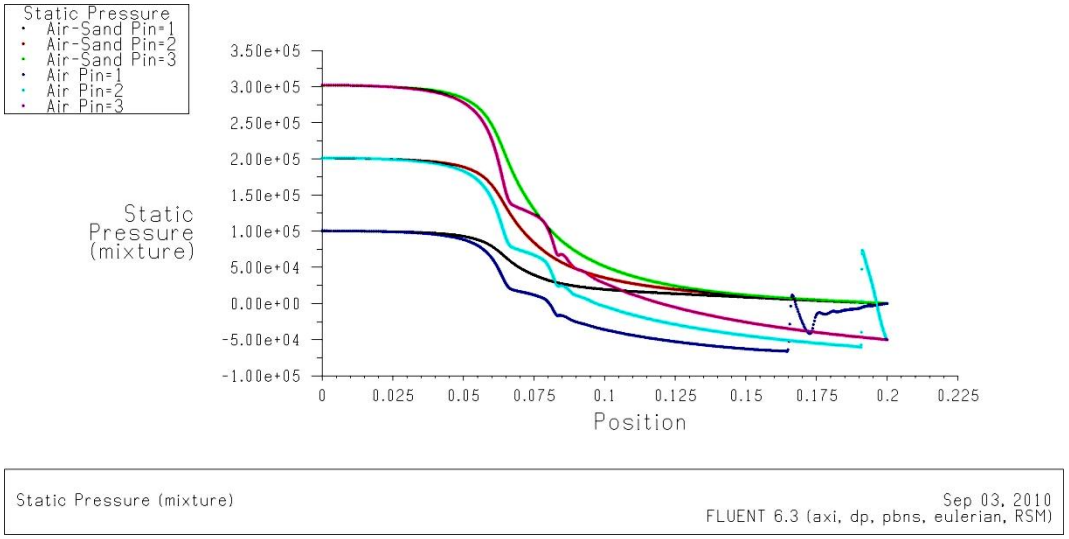

Figure (5. 27). Static pressure profiles comparison between air single-phase and air-sand two-phase flow for different inlet pressure

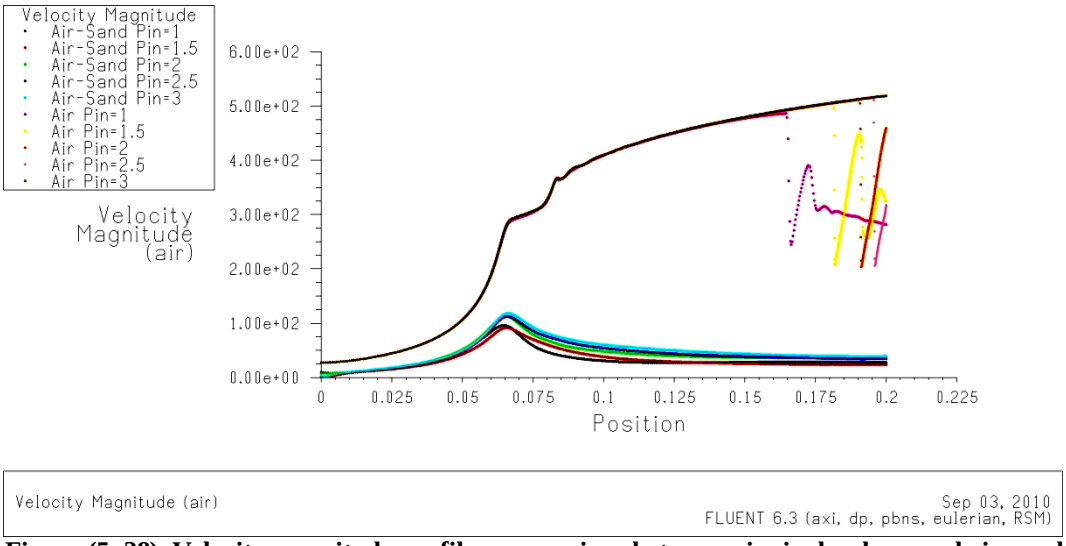

Figure (5. 28). Velocity magnitude profiles comparison between air single-phase and air-sand two-phase flow for different inlet pressure

Figure (5.27) as well as Figure (5.28) shows by adding the sand particles to the nozzle's air flow, the oscillation of static pressure or velocity profiles due to the shock wave, are vanished. As Figure (5.28) shows the main reason for this event is the decreasing of the flow velocity by inserting sand particles, and definitely this is due to the increasing of flow inertia.

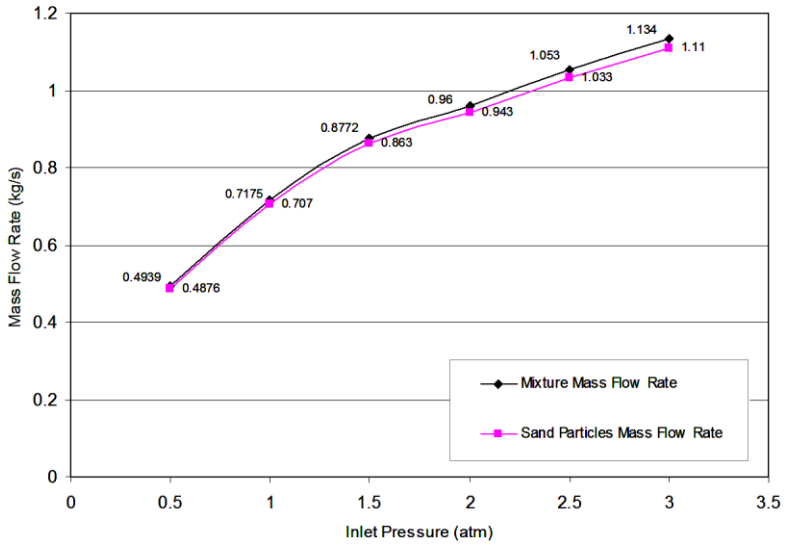

Figure (5. 29). Nozzle mass flow rate of mixture, and sand particles as a function of inlet pressure

In Section 5.1.3 and table (5.1), the dependency of the nozzle mass flow rate on the inlet pressure has been discussed. For the air-sand two-phase flow, Figure (5.29) shows the mixture and sand particles' mass flow rates as a function of inlet pressure. The difference between the mixture and sand mass flow rates is the air mass flow rate. In the

same way as the air single-phase flow, Figure (5.29) shows that air mass flow rate rises by increasing the inlet pressure. On the other hand, as shown, the simulation results in Figure (5.29) have been calculated in the same secondary phase (sand particles) volume fraction, $\left(\dot{v}_{sand}/\dot{v}_{air}\right)=\frac{\left(\dot{m}_{sand}/\rho_{sand}\right)}{\left(\dot{m}_{air}/\rho_{air}\right)}=0.1$, so the sand particles mass flow rates are raised by increasing the air inlet pressure (and hence air mass flow rate). In the above-mentioned equation for the secondary phase volume fraction, obviously the sand density is constant, and the nozzle exhaust air density, ρ_{air}, by attention to the Figure (5.23) and almost the same exhaust static pressure for various inlet pressure, is nearly constant.

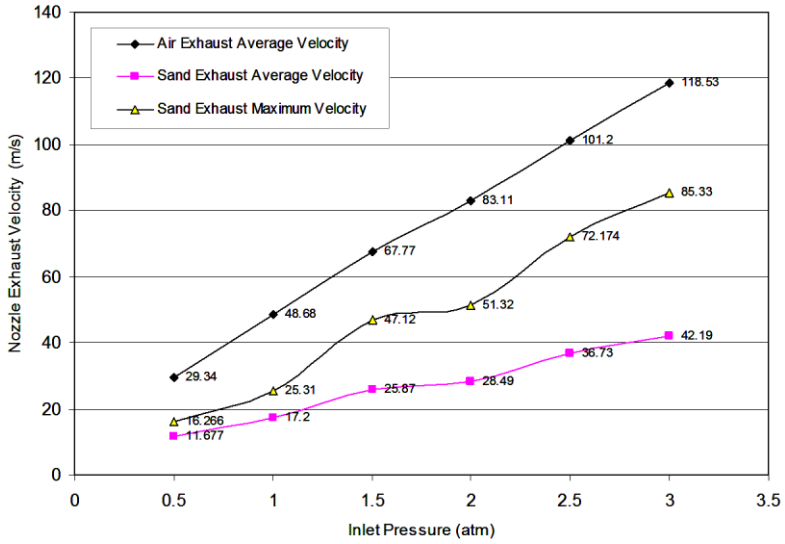

Figure (5. 30). Nozzle exhaust velocity magnitude as a function of inlet pressure

The nozzle exhaust velocity magnitude as a function of the inlet pressure for the air flow and sand particles are shown in Figure (5.30). Indubitably, the sand particles average and maximum exhaust velocity are very important parameters on shot-blasting systems. These values for the air-sand two-phase flow are calculated by different inlet pressure and just for constant inlet temperature at 300 K. In Chapter 6, the sand velocity of the air-sand-water three-phase flow is compared with the abovementioned values, and the effect of water droplets is considered.

5.2.1.2 The effect of sand volume fraction on the Nozzle performance for air-sand two-phase flow

The volume fraction of sand particles, as the abrasive media in a shot-blasting system, has a massive role in the cleaning performance of the system. On the one hand,

by increasing the sand particles' volume fraction the abrasive media quantity increases, but on the other hand, by the same inlet air pressure (constant energy consumption) the abrasive media exhaust velocity decreases. Therefore, in the operation of a sand-blasting machine, not only the sand particles consumption should be considered but also the exhaust abrasive quality has to be contemplated.

The secondary phase volume fraction in reality is about ten times less than the *Eulerian* model lower limit, so the study of the sand volume fraction's effects on a sand blasting machine will be applicable by using the *Discrete-phase* model. Here, just the air and sand particles velocity profiles according to the simulation of the air-sand two-phase flow with the various sand particles volume fractions are presented.

The air flow velocity distribution through the nozzle's centre line has been shown in Figure (5.31). For this simulation, a different sand volume fraction from 10 percent to 16 percent has been applied for the air-sand two-phase flow with air inlet pressure of 2 atm.

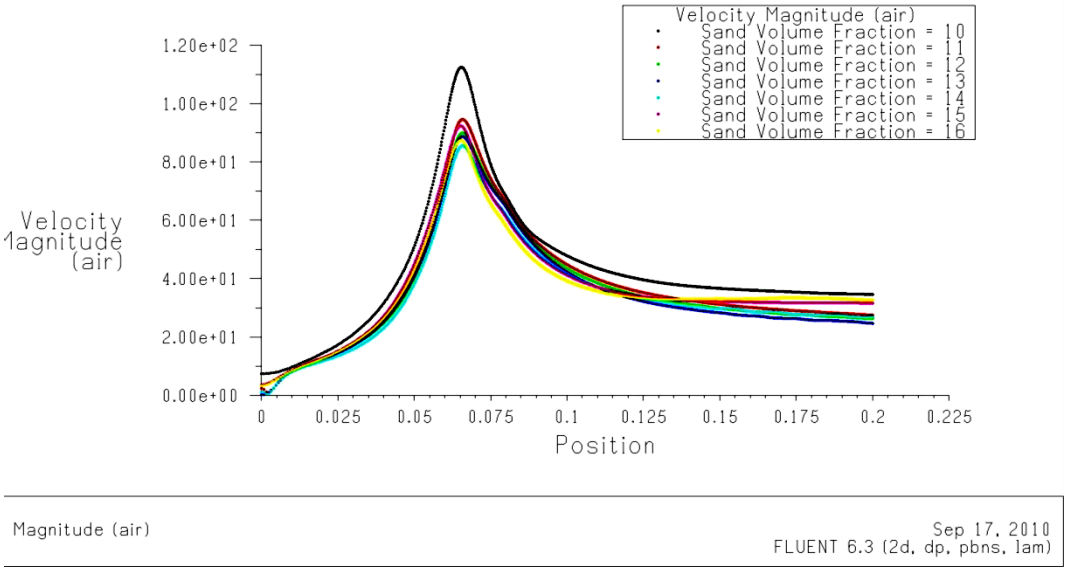

Figure (5. 31). Air flow velocity profiles for different sand volume fraction in air-sand two-phase flow

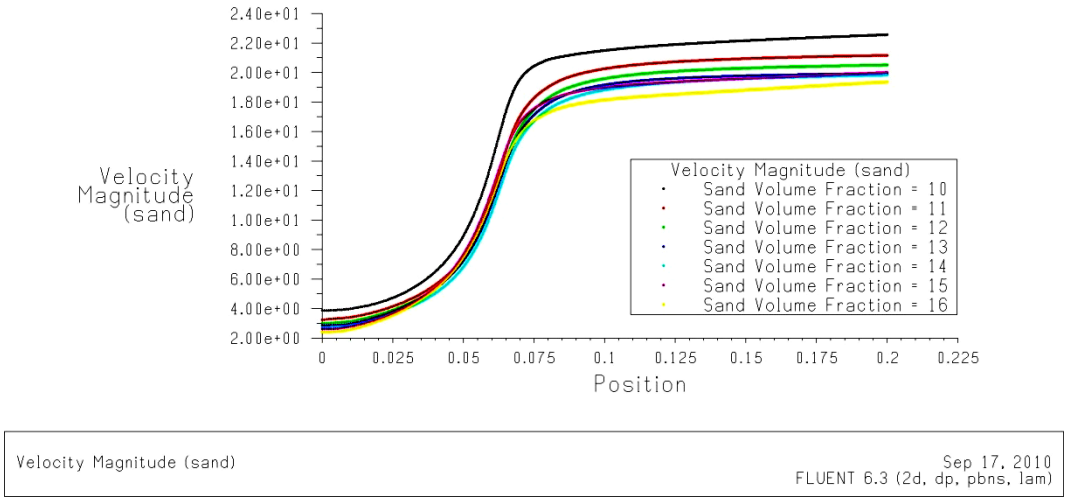

Figure (5. 32). Sand particles velocity profiles for different sand volume fraction in air-sand two-phase flow

For similar conditions, Figure (5.32) shows the sand particles velocity distribution through the nozzle's centre line. This figure confirms that by increasing the sand particles volume fraction the velocity magnitude decreases.

More effects of the secondary phase volume fraction on the performance of the nozzle in a sand-blasting machine is discussed in the following section of the *Discrete Phase* model.

5.2.2 Discrete Phase model for simulation of air-sand two-phase flow

In addition to solving transport equations for the continuous phase, in the FLUENT software package, the sand particles are allowed to simulate in a *Lagrangian* frame of reference. FLUENT computes the trajectories of these particles as well as the heat transfer to or from them. On the other hand, the coupling between the phases in the multi-phase flow and its impact on both the discrete phase trajectories and the air flow can be included.

By defining the initial position, velocity, size, and temperature of particles, the discrete phase is added in the simulating model. The trajectory and heat transfer calculations are based on the force balance on the particle and on the convective and or radiative heat transfer from the particle, using the local continuous phase conditions as the particle moves through the flow.

In this section, the air-sand two phase flow through the nozzle with various sand mass flow ratios, from 0.005 kg/s to 0.03 kg/s, and different inlet pressure are

computed. The sand particles tracks inside the nozzle, the air flow velocity contours for both air-sand two-phase flow and air single-phase flow and the air velocity profiles in the exhaust of the Nozzle are discussed.

The velocity counters of the air single-phase flow through the nozzle have been shown in Figure (5.33 a). For the same air inlet pressure, Figure (5.34 a) shows the air-sand two-phase flow velocity counters. In this simulation the sand particles mass flow rate is 0.01 kg/s. The comparison of these two figures illustrates the effects of the sand particles on the velocity distribution through the nozzle. As Figure (5.33 b) shows, due to the shock wave, the air flow velocity suddenly drops just before the exhaust of the nozzle, whereas, as Figure (5.34 b) shows the sand particles alleviate the shock wave effects on the nozzle.

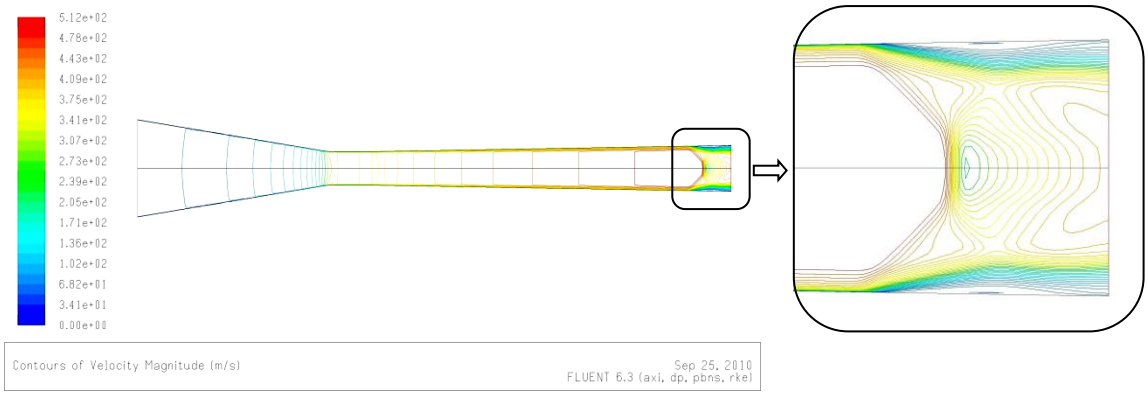

Figure (5. 33). Contours of velocity for air flow (p_{in} = 2 atm)

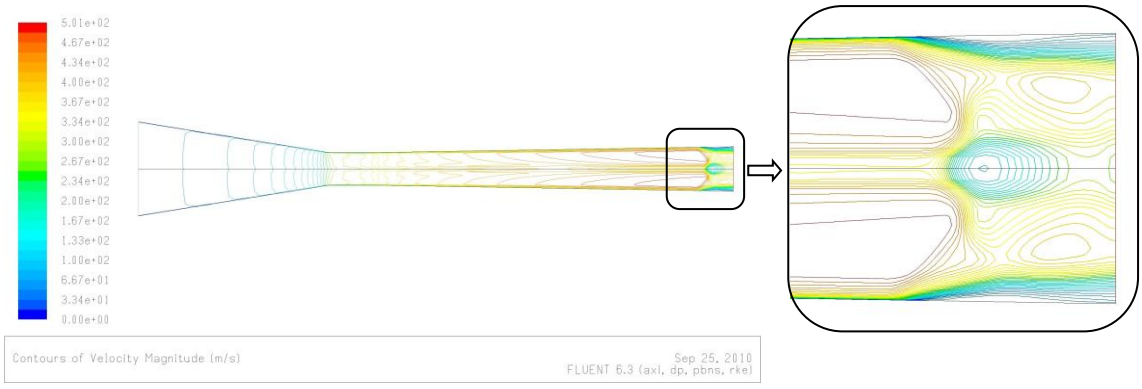

Figure (5. 34). Contours of velocity for air-sand two-phase flow (p_{in} = 2 atm)

The nozzle exhaust air flow velocity vectors are shown in Figures (5.35) and (5.36). Figure (5.35) shows the exhaust velocity has almost uniform distribution along the nozzle axis, whereas, due to the sand particles, this profile in Figure (5.36) has been changed. On the other hand, the maximum air exhaust velocity has been affected by the sand particles and decreases from 511.8 m/s for the air single-phase flow to 500.8 m/s

for the air-sand two-phase flow.

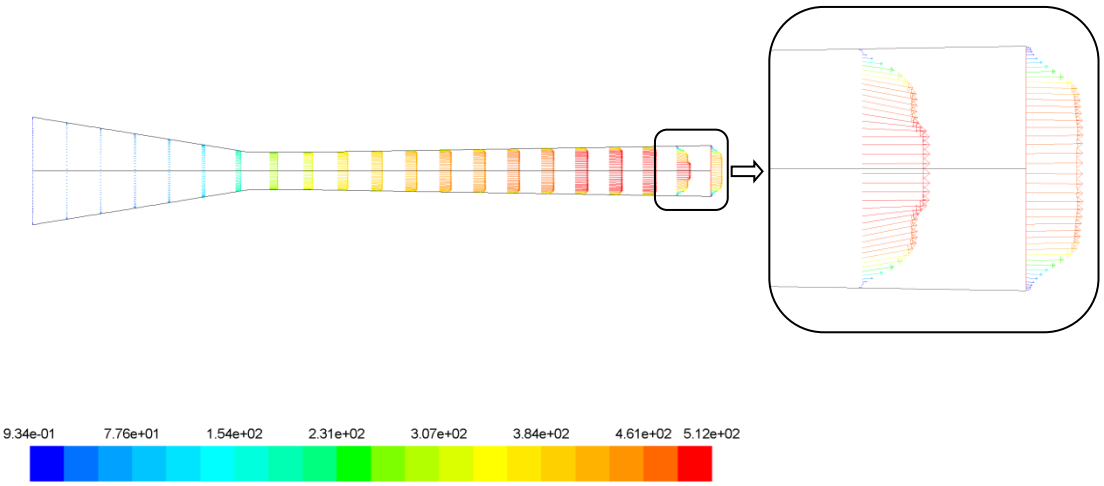

Figure (5. 35). Nozzle exhaust air velocity vectors for air single-phase flow

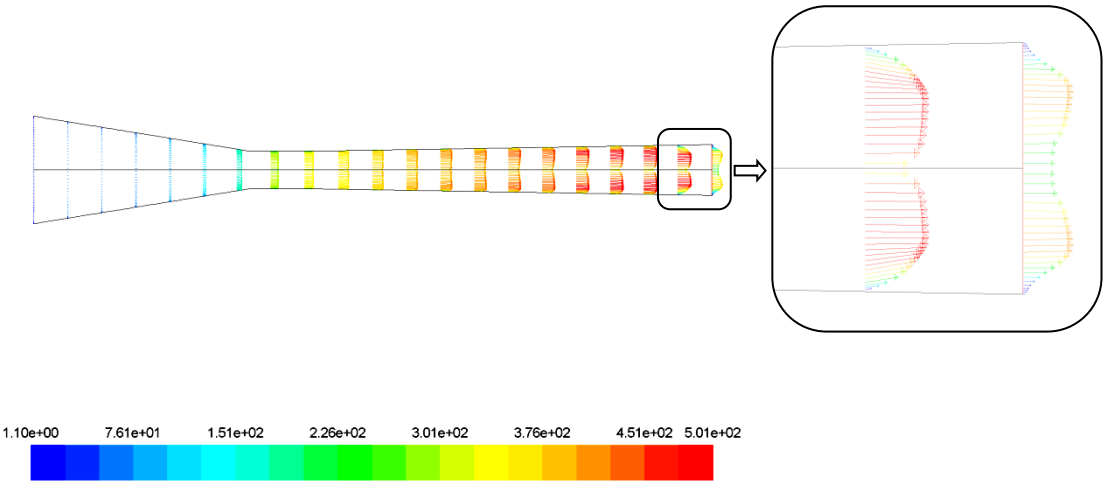

Figure (5. 36). Nozzle exhaust air velocity vectors for air-sand two-phase flow

The sand particles' tracks and velocity magnitudes as a function of residence time are shown in Figures (5.37) to (5.44). All tracks have been coloured by the velocity magnitude. In this simulation, there are 44 tracks on the nozzle entrance. The first track which is started from the nozzle entrance wall is shown in Figure (5.37). In Figure (5.38) the velocity magnitude of the first track is plotted as a function of particle residence time. The simulation result shows that the particles' entrance and exhaust velocity on the first track are 1.64 m/s and 131.03 m/s, respectively. On the other hand the particle residence time inside the nozzle is 10.2 ms.

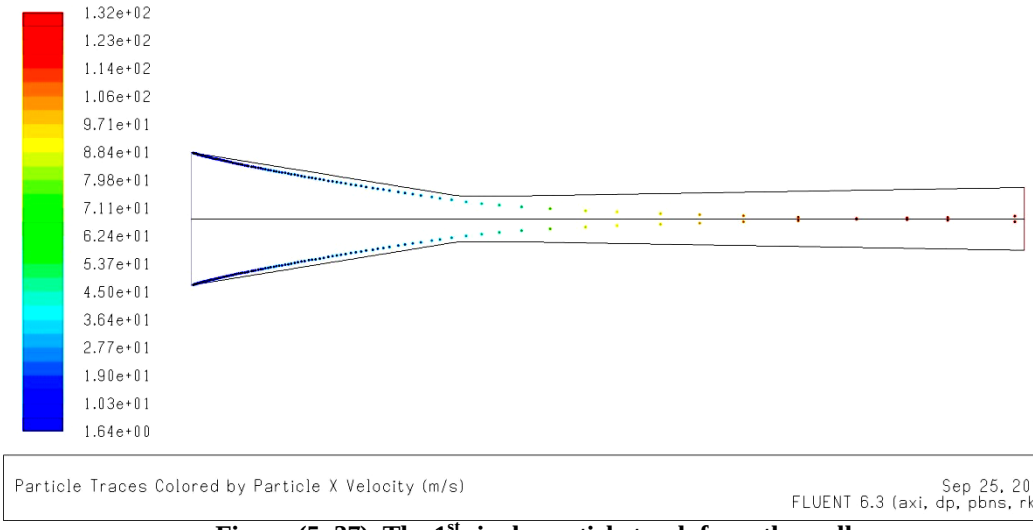

Figure (5. 37). The 1st single particle track from the wall

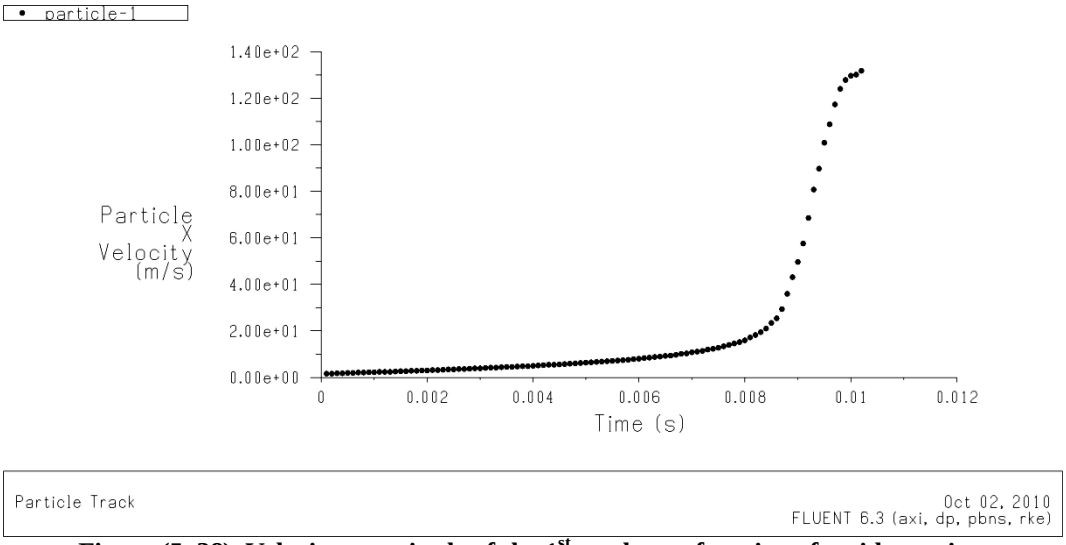

Figure (5. 38). Velocity magnitude of the 1st track as a function of residence time

Figure (5.39) shows the tenth track of sand particles from the nozzle entrance wall. The particles are assumed to enter the nozzle in flow direction i.e. axis-symmetric and after a short distance traverse through the nozzle they hit to the wall. As Figure (5.40) shows, the reflected particles start to move through the nozzle by the minimum velocity of 1.65 m/s; however they enter into the nozzle by a higher velocity. In this case the maximum particle velocity in the exhaust of the nozzle is 129 m/s, and the particle residence time is equal to 6.9 ms.

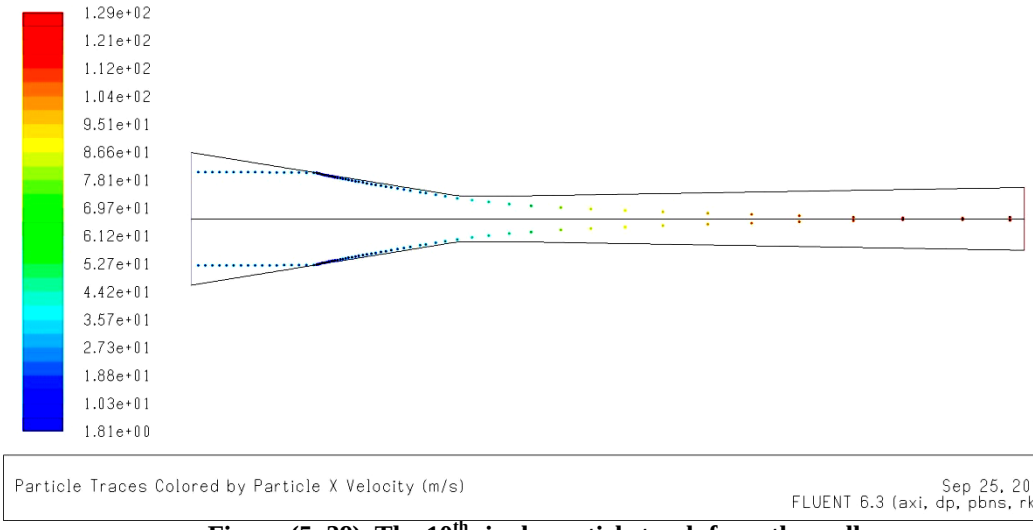

Figure (5. 39). The 10th single particle track from the wall

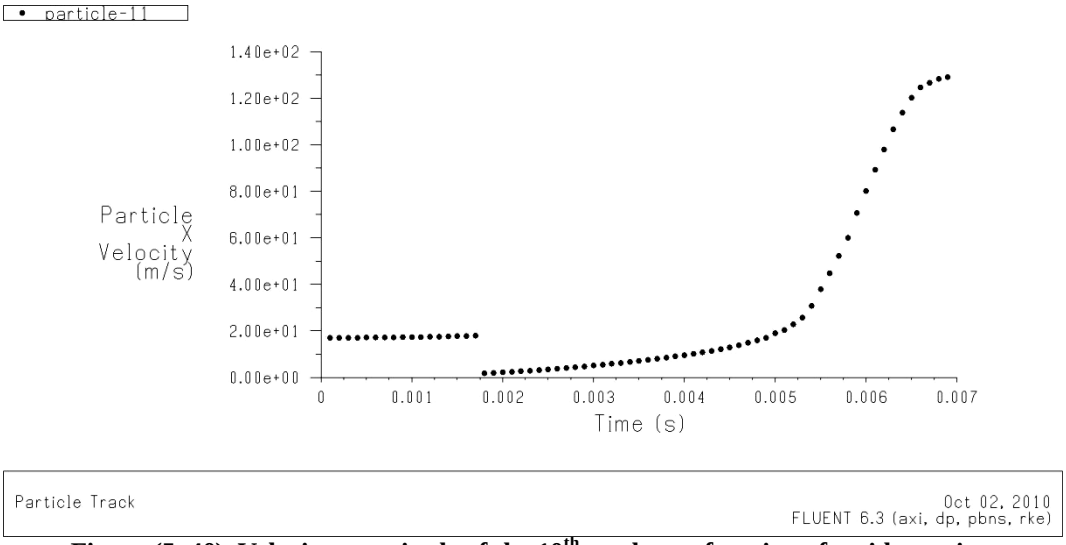

Figure (5. 40). Velocity magnitude of the 10th track as a function of residence time

Some other tracks, such as the twentieth track as Figure (5.41) shows, never contact the nozzle wall, so particles which traverse by these tracks have lower residence time than the abovementioned tracks, however the maximum velocity of the particles depends on the air flow velocity profiles and the particles' concentration. For example the velocity magnitude and residence time of the particles on the 20th track shown in Figure (5.42) are 140.7 m/s and 4.6 ms, which in comparison with the 15th track has not only lower residence time but also has less velocity.

All 44 sand particles' tracks inside the nozzle and the velocity magnitude of each track as a function of residence time are shown in Figures (5.43) and (5.44).

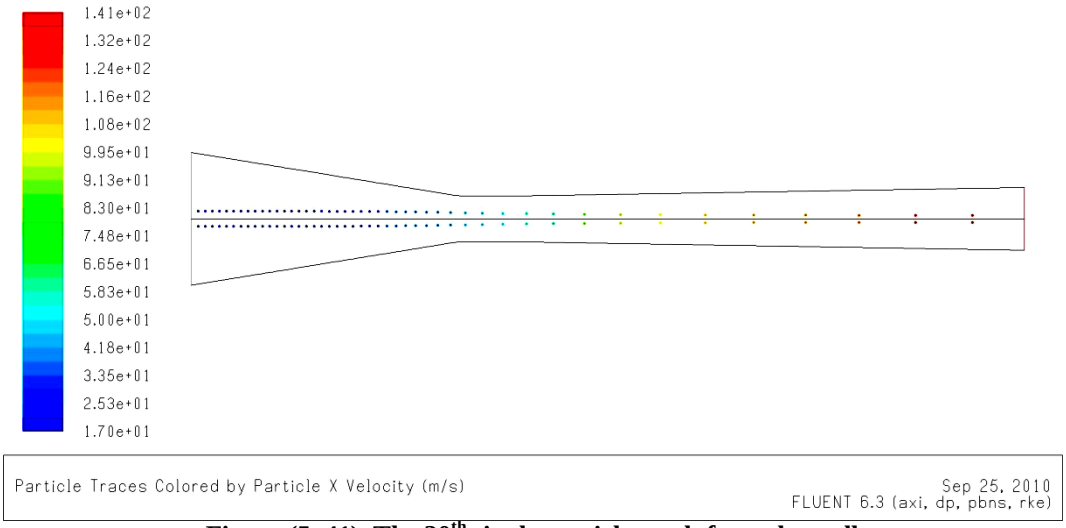

Figure (5. 41). The 20th single particle track from the wall

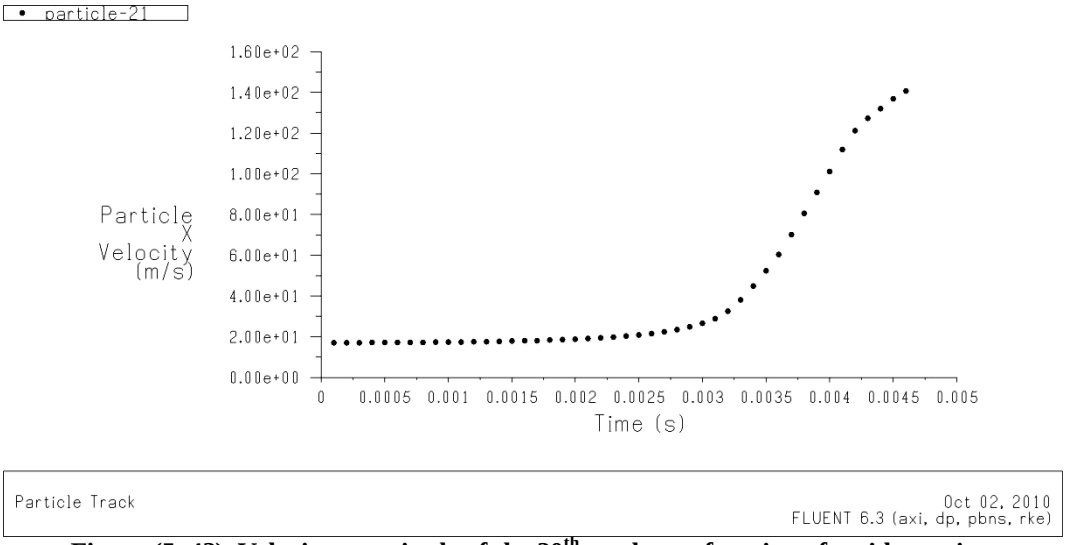

Figure (5. 42). Velocity magnitude of the 20th track as a function of residence time

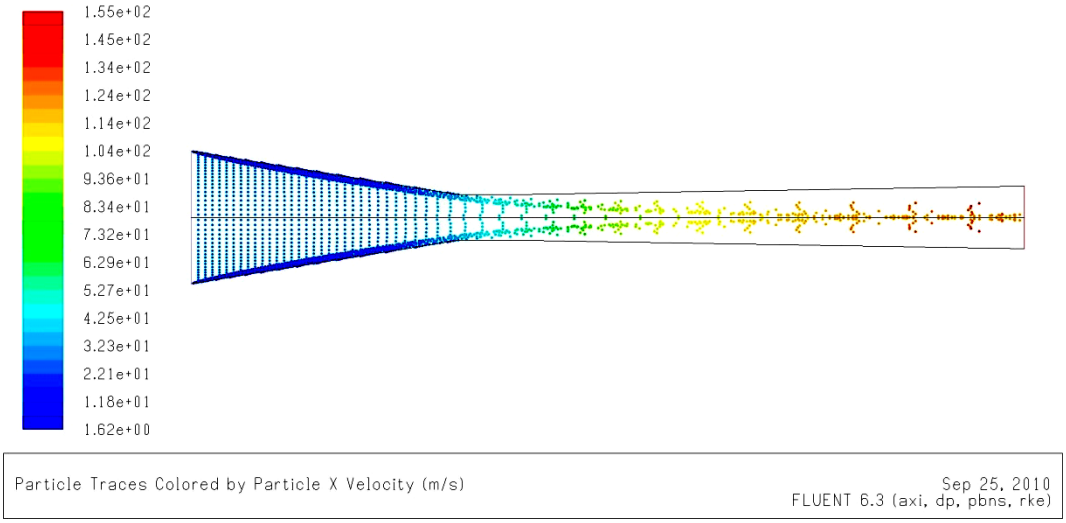

Figure (5. 43). All particle tracks inside the Nozzle

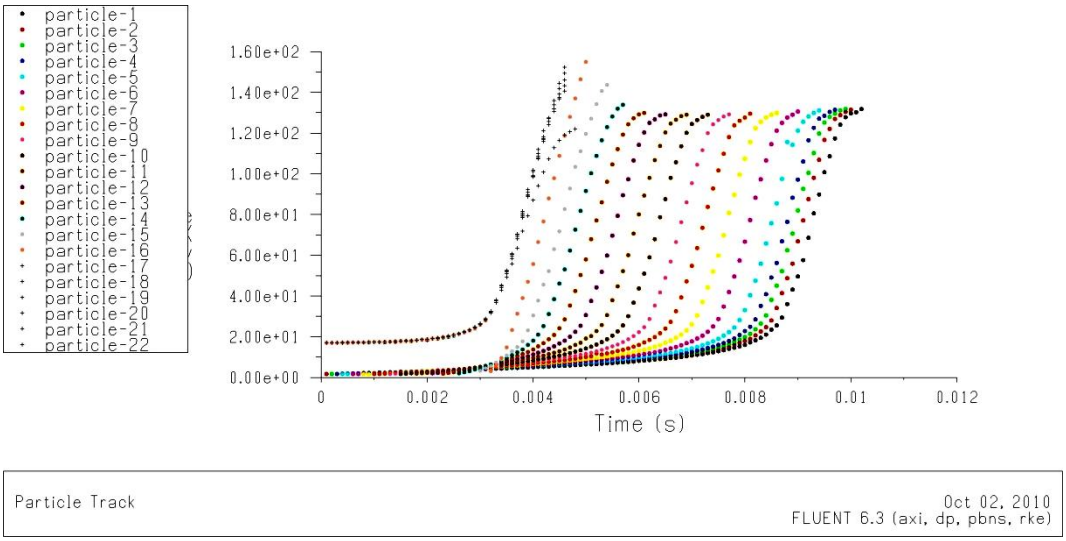

Figure (5. 44). Velocity magnitude of All tracks as a function of residence time

Obviously, the sand particles' mass flow rate has significant effects on the nozzle two-phase flow characteristics. For example, as Figure (5.45) shows, by increasing the mass flow rate, from 0.005 kg/s to 0.03 kg/s the particles first track exhaust velocity decreases from about 141 m/s to 114 m/s. In this case, the particles residence time as shown in Figure (5.46) increases from 10 ms to 10.6 ms.

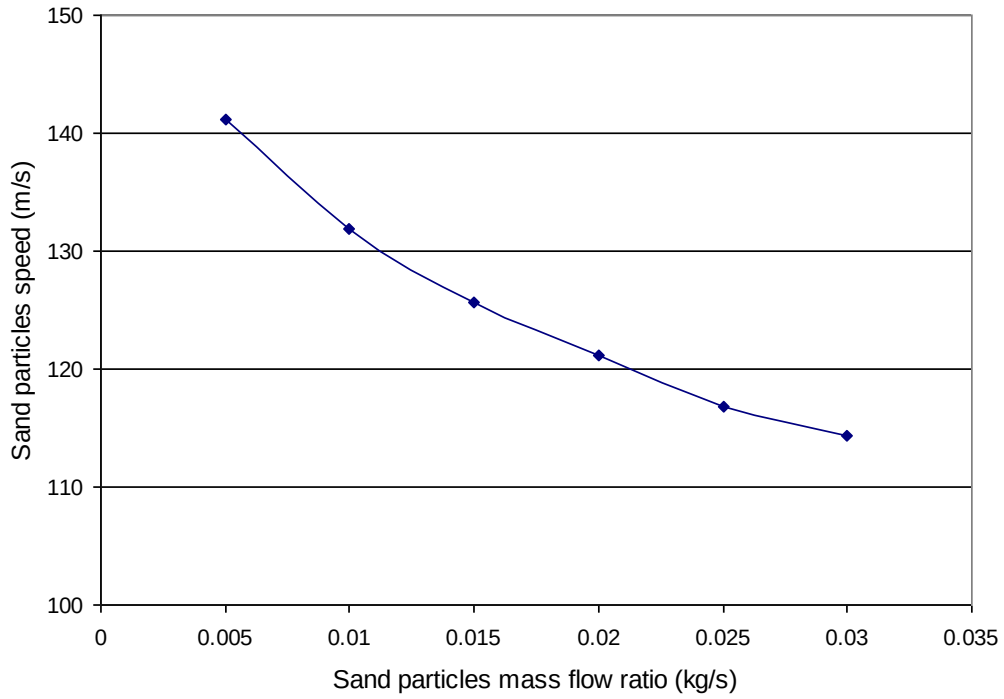

Figure (5. 45). Sand particles velocity as a function of mass flow rate

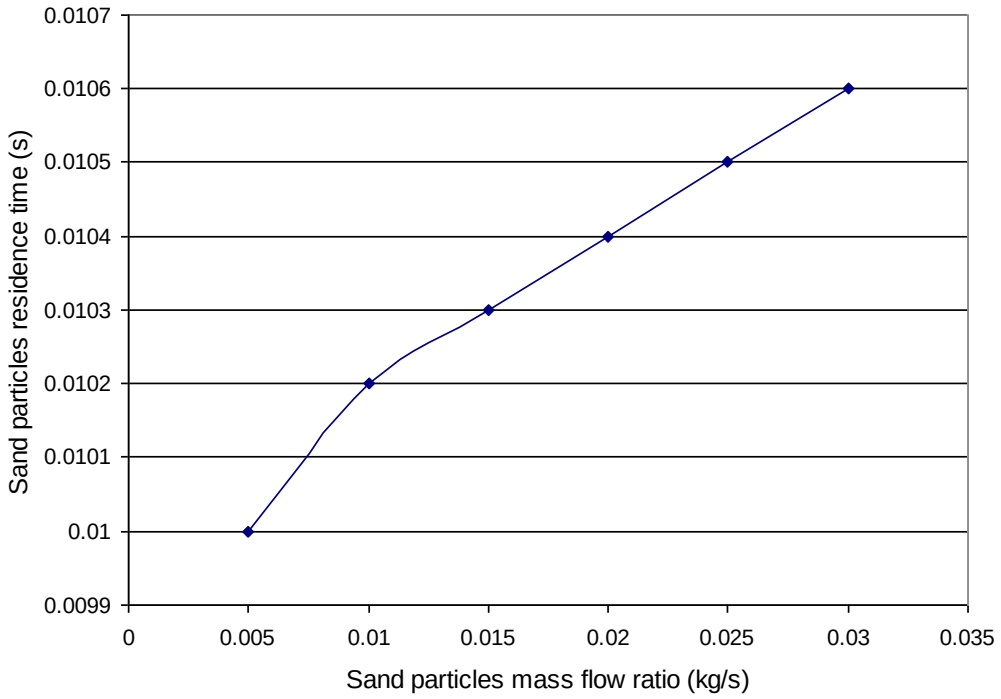

Figure (5. 46). Sand particles residence time as a function of mass flow rate

5.2.2.1 The effects of inlet pressure on Nozzle of air-sand two-phase flow

The air inlet pressure directly effects to the air flow momentum and normally by increasing inlet pressure, the air flow velocity increases. As already mentioned in Section 5.1.2 , by increasing the air inlet pressure, the shock wave moves through the exit of the nozzle. In the same way as the air single-phase flow, this event happened in the air-sand two-phase flow; however, by adding the sand particles, the shape and vigour of the shock wave is slightly changed.

In this section, for the various air inlet pressure and sand mass flow rate of 0.02 kg/s, the air-sand two-phase flow is simulated. The air velocity counters/vectors for the air single phase flow and the air-sand two-phase flow are compared in Figures (5.47) to (5.50). The air inlet pressure for both simulations is 0.5 atm, and for the air-sand two-phase flow the sand particles' diameter is assumed as 0.0002 m. Due to the fact that the sand particles' concentration in and around the axis of the nozzle is more than other part and near to the wall, so in this area the air-sand momentum transfer occurs further than in other domains. The air flow velocity counters in Figure (5.47) confirm this event, and as this figure shows the air velocity profiles are changed in the mentioned area.

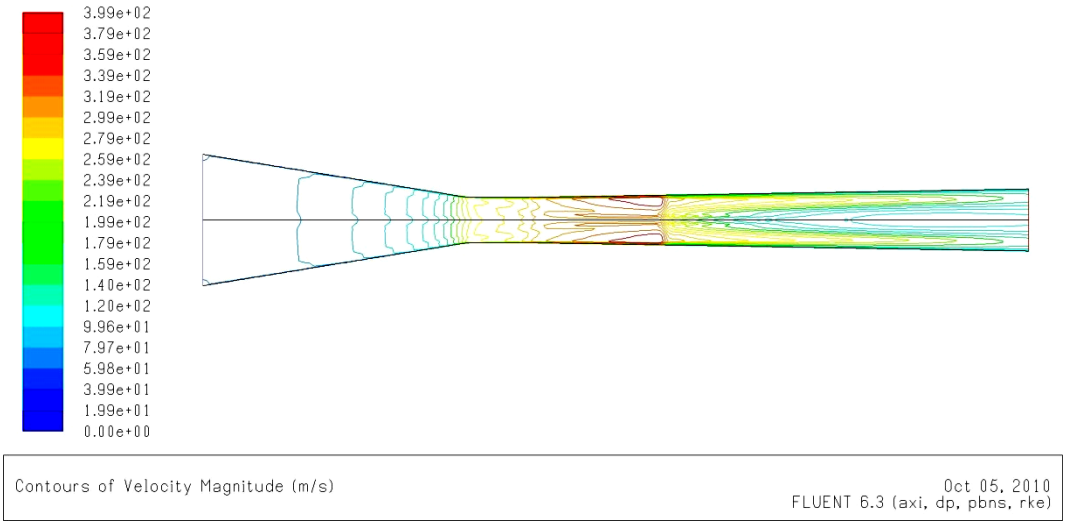

Figure (5. 47). Contours of velocity for air-sand two-phase flow (p_{in} = 0.5 atm)

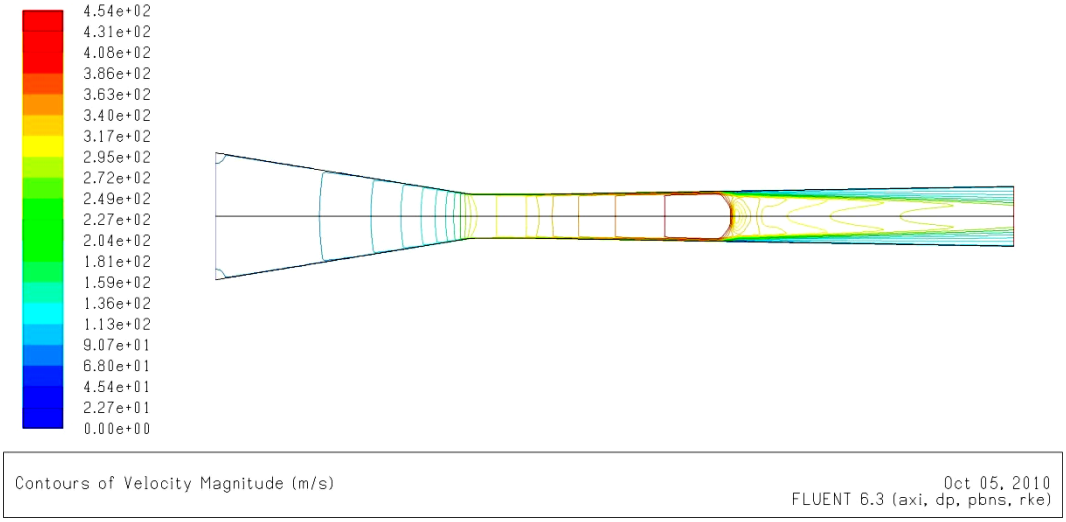

Figure (5. 48). Contours of velocity for air single-phase flow (p_{in} = 0.5 atm)

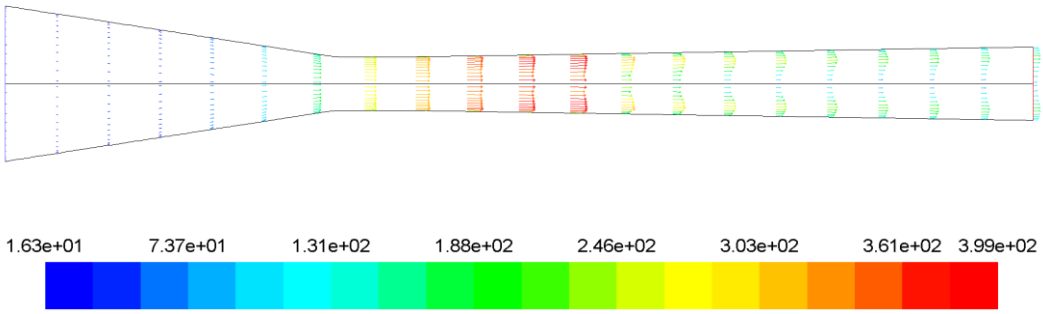

Figure (5. 49). Velocity vectors for air-sand two-phase flow (p_{in} = 0.5 atm)

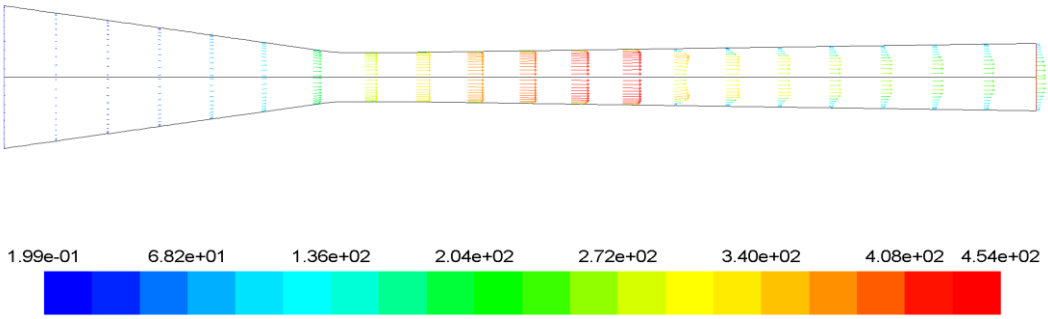

Figure (5. 50). Velocity vectors for air single-phase flow (p_{in} = 0.5 atm)

Figures (5.51) to (5.58) show the contours of velocity for the air-sand two-phase flow and the air single-phase flow in various air inlet pressures from 1 atm to 3 atm. A comparison of these figures confirms the moving out of the shock wave by increasing the air inlet pressure. On the other hand, a comparison of the air-sand two-phase flow with the air single-phase flow for each inlet pressure, shows the slight moving out of the shock wave by adding the sand particles to the air flow in the nozzle.

All velocity contours for the air-sand two-phase flow in the following figures show that the sand particles' concentration into the nozzle decreases by moving toward the wall from the axis of the nozzle.

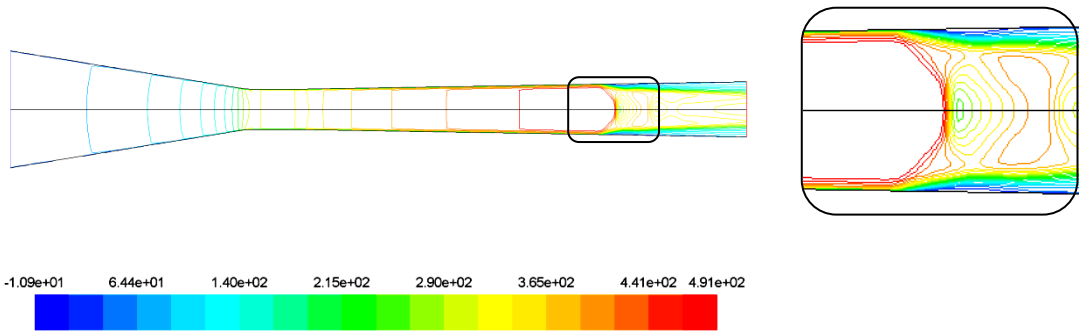

Figure (5. 51). Contours of velocity for air single-phase flow (pin = 1 atm)

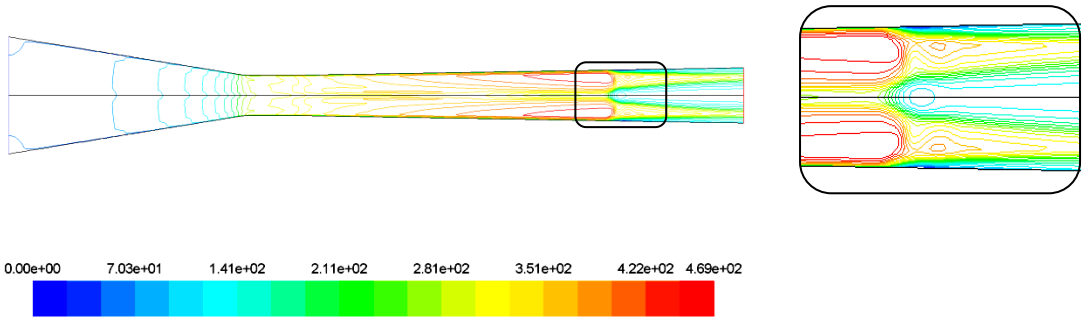

Figure (5. 52). Contours of velocity for air-sand two-phase flow (p_{in} = 1 atm)

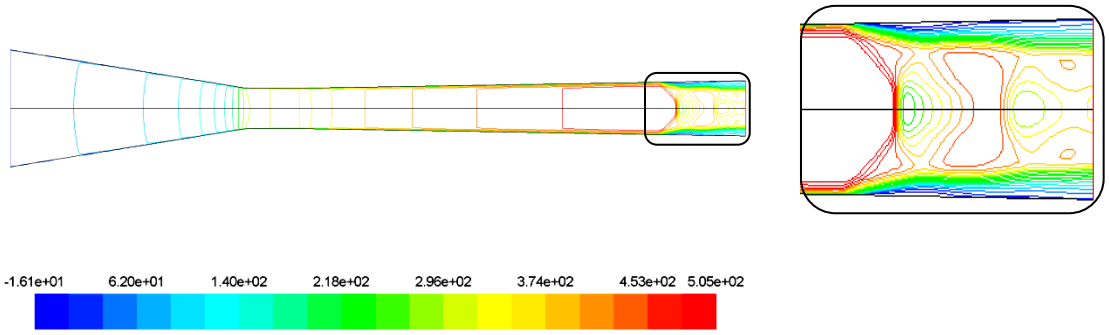

Figure (5. 53). Contours of velocity for air single-phase flow (p_{in} = 1.5 atm)

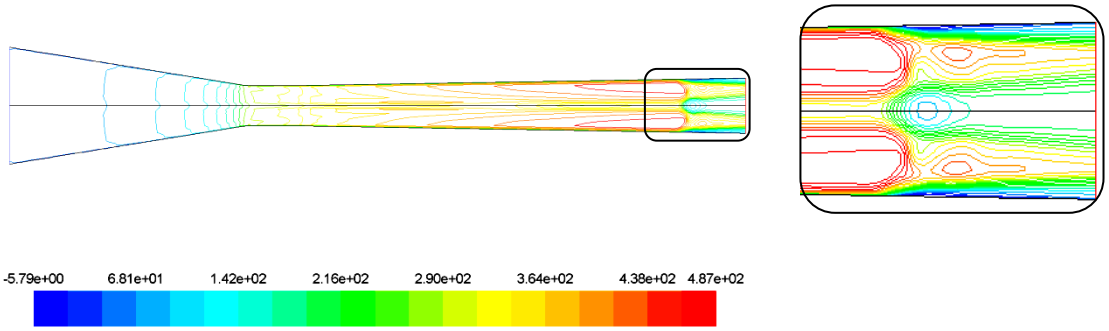

Figure (5. 54). Contours of velocity for air-sand two-phase flow (p_{in} = 1.5 atm)

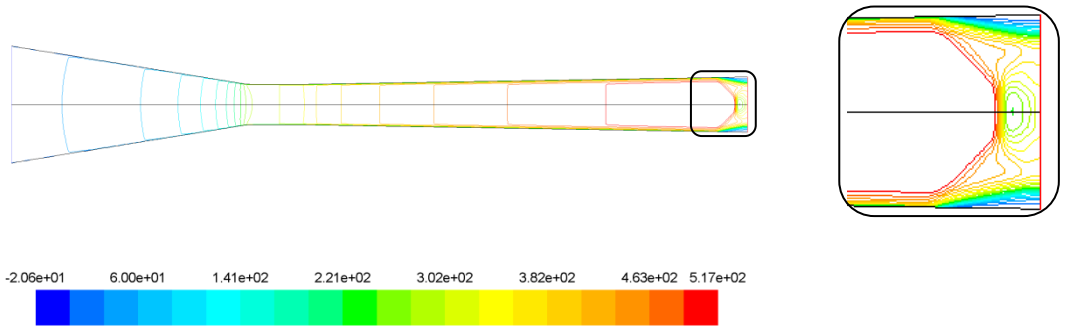

Figure (5. 55). Contours of velocity for air single-phase flow (p_{in} = 2.5 atm)

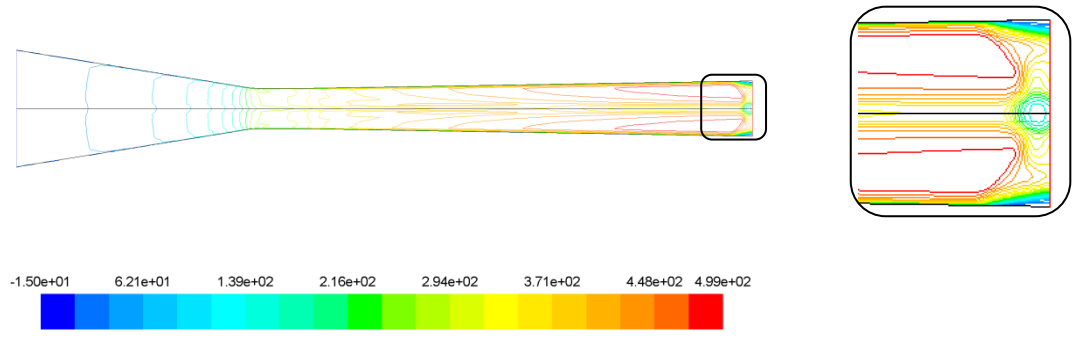

Figure (5. 56). Contours of velocity for air-sand two-phase flow (p_{in} = 2.5 atm)

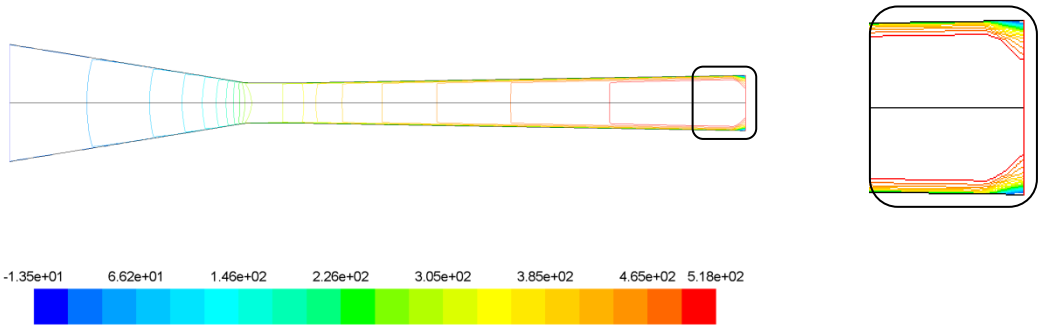

Figure (5. 57). Contours of velocity for air single-phase flow (p_{in} = 3 atm)

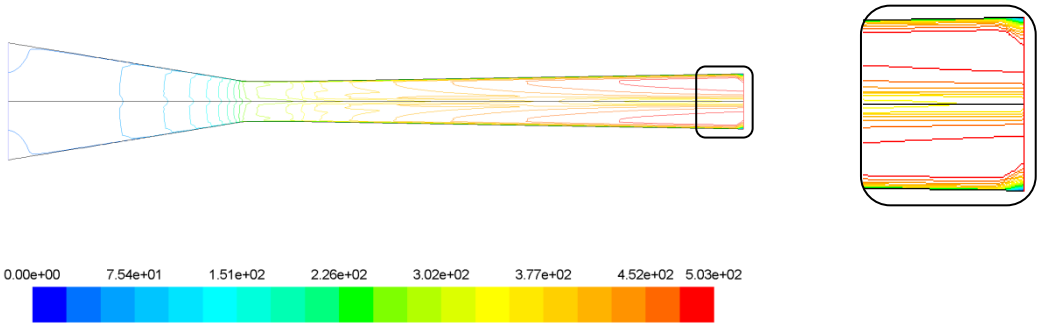

Figure (5. 58). Contours of velocity for air-sand two-phase flow (p_{in} = 3 atm)

The sand particles' exhaust velocity along the first track as a function of inlet pressure is shown in Figure (5.59). Also this figure shows the air mean velocity for the air-sand two-phase flow and the air single-phase flow. However, the velocity of the sand particles has a gentle slope; the air flow curve for the air-sand two-phase flow (red curve) has a variable slope. As Figures (5.55) and (5.57) show this is due to the shock wave event into the nozzle, whereas in Figure (5.55) the shock wave is happened just before exhaust of the Nozzle, in Figure (5.57) the shock wave has almost moved out from the nozzle. On the other hand, Figure (5.59) shows that the shock wave's location inside the nozzle has no significant effect on the velocity of the sand particles.

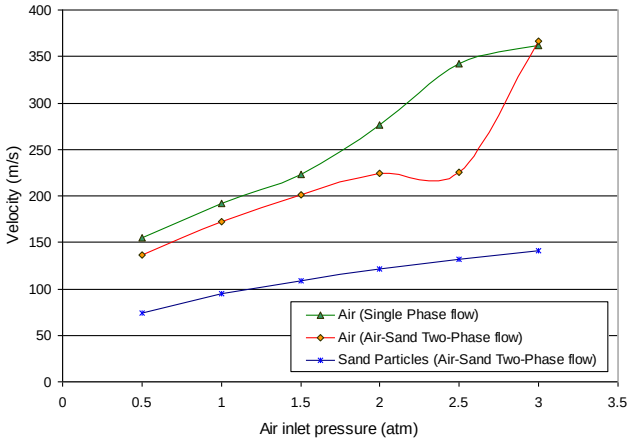

Figure (5. 59). Air flow and sand particles exhaust velocity as a function of air inlet pressure

In all above numerical simulation of the air single-phase flow and the air-sand two-phase flow, the inlet temperature was constant and equal to 300 K. The effect of the inlet temperature as well as the water droplet on the nozzle's performance is presented in Chapter 6, the results and discussion of the air-sand-water three-phase flow.

5.3 Summary and conclusions

In this chapter, air single-phase and air-sand two-phase nozzle flows were computed and discussed. Various turbulence models including the *Standard, RNG* and *Realizable* k-ε models, *Spalart-Allmaras* and *Reynolds Stress* turbulent models were examined for the air single-phase flow through the nozzle. The simulation results confirmed that the choice of the turbulence model has no significant effect on the single-phase flow distribution throughout the nozzle.

The significant effects on the Mach number distribution as well as temperature and velocity profiles throughout the nozzle were not observed by utilizing the constant inlet pressure in comparison with constant outlet pressure. Despite this, density and pressure distributions were considerably affected by constant inlet and constant outlet pressures.

In this chapter, the air-sand two-phase flow was simulated for various sand volume fractions and different inlet pressures by employing both the *Eulerian* and *Discrete-phase* models. The flows of sand particles throughout and in the exhaust of the nozzle were analyzed, and average and maximum particles velocity were compared for different inlet air pressure. A comparison between the air single-phase flow and the air-sand two-phase flow indicated that by adding the sand particles to the air flow, not only a significant difference for pressure and velocity distribution through the nozzle could instantaneously be observed but also the oscillation in the static pressure and velocity distributions due to the shock waves vanished.

Finally, utilizing the *Discrete Phase* model for the air-sand two phase flow through the nozzle showed that the sand particles alleviate the shock wave effects on the nozzle. Furthermore, this simulation clearly confirmed that there are considerable differences between the speed of particles which move without hitting the wall and the others which hit the wall in the converging section of the nozzle. The last and very important result is the effect of the shock wave on the sand particles' velocity. This study showed that the location of the shock wave inside the nozzle did not have a significant effect on the velocity of the sand particles.

CHAPTER 6

RESULTS AND DISCUSSION: PART II- AIR-SAND-WATER THREE-PHASE FLOW

Introduction

Most sand-blasting machines use water droplets as well as of sand particles which are propelled by a high inlet pressure air flow through the nozzle. The simulation results of the air single-phase flow and the air-sand two-phase flow have been presented and discussed in Chapter 5. Whereas, in practice and for the Farrow sand-blasting system, heated water droplet are used for improving the blast cleaning performance, and this chapter is going to simulate the air flow through the nozzle with sand particles and water droplets, or air-sand-water three-phase flow.

Abrasive blasting can generate large quantities of dust, which may be toxic, such as Silica dust and Lead dust. The Silica dust can be generated by using river sand, beach sand or quarts rock as abrasive materials. However, Lead dust can be generated by using an abrasive material that contains lead, or abrasive blasting surfaces covered by paint that contains lead. Therefore, as a standard blast machine, compressed air is used to propel the abrasive with just enough water added to suppress the dust. For effective dust suppression the water should be added before the abrasive leaves the nozzle.

There are two approaches for the simulating of the multiphase flow through the nozzle in FLUENT, the Eulerian approach and the Lagrangian approach or Discrete-phase model. The *Eulerian Model* as well as the *Lagrangian approach* have been

applied for the single and two-phase flow. Due to the restriction of the secondary phase volume fraction, the *Lagrangian approach* and the *Discrete Phase Model* were more applicable than the *Eulerian Model*. Therefore, in the present chapter, the *Discrete Phase Model* is used for the simulating of the air-sand-water three-phase flow through the nozzle, meanwhile, the effects of added water droplets to the air-sand flow are compared with the achieved results in Chapter 5.

The sand particles and water consumption in the Farrow sand-blasting machine are about 0.02 kg/s and 0.03 kg/s, respectively; however, this study is going to compute the effects of sand particles and water droplets in some wide ranges than their usual consumption, 0.01 kg/s to 0.03 kg/s for sand particles and 0.01 kg/s to 0.05 kg/s for water droplets. On the other hand, various temperatures for inlet water droplets and sand particles, 300 K to 360 K, are applied for computing the thermal consequence on the nozzle performance.

6.1 The Solvers of Air-Sand-Water Three-Phase Flow in FLUENT

The numerical solvers, *Pressure-Based Solver* and *Density-Based Solver*, for the computing of the multi-phase flow have been introduced in Chapter 3 (Section 3.5). Although there are some advantages and disadvantages for using each mentioned method in literature, this section is going to numerically compare the *Pressure-Based Segregated Solver* (PBSS), as a solver with maximum segregated equations, and the *Density-Based Coupled Solver* (DBCS), as a solver with maximum coupled equations, in the air-sand-water three-phase flow through the nozzle.

Air velocity counters simulated by the PBSS and the DBCS are shown in Figures (6.1) and (6.2). Almost the same counters' array by the slightly displaced shockwave has been observed in the two sketched counters. Figures (6.3) and (6.4) represent the sand particles and water droplets trajectories through the nozzle, which are coloured by the velocity magnitude and simulated by the PBSS and the DBCS, respectively.

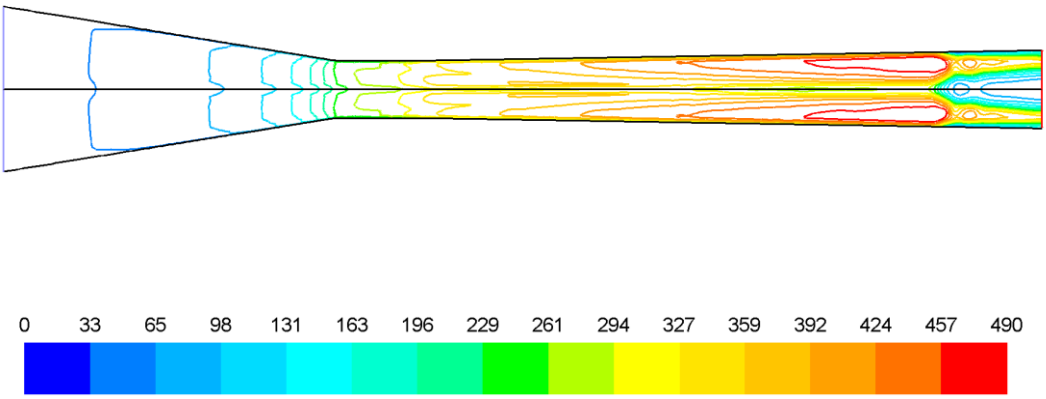

Figure (6. 1). Velocity contours for air flow simulated by PBSS (p_{in} = 1.5 atm)

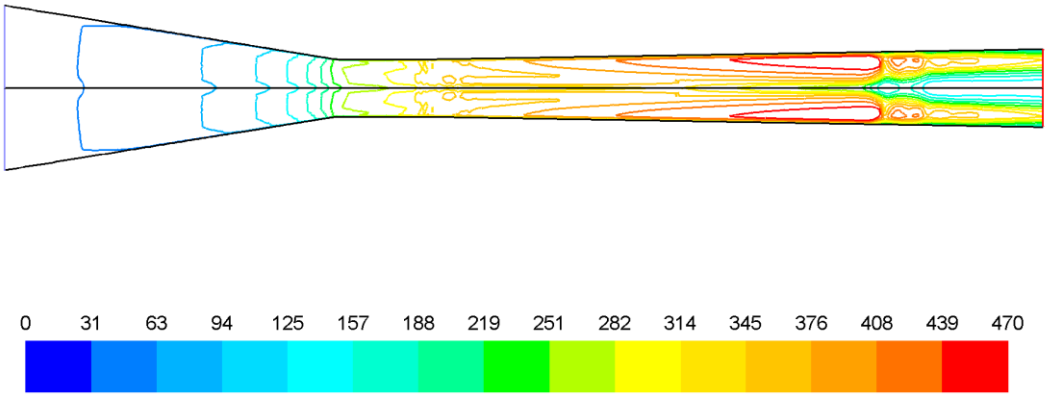

Figure (6. 2). Velocity contours for air flow simulated by DBCS (p_{in} = 1.5 atm)

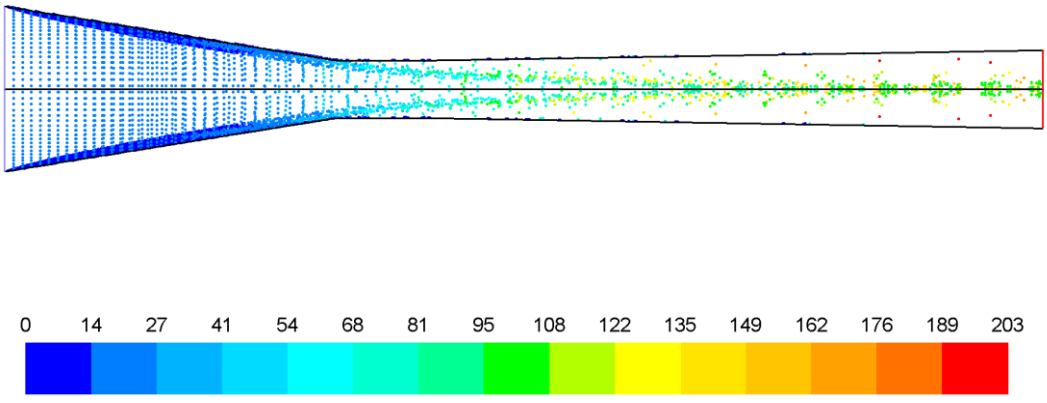

Figure (6. 3). Sand particles and water droplets trajectories through the Nozzle, simulated by PBSS (p_{in} = 1.5 atm)

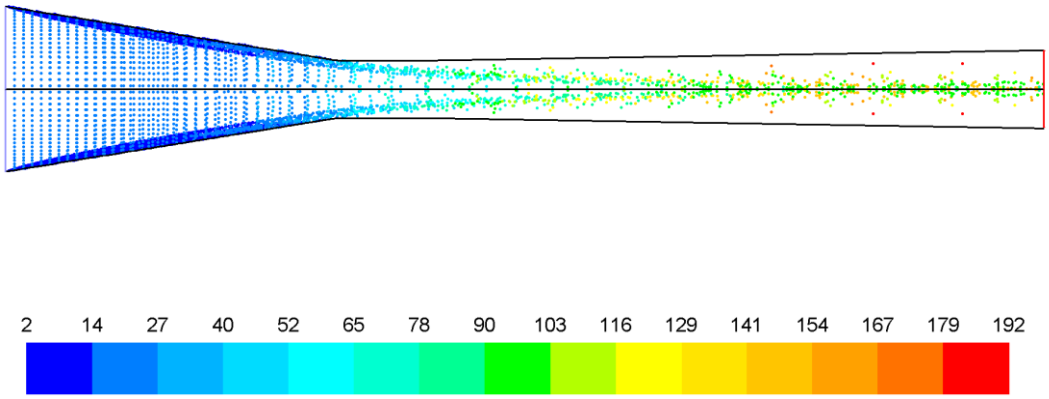

Figure (6. 4). Sand particles and water droplets trajectories through the Nozzle, simulated by DBCS (p_{in} = 1.5 atm)

The velocity magnitudes of sand particles as a function of residence time for some tracks are shown in Figure (6.5). By attention to these figures, the reasonable precision is observed between two different algorithms, PBSS and DBCS.

Both solvers have been applied for the same three-phase flow conditions, $P_{in} = 1.5atm$, $T_{in} = 300K$, $\dot{m}_{sand} = 0.02kg/s$, $\dot{m}_{water} = 0.01kg/s$, and the same sand particles and water droplets diameters.

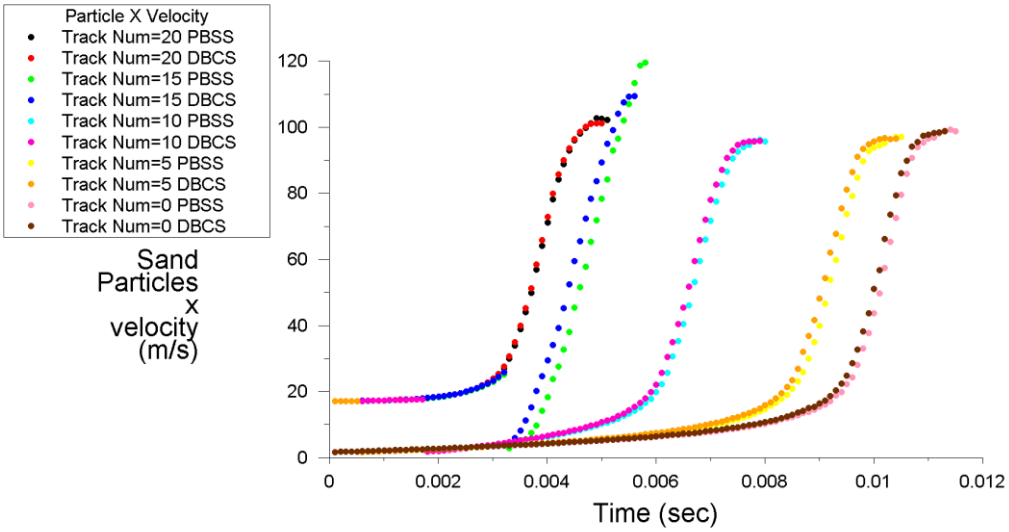

Figure (6. 5). Sand particles velocity magnitude as a function of residence time

The velocity magnitude of the water droplets as well as the sand particles has the same trend in both the PBSS and the DBCS solvers. Figure (6.6) shows the velocity magnitude of the water droplets as a function of residence time inside the nozzle for

both the PBSS and the DBCS. In this figure as well as Figure (6.5) the velocity magnitude of the dispersed phase is compared in two different solvers.

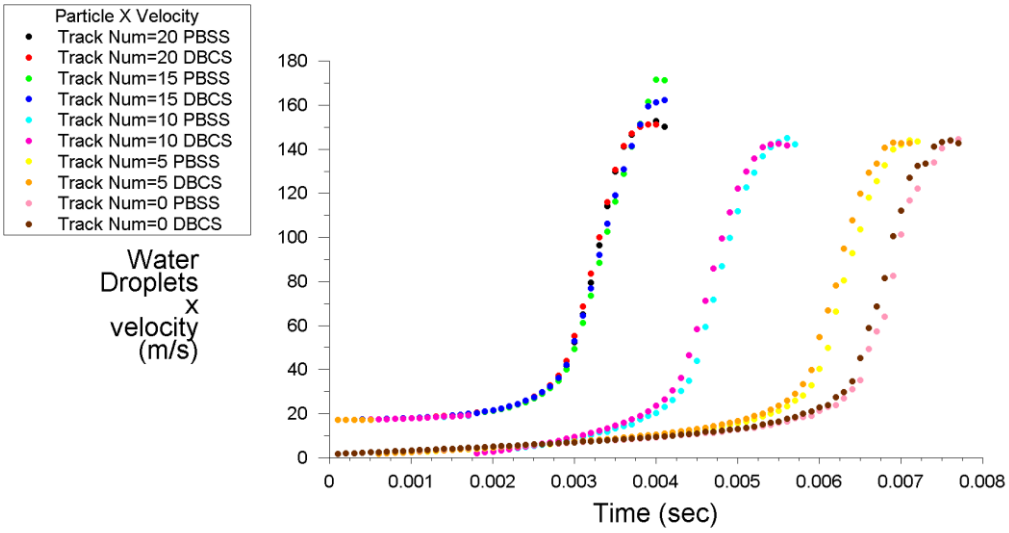

Figure (6. 6). Water droplets velocity magnitude as a function of residence time

In Figure (6.7) the exhaust velocity of the sand particles and water droplets along the trajectories are compared between the PBSS and the DBCS. Finally, this figure clearly shows very good compatibility between the *Pressure-Based Segregated Solver* and the *Density-Based Coupled Solver*.

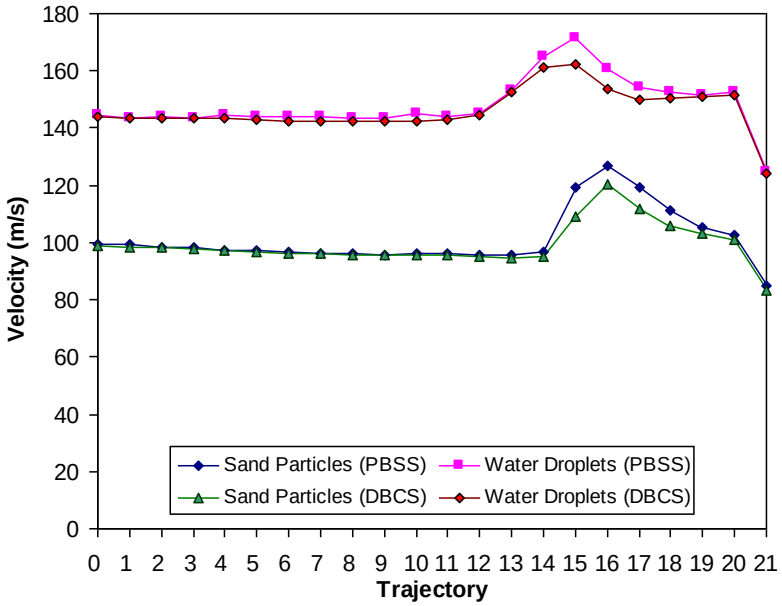

Figure (6. 7). Exhaust velocity of sand particles and water droplets solved by PBSS and DBCS

In this study, whereas the PBSS needs less computing memory than the DBCS, so the *Pressure-Based Segregated Solver* is applied for the simulating of the air-sand-water three phase flow through the nozzle.

6.2 Air-sand-water three-phase flow vs. air-sand two phase flow

The air-sand two-phase flow by different multiphase flow models, various air inlet pressures and a variety of sand mass flow rates have been simulated and compared with the air single-phase flow through the nozzle in Chapter 5. Here, by applying water droplets to the air-sand flow, some differences between the mentioned two-phase flow and the air-sand-water three-phase flow are analysed.

Figures (6.8) and (6.9) show the air velocity counters through the nozzle for the air single-phase flow and the air-sand two-phase flow, and can be compared with the air-sand-water three-phase flow sketched in Figure (6.10).

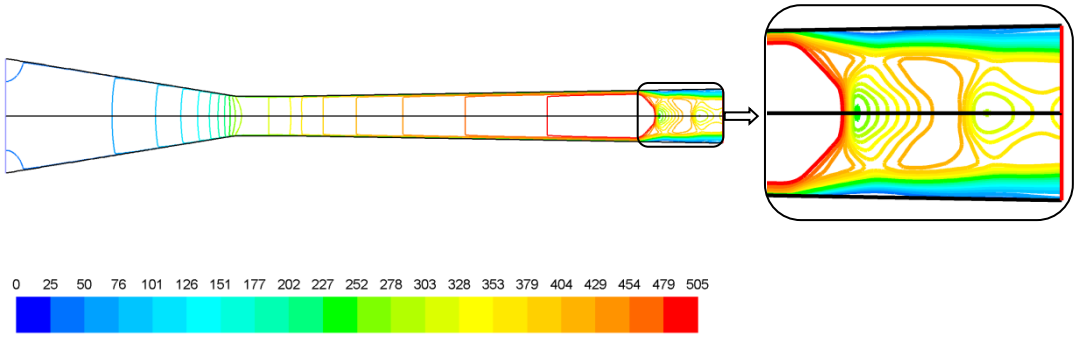

Figure (6. 8). Contours of velocity for air flow (p_{in} = 1.5 atm)

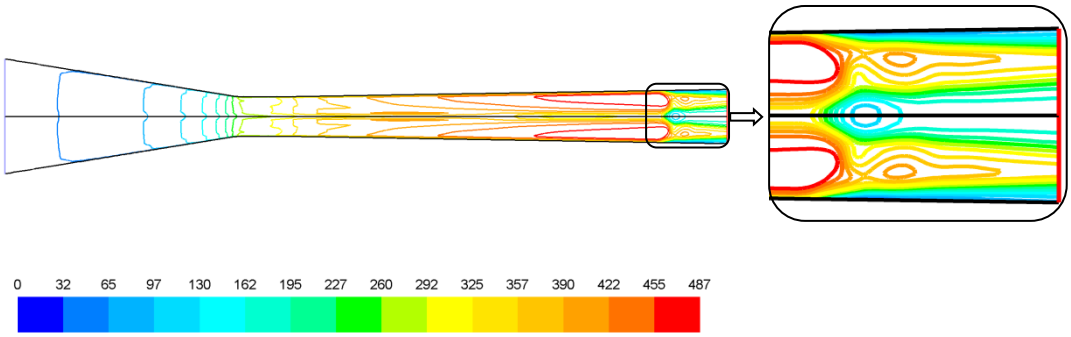

Figure (6. 9). Contours of velocity for air-sand two-phase flow (p_{in} = 1.5 atm)

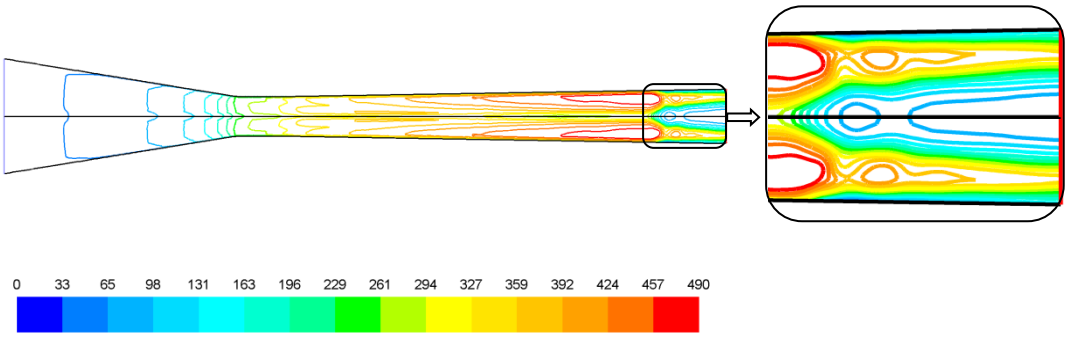

Figure (6. 10). Contours of velocity for air-sand-water three-phase flow (p_{in} = 1.5 atm)

All counters are calculated for the same inlet pressure and temperature, $p_{in} = 1.5atm$ and $T_{in} = 300K$. The sand particles mass flow rate in Figures (6.9) and (6.10) is equal to $0.02\,kg/s$, and the water droplets mass flow rate in Figure (6.10) is equal to $0.01kg/s$. All counters indicate the single and multiphase flows through the nozzle are axisymmetric. Nearly flat velocity profiles around the centre-line of the nozzle in the air single-phase flow have been changed by using sand particles and water droplets. On the other hand, in the two and three phase flows the maximum velocity counters are between the centre-line and walls. A comparison of Figure (6.9) with Figure (6.10) indicates the above-mentioned maximum velocity counters by adding water droplets to the flow, move towards the wall of the nozzle. The main reason for this event is due to the increasing of the flow inertia in and around the nozzle's centre-line by adding the water droplets.

The nozzle air flow velocity vectors for the two and three-phase flows are shown in Figures (6.11) and (6.12). Figure (6.12) shows the profile of the velocity vectors have been slightly changed in comparison with Figure (6.11); however, both profiles confirm the position of the maximum air flow velocity that is between the nozzle's centre-line and wall. Figure (6.13) shows the velocity profiles of the nozzle's exhaust air flow for both the air-sand two-phase flow and the air-sand-water three-phase flow. For the same sand mass flow rate, and air inlet pressure and temperature, Figure (6.13) expresses that the maximum and mean air exhaust velocity decreases by adding water droplets to the flow. The mentioned velocity difference in and around the nozzle's axis is more considerable than any other domain, and it is due to the water droplets concentration inside the Nozzle.

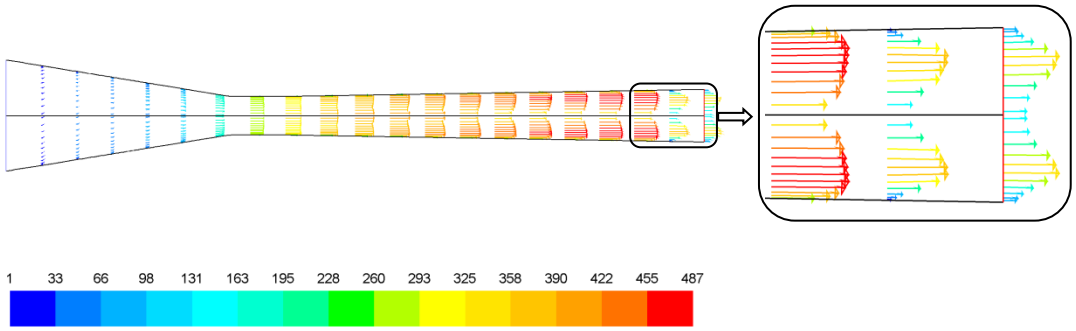

Figure (6. 11). Nozzle exhaust air velocity vectors for air-sand two-phase flow

Figure 6.23:

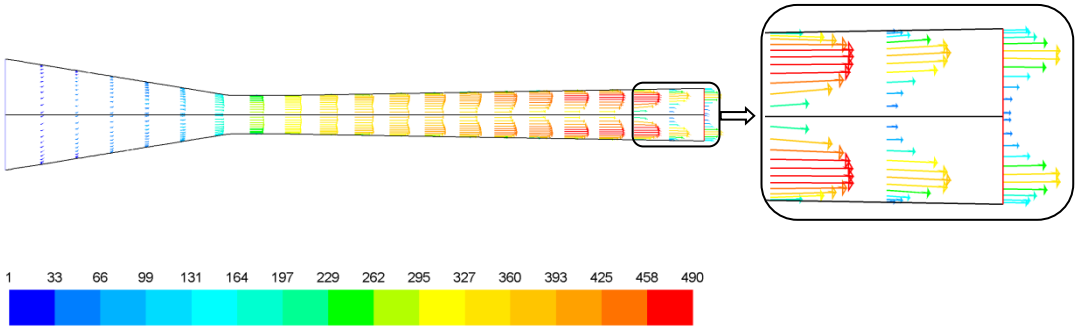

Figure (6. 12). Nozzle exhaust air velocity vectors for air-sand-water three-phase flow

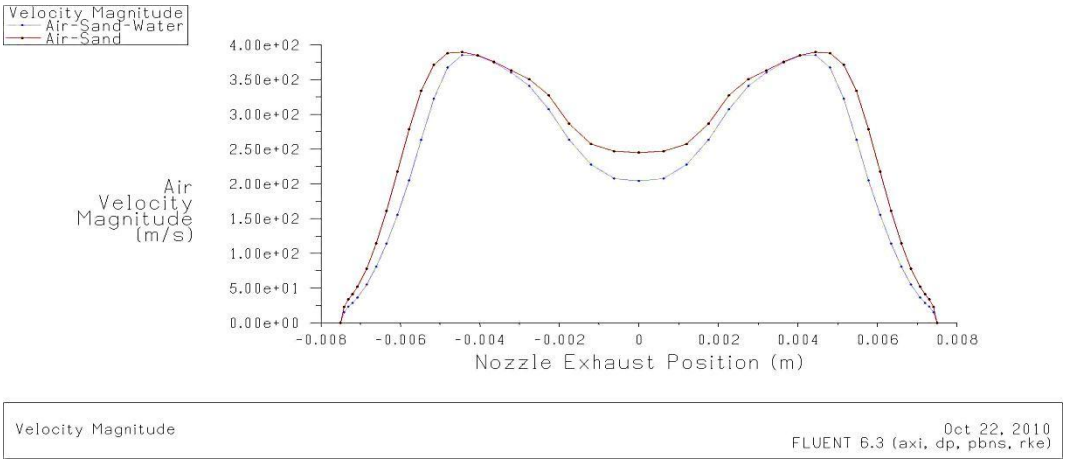

Figure (6. 13). The Nozzle exhaust air velocity profiles comparison between air-sand two-phase and air-sand-water three-phase flow

More details about the flow characteristics of the air-sand two-phase flow and the air-sand-water three-phase flow are summarised in Table (6.1). Regarding this table, the air average exhaust velocity decreases about 10% by inserting water droplets to the air-sand flow, and the sand particles average exhaust velocity in the air-sand two-phase flow is about 6% more than the air-sand-water three-phase flow.

Table (6. 1). Flow characteristics of air-sand two-phase flow vs. air-sand-water three-phase flow through the Nozzle

Flow Characteristics	Air-Sand	Air-Sand-Water
Inlet Air Average Velocity (m/s)	23.2	22.4
Exhaust Air Average Velocity (m/s)	231.5	210.8
Exhaust Air Average Temperature (K)	258	246
Air Mass Flow Rate (g/s)	64.6	62.4
Exhaust Sand Average velocity (m/s)	135.5	127.3
Exhaust Sand Average Temperature (K)	294.5	294.7
Exhaust Water Average velocity (m/s)	-	180.8
Exhaust Water Average Temperature (K)	-	297.9

In the following sections the effects of the water droplets mass flow rates as well as the sand particles mass flow rates, air inlet pressure and abrasive inlet temperature on the nozzle flow characteristics are presented.

6.3 Various mass flow rate of water droplets

Water droplets not only help to suppress the dust in sand-blasting systems but also beside the sand particles it behaves as an abrasive media, and improves the sand-blasting efficiency. The abrasive and dust suppressive performance of water droplets depends on the flow characteristics inside the exhaust of the nozzle. Water droplets as well as sand particles are propelled through the nozzle by high velocity air flow; meanwhile, the momentum of the air has transferred to the water droplets and sand particles. Therefore, the exhaust velocity of the water droplets depends on not only the air inlet flow conditions but also on the sand particles' volume fraction.

In this section, water droplets with various mass flow rates from 0.01 to 0.05 kg/s with increment of 0.01 kg/s are simulated with different air-sand mixtures. In almost the same way as the previous study in Chapter 5, the sand mass flow rate varies from 0.01 to 0.03 kg/s with an increment of 0.005 kg/s. In this section the air inlet pressure is assumed 2 atm, and the abrasive inlet temperature as well as the air inlet temperature is equal to 300 K.

In this section the air average exhaust velocity and mass flow rate, sand particles exhaust velocity as well as the average sand particles exhaust velocity, water droplets average exhaust velocity, and air velocity profiles in the exhaust of the nozzle as a function of the sand particles and water droplets mass flow rates are presented.

Air velocity vectors for the single-phase flow and the three-phase flow with different water mass flow rates are shown in Figures (6.14) to (6.17). The most difference in these figures occurs just before the exhaust of Nozzle, and after the shock wave.

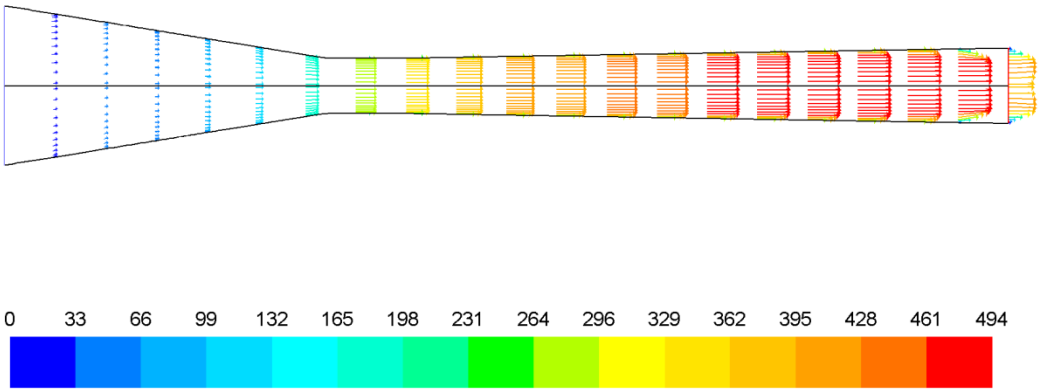

Figure (6. 14). Velocity vectors for air single-phase flow

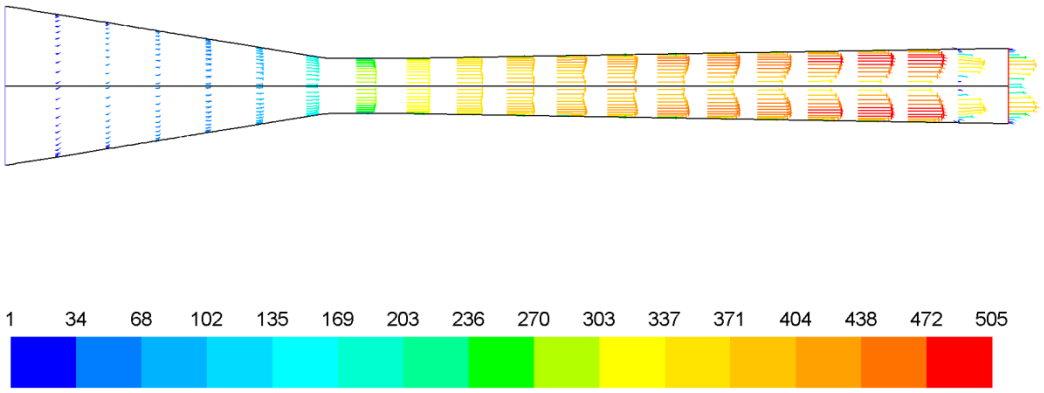

Figure (6. 15). Velocity vectors for three-phase flow with $\dot{m}_{sand} = 0.02$ & $\dot{m}_{water} = 0.01$

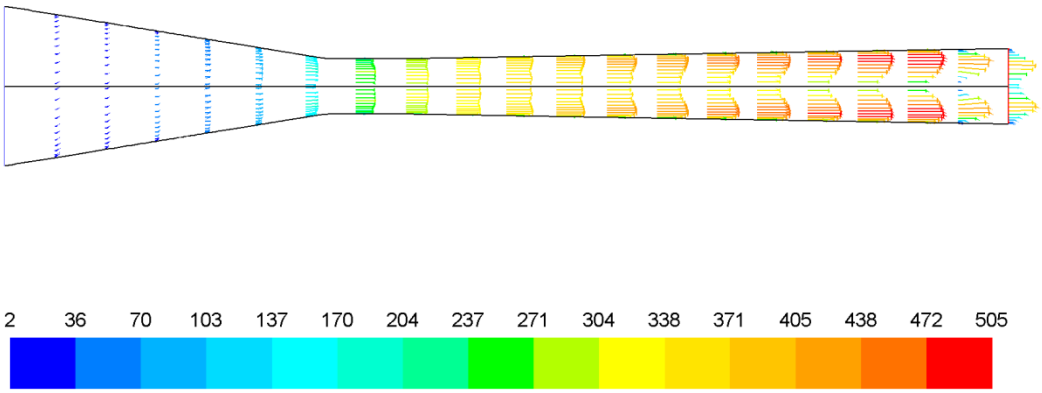

Figure (6. 16). Velocity vectors for three-phase flow with $\dot{m}_{sand} = 0.02$ & $\dot{m}_{water} = 0.03$

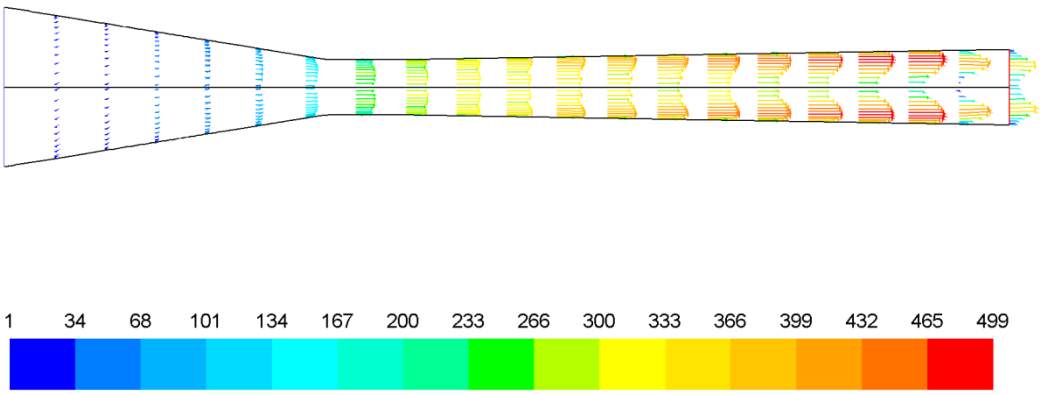

Figure (6. 17). Velocity vectors for three-phase flow with $\dot{m}_{sand} = 0.02$ & $\dot{m}_{water} = 0.05$

By adding more water droplets with a constant sand particles mass flow rate into the air flow through the nozzle, as Figures (6.15) to (6.17) show, more reduction in the air velocity around the axis of the nozzle can be observed.

The pressure distribution among the axis of the nozzle are shown in Figures (6.18) for various water droplets mass flow rates and sand particles mass flow rate of 0.01 kg/s. This figure confirms the above-mentioned trend of static pressure inside the nozzle. By raising the water droplets mass flow rate, from 0.01kg/s to 0.05kg/s, the pressure goes up instead of jumping in the shock wave area. The same trends can be observed in other sand mass flow rates, as shown in Figures (6.19) to (6.22).

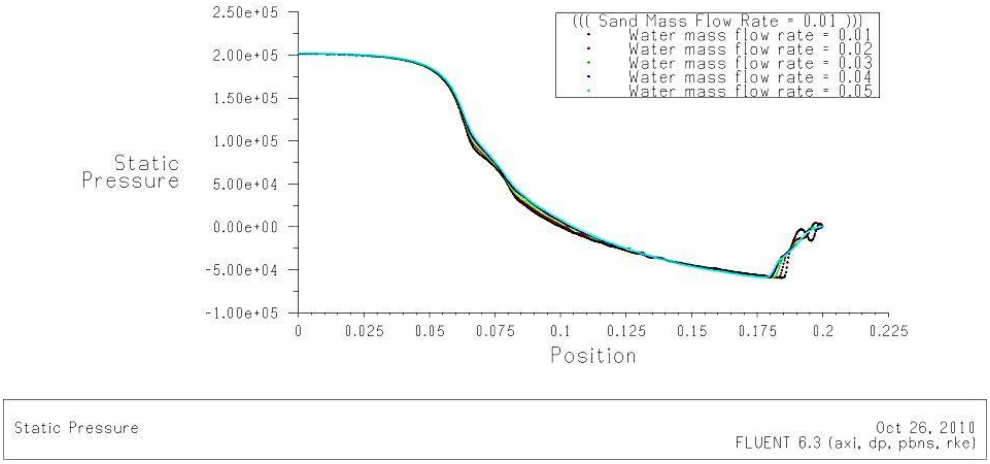

Figure (6. 18). Static pressure distribution for various water mass flow rate and $\dot{m}_{sand} = 0.01$

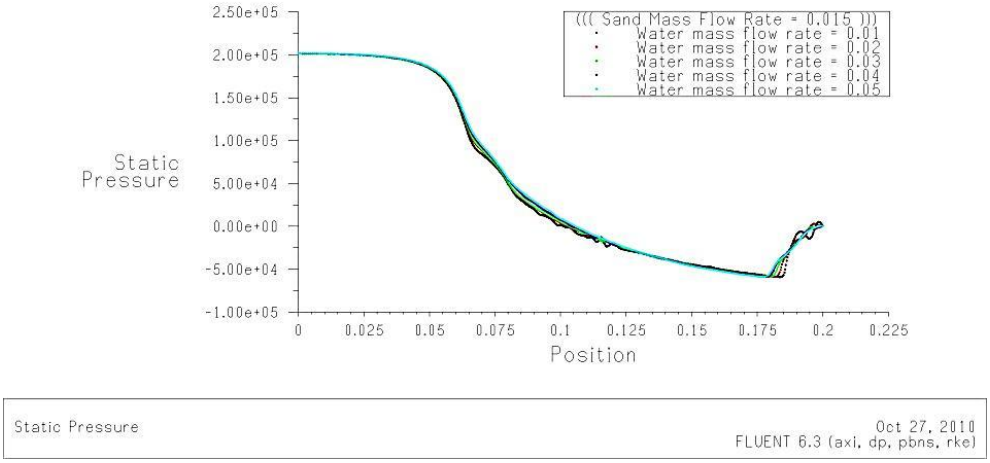

Figure (6. 19). Static pressure distribution for various water mass flow rate and $\dot{m}_{sand} = 0.015$

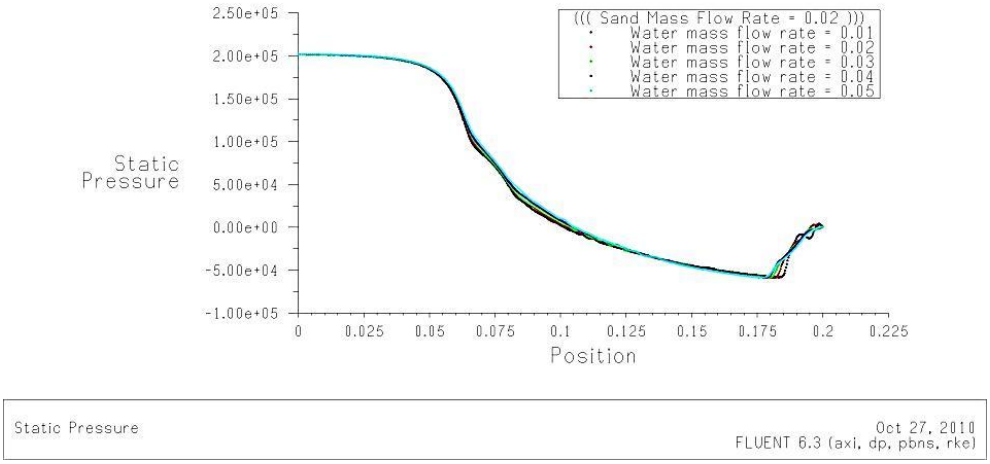

Figure (6. 20). Static pressure distribution for various water mass flow rate and $\dot{m}_{sand} = 0.02$

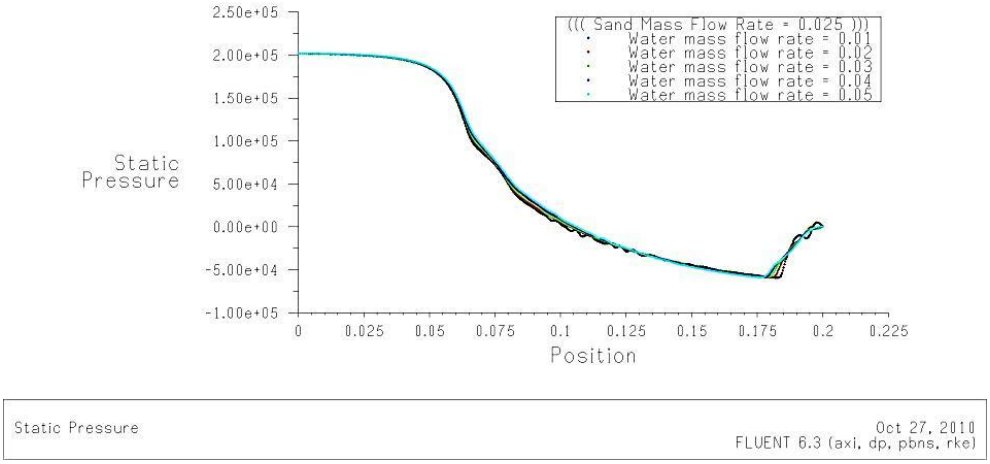

Figure (6. 21). Static pressure distribution for various water mass flow rate and $\dot{m}_{sand} = 0.025$

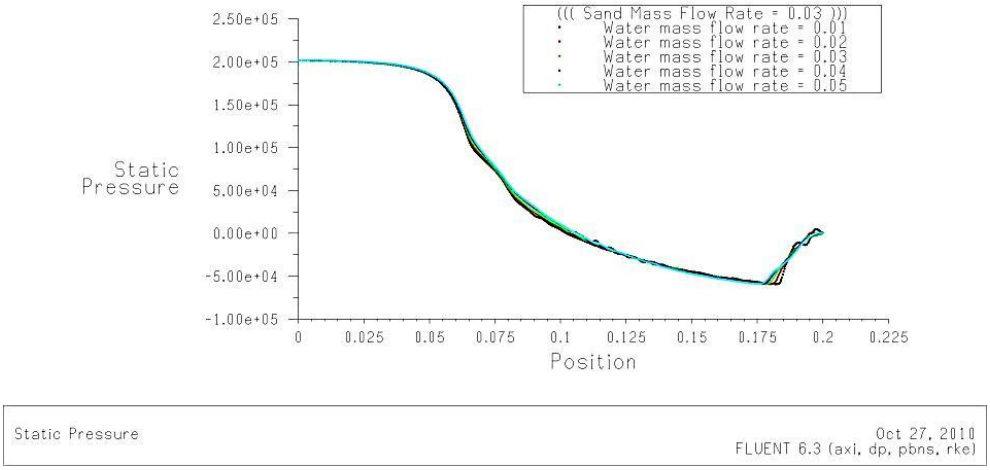

Figure (6. 22). Static pressure distribution for various water mass flow rate and $\dot{m}_{sand} = 0.03$

The velocity profiles of the nozzle exhaust air flow for various water droplets mass flow rates, and the same sand mass flow rate, air inlet pressure and temperature are shown in Figure (6.23). As Figure (6.23) shows the air exhaust velocity decreases in almost all of the nozzle exhaust area by increasing the overall mass flow rate of water droplets. The effect of adding more water droplets on the velocity profiles in the nozzle axis domain is more considerable, and it is due to the water droplets distribution inside the nozzle; because, the sand particles and water droplets trajectories through the nozzle, as shown in Figure (6.3), are more concentrated in and around the axis area. Nearly the same results have been achieved from other sand mass flow rates, 0.015kg/s to 0.03kg/s, which are shown in Figures (6.24) to (6.27).

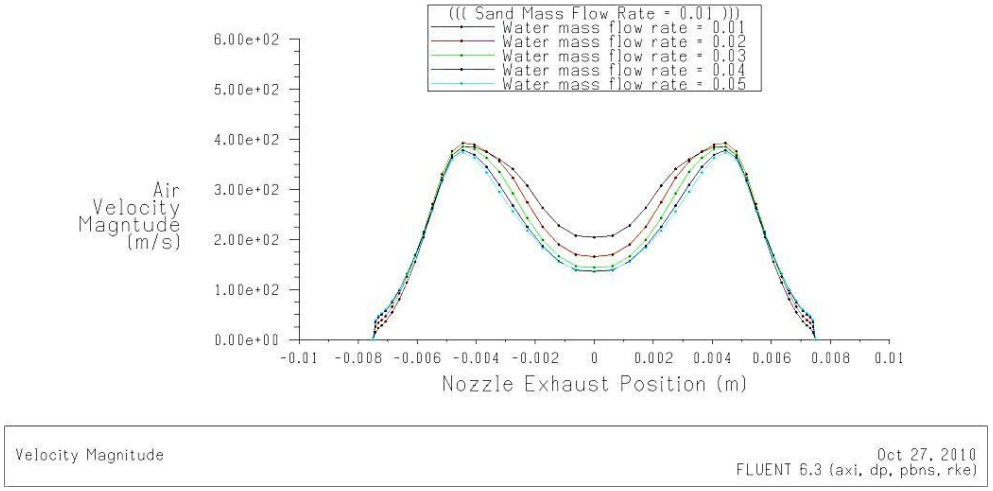

Figure (6. 23). The Nozzle exhaust air velocity profiles comparison between different water mass flow rates and $\dot{m}_{sand} = 0.01$

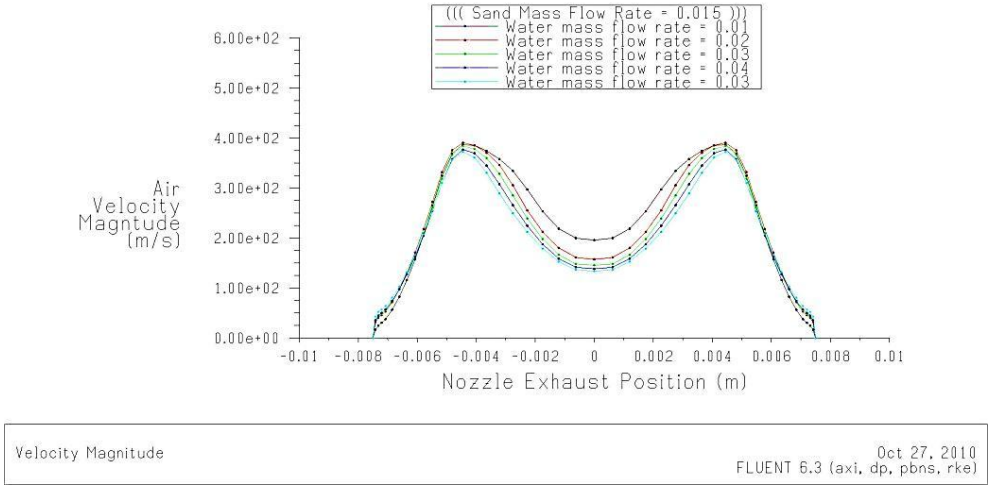

Figure (6. 24). The Nozzle exhaust air velocity profiles comparison between different water mass flow rates and $\dot{m}_{sand} = 0.015$

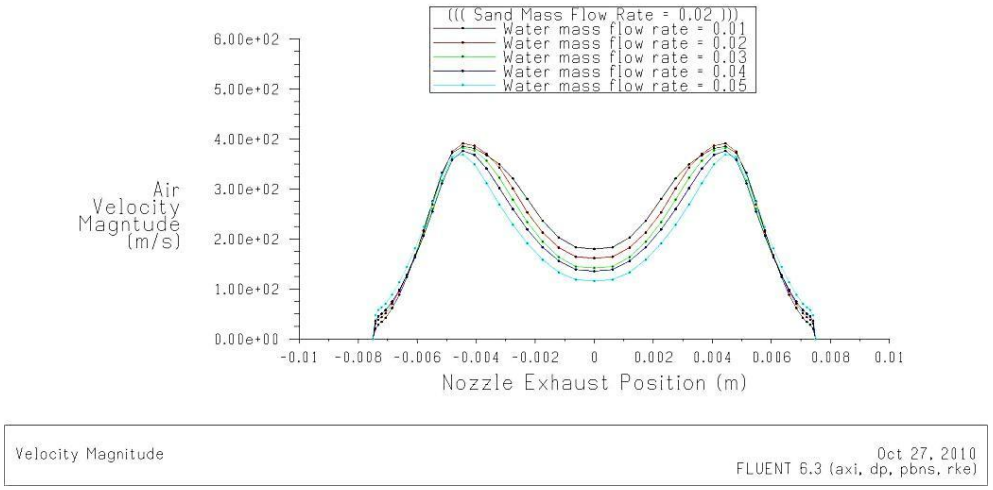

Figure (6. 25). The Nozzle exhaust air velocity profiles comparison between different water mass flow rates and $\dot{m}_{sand} = 0.02$

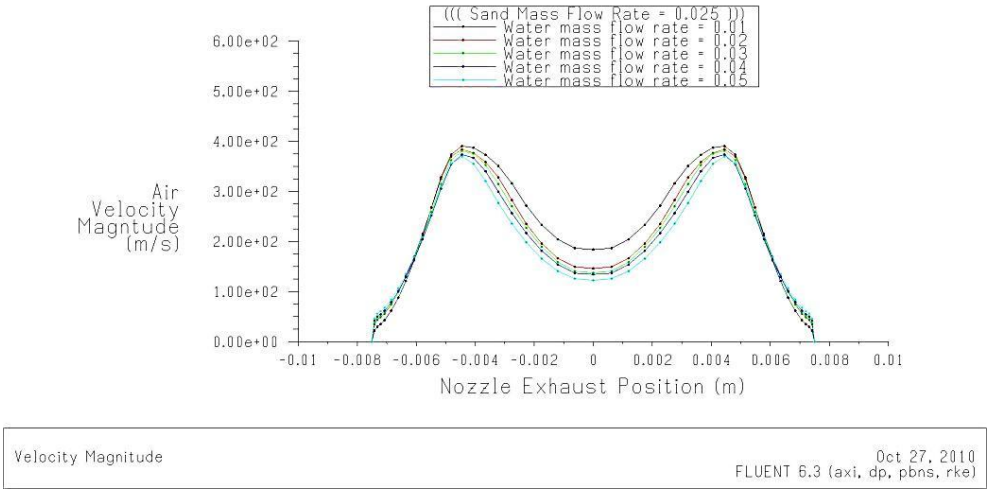

Figure (6. 26). The Nozzle exhaust air velocity profiles comparison between different water mass flow rates and $\dot{m}_{sand} = 0.025$

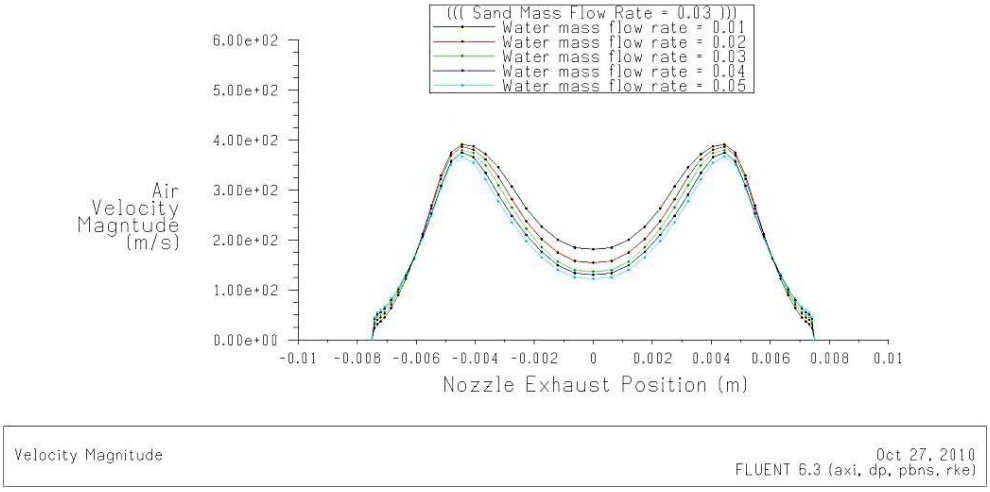

Figure (6. 27). The Nozzle exhaust air velocity profiles comparison between different water mass flow rates and $\dot{m}_{sand} = 0.03$

In general, Figures (6.23) to (6.27) indicate that the average air exhaust velocity is influenced by the water mass flow rate. For different sand mass flow rates, Figure (6.28) as well as Table (6.2) show the dependency of the air exhaust average velocity to the water mass flow rate.

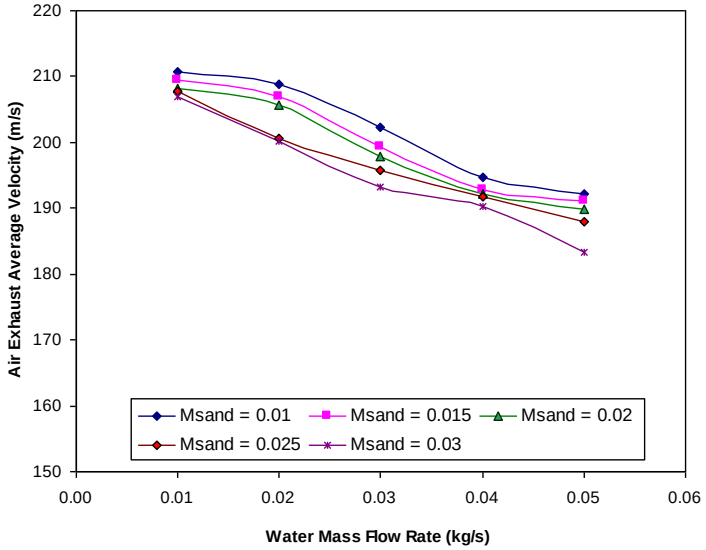

Figure (6. 28). Air exhaust average velocity for different sand mass flow rates

Table (6. 2). Air exhaust average velocity (m/s)

Water Mass Flow Rate (kg/s) \ Sand Mass Flow Rate (kg/s)	0.01	0.015	0.02	0.025	0.03
0.01	210.82	209.56	208.26	207.82	206.91
0.02	208.72	206.83	205.66	200.53	200.18
0.03	202.35	199.32	197.83	195.84	193.26
0.04	194.79	192.8	192.07	191.83	190.26
0.05	192.09	191.1	189.86	187.9	183.23

All the curves in Figure (6.28) indicate that the air exhaust average velocity is almost inversely proportional to the water mass flow rate, and by increasing the water mass flow rate from 0.01kg/s to 0.05kg/s the air exhaust average velocity decreases by about 10%, apart from the sand mass flow rates.

For the same inlet pressure, temperature, and sand mass flow rate, the air mass flow rate and water mass flow rate are in inverse proportion. Figure (6.29) shows this inverse proportion is better than the proportion of air exhaust average velocity and water mass flow rate.

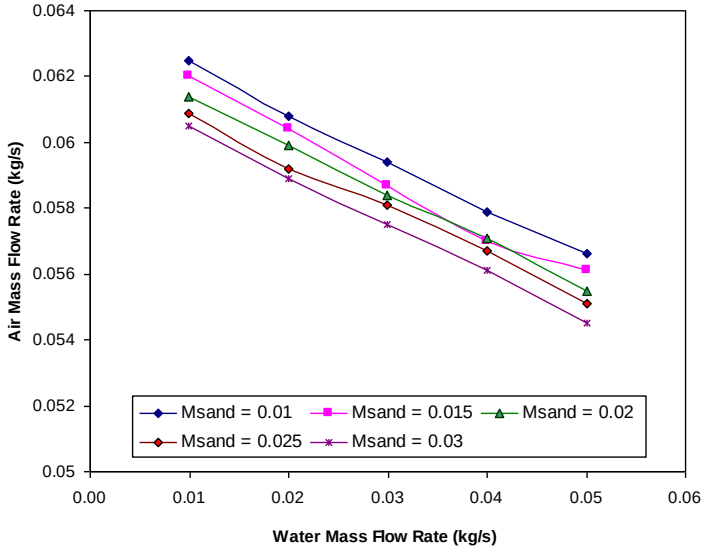

Figure (6. 29). Air mass flow rate as a function of water mass flow rate and sand mass flow rate

As Table (6.3) indicates, about 10% decreases on the air mass flow rates can be observed by increasing the water mass flow rates from 0.01kg/s to 0.05kg/s. This tendency is repeated for all sand mass flow rates, from 0.01kg/s to 0.03kg/s.

Therefore, not only the air mass flow rate diminishes by increasing water droplets amounts, but also the air average velocity exhaust from the nozzle decreases as well. It means the air momentum during the flow through the nozzle has been transferred to the sand particles and water droplets. By the constant sand mass flow rate, this section is going to verify the portion of this momentum which is absorbed by the sand particles by applying different water mass flow rates. In this case and as the mass flow rate of sand particles assumes to be constant, the exhaust sand particles trajectory's velocity as well as mean velocity are computed.

Table (6. 3). Air mass flow rate (kg/s)

		Sand Mass Flow Rate (kg/s)				
		0.01	*0.015*	*0.02*	*0.025*	*0.03*
Water Mass Flow Rate (kg/s)	*0.01*	0.0625	0.062	0.0614	0.0609	0.0605
	0.02	0.0608	0.0604	0.0599	0.0592	0.0589
	0.03	0.0594	0.0587	0.0584	0.0581	0.0575
	0.04	0.0579	0.057	0.0571	0.0567	0.0561
	0.05	0.0566	0.0561	0.0555	0.0551	0.0545

The particles inside the nozzle move through 44 trajectories, and as the flow conditions and geometry are axis-symmetry, so just 22 trajectories, which start from the nozzle inlet wall to the nozzle inlet axis shown in Figure (6.30), are calculated. More details of the trajectories are shown in figures (5.37) to (5.44).

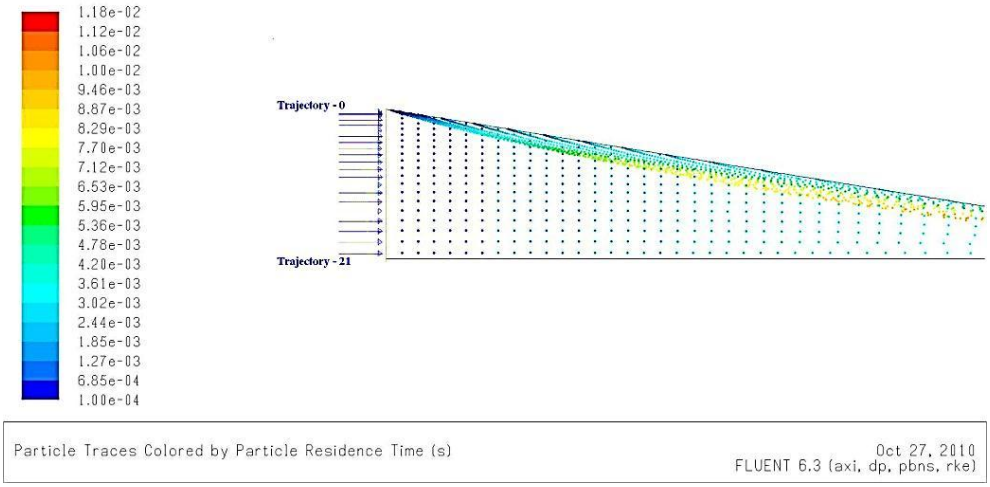

Figure (6. 30). The particle trajectories in entrance and diverging part of nozzle

Unlike the entrance of the nozzle which has almost uniform particle trajectories, as Figure (6.3) shows, the exhaust of the nozzle has non-uniform trajectories. The exhaust velocity of the sand particles, not only are influenced by the entrance trajectory position but also strongly depend on the situation of the trajectory in the exit of the nozzle.

Figure (6.31) shows the sand particles exhaust velocity on the trajectories from 0 to 21, and for the water droplets mass flow rate from 0.01kg/s to 0.05kg/s and the constant sand mass flow rate of 0.01kg/s. Trajectories 0 to 14, which have nearly the same velocities, are hit to the wall in the converging part of the nozzle and are then reflected from the wall. Trajectories 15 and 16, which have maximum sand particles velocity, not only pass through the nozzle without any hitting onto the nozzle's wall, but also they path between axis and wall of nozzle where the air velocity is almost maximums. By increasing the trajectory number from 17 to 21, the particle velocity is coming down because these trajectories, which are quite close to the nozzle axis, are in contact with almost low air velocity (Figure 6.23).

The same tendency is observed for other sand mass flow rates in Figures (6.32) and (6.33).

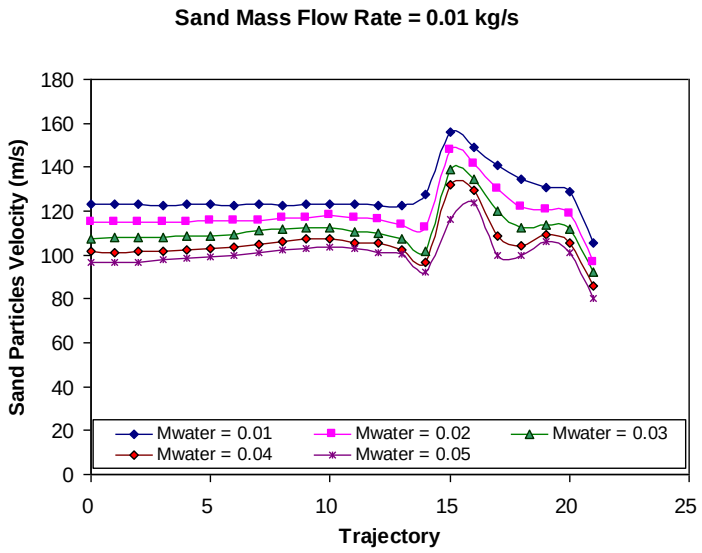

Figure (6. 31). Exhaust velocity of sand particles in three-phase flow with various water mass flow rates and $\dot{m}_{sand} = 0.01$

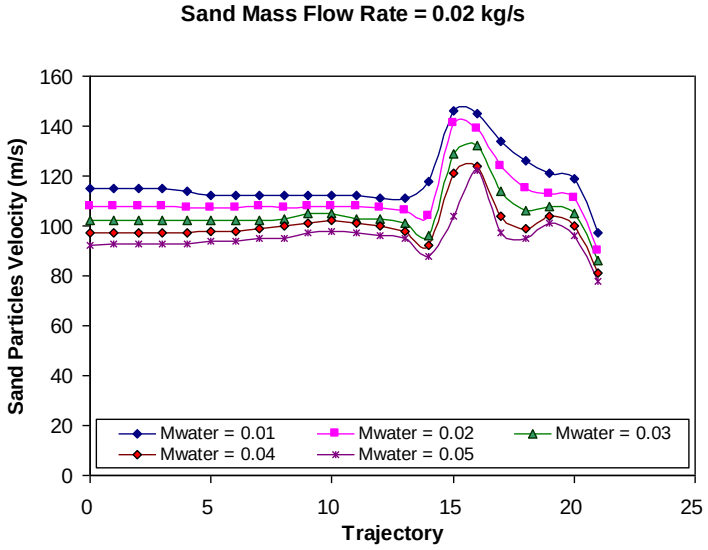

Figure (6. 32). Exhaust velocity of sand particles in three-phase flow with various water mass flow rates and $\dot{m}_{sand} = 0.02$

For cleaning or abrasion of surface, definitely the average sand particles' velocity (or momentum) is more important parameter than velocity (or momentum) of each particles. Figure (6.34) shows the average sand particles velocities which are calculated for air-sand-water three-phase flow. This simulation has been done for air inlet pressure 2atm, inlet temperature of all phases 300K, sand mass flow rate 0.01 kg/s to 0.03kg/s, and water mass flow rate of 0.01kg/s to 0.05kg/s.

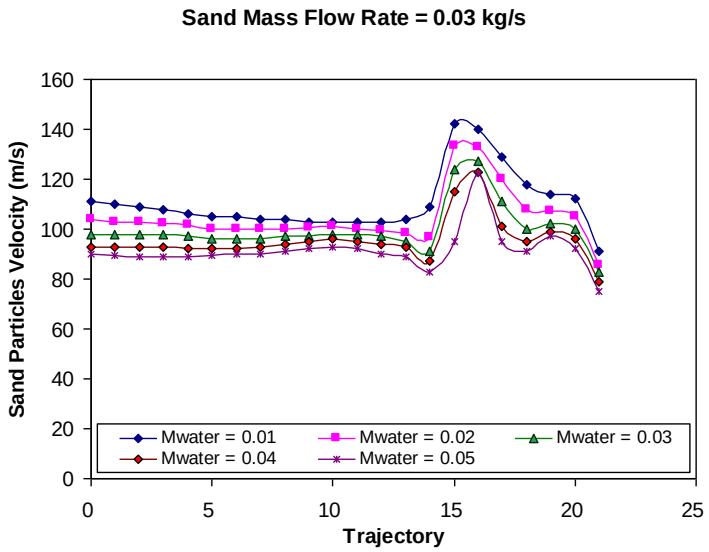

Figure (6. 33). Exhaust velocity of sand particles in three-phase flow with various water mass flow rates and $\dot{m}_{sand} = 0.03$

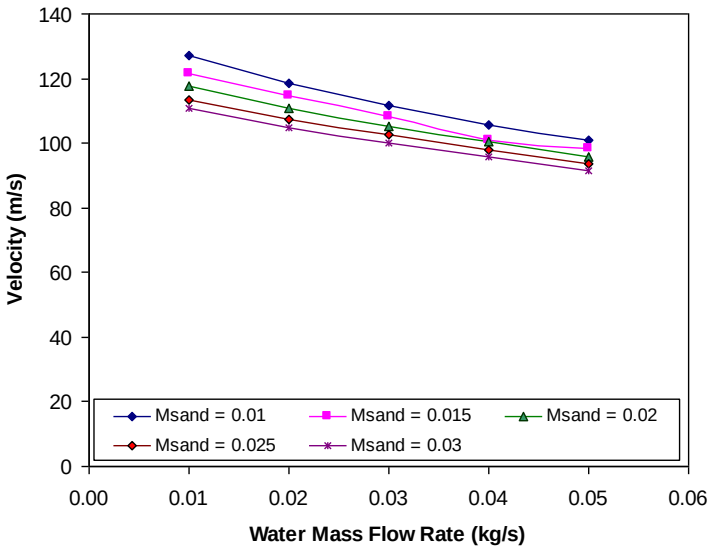

Figure (6. 34). Average sand particles exhaust velocity

Higher water mass flow rates affect the sand particles average velocity, and the velocity decreases by about 20% by increasing the water mass flow rate from 0.01kg/s to 0.05kg/s. As Figure (6.48) and Table (6.4) show, the slope of the curves decreases by increasing the water droplets and sand particles. In this study, the minimum average velocity for sand particles is 91.5m/s, which is calculated for sand and water mass flow rates of 0.03kg/s and 0.05kg/s, respectively.

Table (6. 4). Average sand particles exhaust velocity (m/s)

Water Mass Flow Rate (kg/s) \ Sand Mass Flow Rate (kg/s)	0.01	0.015	0.02	0.025	0.03
0.01	127.0	121.7	117.5	113.2	110.6
0.02	118.6	114.5	111.0	107.3	104.6
0.03	111.7	108.0	105.1	102.8	99.9
0.04	105.7	101.0	100.3	97.9	95.6
0.05	100.8	98.4	95.8	93.5	91.5

Water droplets as well as sand particles are blasted by air flow through the nozzle, and the raised velocity of the water droplets, due to the momentum transferring from the air flow, depends on the secondary phases mass flow rates. The dependency of the water droplets average velocity to the sand particles mass flow rate as well as the water droplets mass flow rate is presented in Figure (6.35) and Table (6.5). This computation has been done for the air-sand-water three-phase flow with an air inlet pressure of 2atm, an inlet temperature of all phases of 300K, a sand mass flow rate 0.01 kg/s to 0.03kg/s and a water mass flow rate of 0.01kg/s to 0.05kg/s.

The average water droplets exhaust velocities shown in Figure (6.35) have almost the same trend as the sand particles exhaust velocity in Figure (6.34). The maximum velocity of the water droplets is about 41% more than the sand particles maximum velocity in the same flow condition and mass flow rates. This is due to the differences of the physical properties between the water droplets and the sand particles. For example the true density of the sand particles is about 3.4 times to the water droplets density.

Table (6. 5). Average water droplets exhaust velocity (m/s)

Water Mass Flow Rate (kg/s) \ Sand Mass Flow Rate (kg/s)	0.01	0.015	0.02	0.025	0.03
0.01	179.7	172.9	166.7	161.6	156.6
0.02	167.0	160.9	157.2	151.8	148.1
0.03	157.7	153.2	149.2	145.6	142.6
0.04	150.0	144.1	142.6	139.5	136.3
0.05	144.4	141.6	138.3	135.1	133.0

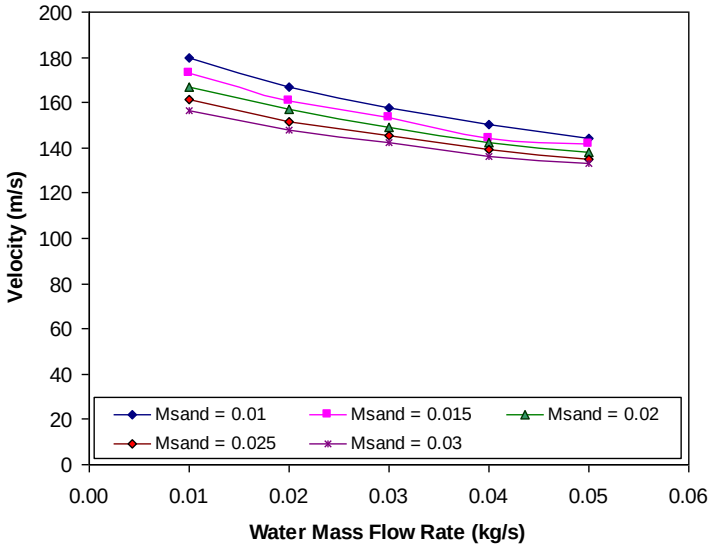

Figure (6. 35). Average water droplets exhaust velocity

In the above simulation, the number of sand particles and water droplets depend on the secondary phase's mass flow rates, and the phase's average residence time inside the nozzle. In this computation, the number of parcels in each trajectory is 1000, and each parcel depending on the phase density and mass flow rate has a different number of particles/droplets. For example in the sand particles mass flow rate of 0.01kg/s and the same water mass flow rate, the sand particles' number in each parcel is 3.210495, and the water droplets number is 10.87104. The equivalent values, for the sand particles mass flow rate of 0.03kg/s and the water droplets mass flow rate of 0.05kg/s, are 9.631485 and 54.3552, respectively.

6.4 Various air inlet pressure

In dry and wet abrasive blasting systems, as presented in Chapter 3, the abrasive or mixture of abrasive and water is propelled toward the nozzle by compressed air. High air static pressure in the entrance of the Nozzle is converted to high dynamic pressure in the exhaust of the Nozzle, with ambient static pressure. As well as air flow, the carried abrasive attains high velocity, through the nozzle. This section is going to show the effect of inlet pressure on air and abrasive exhaust velocity from the Nozzle. In this part of the study, water droplets with various mass flow rates from 0.01 to 0.05 kg/s with an increment of 0.01 kg/s are simulated with different air inlet pressure. The mass flow rate of the sand particles and the abrasive inlet temperature are assumed constant, and equal to 0.02 kg/s and 300 K, respectively.

Pressure distributions through the nozzle are shown in Figures (6.36) to (6.39). The effect of the secondary phases or the abrasive on the static pressure counters are compared in Figures (6.36) and (6.37). Abrasive particles have more effects on pressure distribution around the nozzle's axis than near the wall area. It means the concentration of the secondary phase flow, particularly in the diverging part of the nozzle, is in the centre of the nozzle rather than near the wall area. This confirms the sand particles and water droplets trajectories shown in Figure (6.3).

On the other hand, the effects of the inlet pressure on the static pressure counters, especially on the shock wave situation inside the nozzle, are exposed in Figures (6.37) to (6.39). These figures confirm that by increasing the air inlet pressure the shock wave moves towards the exhaust of the nozzle. Here, the premixed three-phase flow has been simulated for the sand particles and water droplets mass flow rate of 0.02 kg/s and 0.01 kg/s, respectively.

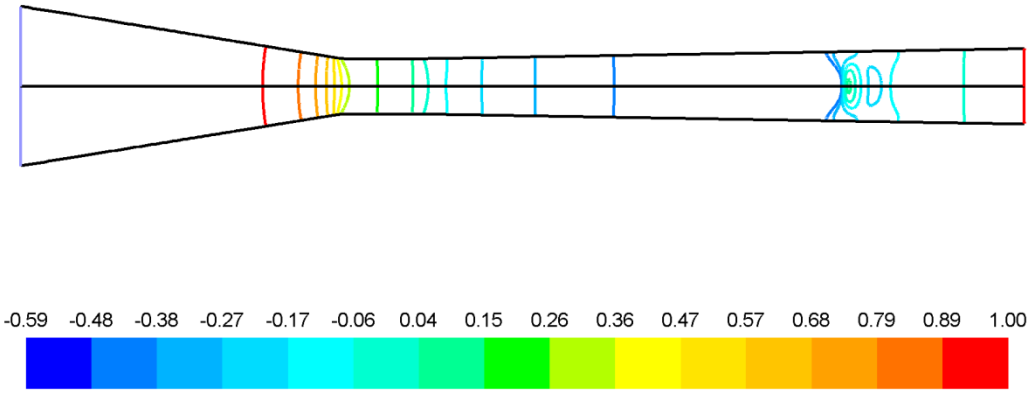

Figure (6. 36). Static pressure counters for air single-phase flow (air inlet pressure = 1 atm)

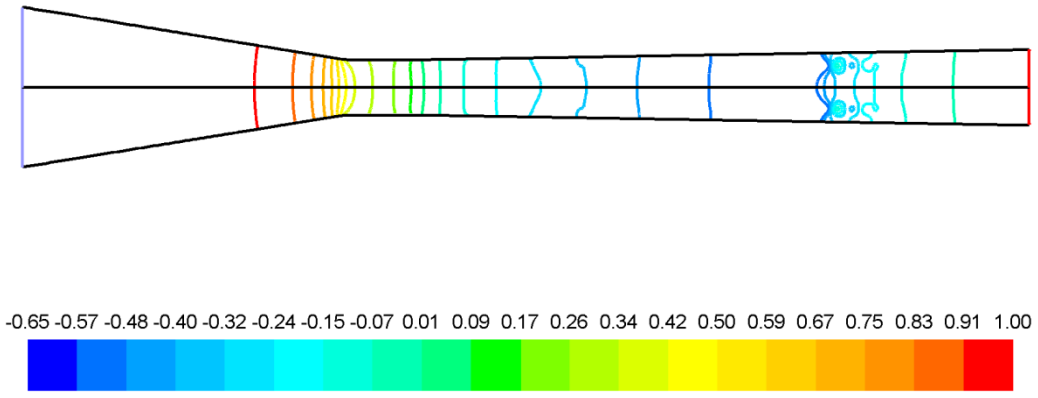

Figure (6. 37). Static pressure counters for three-phase flow (air inlet pressure = 1 atm)

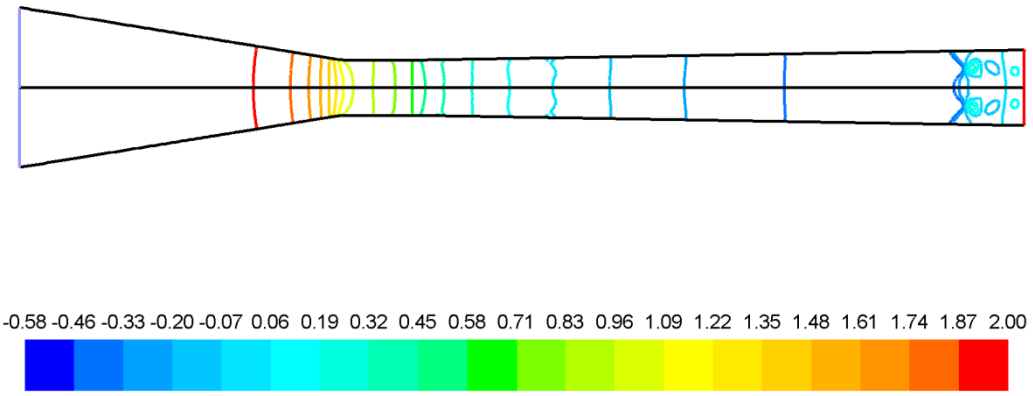

Figure (6. 38). Static pressure counters for three-phase flow (air inlet pressure = 2 atm)

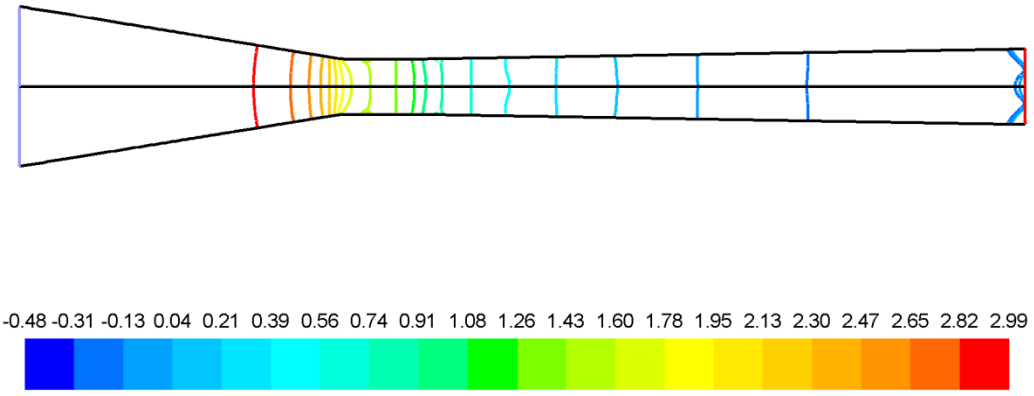

Figure (6. 39). Static pressure counters for three-phase flow (air inlet pressure = 3 atm)

Further details about the influence of the air inlet pressure on the static pressure distribution along the axis of the nozzle are illustrated in Figures (6.40) to (6.44). Different water mass flow rates have been applied for studying the effects of the water mass flow rate as well as various air inlet pressures on the static pressure distribution through the nozzle. These Figures in comparison with Figures (6.18) to (6.22) express the effect that air inlet pressure is more considerable than the water mass flow rate. On the other hand, the comparison of Figures (6.40) to (6.44) with Figure (5.6), computed for air single-phase flow, shows that by adding abrasive media to the air flow through the nozzle, static pressure is rising in the shock wave region instead of jumping, as shown in Figure (5.6).

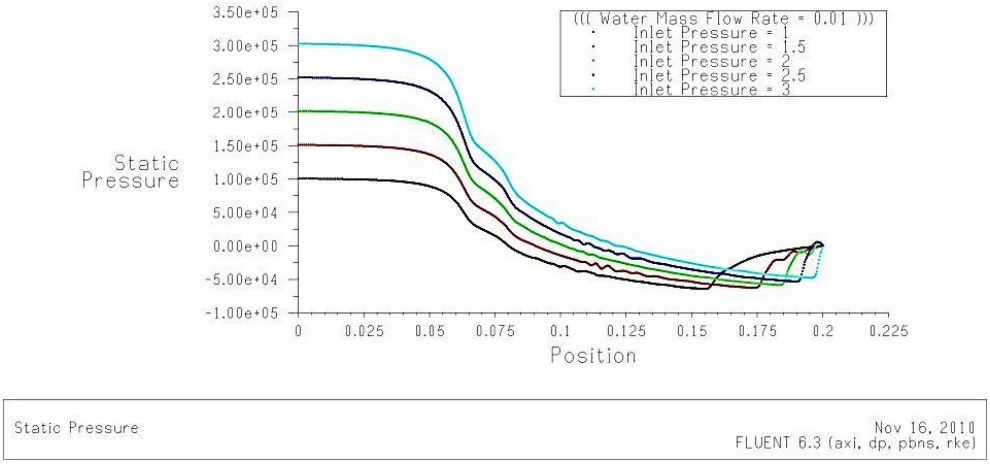

Figure (6. 40). Static pressure distribution for various air inlet pressure and $\dot{m}_{water} = 0.01$

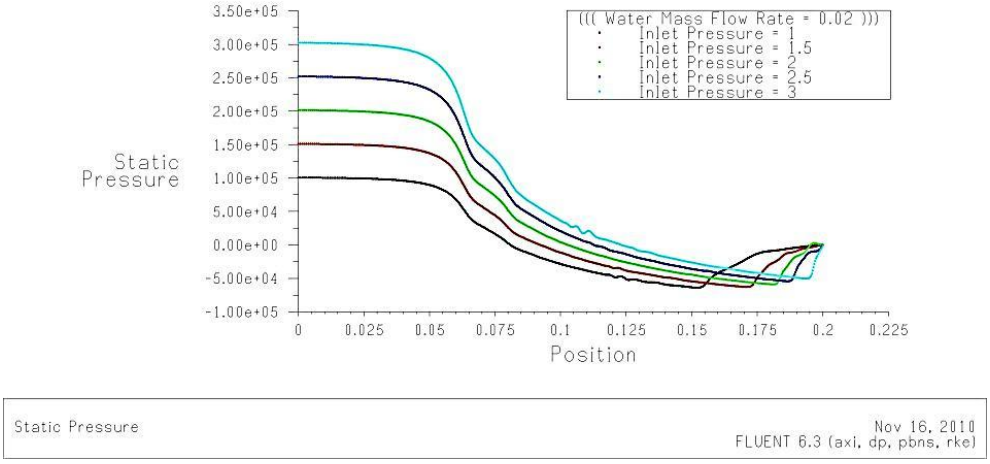

Figure (6. 41). Static pressure distribution for various air inlet pressure and $\dot{m}_{water} = 0.02$

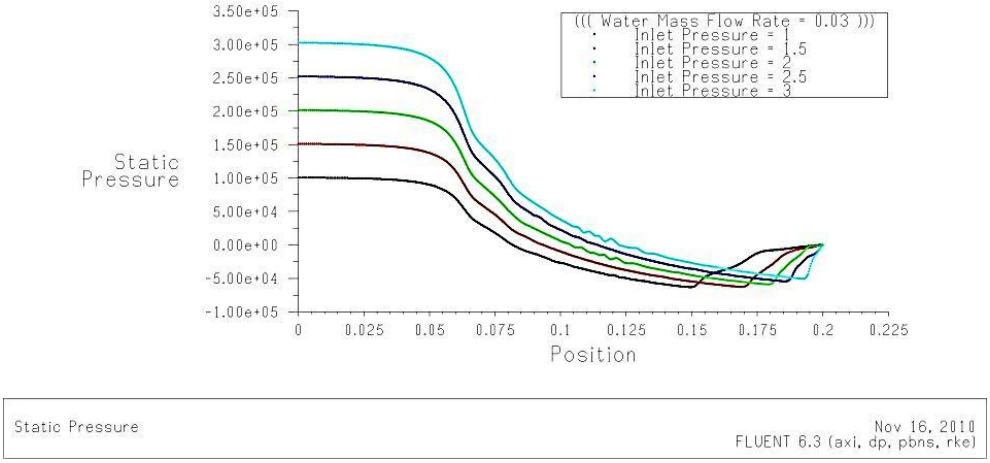

Figure (6. 42). Static pressure distribution for various air inlet pressure and $\dot{m}_{water} = 0.03$

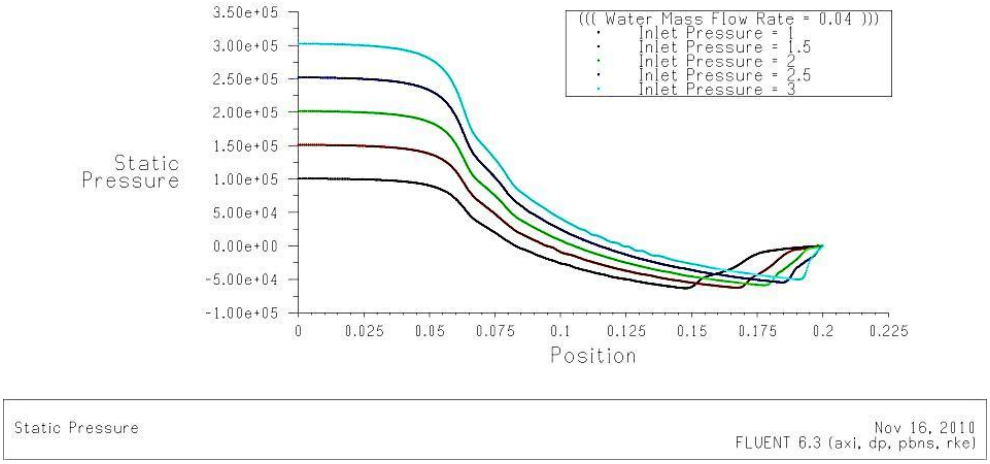

Figure (6. 43). Static pressure distribution for various air inlet pressure and $\dot{m}_{water} = 0.04$

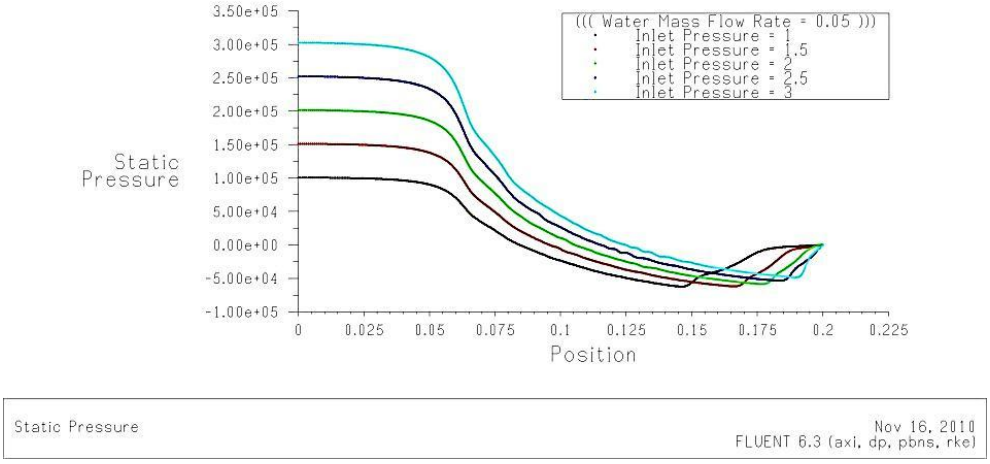

Figure (6. 44). Static pressure distribution for various air inlet pressure and $\dot{m}_{water} = 0.05$

The velocity profiles of the nozzle exhaust air flow for different air inlet pressure and constant water mass flow rate are shown in Figure (6.45). As well as the relevant figures in Section 6.3, this figure shows the air flow in the exhaust of the nozzle has a wavy profile and maximum velocity lies between the wall and the axis of the nozzle. For the different water mass flow rate but the same sand mass flow rate, Figures (6.46) to (6.49) show the exhaust air velocity profiles as a function of air inlet pressure. All figures show that by increasing the air inlet pressure the maximum velocity increases, however, simultaneously due to moving the shockwave toward the nozzle exit, especially for higher pressure, the axis velocity decreases. This phenomenon is highlighted by increasing the water mass flow rate. As Figure (6.48) shows, for the water mass flow rate of 0.04 kg/s and the air inlet pressure 3 atm, the air axis velocity is

nearly equal to 0 m/s. Further details of velocity profiles throughout the exhaust of the nozzle are illustrated in Figures (6.50) to (6.52).

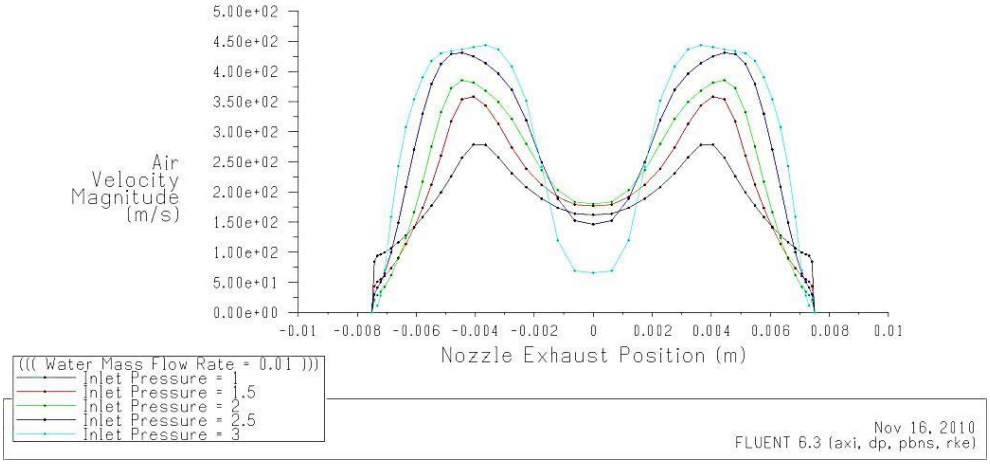

Figure (6. 45). The Nozzle exhaust air velocity profiles comparison between different air inlet pressure and $\dot{m}_{water} = 0.01$

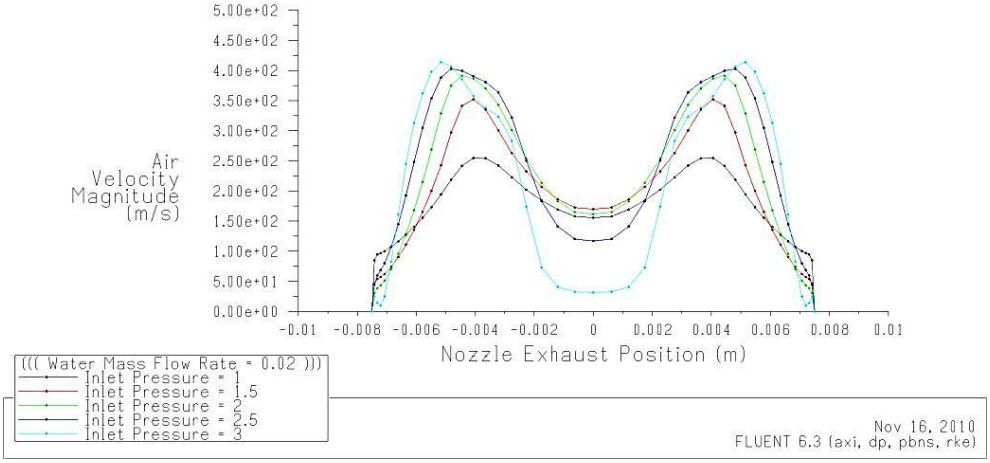

Figure (6. 46). The Nozzle exhaust air velocity profiles comparison between different air inlet pressure and $\dot{m}_{water} = 0.02$

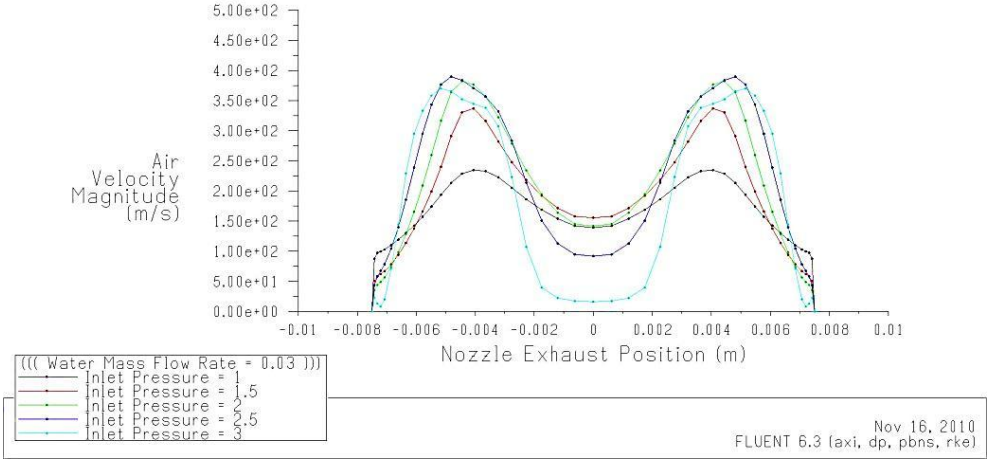

Figure (6. 47). The Nozzle exhaust air velocity profiles comparison between different air inlet pressure and $\dot{m}_{water} = 0.03$

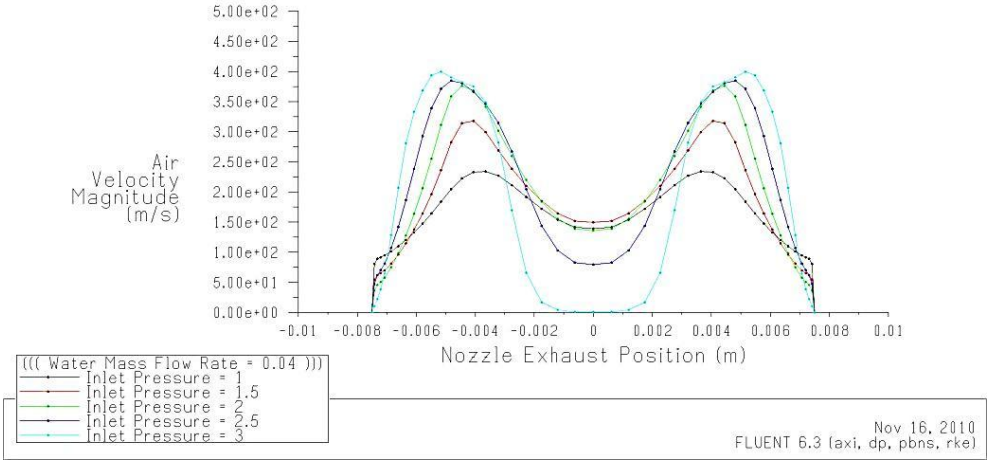

Figure (6. 48). The Nozzle exhaust air velocity profiles comparison between different air inlet pressure and $\dot{m}_{water} = 0.04$

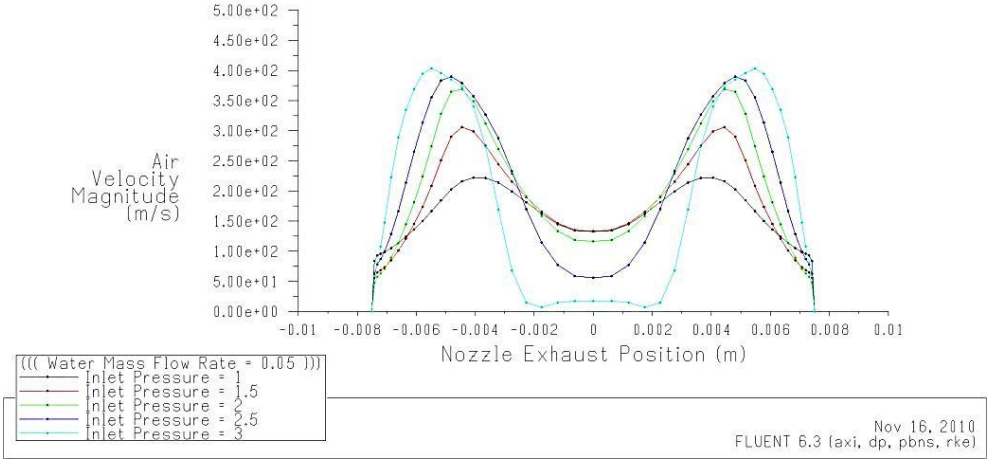

Figure (6. 49). The Nozzle exhaust air velocity profiles comparison between different air inlet pressure and $\dot{m}_{water} = 0.05$

The air velocity vectors shown in Figures (6.50) to (6.52) are computed for the air-sand-water three-phase flow and different air inlet pressure. In these figures the mass flow rates of the sand particles and water droplets are 0.02 and 0.04 kg/s, respectively. Regarding these figures, the most reduction in air velocity happens in the divergent part and near the axis of the nozzle where the shock wave occurs. This minimum velocity moves out by increasing the air inlet pressure. Figure (6.52) as well as Figure (6.48) confirms that the air velocity in the centre of the nozzle's exit is about zero; however, the maximum velocity is expected in the air single-phase flow through the nozzle (as Figure (6.53) shows).

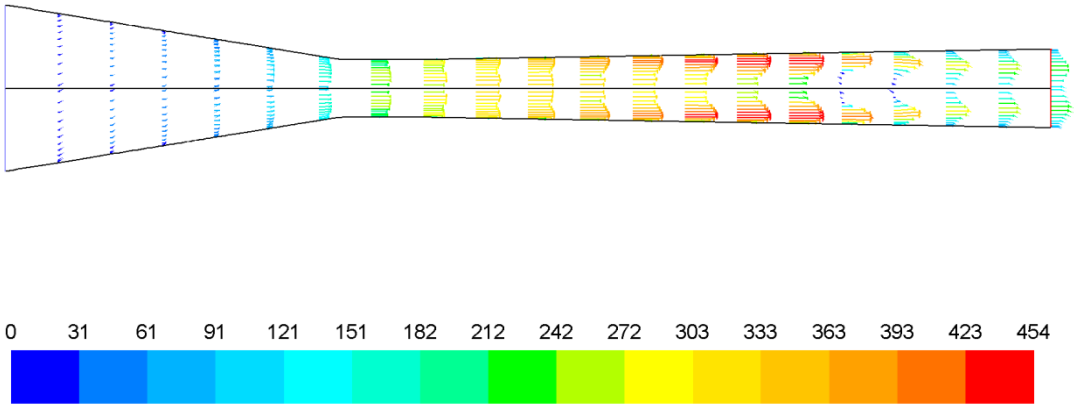

Figure (6. 50). Velocity vectors for three-phase flow ($p_{in} = 1atm$)

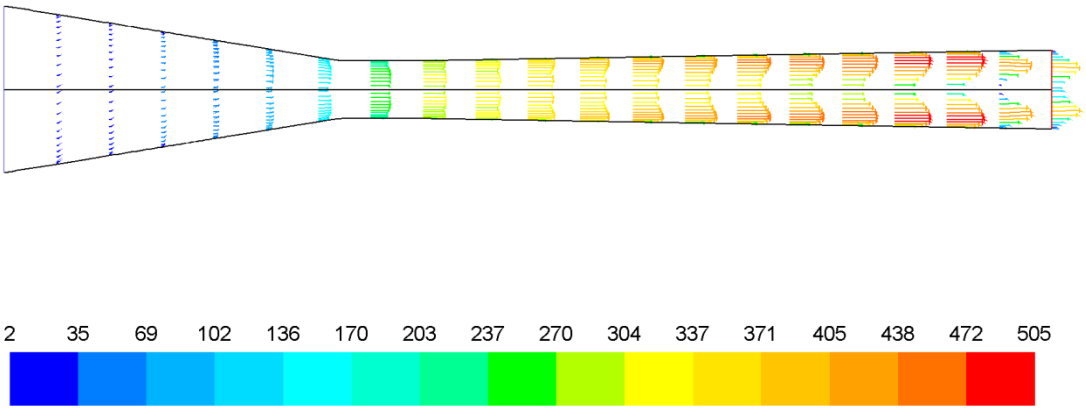

Figure (6. 51). Velocity vectors for three-phase flow ($p_{in} = 2atm$)

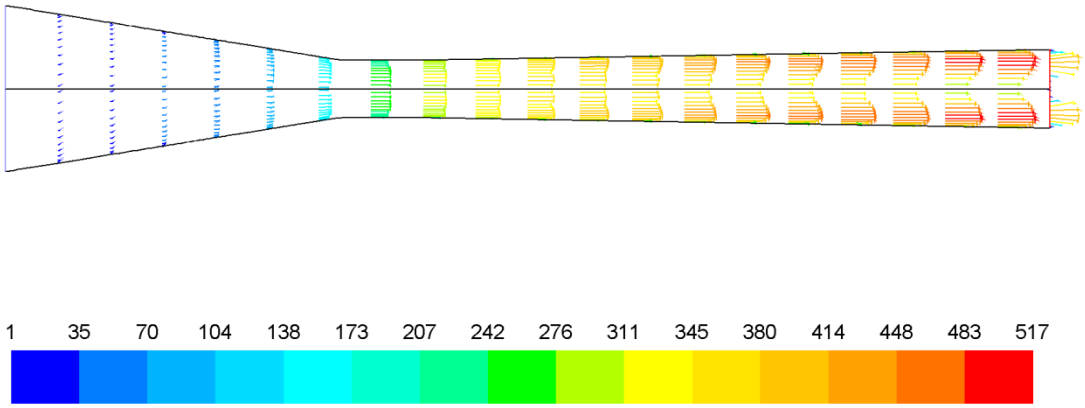

Figure (6. 52). Velocity vectors for three-phase flow ($p_{in} = 3atm$)

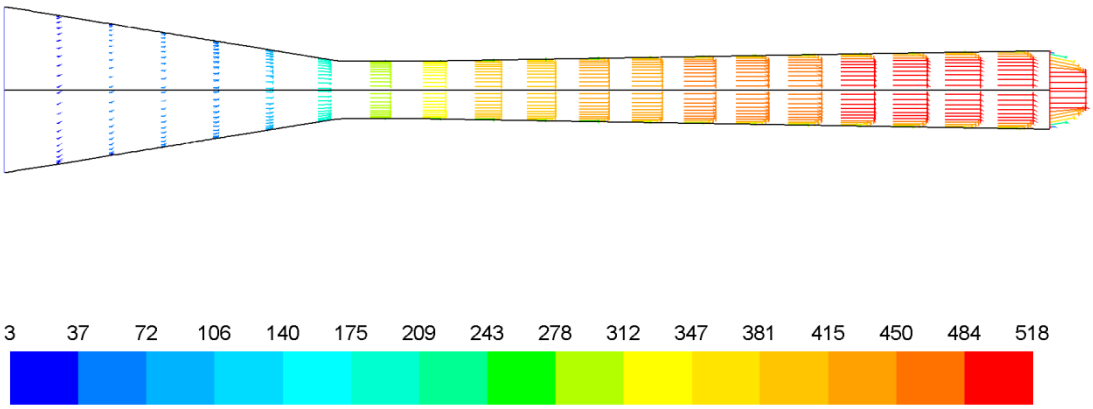

Figure (6. 53). Velocity vectors for air single-phase flow ($p_{in} = 3atm$)

Facet average air exhaust velocity is shown in Figure (6.54). By increasing the water mass flow rate, the average exhaust air velocity decreases. As Figure (6.54) shows this is true for inlet pressure less than 3 atm. For air inlet pressure of 3atm, as Figure (6.39) shows, the shockwave comes out to the nozzle exit and so disturbs the exhaust flow. Similar results are shown in Figure (6.55) which shows the average exhaust air velocity plotted for different water mass flow rate as a function of air inlet pressure. As this figure shows an air inlet pressure of 3atm is acceptable just for the water mass flow rate of 0.01 kg/s, and for other water mass flow rates this pressure has an inverse effect on the average exhaust air velocity; however, in shot-blasting system, the abrasive mean exhaust velocity is more important than air velocity. Computed values of air exhaust average velocity for each air inlet pressure and water mass flow rate are printed in Table (6.6).

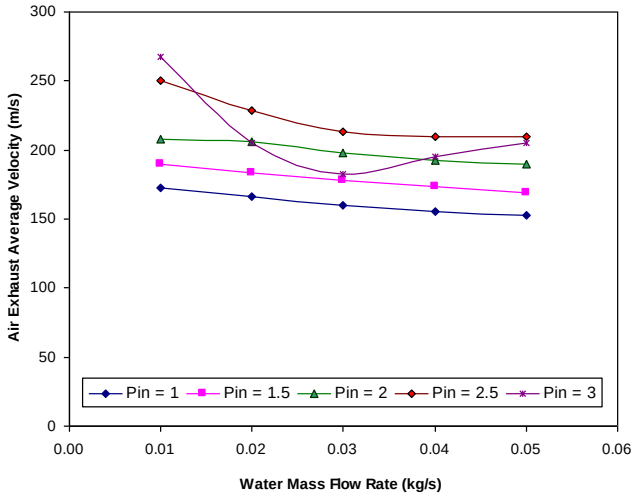

Figure (6. 54). Air exhaust average velocity as a function of water mass flow rate for various air inlet pressure

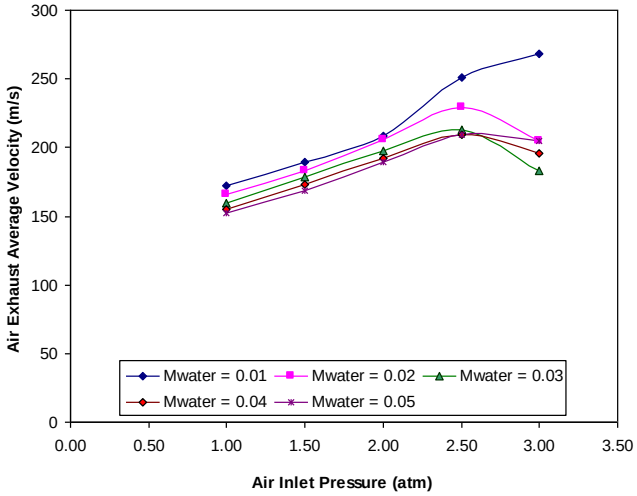

Figure (6. 55). Air exhaust average velocity as a function of air inlet pressure for various water mass flow rate

Table (6. 6). Air exhaust average velocity (m/s)

Water Mass Flow Rate (kg/s) \ Air Inlet Pressure (atm)	*1*	*1.5*	*2*	*2.5*	*3*
0.01	172.14	189.52	208.26	250.73	267.83
0.02	166.29	183.5	205.66	229.04	205.08
0.03	159.82	178.1	197.83	213.42	182.7
0.04	155.38	173.42	192.07	209.33	195.54
0.05	152.53	168.68	189.86	209.81	205.13

As the air average exhaust velocity, the air mass flow rates are dependent on the air inlet pressure and the water mass flow rate. For the constant sand mass flow rate of 0.02 kg/s, Figure (6.56) shows the dependency of the air mass flow rate to the inlet pressure and the water mass flow rate. The air mass flow rate is correlated with the inlet pressure and inversely correlated with the water mass flow rate. On the other hand, unlike the air average exhaust velocity, the air mass flow rate is independent of the situation of the shockwave inside the nozzle.

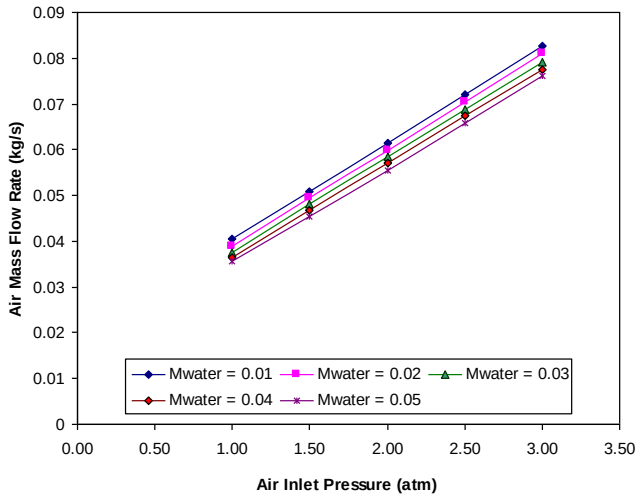

Figure (6. 56). Air mass flow rate as a function of air inlet pressure for various water mass flow rate

The printed values on Table (6.7) show that increasing the air inlet pressure by 3 times, from 1atm to 3atm, the air mass flow rate increases about 110%. While increasing the water mass flow rate has an inverse effect on the air mass flow rate, and that increasing the water mass flow rate by 5 times, from 0.01 kg/s to 0.05 kg/s, the air mass flow rate decreases about 10%.

Table (6. 7). Air mass flow rate (kg/s)

Water Mass Flow Rate (kg/s) \ Air Inlet Pressure (atm)	1	1.5	2	2.5	3
0.01	0.0404	0.0508	0.0614	0.0721	0.0827
0.02	0.0389	0.0494	0.0599	0.0703	0.0811
0.03	0.0375	0.048	0.0584	0.0687	0.079
0.04	0.0364	0.0467	0.0571	0.0673	0.0776
0.05	0.0356	0.0455	0.0555	0.0657	0.076

Water droplets, in the same way as sand particles, pass through the nozzle by 44 trajectories, shown in Figure (6.30). All particles and droplets enter into the nozzle in

low velocity and are accelerated through the nozzle by increasing the air flow velocity in the converging and diverging sections of the nozzle. Definitely, the performance of the nozzle in the shot-blasting system significantly depends on the abrasive exhaust velocity. Figure (6.57) shows the sand particles exhaust velocity along the 22 trajectories for various air inlet pressure and water mass flow rates. This figure confirms almost the same behaviour of the exhaust velocity for water droplets and sand particles as shown in Figure (6.31). In this section, Figure (6.57) has been illustrated as a representative of all other water mass flow rates, which have almost the same trends.

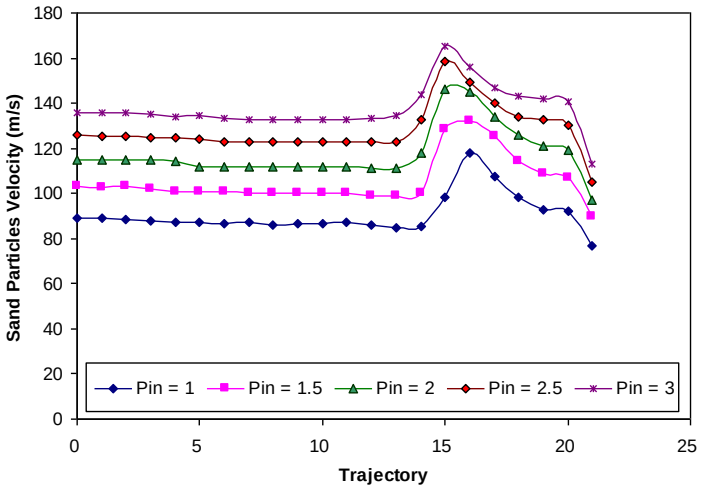

Figure (6. 57). Exhaust velocity of sand particles in three-phase flow with various air inlet pressure (water mass flow rates = 0.01 kg/s)

The average velocity of the sand particles in the exhaust of the nozzle can be found in Figure (6.58). The average velocity of the sand particles unlike the air average velocity, shown in Figure (6.54), has an almost uniform trend by increasing the air inlet pressure. Figure (6.58) shows the sand particles have independent exhaust velocity to the shockwave situation inside the nozzle. Finally, for all the water mass flow rates, as shown in Figure (6.58), the mean velocity of the sand particles are proportional to the air inlet pressure.

The computed values of the mean velocity of the sand particles for the various air inlet pressure and water mass flow rate are printed in Table (6.8). Increasing the air inlet pressure by three times, from 1atm to 3atm, depending on the water mass flow rate the mean exhaust velocity of the sand particles rises from 52 to 62 percent. Meanwhile, by increasing the water mass flow rate five times, from 0.01 kg/s to 0.05 kg/s, for the

various air inlet pressure the mean exhaust velocity of the sand particles declines about 16 to 21 percent.

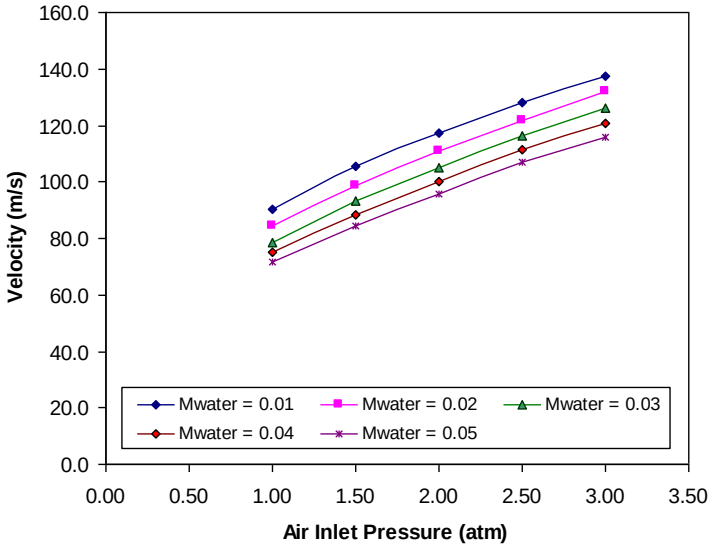

Figure (6. 58). Average sand particles exhaust velocity

Table (6. 8). Average sand particles exhaust velocity (m/s)

Water Mass Flow Rate (kg/s) \ Air Inlet Pressure (atm)	1	1.5	2	2.5	3
0.01	90.4	105.3	117.5	128.0	137.6
0.02	84.3	98.5	111.0	121.9	131.8
0.03	78.7	93.1	105.1	116.5	126.2
0.04	75.1	88.3	100.3	111.3	120.5
0.05	71.7	84.4	95.8	107.0	116.0

Almost the same trend of the sand particles can be observed for the mean exhaust velocity of the water droplets in Figure (6.59) and Table (6.9). The computed results show that by a three times increment of the air inlet pressure, the mean exhaust velocity of the water droplets goes up to 54 percent. On the other hand, during the five times increase of the water mass flow rate, from 0.01 kg/s to 0.05 kg/s, the mean exhaust velocity of the sand particles decreases up to 21 percent.

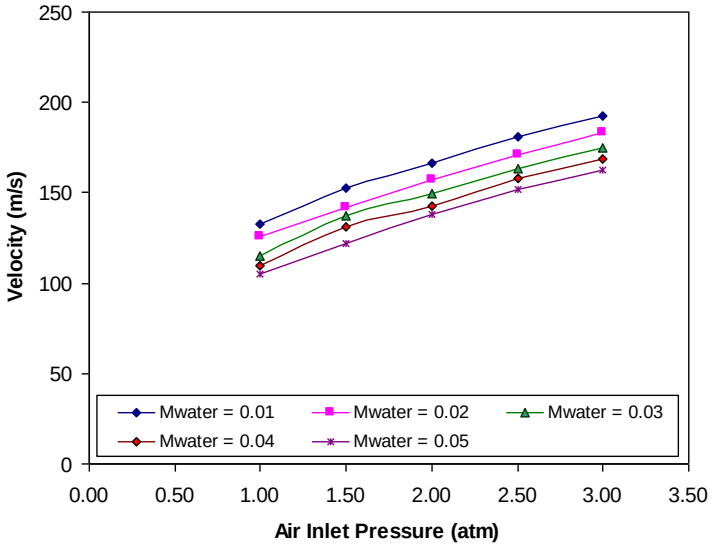

Figure (6. 59). Average water droplets exhaust velocity

Table (6. 9). Average water droplets exhaust velocity (m/s)

Water Mass Flow Rate (kg/s) \ Air Inlet Pressure (atm)	1	1.5	2	2.5	3
0.01	133.0	152.6	166.7	181.3	192.6
0.02	125.7	141.5	157.2	170.8	183.6
0.03	115.3	137.4	149.2	163.1	174.9
0.04	110.0	130.8	142.6	158.0	169.0
0.05	105.4	121.8	138.3	152.1	162.7

6.5 Various mass flow rate of sand particles

The momentum of sand particles is the most important parameter in a shot-blasting system which depends on some other parameter such as the momentum of the air flow, the water droplets' momentum and the inlet temperature of the secondary phase. In Section 6.4 the effect of the various mass flow rates of the water droplets on the air and sand exhaust velocity, with a different mass flow rate of the sand particles has been presented. Here, the main parameter is the mass flow rate of the sand particles and as in Section 6.4, the air inlet pressure and abrasive inlet temperature are assumed constant and equal to 2atm and 300 K, respectively.

The diameter of sand particles the same as the real size in shot-blasting machines are supposed to be equal to 0.0002 m with a constant bulk density of 3380 kg/m^3. The sand

particles exhaust average momentum, which is equal to the particles' mass time to the exhaust average velocity, are shown in Figure (6.60). This figure shows that by increasing the sand mass flow rate as well as the water mass flow rate, the exhaust average momentum of each particle decreases. Obviously, as propellant energy, in this study, is constant so by increasing the mass flow rate of the abrasive media the exhaust momentum of each sand particle decreases. However the sand particle exhaust momentum is inversely proportional to the sand mass flow rate, but the total momentum of sand particles, which exhaust from the nozzle, and the sand mass flow rate are in direct proportion. Figure (6.61) shows the total average momentum of sand particles, which exhaust from the nozzle, per second.

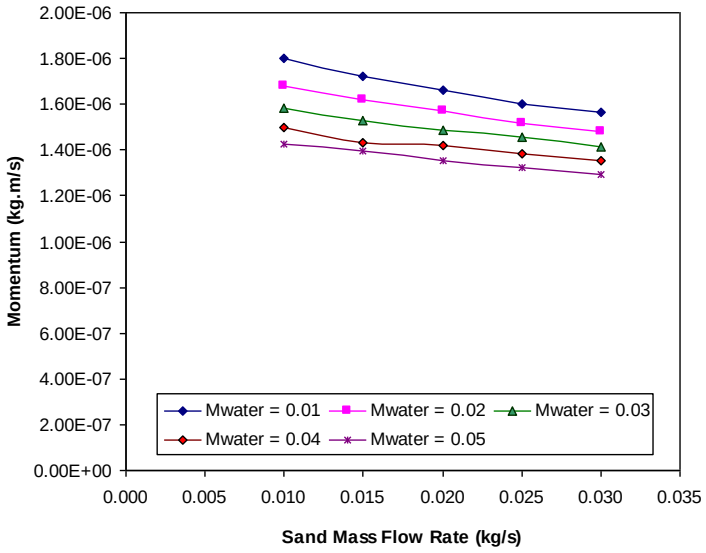

Figure (6. 60). Average momentum of sand particles in exhaust of Nozzle

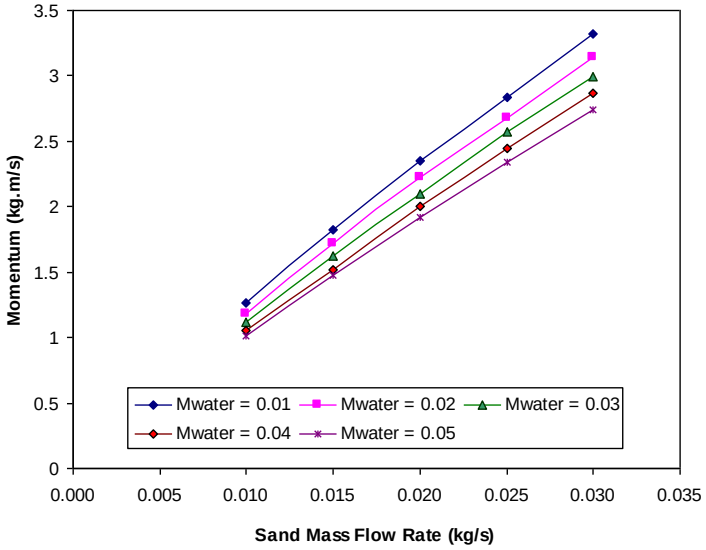

Figure (6. 61). Total average momentum of sand particles in exhaust of Nozzle

The printed data in Table (6.10), for total average momentum, shows that by increasing the sand mass flow three times, from 0.01 kg/s to 0.03 kg/s, the average momentum of all the particles increment about 2.6 to 2.7 times, depending on the water mass flow rates. On the other hand, the water mass flow rate and the total average momentum of the sand particles are in inverse proportion, which by a five times increase of the water mass flow rate, from 0.01 kg/s to 0.05 kg/s, declines about 17 to 20 percent of total momentum of the sand particles.

Table (6. 10). Total average momentum of sand particles in exhaust of Nozzle per second ((kg.m/s)/s)

		Water Mass Flow Rate (kg/s)				
		0.01	*0.02*	*0.03*	*0.04*	*0.05*
Sand Mass Flow Rate (kg/s)	*0.01*	1.27	1.19	1.12	1.06	1.01
	0.015	1.83	1.72	1.62	1.51	1.48
	0.02	2.35	2.22	2.10	2.01	1.92
	0.025	2.83	2.68	2.57	2.45	2.34
	0.03	3.32	3.14	3.00	2.87	2.75

6.6 The effect of inlet temperature of water droplets and sand particles on Nozzle flow characteristic

Heat transfer to water droplets and sand particles in a blasting tank before propelling with an air flow is an initiative for increasing the performance of a shot-blasting machine. The heated sand particles and water droplets during the flow inside the blasting hose can transfer some heat energy to the air flow and increase the dynamic pressure or kinetic energy of the air flow. This will happen before the flow enters into the nozzle and the nozzle inlet flow conditions are almost in thermal equilibrium, however, as this study focuses on the air-sand-water three phase flow through the nozzle, so the effects of heated water, and consequently heated sand particles, on the three-phase flow characteristic are computed in the nozzle. Definitely, this part of the simulation is a case study and can be modelled and practically tested in the future.

The following subsections present the effect of heated abrasive, sand particles and water droplets, on the nozzle flow characteristic in two different inlet boundary conditions, constant air inlet pressure and constant air inlet mass flow rate.

6.6.1 Constant air inlet pressure

Sand particles and water droplets are propelled through the nozzle by high pressure air flow with a static pressure of 2 atm and ambient temperature. This section is going to present the simulation results of the aforementioned multi-phase flow by a various sand mass flow rate, from 0.01 kg/s to 0.03 kg/s with an increment of 0.005 kg/s, a constant water mass flow rate of 0.03 kg/s, a different inlet temperature of sand particles and water droplets, from 300 K to 360 K with an increment of 10 K. Sand particles as well as water droplets are assumed spherical with the same diameter of 0.2 mm.

Figure (6.62) shows the air velocity vectors of the air-sand-water flow through the nozzle with the same mass flow rate of sand particles and water droplets (0.03 kg/s), and an inlet temperature of 300 K. In this simulation the air inlet temperature is 300 K, which means there is not any temperature difference between the air and abrasive inlet flow conditions.

The effect of increasing the inlet temperature of the sand particles and water droplets from 300 K to 360 K has been computed for velocity distribution through the nozzle, and the air velocity vectors for the inlet temperature of 360 K is shown in Figure (6.63).

The comparison of Figures (6.62) and (6.63) show a slight difference, especially in the last part of the nozzle, for velocity vectors by different inlet abrasive temperatures.

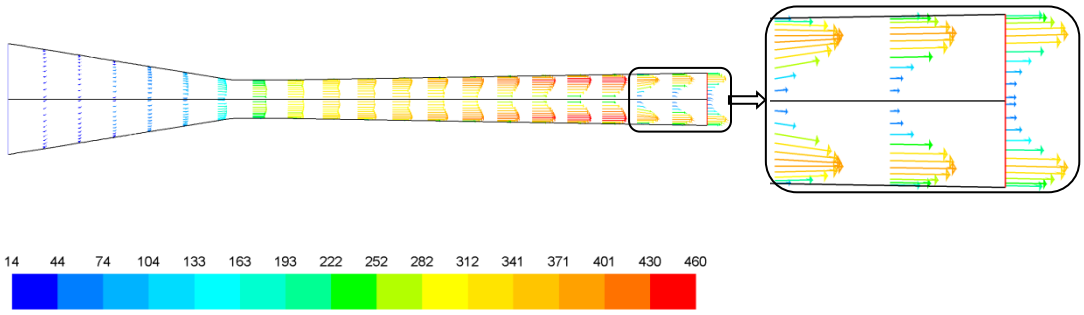

Figure (6. 62). Velocity vectors of multi-phase flow, (T_{inlet} = 300K)

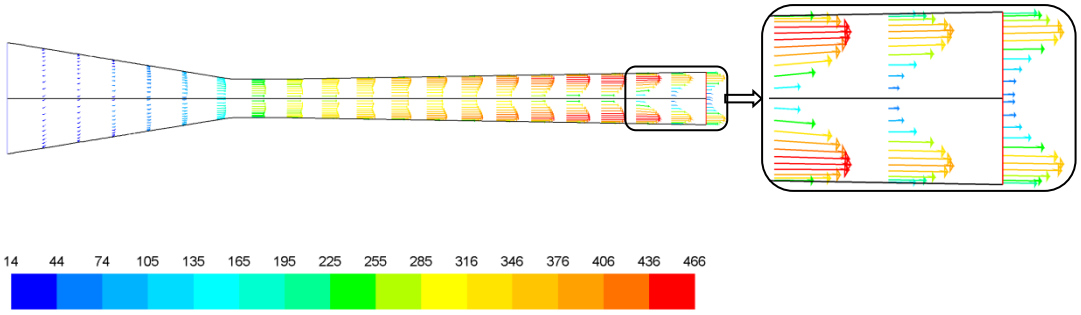

Figure (6. 63). Velocity vectors of multi-phase flow, (T_{inlet} = 360K)

The contours of the air temperature distribution through the nozzle for the inlet water droplets and sand particles temperature of 300 K and 360 K are shown in Figures (6.64) and (6.65). In Figure (6.64) as the inlet air flow has the same temperature of inlet water droplets and sand particles, the temperature contours are due to the compressibility of the air flow inside the nozzle and then heat transfer between the air and the water droplets as well as the sand particles. Therefore, as Figure (6.64) shows in the entrance of the nozzle and in almost the first half of the convergence part of the nozzle, where the flow is incompressible, uniform temperature is experienced.

By increasing the inlet temperature of water droplets and sand particles from 300 K to 360 K, the temperature difference between the air inlet flow and the secondary phases increases up to 60 K. Due to this temperature difference the heat transfer occurs from the water droplets and sand particles to the air flow and starts in the entrance of the nozzle. Therefore, as Figure (6.65) shows the temperature contours, unlike Figure (6.64), have been moved toward the entrance of nozzle.

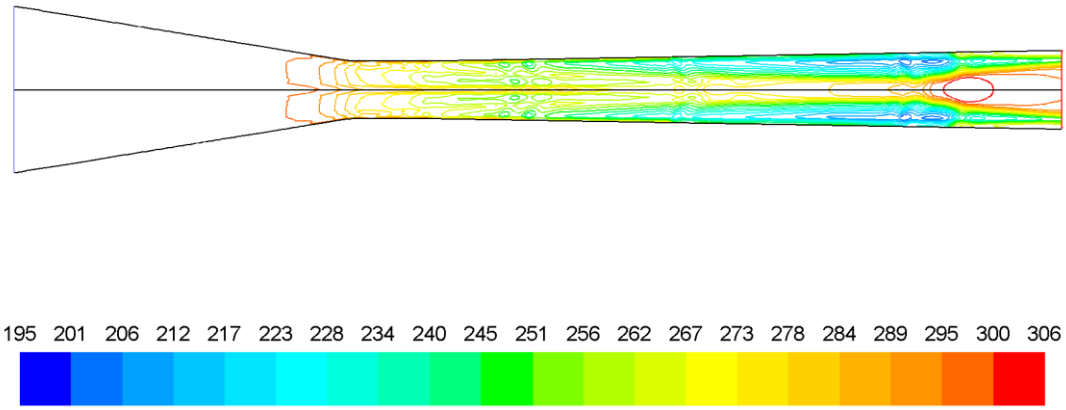

Figure (6. 64). The temperature contours of air in multi-phase flow, (T_{inlet} = 300 K)

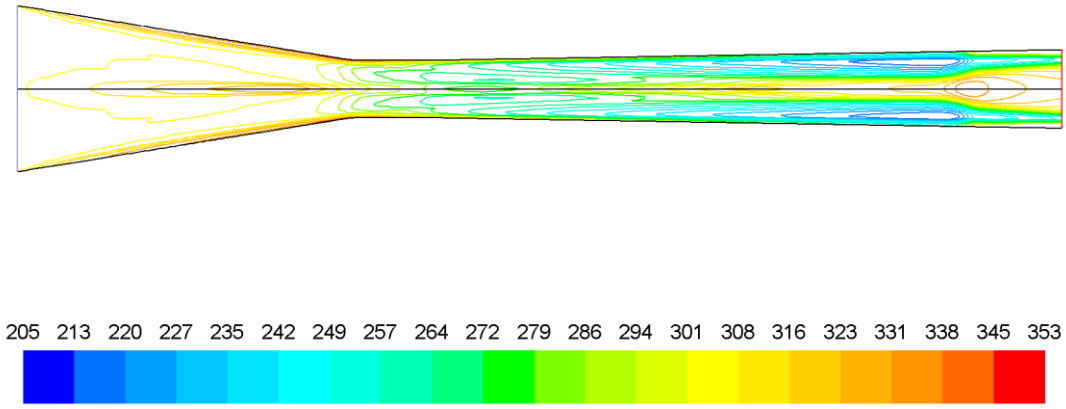

Figure (6. 65). The temperature contours of air in multi-phase flow, (T_{inlet} = 360 K)

Secondary phases, water droplets and sand particles, are propelled through the nozzle by the air flow, and Figure (6.66) shows the distribution of them inside the nozzle. In Figure (6.66), the sand particles and water droplets, which are coloured by static temperature, enter into the nozzle by an inlet temperature of 300 K. Inside the nozzle and especially in the divergence part of the nozzle, the temperature of the particles/droplets has been slightly changed. This phenomenon, according to Figure (6.64), is due to the heat transfer from the sand particles and water droplets to the air flow.

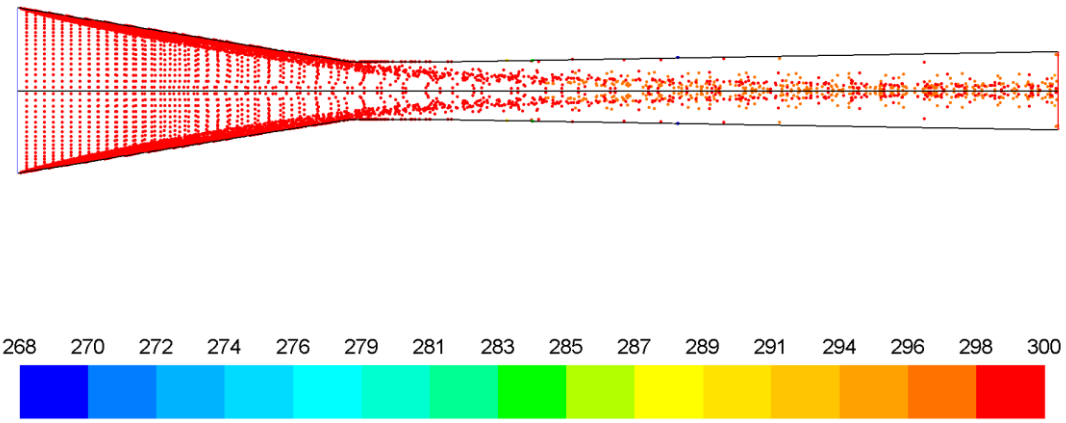

Figure (6. 66). The temperature distribution of sand particles and water droplets through the nozzle (T_{inlet} = 300K)

In Figure (6.67), the sand particles, as well as the water droplets, have a high initial temperature in the entrance of the nozzle. They mix with the air flow just after the nozzle entrance, and the high pressure air flow propels the abrasive media, with 60 K temperature difference, through the nozzle. Because of almost high temperature difference, between the abrasive media and the air flow, heat energy transfer from abrasive media to air flow. Hence the temperature of the sand particles in addition to the water droplets decreases from the inlet temperature of 300 K.

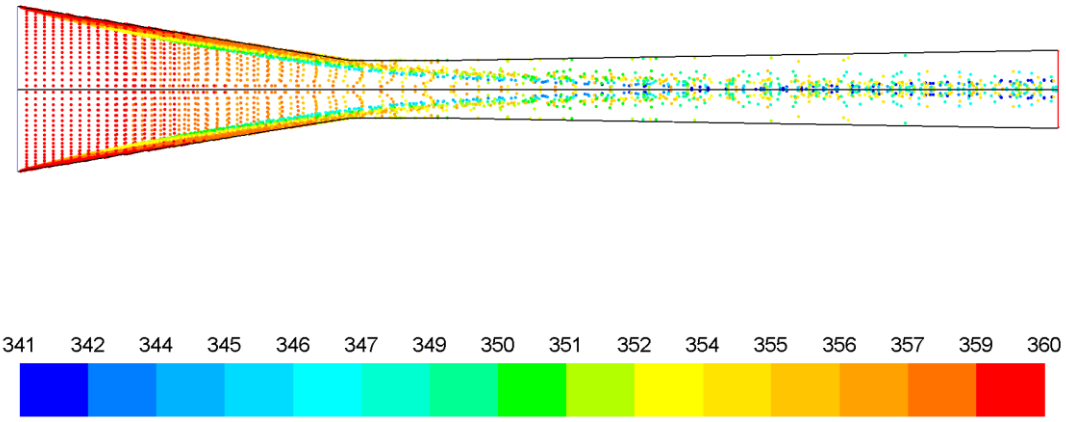

Figure (6. 67). The temperature distribution of sand particles and water droplets through the nozzle (T_{inlet} = 360K)

The profiles of the temperature of the exhaust air flow from the nozzle for the various inlet temperatures of the sand particles and water droplets, the same mass flow rate of the sand particles and water droplets (0.03 kg/s), and an air inlet temperature of 300 K are shown in Figure (6.68). This figure demonstrates the rising of the

temperature's profile by increasing the inlet temperature of the water droplets and sand particles.

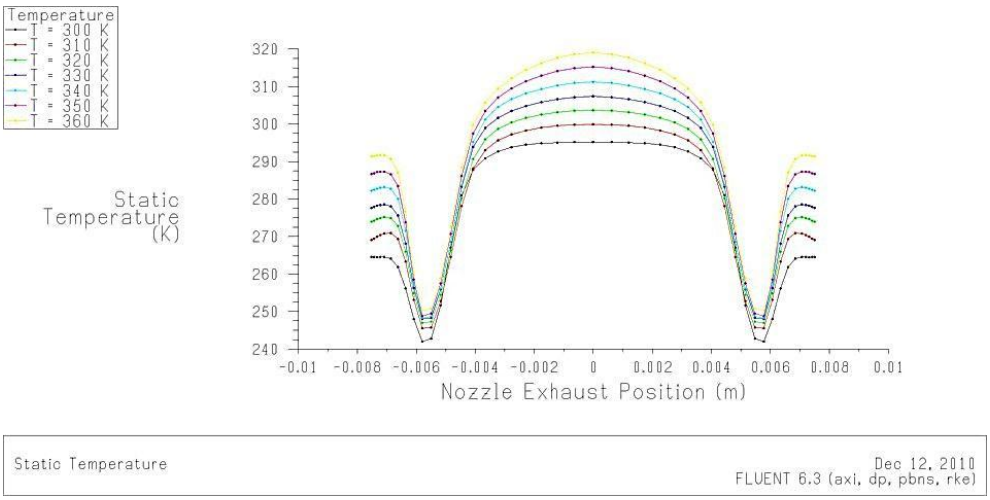

Figure (6. 68). Air temperature profiles of multi-phase flow in exhaust of Nozzle

In constant air inlet pressure and temperature by increasing the inlet temperature of the secondary phases, due to the transfer of thermal energy between the abrasive media and air flow, it is expected to increase the air flow exhaust velocity. The effect of increasing the inlet temperature of the sand particles and water droplets on the air flow exhaust velocity is shown in Figure (6.69).

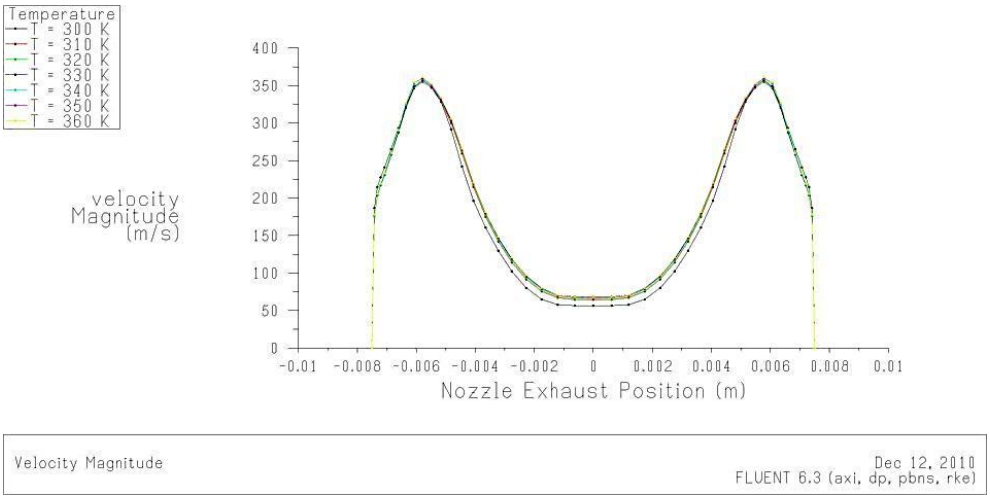

Figure (6. 69). Air velocity profiles of multi-phase flow in exhaust of Nozzle

Some flow characteristics have been compared in Table (6.11) for two different inlet temperatures of the sand particles and water droplets, 300 K and 360 K.

More details of the exhaust air average velocity as a function of the various sand mass flow rates and the inlet temperature related to the sand particles and water droplets are shown in Figure (6.70) and Table (6.12). Increasing the inlet temperature to 360K

raises the air exhaust velocity up to about 3.4 percent. The increase of the air exhaust velocity is due to the heat transfer between the secondary phases and the air flow during flow inside the nozzle.

Table (6. 11). Flow characteristics of air-sand-water flow with inlet temperature 300 K vs. inlet temperature 360

Sand particles and Water droplets Temperature	T = 300 K	T = 360 K
Inlet Air Average Velocity (m/s)	20.3	19.9
Exhaust Air Average Velocity (m/s)	210.7	218.0
Exhaust Air Average Temperature (K)	272.6	291.0
Air Mass Flow Rate (g/s)	56.6	55.2
Exhaust Sand Average velocity (m/s)	93.12	92.4
Exhaust Water Average velocity (m/s)	138.6	138.3

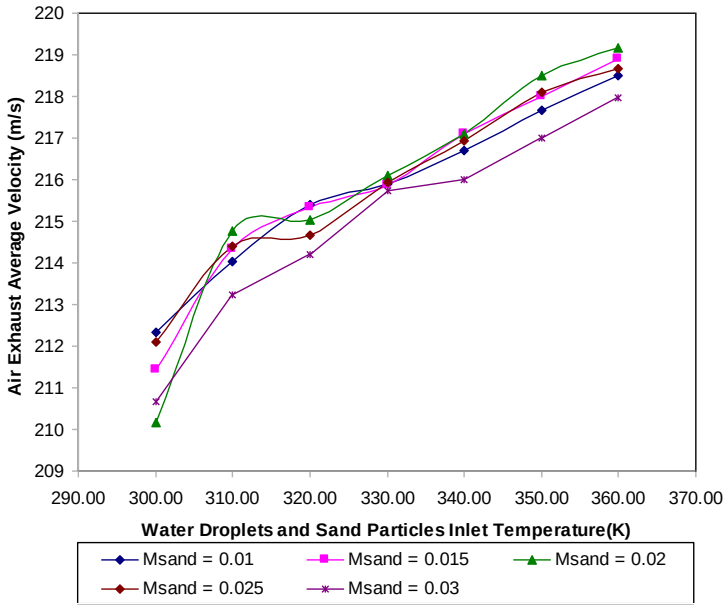

Figure (6. 70). Air exhaust average velocity as a function of abrasive inlet temperature

Increasing the inlet temperature of the sand particles and water droplets has an effect on the air exhaust temperature as well as the mass flow rate of the air flow through the nozzle, too. Figure (6.71) shows that by increasing the inlet temperature of the secondary phases the exhaust temperature of the air flow, which propels the abrasive toward the nozzle exhaust, goes up. The reverse trend is observed on the air mass flow rate through the nozzle by increasing the inlet temperature of the sand particles and water droplets.

Table (6. 12). Air exhaust average velocity for various sand mass flow rates and abrasive inlet temperatures

Sand Particles & Water Droplets Inlet Temperature (K) \ Sand Mass Flow Rate (kg/s)	0.01	0.015	0.02	0.025	0.03
300	212.34	211.45	210.18	212.1	210.67
310	214.04	214.32	214.78	214.41	213.22
320	215.39	215.32	215.04	214.68	214.19
330	215.9	215.86	216.09	215.92	215.73
340	216.71	217.11	217.1	216.93	215.99
350	217.68	217.99	218.5	218.11	217.00
360	218.49	218.91	219.18	218.68	217.98

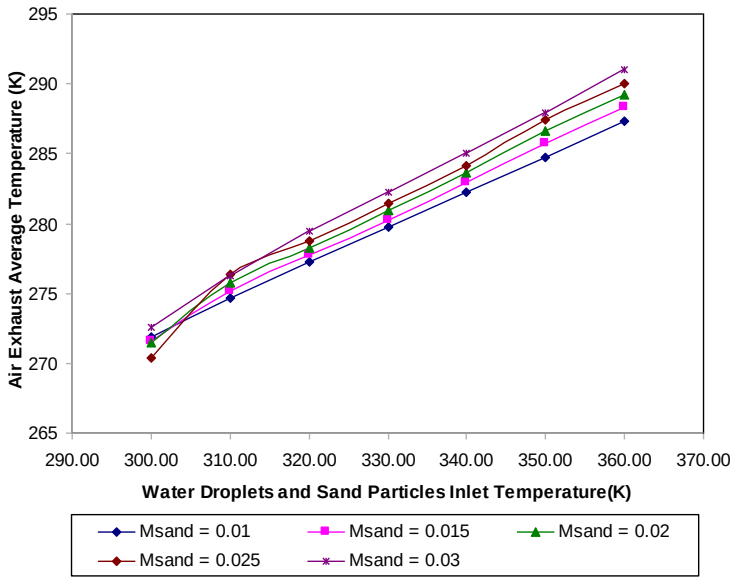

Figure (6. 71). Air exhaust average temperature as a function of abrasive inlet temperature

As Figure (6.72) shows the air mass flow rate has a reverse proportion to the inlet temperature of the abrasive. Definitely, this is because of the expansion of the air flow by increasing its temperature due to the heat transfer from the abrasive media.

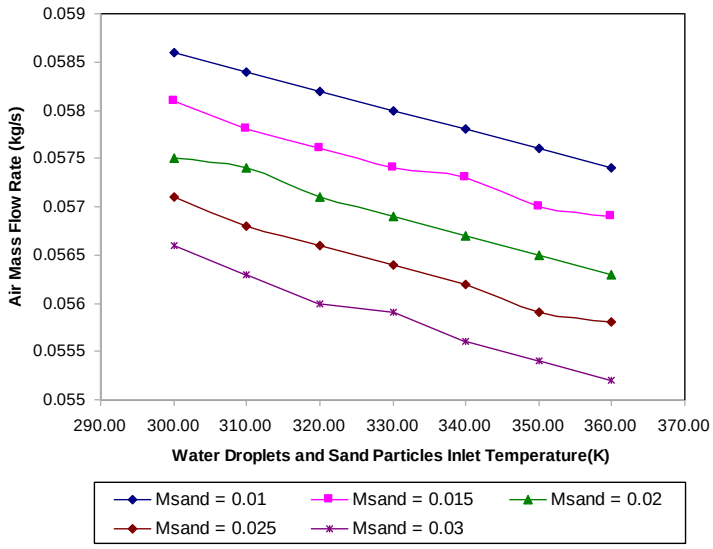

Figure (6. 72). Air mass flow rate as a function of abrasive inlet temperature

The sand particles exhaust average velocity as a function of the abrasive media's inlet temperature, for various sand mass flow rates are shown in Figure (6.73). This Figure shows that by increasing the inlet temperature of the sand particles and the water droplets, the velocity of the sand particles not only is not increased but also it is decreased or almost remains constant.

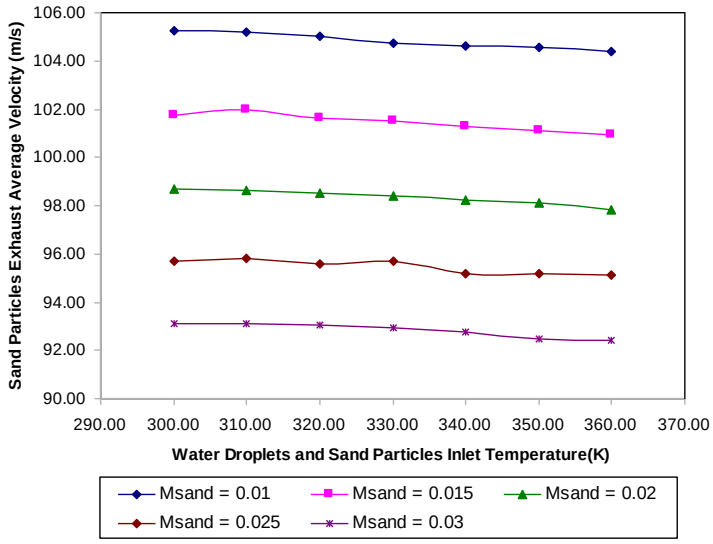

Figure (6. 73). Sand particles exhaust average velocity as a function of abrasive inlet temperature

As Figure (6.70) and (6.72) show, the raising of the inlet temperature of the abrasive media, on the one hand increases the air velocity and on the other hand decreases the air mass flow rates, but simultaneously Figure (6.73) demonstrates that the sand exhaust

velocity decreases. Consequently, due to increasing the inlet temperature of the sand particles and water droplets, the momentum of the air flow must decrease or remain nearly constant.

Figure (6.74) shows the total average momentum of the air flow exhaust from the nozzle, per second.

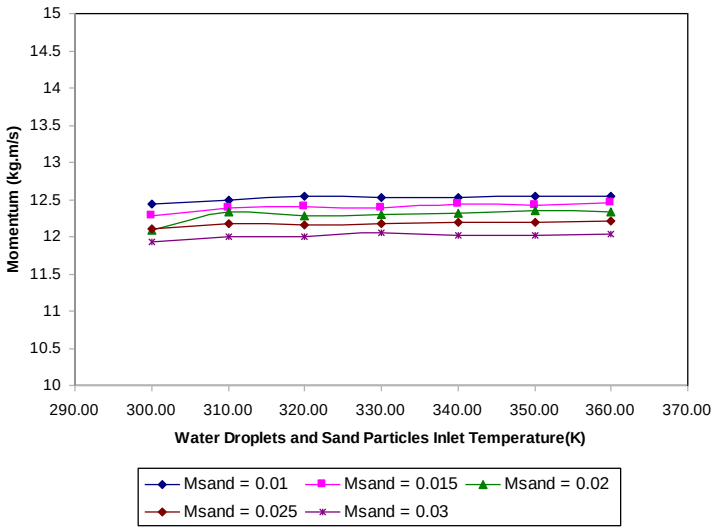

Figure (6. 74). Total average momentum of air flow in exhaust of Nozzle

Figure (6.74) confirms that the air flow momentum almost is not influenced by the inlet temperature of the secondary phases; however, by increasing the sand mass flow rate the exhaust air flow momentum is decreasing.

6.6.2 Constant air inlet mass flow rate

A compressor as a mechanical device, which compresses the air flow is a main part of all dry and wet sand-blasting machines. Compressor maximum flow in addition to compressor maximum pressure is the most important characteristic for selecting the appropriate compressor. Operating flow capacity or the volumetric flow rate of a fluid displaced by a compressor is usually given by CFM which is an acronym for Cubic Foot per Minute. On the other hand as the Mach number of the air flow in the entrance of the nozzle in a sand blasting machine is generally less than 0.3, so in this study the mass flow rate is applied as an inlet condition instead of CFM.

This section is going to show the effect of the secondary phases' inlet temperature on the exhaust momentum of the air and sand flows as well as the air inlet pressure. In the following air-sand-water three-phase flow simulation the air inlet mass flow rate is

equal to 56.6 g/s. The sand particles and water droplets enter into the nozzle by the same mass flow rate of 30 g/s and different temperatures from 300 K to 360 K.

The average momentum of the air flow in the exhaust of the nozzle for different inlet boundary conditions is presented in Figure (6.75) and Table (6.13). The curve of the constant air inlet pressure, the blue curve in Figure (6.75), indicates that increasing the inlet temperature of the water droplets and sand particles has no considerable effect on the air exhaust momentum. Unlike the exhaust momentum of the constant air inlet pressure, this momentum has been influenced by the inlet temperature of the secondary phases for the constant air inlet mass flow rate. The momentum differences of the two different inlet conditions is due to the decreasing of the air mass flow rate on the constant air inlet pressure, as shown in Figure (6.72).

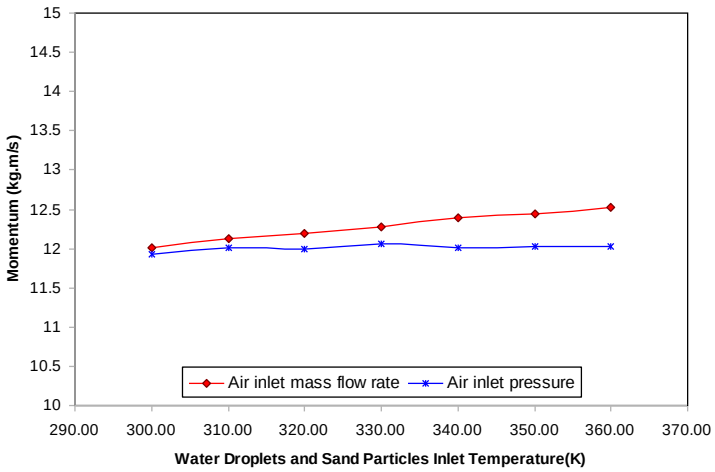

Figure (6. 75). Average momentum of air flow in exhaust of Nozzle

Table (6. 13). Air exhaust average momentum for different boundary conditions

Sand Particles & Water Droplets Inlet Temperature (K)	Inlet Boundary Conditions: *Constant air inlet pressure*	*Constant air inlet mass flow rates*
300	11.9239	12.0167
310	12.0043	12.1209
320	11.9946	12.1877
330	12.0593	12.2720
340	12.0090	12.3903
350	12.0218	12.4362
360	12.0325	12.5312

Figure (6.76) shows the sand particles' total average momentum as a function of the abrasive inlet temperature and the different boundary conditions. As this figure and the printed values in Table (6.14) show there is a slight difference in the momentum of the sand particles for the two different inlet boundary conditions, especially in the high inlet temperature.

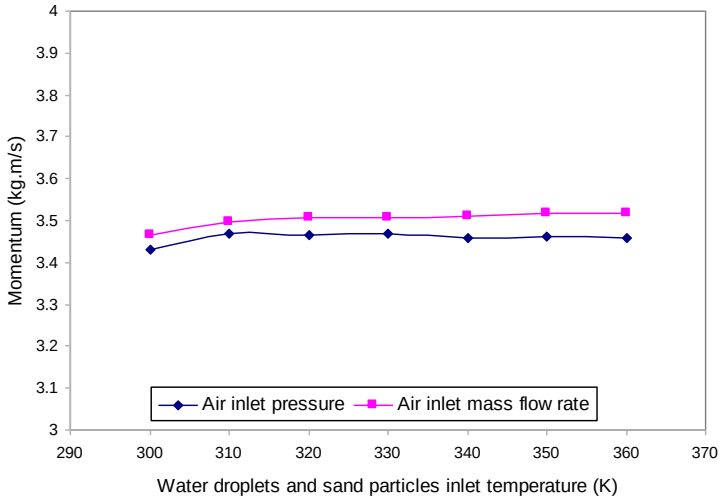

Figure (6. 76). Total average momentum of sand particles in exhaust of Nozzle

Table (6. 14). Sand particles total average momentum for different boundary conditions

Sand Particles & Water Droplets Inlet Temperature (K)	Inlet Boundary Conditions: Constant air inlet pressure	Inlet Boundary Conditions: Constant air inlet mass flow rates
300	3.4320	3.4668
310	3.4698	3.4968
320	3.4668	3.5055
330	3.4677	3.5055
340	3.4593	3.5109
350	3.4620	3.5166
360	3.4578	3.5184

Finally, Table (6.14) presents the gentle increasing of momentum by raising the inlet temperature of the abrasive media. In comparison with the constant air inlet pressure, in the constant air inlet mass flow rates, the sand particles gain higher momentum, during the flow inside the nozzle, by increasing the inlet temperature of the abrasive media. As Figure (6.75) shows this is due to the momentum differences of the air flow through the nozzle in the two different inlet boundary conditions.

6.7 Summary and conclusions

In this chapter, the air-sand-water three-phase nozzle flow was computed and discussed. The *Discrete Phase* model was used to model the air-sand-water three-phase flow through the nozzle with different boundary conditions, various mass flow rates of sand particles and water droplets. In addition, both the *Pressure-Based Segregated Solver* (PBSS) and the *Density-Based Coupled Solver* (DBCS) were employed for this purpose. The variations of velocity magnitude for the water droplets as well as the sand particles had similar trends in both the PBSS and the DBCS solvers. However, since the PBSS needs less computing memory than the DBCS, the *Pressure-Based Segregated Solver* was selected for the modelling of the air-sand-water three phase flows through the nozzle.

In general, the following results from the present numerical investigation can be concluded:

1. In the two and three phase flow the maximum air velocity contours were between the centre-line and the wall.
2. In the two and three phase flow the shock wave was almost eliminated and also slightly moved toward the exit of the nozzle.
3. The sand particles' total average momentum was increased by about 1.47 percent by adding 60K to the secondary phases.
4. By adding 0.05 kg/s of water droplets to the air-sand flow the sand particles' velocity was decreased by about 22%.

CHAPTER 7

Conclusion and Future Works

7.1 Conclusion

The numerical method was used to simulate the air-sand-water three-phase supersonic turbulent flow through the converging-diverging nozzle. The review of literature showed that there is not any substantial analytical or experimental research on gas-liquid-solid three-phase flow through the nozzle. On the other hand, there is a lot of uncertainty about multi-phase turbulence flow that has not been properly modelled, so it is the lack of knowledge, and accuracy of the CFD solution could be affected by the uncertainty. One approach for determining the level of uncertainty and its effect on the analysis is to run a number of simulations with a variety of turbulence models and find out how the chosen model will deliver a series of desired results. Therefore, a comparative study of the results obtained from the combination of various turbulent and multi-phase models is considered as a reasonable approach on the validating of the air-sand-water three-phase flow through the nozzle. Similar turbulent and multi-phase models were used to simulate the air-water two-phase flow through the nozzle. A comparison of these results with the available experimental results would provide a measure of accuracy for the employed model for the air-sand-water three-phase flow.

In this study, the *Standard*, *RNG* and *Realizable k-ε* models as well as the *Spalart-Allmaras* and *Reynolds Stress* turbulence models were studied. In addition, the *Eulerian* and *Discrete Phase* models were utilized to simulate multi-phase flow through the nozzle. Following the presented results and discussion in previous chapters, this chapter will present a brief summary and main conclusions from the current study. This will include observation from the validation, single-phase and two-phase flow and air-sand-water three-phase flow.

Validation: The *discretisation error* is the most considerable error in the CFD. It is dependent on the quality of the computational grid. However, it is often quite difficult to exactly indicate the relationship between the quality of the computational mesh and accuracy of the solution before conducting the simulation itself. To arrive at a conclusion on the resolution of the computational mesh, it was necessary to pave the nozzle geometry with various numbers of meshes. In addition, the shape of the computational meshes (e.g. being tetrahedral or quadrilateral) was of importance as well. By computing of the wall y^+ distance (required for turbulent modelling) for various generated grids inside the nozzle and comparison of y^+ as well as static and dynamic pressure distributions through the nozzle, it was possible to conclude that the quadrilateral meshes with a resolution of 44×630 were an ideal choice of shape and size.

In this study, the three-phase flow through the nozzle was modelled by utilizing the *FLUENT* package. Therefore, the *computer programming error check* and *usage error check* was focused on utilization of *FLUENT* software for simulating of the three-phase flow through the nozzle. As a first step, the results from the modelling of air-water un-premixed two-phase flow through the nozzle was compared and validated with experimental and analytical data. In this simulation, the *Realizable k-ε* and *Discrete Phase* models were employed. The comparison between the

current numerical results and the results from analytical calculations as well as available experimental data indicated a good range of accuracy for the numerical analyses. The correlation between the numerical and experimental results was even higher than those between the analytical and experimental results.

In the second step of *computer programming error check*, the results from the modelling of the air-water premixed two-phase flow was compared with those from the air-water un-premixed two-phase flow. The results confirmed that by increasing the pressure difference, the quality of the mixture at the nozzle's exhaust for the un-premixed flow increases and it is going to be same as the premixed flow.

Single-phase and two-phase flows: In this study, the air single-phase flow through the nozzle was computed not only for the sake of the validation with available analytical data, but also for the assessment of the effects of secondary phases on the nozzle performance. Various turbulence models including the *Standard*, *RNG* and *Realizable k-ε* models, *Spalart-Allmaras* and *Reynolds Stress* turbulent models were examined for the air single-phase flow through the nozzle. The simulation results showed that the choice of turbulence model has no significant effect on the single-phase flow distribution throughout the nozzle.

The study of the effects of various inlet and/or exhaust pressures, pressure differences, and pressure ratios on the characteristics of the air flow through the nozzle was the second step in this study. The study of Mach number, temperature, and velocity distributions for constant inlet pressure versus constant outlet pressure confirmed that the constant inlet or outlet pressure has no significant effects on the Mach number distribution as well as temperature and velocity profiles throughout the nozzle. Despite this, density and pressure distributions were considerably varied throughout the nozzle for constant inlet and constant outlet pressures.

The third step of simulation of the single-phase flow consisted of employing various inlet temperatures. The results showed that the inlet temperature does not have a significant effect on the Mach number as well as the static and dynamic pressures whilst the velocity of flow in the nozzle as well as its density and temperature profiles were considerably dependent on the inlet temperature.

The air-sand two-phase flow was simulated for various sand volume fractions and different inlet pressures by employing both the *Eulerian* and *Discrete-phase* models. The flow of sand particles throughout and the exhaust of the nozzle were analyzed, and average and maximum particles velocity were compared for different inlet air pressure.

In the *Eulerian* model the employed sand volume fraction was between 10% and 16%. Comparison between the air single-phase flow and the air-sand two-phase flow indicated that by adding the sand particles to the air flow, not only a significant difference for pressure and velocity distribution through the nozzle could instantaneously be observed but also the oscillation in the static pressure and velocity distributions due to the shock waves vanished. The simulation results also revealed that by increasing the volume fractions for the sand particles the velocity magnitude of the air flow as well as sand particles decreases.

In the *Discrete Phase* model the air-sand two phase flow through the nozzle with various sand mass flow ratios, from 0.005 kg/s to 0.03 kg/s, and different inlet pressures were computed. The following results could be confirmed from these simulations:

a) The sand particles alleviate the shock wave effects on the nozzle.

b) The maximum and mean air exhaust velocity was decreased by adding sand particles.

c)There are considerable differences between the speed of particles which move without hitting the wall and the others which hit the wall in the converging section of the nozzle.

d) By increasing the sand particles mass flow rate, from 0.005 kg/s to 0.03 kg/s, the particles exhaust velocity was decreased.

e) The location of the shock wave inside the nozzle did not have a significant effect on the velocity of the sand particles.

Air-sand-water three-phase flow: Most sand-blasting machines use water droplets besides of sand particles which are propelled by high inlet pressure air flow through the nozzle. The *Discrete Phase* model was used to model the air-sand-water three-phase flow through the nozzle with different boundary conditions, various sand particle and water droplet mass flow rates. In addition, both the *Pressure-Based Segregated Solver* (PBSS) and *Density-Based Coupled Solver* (DBCS) were employed for this purpose.

The comparison of the PBSS and the DBCS was made by considering a three-phase flow with the following boundary and flow conditions: $P_{in} = 1.5atm$, $T_{in} = 300K$, $\dot{m}_{sand} = 0.02kg/s$, $\dot{m}_{water} = 0.01kg/s$. In addition, the same sand particle and water droplet diameters were used in both cases. The variations of velocity magnitude for the water droplets as well as the sand particles had similar trends in both the PBSS and the DBCS solvers. However, since the PBSS needs less computing memory than the DBCS, therefore the *Pressure-Based Segregated Solver* was selected for the modelling of the air-sand-water three phase flows through the nozzle.

The results from all the one, two and three phase flows through similar geometries and boundary conditions were compared in order to realise the effect(s) of secondary phases on the main flow characteristics. The comparison results revealed the following main conclusions:

a) In the two and three phase flows the counters of maximum air velocity are between the centre-line and walls.

b) The aforementioned velocity counters move towards the nozzle wall by adding water droplets to the flow.

c) The maximum and mean exhausts velocity for air decreases by adding water droplets to the flow.

d) By employing the same mass flow rates for sand particles and water droplets (i.e. 0.01 kg/s) and air inlet pressure of 2 atm, the average exhaust velocity for air and sand particles decrease about 10% and 6%, respectively compared with the average exhaust velocity for the two-phase flow.

In this study the effect of three main parameters influential on the nozzle flow characteristics including various mass flow rates of water droplets and sand particles, different air inlet pressures and the effects of increasing inlet temperature of water droplets and sand particles were also examined. The extracted conclusions from studying of each one of those main parameters are listed below:

1. **Various mass flow rates of water droplets and sand particles**:

Water droplets and sand particles with various overall mass flow rates from 0.01 to 0.05 kg/s and 0.01 to 0.03 kg/s, respectively, were propelled into the nozzle by air flow with 2atm inlet pressure. The inlet temperatures of abrasive material and air were equal to 300K. From this test, the following conclusions could be achieved:

a. By adding more water droplets into the constant mass flow rate of sand particles and air flowing through the nozzle, the shock wave effects on the pressure distribution was suppressed.
b. By increasing the water mass flow rate from 0.01kg/s to 0.05kg/s, the air exhaust average velocity was decreased about 10% excluding sand mass flow rates.

c. For the same inlet pressure, temperature and sand mass flow rates, about 10% decrease on air mass flow rate was observed when the water mass flow rates were increased from 0.01kg/s to 0.05kg/s.
d. Higher water mass flow rates can have some effect on the average velocity of sand particles. A reduction of about 20% was observed when the water mass flow rate was increased from 0.01kg/s to 0.05kg/s.
e. The maximum velocity of water droplets is about 41% more than that of sand particles at the same flow condition and mass flow rates.
f. The water mass flow rate and total average momentum of sand particles at the exhaust have an inverse relation. A five times increment in water mass flow rate, from 0.01 kg/s to 0.05 kg/s, could decrease the total momentum of sand particles at around 17 to 20 percent.

2. Various air inlet pressures:

Water droplets with various overall mass flow rates from 0.01 to 0.05 kg/s were simulated with constant sand mass flow rate of 0.02 kg/s. The inlet air flow pressure was varied from 1 to 3atm with increment steps of 0.5atm. In addition, the inlet temperature for the abrasives as well as air flow was set to be 300K. The following results could be highlighted from this test:

a. The maximum air exhaust velocity lies between the wall and axis of the nozzle. By increasing the air inlet pressure, the maximum velocity increases too whilst the velocity in the nozzle's axis decreases. For instance, a water mass flow rate of 0.04kg/s with air inlet pressure of 3atm could result in an exhaust velocity for air on the nozzle axis which is nearly equal to zero.
b. By a three times increase in air inlet pressure, from 1atm to 3atm, the mean exhaust velocity of sand particles rises up to 52 to 62 percent

depending on the water mass flow rate.

c. A fivefold increase in the water mass flow rate, from 0.01kg/s to 0.05kg/s, for various air inlet pressures, could also result in a decline of about 16 to 21 percent in the mean exhaust velocity of sand particles.

3. Various inlet temperature of water droplets and sand particles:

By increasing the initial temperature of water droplets and sand particles from ambient temperature of 300K to 360K the following could be observed:

a. The air exhaust velocity shows an increase of up to about 3.4%.
b. A reduction in the mass flow rate through the nozzle could be achieved by increasing the inlet temperature of the sand particles as well as the water droplets.
c. In constant inlet pressures for air, increasing inlet temperature of the sand particles and the water droplets, had no significant effect on the velocity of the sand particles.
d. In constant inlet mass flow rates for air, increasing inlet temperature of abrasive media could provide a higher momentum for the sand particles.

In the current study, the best model for simulating the air-sand-water three-phase flow was concluded to be the *Discrete Phase Model.* Although the commercial CFD software of FLUENT 6.3.26 was capable of employing this model, some limitations were observed in practice. These can be summarised in the following:

a. In the Discrete Phase model, particles' trajectories start from inlet boundary grids. On the other hand since the boundaries do not usually consisting of uniform grid distribution, therefore there is no appropriate way to enter uniform particles or droplets to the

computational domain.

b. There is no choice of selecting different Discrete Phase model conditions for various secondary phases in the wall boundary panel. For example, the discrete phase reflection coefficients for all secondary phases are defined the same and simultaneously.
c. Although in the Discrete Phase model, the erosion, accretion, collision and break-up options are available for selecting or deselecting simultaneously for both droplets and particles, whilst some of these parameters are important to droplets and some others are good for simulation of particles' behaviour in multi-phase flows.

7.2 Future Works

This study carried out some basic simulations of the air-sand-water three-phase supersonic flow through the nozzle. In addition, the effects of some important parameters on the nozzle three-phase flow characteristics were investigated and the optimum parameters and conditions were demonstrated accordingly. The following remarks can be made for the future research on the optimization of sand blasting nozzles:

1. Investigating the three-phase flow through the nozzle with various diverging cone angles.
2. A study of supersonic three-phase flow separation throughout the nozzle and the effects of this separation on the quality for the three-phase flow at the nozzle's exhaust.
3. Considering the effects of a modified nozzle with circular thread(s) in the diverging part on the quality of the three-phase flow exiting the nozzle.
4. Investigating the impinging of a three-phase supersonic flow jet over the force-plate. The flow can exit from both separation nozzles and nozzles with circular thread(s).
5. Evaluation of heated water's effects on air-sand-water three-phase flow through the sand blasting hose.
6. Investigating the effects of a modified nozzle with a swirl multi-phase flow in the entrance of the nozzle on the performance of a sand blasting system.

REFERENCES

Achtsnick, M. Geelhoed, P.F. Hoogstrate, A.M. and Karpuschewski, B., 2005. Modelling and evaluation of the micro abrasive blasting process. *Wear,* 259, pp.84-94.

AIAA, 1998. *Guide for the Verification and Validation of Computational Fluid Dynamics Simulations,* American Institute of Aeronautics and Astronautics, AIAA-G-077-1998, Reston, VA.

Anderson, I.E. and Terpstra, R.L., 2002. Progress toward gas atomization processing with increased uniformity and control. *Materials Science and Engineering,* A326, pp.101-109.

Aydin, O. and Unal, R., 2011. Experimental and numerical modeling of the gas atomization nozzle for gas flow behaviour. *Computers & Fluids,* 42, pp.37-43.

Balachandran, P., 2006. Fundamentals of Compressible Fluid Dynamics. Prentice-Hall of India.

Bejan, A. and Kraus, A.D., 2003. *Heat Transfer Handbook.* New Jersey: JOHN WILEY & SONS.

Bejan, A., 2004. Convection Heat Transfer. 3rd ed. John Wiley & Sons.

Brennen, C.E., 2005. *Fundamentals of Multi-phase Flow.* Cambridge University Press.

Cebeci, T. Shao, J.P. Kafyeke, F. and Laurendeau, E., 2005. *Computational Fluid Dynamics for Engineers.* Long Beach: Horizons Publishing, Springer.

Cebeci, T., 2002. *Convective Heat Transfer.* 2nd ed. Long Beach: Horizons Publishing, Springer.

Cebeci, T., 2003. *Turbulence Models and Their Application.* Long Beach: Horizons Publishing, Springer.

Chen, Z. Zheng, C. Feng, Y. and Hofmann, H., 1995. Distributions of flow regimes and holdups in three-phase fluidized beds. *Chemical Engineering Science,* 50 (13), pp.2153-2159.

Choudhury, D., 1993. *Introduction to the Renormalization Group Method and Turbulence Modelling.* FLUENT Inc., Technical Memorandum TM-107.

Ciampini, D. Spelt, J.K. and Papini, M., 2003a. Simulation of interference effects in particle streams following impact with a flat surface: Part I. Theory and analysis. *Wear*, 254, pp.237-249.

Ciampini, D. Spelt, J.K. and Papini, M., 2003b. Simulation of interference effects in particle streams following impact with a flat surface: Part II. Parametric study and implications for erosion testing and blast cleaning. *Wear,* 254, pp.250-264.

Cinar, G. Yilbas, B.S. and Sunar, M., 1997. Study into nucleation of steam during expansion through a Nozzle. *International Journal of Multiphase Flow*, 23 (6), pp.1171-1188.

Crowe, C.T., 2005. Multiphase Flow Handbook. Taylor & Francis Group.

Crowe, C.T., 2006. *Multi-phase flow handbook.* CRC Press, Taylor & Francis Group.

Davidson, P.A., 2004. *Turbulence: An Introduction for Scientists and Engineers.* New York: Oxford University Press Inc.

Environmental Protection Agency, 1997. Emission factor documentation for AP-42: Section 13.2.6 Abrasive Blasting, final report. [online] Available at: <www.epa.gov/ttn/chief/ap42/ch13/bgdocs/b13s02-6.pdf> [Accessed 15 September 2010]

Fairchild, C.N., 1929. *Sand blast nozzle.* U.S. Pat. 1,703,029.

Fan, J.M. Wang, C.Y. and Wang, J., 2009. Modelling the erosion rate in micro abrasive air jet machining of glasses. *Wear,* 266, pp.968-974.

FLUENT User Guide, 2006. *FLUENT 6.3.* FLUENT Inc.

Gerber, A.G. and Kermani, M.J., 2004. A pressure based Eulerian–Eulerian multi-phase model for non-equilibrium condensation in transonic steam flow. *International Journal of Heat and Mass Transfer*, 47, pp.2217-2231.

Gidaspow, D., Bezburuah, R. and Ding, J., 1992. Hydrodynamics of Circulating Fluidized Beds, Theory Approach. Proceedings of the 7th Engineering Foundation Conference on Fluidization, pp. 75-82.

Gimbun, J. Chual, T.G. Choong, T. S. Y. and Fakhru'l-Razi A., 2005. Prediction of the effects of cone tip diameter on the cyclone performance. *Journal of Aerosol Science*, 36 (8), pp.1056-1065.

Graebel, W.P., 2007. *Advanced Fluid Mechanics*, Burlington: Elsevier.

Hemidi, A. Henry, F. Leclaire, S. Seynhaeve, J.M. and Bartosiewicz, Y., 2009. CFD analysis of a supersonic air ejector. Part I: Experimental validation of single-phase and two-phase operation. *Applied Thermal Engineering*, 29, pp.1523-1531.

Karpuschewski, B. Hoogstrate, A.M. and Achtsnick, M., 2004. Simulation and improvement of the micro abrasive blasting process. *Annals CIRP*, 53 (1), pp.251-254.

Kennedy, D.M. Vahey, J. and Hanney, D., 2005. Micro shot blasting of machine tools for improving surface finish and reducing cutting forces in manufacturing. *Materials and Design*, 26, pp.203-208.

Kheloufi, K. and Amara, E.H., 2010. Numerical modelling of gas/particles diphasic jet in laser cladding by coaxial Nozzle. *Physics Procedia*, 5, pp.347-352.

Kolev, N. I., 2007. *Multi-phase flow dynamics, thermal and mechanical interactions*, 3rd ed. New York: Springer

Lear, W.E. and Sherif, S.A., 1997. Two-phase non-dissipative supersonic nozzle flow analysis for maximum condensed phase momentum flux. *Acta Astronautica*, 40 (10), pp.707-712.

Lemonnier, H. and Selmer-olsen, S., 1992. Experimental investigation and physical modelling of two-phase two-component flow in a converging-diverging nozzle. *Int. Journal of Multiphase Flow*, 18 (1), pp. 1-20.

Lemonnier, H. and Selmer-Olsen, S., 1992. Experimental investigation and physical modelling of two-phase two-component flow in a converging-diverging nozzle. *International Journal of Multiphase Flow*, 18 (1), pp.1-20.

LI, Z.D. Zhang, C.Q. LI, Z. Zhang, Y. and Xu, W.Y., 2008. Simulation of gas flow field in Laval Nozzle and straight Nozzle for powder metallurgy and spray forming. *Journal of Iron and Steel research, International*, 15 (6), pp.44-47.

Liu, H. Wang, J. Kelson, N. and Brown, R.J., 2004. A study of abrasive waterjet characteristics by CFD simulation. *Journal of Materials Processing Technology*, 153-154, pp.488-493.

Miao, H.Y. Demers, D. Larose, S. Perron, C. and Levesque, M., 2010. Experimental study of shot peening and stress peen forming. *Journal of Materials Processing Technology*, 210, pp.2089-2102.

Moshfegh, A. Shams, M. Ebrahimi, R. and Farnia, M.A., 2009. Two-way coupled simulation of a flow laden with metallic particulates in overexpanded TIC nozzle. *International Journal of Heat and Fluid Flow*, 30, pp.1142-1156.

Moukalled, F. Darwish, M. and Sekar, B., 2003. A pressure-based algorithm for multi-phase flow at all speeds. *Journal of Computational Physics*, 190, pp.550-571.

Mulhall, R.C. and Nedas, N.D., 2007. Impact blasting with glass beads. *Metal Finishing*, 105 (10), pp.65-71.

Nag, P.K., 2008. Engineering Thermodynamics. 4th ed. McGraw-Hill.

Nudelman, and Abbott, K., 2000. Plastic media blasting. *Metal Finishing*, 98 (6), pp.485-492.

Occupational Safety & Health Administration, 2010. Silicosis in sandblasters use silica substitutes. [online] available at: <http://www.osha.gov/SLTC/etools/silica/protect_against/stopsandblasters/stopsandblasters.html> [Accessed 21 April 2010]

Ozalp, N. and Kanjirakat, A., 2010. Lagrangian characterization of multi-phase turbulent flow in a solar reactor for particle deposition prediction. *International Journal of Hydrogen Energy*, 35, pp.4496-4507.

Park, J.S. and Baek, S.W., 2003. Interaction of a moving shock wave with a two-phase reacting medium. *International Journal of Heat and Mass Transfer*, 46 (24), pp.4717-4732.

Patil, D.J. van Sint Annaland, M. and Kuipers, J.A.M., 2005. Critical comparison of hydrodynamic models for gas–solid fluidized beds-Part I: bubbling gas-solid fluidized beds operated with a jet. *Chemical Engineering Science*, 60 (1), pp.57-72.

Pirker, S. Kahrimanovic, D. Kloss, C. Popoff, B. and Braun, M., 2010. Simulating coarse particle conveying by a set of Eulerian, Lagrangian and hybrid particle models. *Powder Technology*, 204, pp.203-213.

Pougatch, K. Salcudean, M. Chan, E. and Knapper, B., 2008. Modelling of compressible gas-liquid flow in a convergent–divergent nozzle. *Chemical Engineering Science*, 63, pp.4176-4188.

Pougatch, K. Salcudean, M. Chan, E. and Knapper, B., 2009. A two-fluid model of gas-assisted atomization including flow through the nozzle, phase inversion, and spray dispersion. *International Journal of Multiphase Flow,* 35, pp.661-675.

Ranade, V.V., 2002. *Computational flow modeling for chemical reactor engineering.* Vol. 5. Academic Press.

Raykowski, A. Hader, M. Maragno, B. and Spelt, J.K., 2001. Blast cleaning of gas turbine components: deposit removal and substrate deformation. *Wear*, 249, pp.127-132.

Rosenberg, B. Yuan, L. and Fulmer, S., 2006. Ergonomics of abrasive blasting: A comparison of high pressure water and steel shot. *Applied Ergonomics,* 37, pp.659-667.

Samuelsberg, A. and Hjertager, B.H., 1996. An experimental and numerical study of flow patterns in a circulating fluidized bed reactors. *International Journal of multiphase flow,* 22 (3), pp.575-591.

Shipway, P.H. and Weston, D.P., 2009. Thermal effects in blasting and erosion of polymeric materials. *Journal of Materials Processing Technology*, 209, pp.6161-6167.

Simpson, D.A. and White, A.J., 2005. Viscous and unsteady flow calculations of condensing steam in nozzles. *International Journal of Heat and Fluid Flow*, 26, pp.71-79.

Spur, G. Uhlmann, E. and Elbing, F., 1999. Dry-ice blasting for cleaning: process, optimization and application. *Wear*, 233-235, pp.402-411.

Stevens, T. and Hobart, H.M., 1906. *Steam Turbine Engineering.* New York: The MacMillan Co.

Stoltz, W.W., 1991. *Sand blast nozzle.* U.S. Pat. 5,036,631.

Syamlal, M. and O'Brien, T.J., 1989. Computer Simulation of Bubbles in a Fluidized Bed. AIChE Symposium Series, vol. 85, pp. 22-31.

Tilghman, B.C., 1870. *Improvement in cutting and engraving stone, metal, glass, etc.* U.S. Pat. 108,408.

Tsinontides, S.C., 1999. A theoretical investigation of gas–solid flow exiting a fluidized bed into a standpipe. *Powder Technology,* 101, pp.211-228

Vatanakul, M. Zheng, Y. Jia, L. Zhang, K., 2005. Regime transition in a gas-liquid-solid fluidized bed. *Chemical Engineering Journal,* 108, pp.35-45.

Wen, C.Y. and Yu, Y.H., 1966. Mechanics of Fluidization. Chemical Engineering Progress Symposium Series, vol. 62, pp. 100-111.

Weston, D.P. Shipway, P.H. and Harris, S.J., 2005. Coating removal from an industrial polypropylene blend by cryogenic blasting: the development of substrate damage. *Wear*, 258, pp.392-401.

White, F.M., 2003. *Fluid Mechanics.* 5th ed. McGraw-Hill.

Wilcox, D.C., 1994. *Turbulence Modelling for CFD.* California: DCW Industries.

Winkler, F., 1926. *Manufacturing active carbon*. U.S. Pat. 1,582,718.

Xiao, Q. Tsai, H.M. and Papamoschou, D., 2007. Numerical Investigation of Supersonic Nozzle Flow Separation. *American Institute of Aeronautics and Astronautics (AIAA),* 45 (3), pp.532-541.

Xu, J. and Zhao, C., 2007. Two-dimensional numerical simulations of shock waves in micro convergent–divergent nozzles. *International Journal of Heat and Mass Transfer,* 50, pp.2434-2438.

Yang, Y. and Shen, S., 2009. Numerical simulation on non-equilibrium spontaneous condensation in supersonic steam flow. *International Communications in Heat and Mass Transfer*, 36, pp.902-907.

Yin, S. Wang, X.F. and Li, W.Y., 2011. Computational analysis of the effect of nozzle cross-section shape on gas flow and particle acceleration in cold spraying. *Surface & Coatings Technology,* 205, pp.2970-2977.

Zekovic, S. Dwivedi, R. and Kovacevic, R., 2007. Numerical simulation and experimental investigation of gas–powder flow from radially symmetrical nozzles in laser-based direct metal deposition. *International Journal of Machine Tools & Manufacture,* 47, pp.112-123.

Zeoli, N. and Gu, S., 2006. Numerical modelling of droplet break-up for gas atomization. *Computational Materials Science,* 38, pp.282-292.

Zhang, J.P., Grace, J.R., Epstein, N. and Lim, K.S. 1997. Flow regime identification in gas-liquid flow and three-phase fluidized beds. *Chemical Engineering Science,* 52, pp.3979-3992.

Zhao, Y. Tang, L. Luo, Z. Liang, C. Xing, H. Wu, W. and Duan, C., 2010. Experimental and numerical simulation studies of the fluidization characteristics of a separating gas–solid fluidized bed. *Fuel Processing Technology*, 91, pp.1819-1825.

Zhu, G. Li, D. Zhang, A. and Tang, Y., 2011. Numerical simulation of metallic powder flow in a coaxial nozzle in laser direct metal deposition. *Optics & Laser Technology*, 43, pp.106-113.

Zucker, R.D. and Biblarz, O., 2002. Fundamentals of Gas Dynamics. 2nd ed. John Wiley & Sons, Inc.

APPENDIX

Abrasive Blasting Media

There are a variety of abrasive blast materials that can be used in air or water blasting processes used to remove paint or any other contaminants from engine heads, valves, pistons, turbine blades in the aircraft, automotive industries, vessels and marine structures, and etc. Blast material particles, also referred to as "grit", are about 1/8" in diameter. These normally jagged or sharp-edged particles become rounded and somewhat reduced in size after being blasted against work-pieces (for example to remove paint).

Spent abrasive blast material may contain a variety of pollutants. Fresh, or unused abrasive blast media is even considered a "dangerous" or "special" waste in some states due to gill abrasion which can be fatal to some fish; therefore, abrasive blast media, used or unused, should not be discharged into State waters.

The general information of some common abrasive blasting media are summarized in following sections of the present appendix.

Aluminium Oxide

Aluminium oxide is an amphoteric oxide with the chemical formula Al2O3. It is commonly referred to as alumina, Aluminium oxide is a sharp, abrasive blasting material used in sand blast finishing. It is harder than most common dry abrasive blast media and will cut even the hardest metals and surfaces.

Density	3.95-4.1 g/cm^3
Melting point	2072 °C
Boiling point	2977 °C
Solubility in water	insoluble

Approximately 50% lighter than metallic media, aluminium oxide abrasive grain has twice as many particles per pound. The fast-cutting action minimizes

damage to thin materials by eliminating surface stresses caused by heavier, slower cutting media.

Aluminum oxide grit powder has a wide variety of applications, from cleaning engine heads, valves, pistons and turbine blades in the aircraft industry to lettering in monument and marker inscriptions. It is also commonly used for matte finishing, as well as cleaning and preparing parts for metalizing, plating and welding. Aluminum oxide abrasive grain is the best choice for an abrasive sand blasting and polishing grain as well as for preparing a surface for painting.

White Aluminium Oxide

White aluminium oxide (or white aluminium oxide) grit is a 99.5% ultra pure grade of blasting media. White aluminium oxide is increasingly being used in critical, high-performance microdermabrasion equipment. The purity of this media along with the variety of grit sizes available make it ideal for both traditional microdermabrasion processes as well as high-quality exfoliating creams.

Density	3.96 g/cm^3
Melting point	2000 °C
Max usable temp.	1900 °C
Hardness	2000-2200 kg/mm^2

White aluminium oxide is an extremely sharp, long-lasting blasting abrasive that can be recycled many times after the initial media blasting. It is the most widely used abrasive in blast finishing and surface preparation because of its cost, longevity and hardness. Harder than other commonly used blasting materials, white aluminum oxide grains penetrate and cut even the hardest metals and sintered carbide.

Approximately 50% lighter than metallic media, white aluminum oxide has twice as many particles per pound. The fast-cutting action minimizes damage to thin materials by eliminating surface stresses caused by heavier, slower-cutting media blasting grits. White aluminum oxide blasting media has a wide variety of applications, including cleaning engine heads, valves, pistons and turbine blades in the aircraft and automotive industries. White aluminum oxide is also an excellent choice for preparing a hard surface for painting.

Corn Cob

Density	20-30 g/cm^3
Particle Shape	Angular, multi-faceted
Hardness	4.5 Moh's

Corn cob blasting grit is a safe blasting media for delicate parts in addition to use as the preferred blasting grit for log homes and other wood surfaces. Corn cob grit abrasive will remove surface contamination, debris and coatings with little to no impact on the substrate. Corn cob is a biodegradable, organic blasting media that is obtained from the hard woody ring of the cob. It is resistant to break down and can be re-used multiple times in the blasting process. Corn cob is available in a variety of grit sizes and presents no health or environmental hazards. Virtually dust-free blasting with no sparking leaves a clean and dry surface.

Proper selection of corn cob grit size is important in blasting operations to balance aggressiveness with desired results.

Crushed Glass Grit

Density	1300 kg/m^3
Shape	Angular
Hardness	5-6 Moh's

Crushed glass grit is manufactured from 100% post-consumer, recycled bottle glass. This glass grit delivers superior performance relative to mineral/slag abrasives. Crushed glass grit contains no free silica, is non-toxic and inert and contains no heavy metals typically found in coal and copper slags.

The angular particles in crushed glass grit allow for aggressive surface profiling and removal of coatings such as epoxy, paint, alkyds, vinyl, polyurea, coal tar and elastomers. Glass grit is lighter weight than many slags, allowing for increased consumption efficiency and production time – up to 30-50% less glass grit used. Crushed glass grit delivers very

low particle embedment, which produces a whiter, cleaner finish. Similar to many slags, crushed glass grit has a hardness of 5.0 – 6.0 on the Moh's Hardness Scale.

Since crushed glass grit is manufactured from recycled bottle glass, it contains no free silica which is commonly found in blasting sand. The use of post-consumer glass directly benefits the environment by diverting waste from landfills. Crushed glass grit is free of heavy metals such as arsenic, lead, asbestos, beryllium, titanium, etc., all typically found in coal and mineral slags.

Glass Beads

Density	2500 kg/m^3
Shape	Round
Hardness	5-6 Moh's

Glass bead or dry bead blasting uses spherical beads for cleaning metal parts without damaging the surface. This media offers a gentle cleaning process creating a softer, more cosmetic finish than angular abrasives. Glass bead abrasives provide a silica-free option for blast cleaning, peening, honing, descaling and light deburring. Glass beads can be recycled approximately 30 times. Chemically inert and environmentally friendly, glass beads are an acceptable method of metal cleaning or surface finishing when properly controlled.

Glass bead cleaning is suitable for soft metals such as aluminum and brass. Ideal for pistons, engine blocks and light rust removal. Glass bead is a good choice for the restoration of car parts, motorcycles and other components where a gentle cleaning action is required.

Plastic Abrasives

Plastic Abrasives such as Urea, Acrylic, and Melamine deliver a highly effective stripping rate, removing coatings and contaminants without damaging the base metal. They are ideal for paint stripping, cleaning, deflashing and deburring operations on aluminium and other soft metals.

Plastic abrasives are widely used for restoring components in the aerospace and automotive industries.

Arcylic

Acrylic media is the longest lasting media on the market. It is very gentle on the substrate and engineered for stripping the most sensitive surfaces while providing an effective stripping rate. Acrylic media offers an excellent range of stripping capabilities and is termed a multipurpose media by its users. Standard mesh sizes are 16-20, 20-30 and 30-40.

Density	1.16-1.5 g/cc
Shape	Angular- cubical
Hardness	3.2-4 Moh's

Melamine

Melamine is engineered for stripping the most difficult surfaces while providing an effective stripping rate. Melamine is the most aggressive plastic abrasive, offering an excellent range of stripping capabilities. Melamine can be used as a replacement for glass beads and other harsh abrasives. Standard mesh sizes are 8-12, 12-16, 16-20, 20-30, 30-40 and 60-80.

Urea

Urea is a plastic grain stripping abrasive used in sandblasting operations. It is the most widely used plastic media. Urea is environmentally friendly and recyclable - an alternative to chemical stripping. Urea is formulated to meet an increased level of stripping performance where stripping speed outweighs other considerations. Urea is able to strip tough coatings with an impressive strip rate. Urea is typically used for less sensitive applications. Standard mesh sizes are 8-12, 10-20, 12-16, 16-20, 20-30, 30-40 and 40-60.

Pumice

Pumice is a natural mineral - volcanic ash formed by the solidification of lava that is permeated with gas bubbles. Pumice powder is used chiefly as an abrasive and is among the softest of all media. Use pumice powder for less aggressive operations where the protection of the surface is of supreme importance. Pumice is the best media choice for tumbling plastics.

Silicon carbide

Silicon carbide is the hardest blasting media available. High-quality silicon carbide media is manufactured to a blocky grain shape that splinters. The resulting silicon carbide abrasives have sharp edges for blasting. Silicon carbide has a very fast cutting speed and can be recycled and reused many more times than sand. The hardness of silicon carbide allows for much shorter blast times relative to softer blast media.

Density	3.21 g/cm^3
Melting point	2730-3003 °C
Hardness	9-9.5 Moh's

Silicon carbide grit is the ideal media for use on glass and stone in both suction or siphon and direct pressure blast systems. The ability to be recycled multiple times results in a cost-effective silicon carbide grit blast media with optimal etching results.

Since silicon carbide grit is harder than aluminum oxide, it can be used efficiently for glass engraving and stone etching. Silicon carbide grit blast media has no free silica, does not generate static electricity and is manufactured to contain minimal magnetic content.

Steel grit

Steel grit blasting is used for aggressive cleaning projects such as stripping contaminants from steel and other industrial metals. The cleaning action of steel grit produces an etched surface providing excellent adhesive properties for a variety of paints and coatings.

Density	3.7-4.4 g/cm^3
Shape	Angular
Hardness	40-60 RC

Steel grit blasting is suitable for steel and foundry metals and is also used for aircraft and aero-space components.

Steel shot

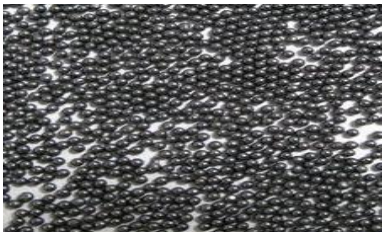

Density	4.5-4.7 g/cm^3
Shape	Round
Hardness	40-51 RC

Steel ball shot-blasting is one of the most widely used methods for cleaning and stripping metal surfaces and components. The process involves firing small steel balls (1-6mm diameter) at high speed against the surface of the metal or component. The finish is determined by the size of the steel shot. Larger shot has a more aggressive cleaning action and produces a rougher finish. Smaller steel shot creates a smoother, more polished surface.

Larger steel shot is ideal for removing rust, scale and other contaminants from heavy steel, malleable iron and grey iron castings. Smaller steel shot is suitable for cleaning small to medium sized ferrous and non-ferrous castings and machined parts.

Walnut shell

Density	0.5-0.7 g/cm^3
Shape	Angular
Hardness	3 Moh's

Walnut shell grit is the hard fibrous product made from ground or crushed walnut shells. When used as a blasting media, walnut shell grit is extremely durable, angular and multi-faceted, yet is considered a 'soft abrasive'. Walnut shell blasting grit is an excellent replacement for sand (free silica) to avoid inhalation health concerns. Cleaning by walnut shell blasting is particularly effective where the surface of the substrate under its coat of paint, dirt, grease, scale, carbon, etc. should remain unchanged or otherwise unimpaired. Walnut shell grit can be used as a soft aggregate in removing foreign matter or coatings from surfaces without etching, scratching or marring cleaned areas. When used with the right walnut shell blasting equipment, common blast cleaning applications include stripping auto and truck panels, cleaning delicate molds, jewellery polishing, armatures and electric motors prior to rewinding, deflashing plastics and

watch polishing. When used as a blast cleaning media, walnut shell grit removes paint, flash, burrs and other flaws in plastic and rubber molding, aluminium and zinc die-casting and electronics industries. Walnut shell can replace sand in paint removal, graffiti removal and general cleaning in restoration of buildings, bridges and outdoor statuaries. Walnut shell is also used to clean aircraft engines and steam turbines.

Olivine Sand

Olivine Sand as an abrasive media,is noted for its high Mohs Hardness, low uniform thermal expansion, sharp edges and its remarkable ability to resist fracture from thermal and impact shock. Olivine has been famous for years as an excellent abrasive media for Sand Blasting and Waterjet Cutting. Especially Indian Olivine Sand is having Highest Hardness and Lowest Loss on Ignition makes it an ideal and economical abrasive media for Sand Blasting and Waterjet Cutting.

Density	1.75 g/cm^3
Melting Point	1600 °C
Hardness	3 Moh's
Thermal Expansion	0.0083 in./in.
Thermal Conductivity @1000°C	0.0025 cal/s-cm -°C
Hardness	7 Moh's

Applications

- Refractory Sand, to manufacture manganese steel castings, and to form alloys
- Refractory Industry uses Olivine Sand for forming bricks and shapes, as it has a high melting point, moderate thermal expansion, and stable crystalline structure.
- Temperature-loadable moulding sand and facing sand in foundry.
- Replacement of Garnet Sand for Shot Blasting.

Typical Specification	
MgO	49% Max
SiO2	41% Max
Fe2O3	12 % Max
Al2O3	0.5-2.0% Max
Cr2O3	0.25% Max
CaO	0.2% Max
L.O.I.	1.50 Max

In this study Olivine particles were used as a sand particles' flow through the Nozzle. The following picture shows the microscopic photos of different size of olivine particles.